Density Functional Theory screening of molecular strategies for emergent magnetism at Copper interfaces

Thesis submitted in accordance with the requirements of the University of Liverpool for the degree of Doctor of Philosophy by

Lorena Martín Olivera

September 2017

To my parents and to everyone who has supported me during these years.

Density Functional Theory screening of molecular strategies for emergent magnetism at Copper interfaces

Lorena Martín Olivera

This Thesis aims to extend the available understanding of emergent magnetism at the interfaces between Cu and organic substrates by providing new insights into the role of metal distortion, metal-organics charge-transfer, organic π-conjugation and strain of the π-systems for ensuing appearance of magnetic ordering.

The first Chapter describes an overview of the molecular electronics and spintronics fields, discussing the most relevant experimental and theoretical progress in hybrid metal-organic interfaces and introducing some of the unsolved challenges that will be investigated in this Thesis. Chapter 2 provides a brief description of Density Function Theory as implemented in the VASP code. This Chapter also provides a description of the Stoner model for ferromagnetism and itinerant metamagnetism.

The influence of the Cu lattice distortion on the electronic and magnetic properties of bulk Cu is investigated in Chapter 3. It is found that the expansion of the FCC lattice enhances the Cu magnetic hardening. Chapter 4 aims to uncover the role of molecular π-conjugation for the magnetic hardening at Cu-organics interfaces. The results of my research suggest that neither molecular π-conjugation nor substantial charge-transfer may be strictly needed for magnetic hardening of Cu-substrates. Chapter 5 extends the research to other fullerenes in order to investigate the relationship between the strain on the molecular π-system and the magnetic

hardening at Cu-fullerene interfaces. The results of the simulations indicate that slightly strained π-systems lead to an enhancement of the interfacial magnetic hardening.

The final Chapter explores the potential of carbon-onions and the interplay between the strain of the π-system of the inner and outer fullerenes for the magnetic hardening at the interfaces between Cu and encapsulated fullerenes. Overall, the results of these investigations lead to the conclusion that intermediate strain of the π-system, as present in C_{60}, offers the most favourable interface re-hybridisation for emerging magnetic hardening out of all the systems considered.

Contents

Scientific Dissemination List

Under review article

L. Martin-Olivera, G. Teobaldi, D. Shchukin. The role of metal lattice expansion and molecular π-Conjugation for the Magnetic hardening at Cu-organic interfaces. The Journal of Physical Chemistry C, 2017.

Article being finalised for submission

L. Martin-Olivera, G. Teobaldi, D. Shchukin. The role of fullerene curvature the Magnetic hardening at Cu-fullerenes interfaces. Tentative submission to The Journal of Physical Chemistry Letters.

Conference contributions

September 2016: European Physical Society: Condensed Matter Division, CMD26. Groningen, The Netherlands. Poster contribution.

February 2016: The Frontiers of Materials Modelling: 10th Anniversary Symposium. The Thomas Young centre, university College London, London, United Kingdom. Poster contribution.

September 2015: Energy Material Symposium. Bath University, Bath, United Kingdom. Poster contribution.

List of Figures

List of Tables

List of Acronyms

aC	Amorphous carbon
AFM	Antiferromagnetic
APW	Augmented Plane Wave
BCC	Body-centred cubic
BFGS	Broyden-Fletcher-Goldfarb-Shanno
BzV	Metal-benzene complex
c	Centre
CM	Centre of mass
co	Compression
Cp	Cyclopentadienyl
d	Down
DFP	Davidon-Fletcher-Powell
DFT	Density Functional Theory
DOS	Density of States
DOS(E_F)	Density of States at the Fermi energy
e	Charge of the electron
E_0	Ground-state energy
EA	Electron affinity
E_F	Fermi Energy
E_{LUMO}	Energy of the LUMO level
ex	Expansion
FCC	Face-centered cubic
F_{HK}	Hohenberg-Kohn functional
FM	Ferromagnetic
GGA	General Gradient Approximation
GMR	Giant magnetoresistance

$\hat{H}$	Hamiltonian
h	Horizontal
ħ	Planck's constant/2π
H-DOO-PPV	Poly(dioctyloxy) phenyl vinylene
H_{ext}	External field
HFIs	Hyperfine interactions
HK	Hohenberg-Kohn
IP	Ionisation potential
Is	Stoner exchange integral
JT	Jahn-Teller effect
KS	Kohn-Sham
LAPW	Linear augmented plane wave
LDA	Local Density Approximation
LEDs	Light-emitting diodes
LSMO	$La_{x-1}Sr_xMnO_3$
m	Atomic magnetic moment
M	Magnetization
M	Monoclinic
M_∞	Saturation magnetization
MAEs	Magneto-crystalline anisotropy Energies
m_e	Mass of the electron
M_I	Mass of I^{th} nucleus
ML	Mono-layer
MPc	Metal phthalocyanines
MR	Magnetoresistance
MTJ	Magnetic tunnel junction
n(**r**)	Density of the system
NN	Nearest-Neighbour
O	Orthorhombic
OFETs	Organic field effect transistors
OLEDs	Organic light-emitting diodes
OMAR	Organic magnetoresistance

OSCs	Organic semiconductors
OSCs	Organic solar cells
PAC	Polyacetylene
PAW	Projected-Augmented Wave
PAW	Projector Augmented Wave
PBC	Periodic Boundary Conditions
PCP	Paracyclophane
PDOS	Projected density of states
PE	Polyethylene
PET	Polyethylene terephthalate
PFO	Polyfluorenes
PLEDs	Polymer light-emitting diodes
PP	Polaron pair
PPP	Poly(1,4-phenylene)
PPV	Poly(1,4-phenylene vinylene)
PS	Pseudo
PSCs	Polymer solar cells
PUR	Polyurethane
PVDF	Poly(vinylidene fluoride)
PW	Plane waves
Q	Charge transfer
r_c	Core region
R_{max}	Largest radius
R_{min}	Shortest radius
RMM-DIIS	Residual minimisation method-direct inversion in the iterative subspace
R_{MT}	Radius of the muffin-tin spheres
RPA	Random phase approximation
RRP3HT	3-hexylthiophene
RRP3HT	Poly 3-hexylthiophene
SCF	Self consistent field
SOC	Spin orbit coupling

SV	Spin valves
T	Tetragonal
T6	Sexithienyl
TMR	Tunnel magnetoresistance
TNAP	11,11,12,12-tetracyanonaptho-2,6-quinodimethane
T_S	Kinetic energy
u	Up
v	Vertical
VA	Vacuum level
vdW	Van der Waals
V_{ext}	External potential
XC	Exchange-correlation
Z_I	Nuclear charge of the I^{th} atom
ZMP	Zinc methyl phenalenyl
ΔE	Band-splitting
θ_p	Pyramidalisation angle
ψ	Wave function

Chapter 1

Recent progress and further research opportunities in electronic hybridisation at metal organic interfaces

Abstract

This Chapter presents an overview of recent progress in understanding the role of electronic hybridisation at the interface between a metal and an organic substrate for applications in the rapidly growing fields of molecular electronics and spintronics. Recent relevant experimental and theoretical progress is briefly reviewed to highlight the motivations behind research in the field, the available understanding as well as the unsolved challenges that require further fundamental insights into hybrid metal-organic interfaces, the subject of this Thesis.

1.1 Introduction

Energy consumption is increasing with the growth of the world population and the continuous economic expansion [1]. Development of sustainable energy technologies capable of improving generation, transmission, storage and use of renewable sources is needed to be able to accommodate the increasing demand. Magnetic materials play a major role in energy-based technologies; most often they are responsible for improving the overall performance by raising energy efficiency due to the possibility of decreasing the size, weight and maintenance cost of electric motors, leading to substantial economic and environmental benefits [2].

These technologies require magnetic materials thermodynamically and physically stable at operation conditions with high flux density and coercivity large enough to resist demagnetisation at high temperature [3]. In particular, wind turbines, motors in electric and hybrid vehicles and magnetic refrigeration technology rely on heavy rare-earth materials such as neodymium, dysprosium and praseodymium for permanent magnets. [4]. However, the current limited availability and their escalating price [5] are promoting the research and design of abundant new light atom rare-earth-free magnetic materials.

Some alternatives to substitute rare-earth materials such as ceramic magnets, molecular-based magnets and metamagnetic interfaces have been investigated. Ceramic magnets have high coercivity, they are cheap and easy to product however they are relatively brittle [6]. Molecular-based magnets have quite high coercivity but a low critical temperature, which means that they become demagnetize at low temperatures [7, 8]. Moreover, these materials are not conductors. Hence, ceramic and molecular magnets are unsuitable to substitute rare-earth magnets in energy applications where the magnet material must resist high mechanical stresses, high temperatures and needs to conduct electricity.

Hybrid (meta)magnetic materials and interfaces between differently magnetic components may be a versatile and low-cost approach to the development of new magnetic materials. However, the successful application of metamagnetic interface materials relies on new pathways to specific, controllable magnetic behaviours.

Several strategies to the design of cost-effective (meta)magnetic material can be employed: (1) one approach is the adsorption of organic substrates (molecules en/or polymers) on ferromagnetic substrates and (2) another strategy is the adsorption of molecules or polymers on non-magnetic metallic surfaces and generation of emergent magnetism via interfacial re-hybridisation.

Polymers in contact with magnetic materials are widely employed in organic electronics applications such as polymer light emitting diodes, solar cells, transistors and spintronic devices. The key challenge to develop new technologies based on this strategy is to understand the physics of charge transport, charge transfer, magnetism and luminescence, as well as, understanding the metallo-organic interfaces [9-13].

In this Chapter, I will first describe different organic electronics devices presenting metal/polymer interfaces, whose functioning depends on the control and manipulation of the electronic charge ignoring the spin of the electron. Then, we will introduce organic spintronics where the spin of electrons is taking into consideration to extend the functionality of the conventional metal-organic interfaces.

1.2 Organic electronics

Optoelectronic devices convert electrical power into (visible) light (light-emitting diodes, LEDs) or light into electrical power (solar cells, SCs). When the LED is made up of a polymer or an organic molecule they are called polymer light-emitting diodes (PLEDs) or organic light-emitting diodes (OLEDs) respectively. Following the same nomenclature, SCs made by polymers are called polymer solar cells (PSCs) while if they are made by organic molecules they are called organic solar cells (OSCs). In addition to these technologies, further application of organic electronics is found in organic field effect transistors (OFETs): (organic) semiconductor devices that enable use of one electrical signal to control another.

Functional polymers are used in organic electronics devices for their low cost and flexibility. Moreover, they offer the possibility to tune the polymer chemical structure and emerging physical properties in order to meet the requirements needed

to improve the device performance. Functional polymers for optoelectronic applications must be semiconductors in order to enable light absorption (emission) or voltage-dependent electrical conductivity as required for LEDs, SCs and OFETs. Most semiconductor polymers used to develop optoelectronic devices are π-conjugated polymers such as polyflourene [14], polyacetylenes [15] or poly(para-phenylene) due to their low-cost and ease of processing [16].

All these devices work due to the charge transfer through the organic semiconductor and optimisation of their efficiency rests on understanding of their fundamental properties as governed by the materials composition, morphology and processing as well as their interfaces with the electrodes and/or electrolytes were presents. In the following, I will introduce the basic design and working principles of each type of device.

1.2.1 Polymer light emitting diode

A polymer light-emitting diode (PLED) is a light-emitting diode in which the emissive electroluminescent layer is a polymer film that emits light in response to an electric current.

A schematic energy–level working principle diagram for PLED which represents the exciton dissociation mechanism is shown in Fig. 1.1. A PLED device is formed by a negative terminal (cathode) and a positive terminal (anode). Between the anode and cathode there are two layers made from polymers called the electron-conductive layer, which is next to the cathode, and the hole-conductive layer, next to the anode. As the electric current starts to flow, the polymer is oxidised in the anode side produced by the hole injection in the HOMO of the organic layer. Conversely, at the cathode, the polymer is reduced because electrons are injected in the LUMO of the functional material, thus a negative charge carried (electron) appear at the interface (step 1, in Fig. 1.1). The electron-conductive layer becomes negatively charged while the hole-conductive layer becomes positively charged. When an electron meets a hole in the light emitting layer, the recombination forms a bound electron-hole pair called polaron pair exciton, PP (step 2, in Fig. 1.1). The emission of light (photo-

luminescence) is produced when the excitons are relaxed into the ground state (step 3, in Fig. 1.1).

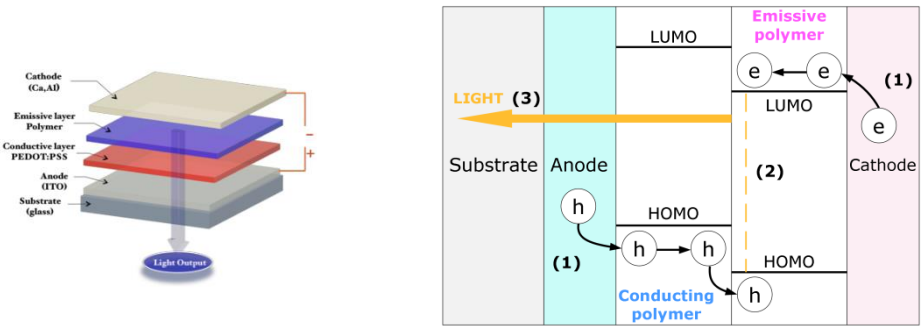

Figure 1.1: Adapted from [17]. Working principle of OLED: (1) charge injection and charge transport; (2) recombination of positive and negative polarons to form loosely bound PP; and (3) exciton formation and emission.

The energy difference between the HOMO (LUMO) level of the conducting polymer (emissive polymer) and anode (cathode) layer correspond to the energy offset of the ionisation potential (electron affinity). Therefore, the emissive polymers must have the LUMO energy similar to the cathode work function while the conductive polymer must have similar HOMO energy to the anode work function to facilitate charge injection [10, 11]. Some π-conjugated polymers films employed as electron-conductive layer in PLEDs are polyfluorenes (PFO), poly(1,4-phenylene) (PPP), poly(1,4-phenylene vinylene) (PPV) [18].

1.2.2 Solar cells

Solar cells convert (solar) light into electricity. Polymer solar cell (PSCs) devices can be composed by a single layer, a bilayer or a bulk hetero junction. The difference between them is the charge generation mechanism. Single layer devices are formed by only one active material while bilayers and bulk hetero junctions are based in two types of materials, an electrons donor layer and electrons acceptor layer.

Single active layer devices are formed by a sandwich of two electrodes, anode and cathode, with different work function and an organic layer in the middle. The

electrodes set up an electric field in the organic layer and this facilitates the separation of polaron pairs and the transport of the electrons to the anode and the holes to the cathode. However, single layer devices have very low efficiency [19].

Bilayer PSCs are formed by a cathode and an anode used for extracting the charges from the solar cell. Between them, electrons acceptor and holes acceptor layers and a central layer called light-harvesting layer which separate the excitons into electrons and holes. However, due to the short diffusion lengths of excitons in most conjugated polymer film, only a low rate of excitons can diffuse to the interface [20].

To solve this problem, bulk heterojunctions have been widely employed where the donor and the acceptor materials are mixed together to form a polymer blend. This approach improves the excitons dissociation because the length scale of the polymer blend is smaller than the diffusion length, favouring the harvest of excitons at the interface [21]. Therefore, polymer bulk heterojunction is one of the most promising types of solar cells due to its low-cost, larger efficiency and large scale fabrication by solution processing [22].

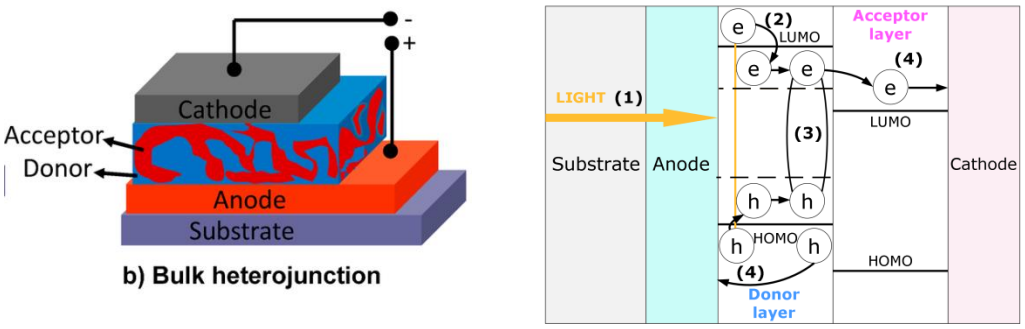

Figure 1.2: Adapted from [22]. **a)** Sandwich architecture of a polymer bulk heterojunction device. **b)** A schematic representation of the working principle of an OSC.

Fig. 1.2 shows the schematic structure representation of a bulk heterojunction PSC and the schematic energy-level diagram representing the exciton dissociation mechanism. The fundamental processes in a bulk heterojunction PSC are the inversed from PLEDs. In PSCs, driven by the absorption of light (step 1), highly localised excitons are generated (step 2). The next stage is the excitons diffusion to

the donor-acceptor interface. The excitons must be dissociated to generate electrical current, first creating charge transfer states (polarons pairs); then the polarons will be separated into a hole and an electron (step 3). Finally, the free charge carriers must move to the cathode and anode respectively (step 4). The overall device performance depends on the efficiency of all the steps, from light absorption to charge extraction.

Thin film polymer solar cells offer a low cost, light weight, flexibility and environmental friendly alternatives to their inorganic counterpart based on materials such as crystalline silicon, cadmium telluride, or copper indium germanium selenide [21]. Functional polymers employed in optoelectronic devices need to accomplish certain specifications. For instance, the first criteria to choose a polymer for solar cell application is the efficiency absorbing solar energy, the polymer band gap should be between 1 and 2 eV to match the energy of the maximum fraction of visible light photon reaching the Earth [23].

Moreover, they must be able to transport charge carriers (electrons and holes) from the electrodes to the recombination in the case of the PLEDs or the inverse, from the central layer to the respective electrodes for PSCs. Furthermore, semiconductor polymers must be insulators in the ground state and conductive after the injection or formation of charge carriers. Semiconductor polymers for OLEDs should offer adequate charge-carrier mobility for electrons and holes. Nevertheless, in PSCs, the semiconductor polymers must ensure correct mobility for separate for electron and holes to avoid excessive loss of energy in the separation of the electrons and holes [24]. Polymer–fullerene solar cells show efficiencies around 10%, which indicates remarkable progress towards a promising future [25-27].

All-organic SCs present lower cost, more environmental friendly production and flexibility in the molecular design. Optoelectronic polymers such as polythiophenes polymers [28] may be used as electrode materials. However, although they show energy conversion around 9 % they have to overcome several disadvantages as their tendency to aggregate, shorter excitons lifetime and relatively narrow absorption in the visible region [29].

1.2.3 Organic field-effect transistors

Organic field-effect transistors (OFETs) are cheap and flexible devices with potential applications in electronics circuits [30]. Field-effect transistors have the following components: a semiconducting layer, a gate electrode, a dielectric gate, source and drain electrodes that are in contact with the semiconducting layer as is shown in Fig. 1.3. The gate electrode can be a metal or a conducting polymer, while the gate dielectrics must be an inorganic or polymeric insulator. The source and drain electrodes, which inject charges into the semiconductor may be a conducting polymer. OFETs work by accumulation of charge at the semiconductor/dielectric interface between the semiconductor and dielectric upon the application of voltage. Voltage is applied to the gate and drain electrodes while the source electrode is grounded. The source is the charge-injecting electrode being more negative than the gate electrode when electrons are injected and more positive than the gate electrode when holes are injected [31].

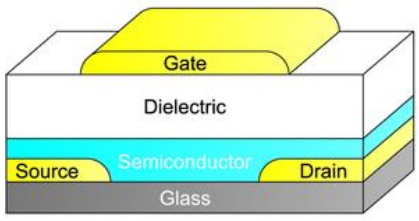

Figure 1.3: Adapted from [13]. Schematic representation of the transistor geometry.

The efficiency of the device is based on the charge transport characteristics at the two interfaces: the electrode/semiconductor and the insulator/semiconductor interfaces. The electronic energy levels of these materials should match in order to reduce the contact resistance and increase the carrier transport performance. However, the extent of the interfacial accumulation layer into the bulk of the semiconductor, the relation between carrier distribution in the interfaces and

transport properties and how optimise the device by all these factors still need further investigation [12, 13].

1.3 Organic spintronics

The field of molecular electronics is based on the electron charge without having into account the spin degree of freedom. Molecular electronics devices have high power consumption, heat dissipation and information storage based on them is volatile, i.e. stored data need electricity to be preserved. Furthermore, the downscaling of electronics devices has become an important feature to store and operate as many operations as possible in the smallest possible volume, thence amount of active material [32]. In order to overcome these limitations, spintronics has recently attracted significant attention. Spintronics aims to exploit the electron spin degree of freedom rather that its charge to carry and store information. Spintronics offers the possibility of enhanced functionalities, higher speed, and reduced power consumption. Furthermore, the spin lifetime and the spin currents can be manipulated. Therefore, the field of molecular electronics in combination with the spintronics aim to progress toward the development of high performance, miniaturised magnetic devices with increased functionalities. Spintronics solutions hold great potential for a wide range of applications such as logic, information storage, communications, and quantum computing [33].

Organic spintronics employs organic semiconductors (OSCs) such as organic molecules, (π-conjugated) polymers and amorphous carbon, as active materials due to their low cost, light weight and flexibility. In addition, the properties of organic materials can be modified by external stimuli such as magnetic or electric fields, temperature, current, light, etc. Furthermore, polymers films offer the possibility of adjusting their properties by modifying the chemical structure, side groups, heteroatoms, molecular weight, etc. overall offering several potential advantages with respect to inorganic semiconductors.

The transport mechanism of the inorganic SC is based in the band transport; electrons are delocalised due to the strong overlap between π-orbitals and give rise to

energy bands (see Fig. 1.4a). On the other hand, in OSCs, the main transport mechanism is charge hopping, charges jump from one localised state of a molecule to another (see Fig. 1.4b). Charge hopping leads to smaller carrier mobility than band transport which favours the hole-electron recombination [34].

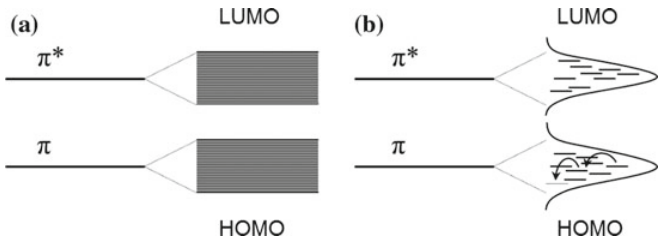

Figure 1.4: Adapted from [35]. **a)** Representation of the structure for band transport. If the overlap between molecules is strong enough, the overlap of bonding and anti-bonding π-orbitals leads to the formation of energy bands formed by a quasi-continuum of states. **b)** Representation of the structure for hopping transport. In an amorphous material disorder leads to a dispersion of localised states [36-38].

Long spin-relaxation time, time for loosening the spin-polarisation, allows increasing the spin-diffusion length which is an important feature to create efficient spintronic devices. The spin-relaxation time is related to the spin orbit coupling (SOC), interaction between the electron's spin and its orbital motion around an atomic nucleus, and the hyperfine interactions (HFIs), interactions between the spin of the mobile carriers and the nuclei spins. Inorganics SCs contain heavy atoms leading to large SOC. On the contrary, OSCs are normally composed by light molecular weight materials leading to weaker SOC [39].

HFIs in OSCs are mainly due to the presence of H atoms, because they possess a nonzero nuclear spin. Conversely, the most common isotope of C (^{12}C) does not exhibit any HFI lacking a nuclear spin. Therefore, HFI can be effectively reduced by using π-conjugated systems due to the minimum presence of H atoms. It is important to note that, although residual HFI can be present in OSCs, its influence is less severe than SOC in inorganic materials.

To explore the influence of the HFI on the spin-relaxation, Nguyen et al. studied the impact of isotope exchange of organic π-conjugated polymers poly(dioctyloxy) phenyl vinylene (H-DOO-PPV). The strongly coupled hydrogen atoms were substituted by deuterium atoms having much smaller hyperfine coupling constant. The results show that D-DOO-PPV shows spin-diffusion length three times longer compared to H-DOO-PPV. This indicated that HFI in DOO-PPV are a crucial spin loss mechanism [40]. According to this, fullerenes which have spinless nucleus, and thus zero HFI should show larger spin-diffusion lengths. However, the spin-diffusion lengths are not as long as expected. This is due to the SCO that, in the case of fullerenes, is the limiting factor [41].

Accordingly, fine-tuning of both SOC and HFI, that majorly affect to the response to magnetic fields in OSCs, is essential for their potential use in spintronic devices [13, 42]. However, as described in this literature review, there are several factors that play an important role for these features including the composition and structure of the OSCs [43]. Therefore, a better understanding is crucial to progress the field towards large-scale industrial implementation.

The operation of spintronics device rests on three different actions on the spin degrees of freedom: spin-injection, spin-transport and manipulation and spin-detection. A basic spintronics device is shown in Fig. 1.5. It consists of a non-ferromagnetic spacer sandwiched between two ferromagnetic (FM) electrodes with different coercivity, i.e. different intensities of the applied magnetic field is required to drop to zero the magnetisation of the FM electrodes after the material magnetisation has been saturated.

The first electrode is used as a spin-injector, the spin-polarised current is propagated along the non-magnetic spacer and finally detected by the second FM electrode [35]. When a positive magnetic field is applied to the device, the electron spins in the FM electrodes are forced to be parallel resulting in a low resistance for the overall junction. Conversely, when the magnetic field is decreased below zero, the electrode with lowest coercivity field is the first one to switch its magnetisation into an antiparallel configuration, resulting in a higher resistance. The magnetoresistance

(MR) is defined as the relative change on the resistance between the parallel and antiparallel configuration [44]. Recently, an additional magnetoresistance called organic magnetoresistance (OMAR) related to change in electrical resistivity was measured in organic light emitting diodes. However, the OMAR mechanisms are still unclear, although understanding them would be desirable for the improvement of magnetic sensor and lighting devices [17].

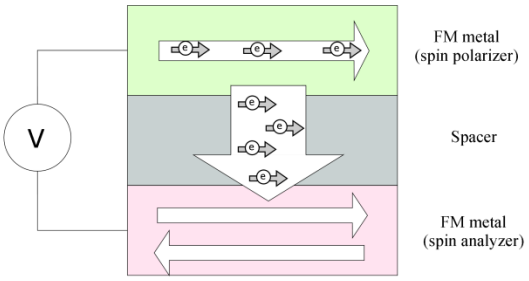

Figure 1.5: Adapted from [35]. Schematic representation of a basic spintronic device. The first FM electrode acts as a spin-polariser capable of spin-injection into the spacer. Spin-polarised current is transported through the spacer and it is finally detected by the second FM electrode.

Depending on the nature of the spacer two different spintronic device can be envisaged. In spin valves (SV) devices, the spacer is a non-magnetic conductor or semiconductor. SVs are based on the giant magnetoresistance (GMR) which arises from spin dependent scattering of the conduction electrons at the FM/semiconductor interface. On the other hand, in magnetic tunnel junction (MTJ) devices, the spacer is a thin insulator and the physical property that permits to modulate the measured signal is tunnel magnetoresistance (TMR) [45].

In 2002, Dediu et al. reported the first evidence of spin-injection and spin-transport in an organic spintronic device. The SV experimental device had a three layers configuration: a conjugated OSC, sexithienyl (T6) film (100-150 nm) was sandwiched, between two LSMO ($La_{x-1}Sr_xMnO_3$) ferromagnetic layers. The measured MR was negative (see inset in Fig. 1.6), which corresponds to low

resistance when the two FM layers are parallel, and large resistance in the antiparallel case [46].

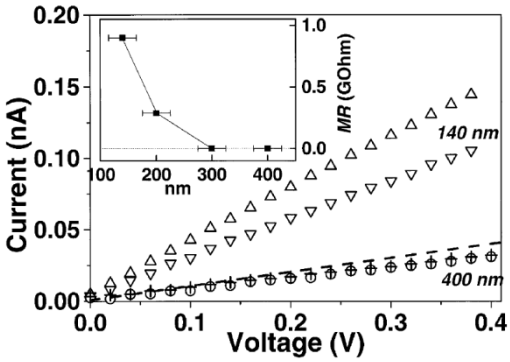

Figure 1.6: Adapted from [46]. I–V characteristics of a $La_{0.7}Sr_{0.3}MnO_3$/T6/$La_{0.7}Sr_{0.3}MnO_3$ junction as a function of the applied magnetic field for 140 and 400 nm channel lengths. Down triangles and circles correspond to the system without applying a magnetic field, while for up triangles and crosses a perpendicular magnetic field of 3.4 kOe was applied. The dashed line indicates the expected slope for 400 nm junction as calculated from 140 nm junction by assuming a linear resistance increase versus channel length. The inset reports the measured MR as function of the OSC width, where $\boldsymbol{MR = R(0) - R(3.4\ kOe)}$.

Qualitatively similar behaviour was found when small organometallic molecules are in contact with FM metals. In 2004, Xiong et al. reported a fundamental work where a negative MR of 40% was found in an organic SV formed by LSMO/Alq_3(130 nm)/Co. The π-conjugated OSC Alq_3 (tris[8-hydroxyquinoline] aluminium, $Al(C_9H_6NO)_3$) is the most widely used electron transporting and light-emitting material in OLEDs. They confirmed that spin-polarised carrier injection, transport and detection, is possible using π-conjugated OSC [47].

In 2006, Majumdar et al. built a polymeric SV using conjugated polymer poly 3-hexylthiophene (RRP3HT) as the spacer layer (70-80 nm) between FM LSMO and Co. They observed spin-selective tunnelling at the LSMO/RRP3HT interface which leads to positive MR of 80% at low temperatures (5 K). These results indicate that organic polymers can be a potential candidate for spintronics applications [48].

The proof of concepts confirm that spin-injection, transport and detection is possible using OSC (small molecules and polymers). The value of the MR is determined by the injection/detection efficiency at the organic molecule/electrode interface which is related to the interactions at the hybrid interface [49]. As a result, fundamental understanding of the electronic and magnetic properties of such hybrid interfaces holds the key to rational progress in the field.

1.4 Fundamental insights into the FM metal/organic interfaces

To better understand the physics of organic spintronics, it is helpful to disentangle the bonding mechanism at the OSC/FM metal interfaces. Fig. 1.7a shows that when the molecule is isolated from the ferromagnetic metal, the electronic structure of the magnetic metal is described by a broad spin-split density of states (DOS) for spin-up and spin-down electrons. On the other hand, the isolated molecule shows discrete energy levels, indicative of an infinite lifetime, (the width of the peak is inversely proportional to the lifetime of the state once populated) in the absence of any interaction with the surrounding environment. Fig 1.7b and Fig 1.7c show that the DOS of the molecule are modified when the molecule and the metal are brought together. First, owing to the broadening, the lifetime of the electronic state is no longer infinite: electrons can leak in and out of such a state. The broadening depends on the FM metal/molecule interactions and the symmetry of the molecular levels [50]. The second effect is related to the energy shift of the molecular level from the initial position when the molecule is isolated to the final energy one. Such a shift is also the result of the interactions (and charge-transfer) with the metal. As a result, if understood and controlled, the interface hybridisation can be used to modify the spin-polarisation and thus tune the characteristics of spintronics junctions and devices [51].

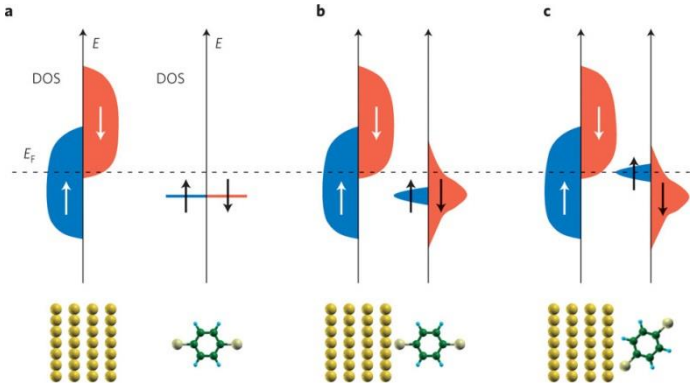

Figure 1.7: Adapted from [52]. Schematic representation of the OSC/FM metal hybrid interface. **a)** The FM metal (left) and the molecule (right) are separated and non-interacting. The metal presents broad spin-polarised density of states (DOS) split in spin-up DOS (blue) and spin-down (red) while the molecule shows a series of discrete energy levels (here only the HOMO is represented). In this case, the DOS of the metal alone determines the spin-polarisation of the tunnelling current. When the molecule is brought into contact with the metal the DOS is modified in two ways: **b)** the energy levels broaden and **c)** their energy position shifts. In both cases new peaks in the DOS might appear at the Fermi level (E_F) of the electrodes, arising from new hybrid interfacial states. It is this new DOS that determines the spin-polarisation of the injected current.

The interface hybridisation depends on the adsorption strength of the molecule onto the substrate. The strength of the molecule-surface interaction can be calculated using the adsorption energy:

$$E_{\text{ads}} = E_{\text{tot}} - (E_{\text{surface}} - E_{\text{molecule}}), \quad (1)$$

where E_{tot} is the total energy of the molecule-surface system, E_{surface} is the energy of the clean surface and E_{molecule} is the energy of the molecule.

Fig. 1.8 shows the two main bonding mechanisms for organic materials adsorbed into FM substrates: physisorption and chemisorption. Physisorption is a weak adsorption produced by the molecule-surface attractive interactions, Van der Waals forces. Physisorption results in small adsorption energies (< 0.1 eV) and modifies the electron density leading to a reorganization of the HOMO-LUMO gap. On the other hand, the chemisorption interaction is characterised by a strong re-hybridisation of the molecular orbitals and the *d*-states i.e. the valence orbitals of the substrate, that

are involved in chemical bonding and interfacial re-hybridisation. Chemisorption presents larger absorption energy (>0.5 eV). Strong molecular adsorption into a FM substrate produces a larger Density of States at the Fermi energy DOS(E_F), which gives to the molecule a metal-like character. In that case, the DOS at spin-up is different to the DOS at spin-down leading to a spin-polarisation at the Fermi level. The two bonding mechanism can have charge transfer and both can modify the electronic structure of the molecule [53].

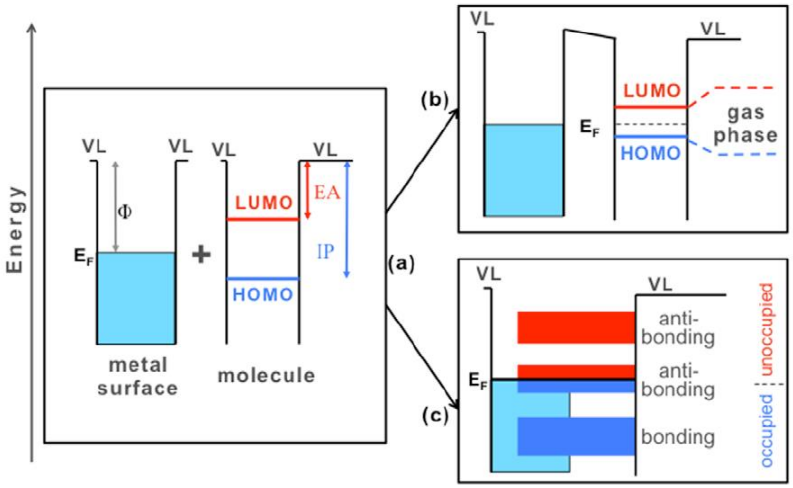

Figure 1.8: Adapted from [54]. **a)** Schematic illustration of the energy level alignment between a molecule and a surface. Depending on the strength of the molecule-surface interaction, the adsorption process can be labelled as **b)** physisorption or **c)** chemisorption. Note that, in the case of a weak molecule-surface interaction leading to a physisorption bonding mechanism, a renormalisation of the HOMO-LUMO gap can occur on polarisable substrates. In the case of the chemisorption bonding mechanism that implies a strong molecule-surface interaction, the molecular orbitals hybridise with the electronic states of the substrate in question, leading to bonding and anti-bonding electronic states with a mixed molecular-surface character. EA: electron affinity, IP: ionisation potential, VL: vacuum level.

1.5 Interface spin-filters

The spin-injection efficiency depends on the hybrid interface and it is based on the spin- injection barrier, the conductance and the spin-polarisation. The spin-injection barrier, which is the energy difference between the HOMO or LUMO and the E_F, must be minimised for spin injection (see Fig 1.9a) [55].

The second factor is the conductance at the interface, the conductance of the electrodes and the OSCs at the interface should match to prevent charge accumulation and the onset of additional polarisations across the junction. However, the conductance difference between FMs and OSCs generate a so-called conductance mismatch (see Fig 1.9b).

There are two methods to overcome the conductance mismatch problem: (i) include a tunnelling barrier between the FM electrode and OSC and (ii) direct hybridisation of the FM/OSCs interface. The first option is to use a tunnel barrier layer as a spin selective resistance which act as a spin-filter, as is shown in Fig 1.9c. Spin-filters are systems which transport electrons of a certain spin orientation facilitating a highly spin-polarised current. The exchange splitting of the conduction band of spin-filter materials creates two different energy tunnel barriers: a lower one for spin-up (spin-down) and a higher on for spin-down (spin-up) electrons. Thus, spin-up (spin-down) electrons exhibit larger tunnelling probabilities leading to spin-polarisation, unbalanced number of spin-up and spin-down hybrid states close to E_F on the molecular orbital [56].

The second method takes advantage of the hybrid interface features. The new DOS near the E_F formed by the hybridisation between the molecular and surface electronic states at the OSC/FM interface may act as spin-filter (see Fig. 1.9d). Spin-filter molecule/FM interface may exhibit opposite spin-polarisation compared to the underlying FM substrate because of the spin-split hybridisation of electronic states at these interfaces [57]. Therefore, these spin-polarised hybrid states determine the spin-injection on the organic molecule. The wide range of OSC molecules available offers the possibility of using a specific OSC molecule to induce a desired hybrid

interface states in order to tune the energy level alignment and spin-polarisation at the interface.

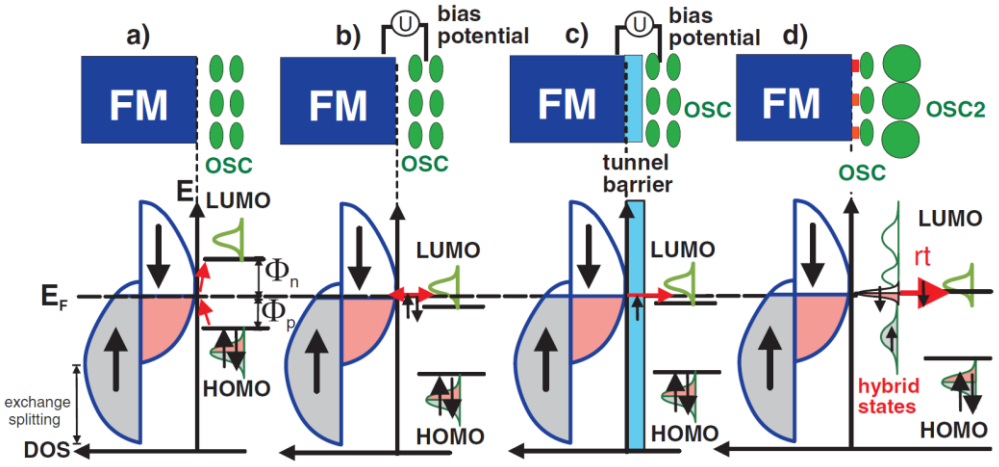

Figure 1.9: Adapted from [58]. Schematic model of the energy level alignment and the DOS at the FM/OSC interfaces. **a)** Injection barrier formed at an idealised interface between a spin-polarised (due to exchange splitting) FM substrate and OSC for effective electrical charge injection without any voltage applied. The spin-injection barrier must be overcome because this process is spin-undiscriminating. **b)** Application of a bias voltage. Due to the conductance mismatch, there is a vanishing spin-injection into the OSC. **c)** Tunnelling barrier approach: inserting a highly resistive spin-selective tunnel barrier (light blue) at the FM/OSC interface which acts as a spin-filter. **d)** Hybrid interface states approach: DOS modification and spin-split states at E_F induced by chemisorption creates new spin-polarised states at E_F which can couple in a resonant tunnelling process to a second OSC 2 (large green circles) with suitable charge transport levels. Such interface engineering can conserve the spin-polarisation, and in combination with a second appropriate organic molecule in the subsequent layers can be used to overcome the conductance mismatch.

Some OSC/FM interfaces show local inversion of the spin-polarisation close to E_F, i.e. there is a switch of the spin-polarisation sign at the molecular site with respect to the FM surface. The sign and magnitude of the spin-polarisation is related to the strength of the OSC/substrate binding [51]. In turn, the adsorption strength depends on (i) the substrate: reactivity, reconstruction (ii) the type of molecule: electronegativity, symmetry of the molecule and symmetry of the d-orbitals in the case of organometallic, and (iii) the adsorption geometry. Therefore, the physical

properties of a given spintronics device depend on the composition and the structure of the systems used in the spintronics junction.

1.6 Not just one spintronics interface

In the last years, the research on organic spintronics has focussed on developing new spintronics functionalities merging from the hybrid molecule/substrate interface and the understanding of how the molecule-surface interactions alter the emerging interfacial magnetic properties [42, 51, 53]. The adsorption of a molecule on a magnetic substrate modifies the magnetic exchange coupling interface. The magnetic exchange coupling due to the charge transfer between the organic molecule and the FM surface at the organic/FM metal interface is understood to stabilise the molecular spin at the interface and to determine the joint electronic and magnetic properties of the system. An increment of the magnetic exchange coupling (magnetic hardening) or decrement (magnetic softening) due to molecular adsorption depends on both: (i) the interface hybridisation of the molecular electronic states with those on the substrate and (ii) the interface reconstruction due to geometrical changes induced by molecular adsorption (geometrical effect) [59]. These elements reiterate that a better understanding of the OSC/substrate hybrid interfaces is required for progress in the field towards development of high-efficiency spintronic devices capable of large scale industrial take up.

In the following, I review different OSC/substrate interfaces. The OSCs involves molecules and polymers. We will describe systems with (i) non-metallic molecules such as fullerenes, graphene and polymers; and (ii) organometallic. Fullerenes and graphene are π-conjugated systems particularly interesting for spintronics applications due to the absence of hydrogen atoms that lead to spin de-phasing caused by HIF. Furthermore, these molecules feature very weak SOC due to their light atoms composition. In addition, polymers exhibit larger spin-polarisation and transport compared to small molecules and they show adjustable spin-filter that improves the spin-injection. This is attributed to a better conjugation, leading to better transport and longer spin-relaxation length [60]. Furthermore, the soft flexible

atomic configuration of polymers facilitates well-contacted interfaces which may enhance the magnetic properties of the system [61]. On the other hand, organometallic are OSC materials that contain at least one bond between a carbon atom and a metal. They will be used to study the influence of the central metal atom to tune the organometallic/substrate interface properties.

1.6.1 Organic materials/FM substrate interface

1.6.1.1 Strength of interaction with the metallic substrate

As mentioned before, the substrate reactivity influences the adsorption strength, interface re-hybridisation and emerging spin-polarisation. Physisorbed MnPc onto a non-magnetic substrate as Cu(001) exhibit a very weak hybridisation between the Mn 3*d*-states and Cu 3*d*-states at/or close to the E_F leading to a magnetically inactive interface, i.e. there is no spin-polarisation at the ground state. On the other hand, the same organometallic chemisorbed onto FM Co(001) leads to a magnetically active interface [62]. In addition, adsorption of CoPc on FM substrates such as Co/Cu(111) or Fe/W(110) leads to an enhancement of the spin-polarisation. Nevertheless, the same molecule adsorbed on Fe/W(110) substrate show larger value of spin-polarisation. These results suggest that stronger adsorption interactions between the organometallic and the FM metal lead to an increment of the spin-polarisation on the organic ligand of the organometallic molecule [57].

1.6.1.2 Surface reconstruction

Surface reconstruction refers to the rearrangement of the surface atoms in a different structure from the bulk-like one. The effect of surface reconstruction was studied by the adsorption of C_{60} on Fe(001). The interface properties of non-reconstructed and reconstructed substrate were compared (see Fig. 1.10). The different bonding of the two systems leads to different properties at the interface. The charge transfer to the C_{60} from the reconstructed (unreconstructed) Fe substrate is 3.36 (1.81) electrons. Therefore, the energies of the HOMO and LUMO are lowers in the reconstructed case. Larger values of spin-polarisation at the E_F are found for reconstructed systems

(-0.16 μ_B) than for the unreconstructed structure (0.08 μ_B). Furthermore, for the reconstructed system there is an inversion of the spin-polarisation at the Fermi level. Fig. 1.11 shows the magnetic moments of the reconstructed surface. The inversion of the fullerene C_{60} magnetic moments is larger with shorter C-Fe distances. The Fe magnetic moments are reduced after the fullerene adsorption, the reference Fe magnetic moments value for the first and second layer are 2.98 and 2.37 μ_B respectively. Thus, the reconstruction of the surface leads to larger values of spin-polarisation around E_F and enhances the fullerene magnetic moment [63]. Similar results are found when the substrate is Ni [64]. Therefore, the surface reconstruction is demonstrated to be very effective in inducing magnetic hardening or softening of the interface.

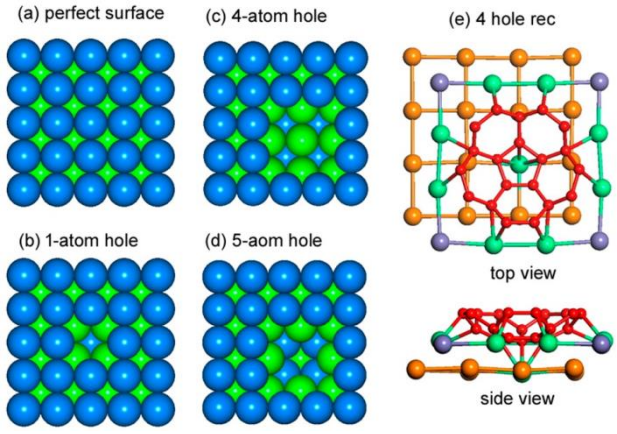

Figure 1.10: Adapted from [63]. Adsorption of C_{60} on reconstructed Fe(001). **a−d)** Different types of reconstruction: perfect surface without reconstruction and 1-, 4-, and 5-atom hole reconstructions. **e)** Top and side views of the most stable reconstructed adsorption structure with C_{60} pentagon sinks-in a 4-atom hole ("4 hole rec"); only C atoms in the lower-half of C_{60} and Fe atoms in the top two layers are shown to display the interfacial structure in a clearer way.

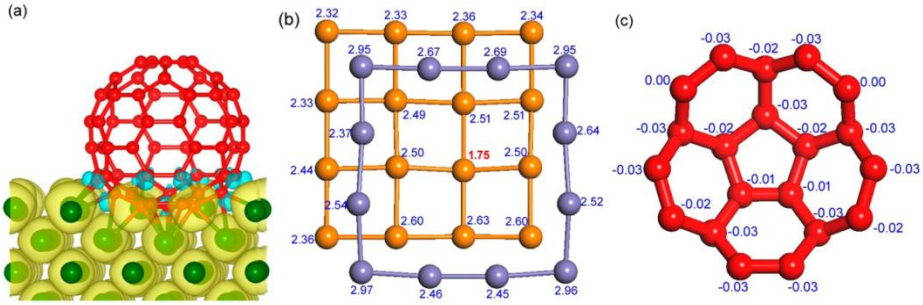

Figure 1.11: Adapted from [63]. **a)** Spin-density plot of the reconstructed structure as shown in Fig. 1.10e, yellow (blue) corresponds to majority (minority) spins. Magnetic moments at the interface (in μ_B), **b)** for Fe(001) top two layers and **c)** for C_{60} bottom part.

1.6.1.3 Molecular electronegativity

Also, the electronegativity and reactivity of the absorbed molecule can influence the hybridisation with the substrate and accordingly the magnitude and sign of the emerging spin-polarisation. The adsorption of cyclopentadienyl radical (Cp, C_5H_5), benzene (C_6H_6, Bz), and cyclooctatetraene (C_8H_8, Cot) on FM Fe/W(110) substrate leads to a strong interaction between the π-molecular orbitals and the *d*-bands of the FM substrate. More reactive molecules such as Cp and Cot lead to a stronger inversion of the spin-polarisation compared to Bz whose interactions with the FM are relatively weak [65]. Moreover, the substitution of the hydrogen atoms of Cp and Bz, by F and Cl show that more electronegative atoms, such as F and Cl, induce larger magnetic moments on the molecule while decreasing the magnetic moments of the Fe atoms underneath. Fig. 1.12 shows that by employing more electronegative atoms (F), the inversion of the spin-polarisation occurs just for energies above the E_F, whereas for energies below E_F, the spin-polarisation of the substrate is preserved [66]. These results provide further evidence of the role of the molecular electronegativity in tuning interfacial re-hybridisation and the emerging electronic and magnetic properties at OSC/FM interfaces.

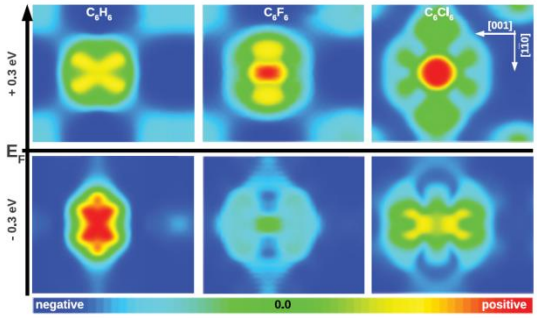

Figure 1.12: Adapted from [66]. The calculated spin-polarisation at 3.0 Å above the C_6H_6, C_6F_6, and C_6Cl_6 molecules adsorbed on a 2 mono-layer (ML) Fe/W(110) surface plotted for occupied ([−0.3, 0.0] eV) and unoccupied ([0.0, +0.3] eV) energy intervals around E_F. The organic molecules containing H and Cl atoms show above and below the Fermi level a high, locally varying spin-polarisation ranging from attenuation to inversion with respect to the FM Fe film. In contrast, C_6F_6 preserve the spin-polarisation of the Fe surface for energy intervals just below the Fermi level and show an inversion of the spin-polarisation only for energy intervals above the Fermi level. The z-scale refers to the sign of the polarisation. The red colour indicates positive polarisation, the green shows the absence of polarisation and the blue colour denotes a negative polarisation.

Furthermore, by affecting the exchange coupling interactions at the interface, the electronegativity the molecule can induce magnetic hardening/softening of the substrate. Replacing a C atom of the ethane (C_2H_4)/FeW(110) interface by a heteroatom (B, N or O) shows that more electronegative atoms such as O induce magnetic softening of Fe. On the other hand, less electronegative atoms such as B and N leads to magnetic hardening of Fe [67]. Therefore, control of the molecular electronegativity by chemical functionalization can provide an effective strategy to tune the interfacial magnetic hardening or softening of originally FM substrates.

1.6.1.4 Symmetry of the d-orbitals in Metal phthalocyanines

Chemical functionalization of metal phthalocyanines (MPc) reveals more information about the importance of the molecule/FM hybrid interfaces on the magnetic behaviour of the systems. The MPc/FM interface couples the central metal ion to the FM substrate via exchange interactions (see Fig. 1.13c). Partially occupied *d*-states of the central metal atom of the organometallic molecule (Fe d^6, Co d^7 and

Cu d^9) and the symmetry of the *d*-orbitals of the metal of the MPc play a crucial role on the spin-polarisation at the interface.

The spin and atom resolved density of states (LDOS) of the different interfaces (see Fig. 1.13b) shows that CuPc exhibits larger spin-polarisation at the E_F than FePc and CoPc when they are adsorbed on FM Co(001). Nevertheless, the magnetic moment of CuPc after the adsorption is zero while CoPc and FePc exhibit magnetic moments of 0.515 μB and 1.94 μB respectively due to the strong FM coupling. This difference arises from the symmetry of the *d*-states of the metal central atom, which contribute the most to the interface hybridisation. CoPc and FePc exhibit strong π-orbital interactions with the *d*-states of the substrate due to the large contribution of orbitals perpendicular to the molecular plane. On the other hand, CuPc/Co shows only weak interactions through the orbitals perpendicular to the molecular plane [58]. Similar results were found when CoPc is adsorbed on Fe substrate. The interface exhibits local spin-polarisation values that range from inversion up to amplification (see Fig. 1.14) with respect to the FM metal. These results confirm that the emerging interface spin-polarisation depends on details of the molecule/substrate hybrid states with non-negligible effects from the symmetry of the *d*-states in the molecule, if present [68].

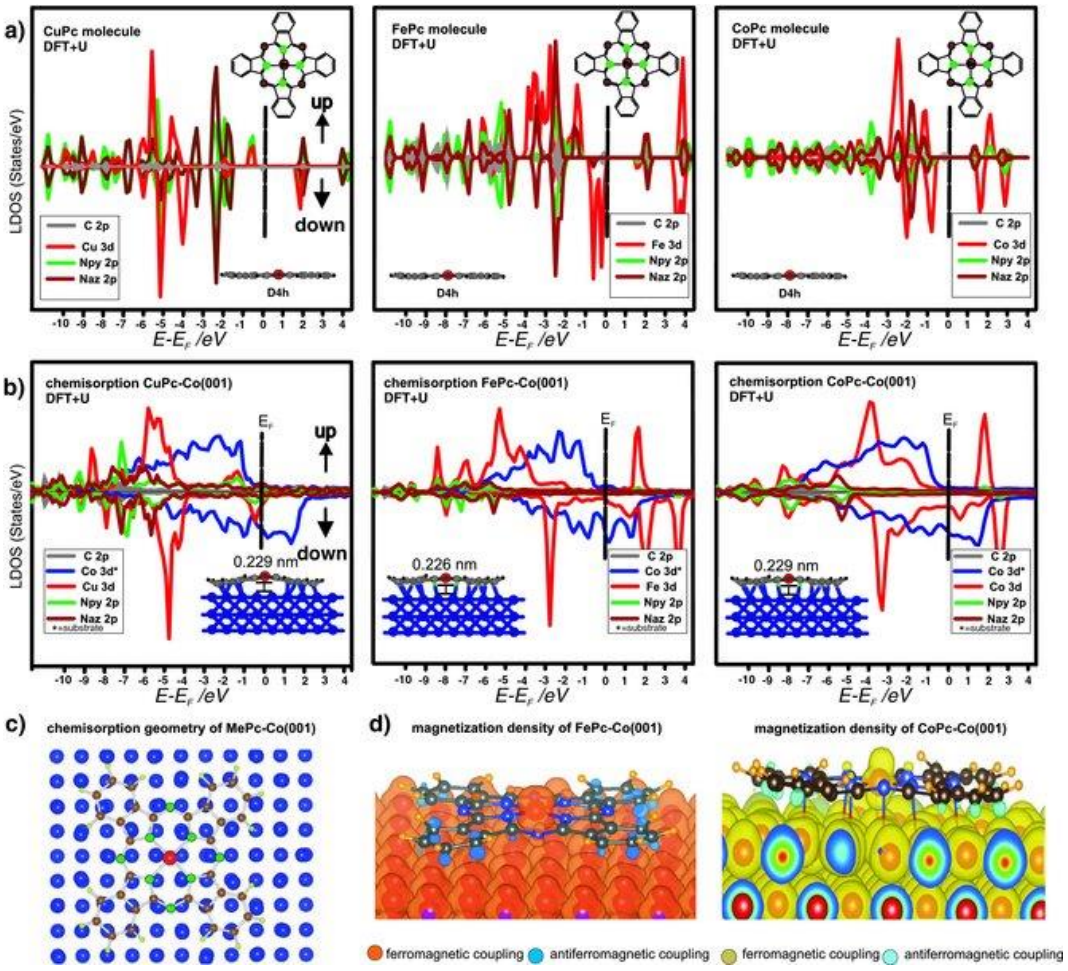

Figure 1.13: Adapted from [58]. LDOS calculated with DFT+U, for **a)** free CuPc, CoPc, and FePc molecules and **b)** the molecules when chemisorbed on Co(001) in a bridged position shown in **c)**. The horizontal energy scale has been stretched for better comparability with the experimental data by a factor of 1.4. The insets show the relaxed adsorption geometry of the molecules on the Co surface. In case of chemisorption (b), the Cu ion bends out of the molecular plane whereas the phenyl rings of CuPc are drawn by up to 0.03 nm toward the surface and away from the plane defined by the Cu ion and the pyrrolic N atoms. For all three molecules the H atoms are pointing away from the surface. The magnetic coupling of FePc and CoPc to Co is shown in **d)** where the spin-polarisation density is dominated by the iron and cobalt central atom at the molecular side in an out-of-plane geometry. Note the spin-polarisation present on carbon and nitrogen atoms of the phenyl rings, which is created through interaction with the spin-polarised Co-d states of the substrate.

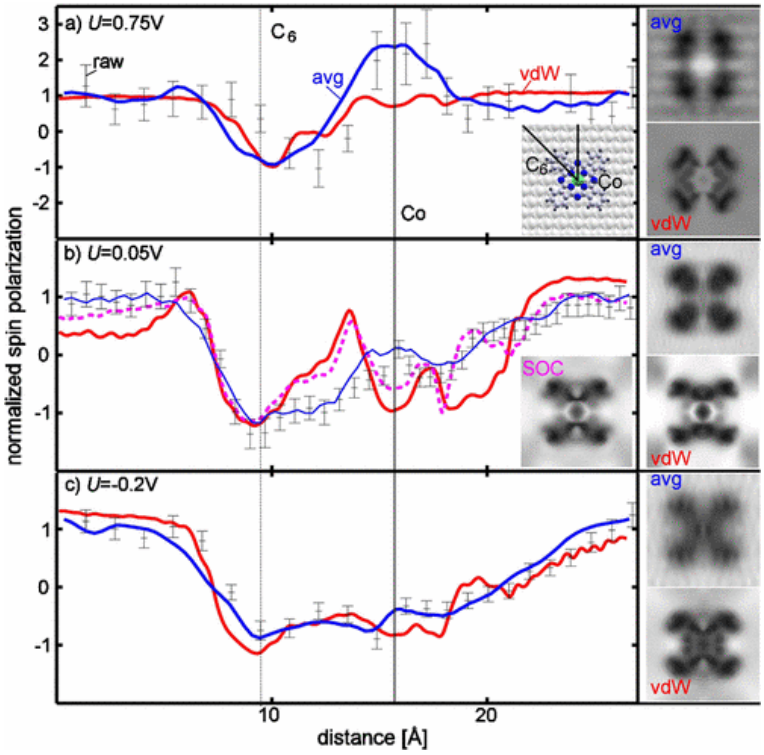

Figure 1.14: Adapted from [68]. Local spin-polarisation of CoPc adsorbed on Fe at three representative energies. Raw- and average experimental data (blue trace) are compared with DFT simulations including Van der Waals (red trace) and including SOC (pink trace). Simulated data including SOC is only given in b) as the SOC corrections for a) and c) are negligible.

1.6.1.5 Molecular symmetry

Interfacial re-hybridisation between the FM metal substrate and the adsorbed molecule can also be affected and tuned by symmetry of the molecules. Thiophene/Co interface exhibits inversion of the spin-polarisation in some atoms of the molecule while the others show no inversion. Fig. 1.15 shows that this feature is due to the influence of the S atoms on the metal-molecule orbital overlapping. Carbon atoms far from the S atoms present larger orbital overlap with the substrate, which leads to larger exchange coupling and spin-polarisation inversion [69].

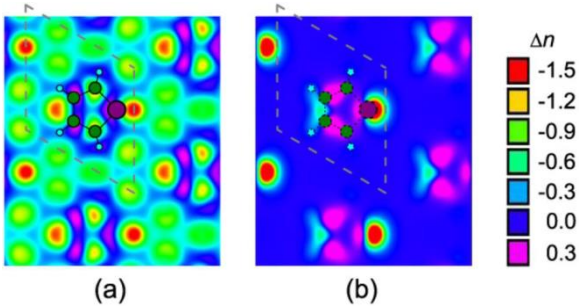

Figure 1.15: Adapted from [69]. Local spin-polarisation Δn (10^{-3} e/bohr^3) of electrons in the energy range [E_F−0.4 eV, E_F] at **a)** the interface between the substrate and the thiophene and **b)** the surface above the thiophene.

Similar results are found when organic molecules such as Bz, Cot or small transition metal-benzene complex (BzV) are absorbed onto an antiferromagnetic (AFM) substrate such as Mn/W(110). Fig. 1.16, 1.17, 1.18 reveal that different regions on the molecules show different signs of spin-polarisation. Furthermore, charge transfer from the Mn to the molecules induces a small magnetic moment on the molecule while reducing the atomic magnetic moment of the Mn layer. This effect is stronger in the case of the magnetic molecule (BzV) [70]. Therefore, use of asymmetric organic molecules is also demonstrated to be an effective way to design the spin-polarisation of organic/AFM interface.

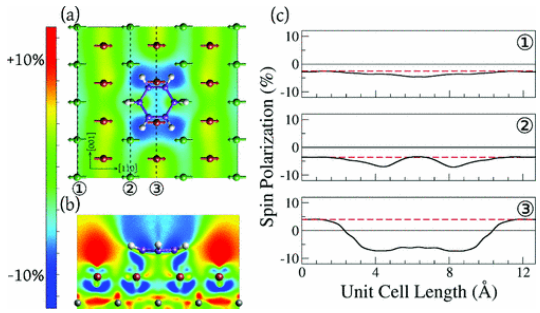

Figure 1.16: Adapted from [70]. **a)** Spin-polarisation in the vacuum 3.0 Å above a Bz molecule adsorbed on Mn/W(110), calculated for occupied energy levels [-0.4 eV, E_F]. **b)** Slice of the spin-polarisation perpendicular to the surface plane along line 3 in panel (a). **c)** Selected line profiles of the spin-polarisation. The red dashed line approximates the line profile in the absence of any adsorbed molecule. The z-scale refers to the sign of the polarisation. The red colour indicates positive polarisation, the green shows the absence of polarisation and the blue colour denotes a negative polarisation.

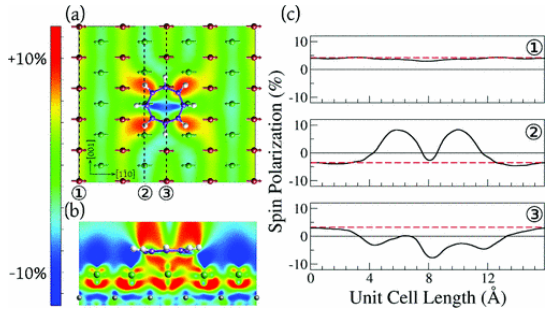

Figure 1.17: Adapted from [70]. **a)** Spin-polarisation in the vacuum 3.0 Å above a Cot molecule adsorbed on Mn/W(110), calculated for occupied energy levels [-0.4 eV, E_F]. **b)** Slice of the spin-polarisation perpendicular to the surface plane along line 3 in panel (a). **c)** Selected line profiles of the spin-polarisation. The red dashed line approximates the line profile in the absence of any adsorbed molecule. The z-scale refers to the sign of the polarisation. The red colour indicates positive polarisation, the green shows the absence of polarisation and the blue colour denotes a negative polarisation.

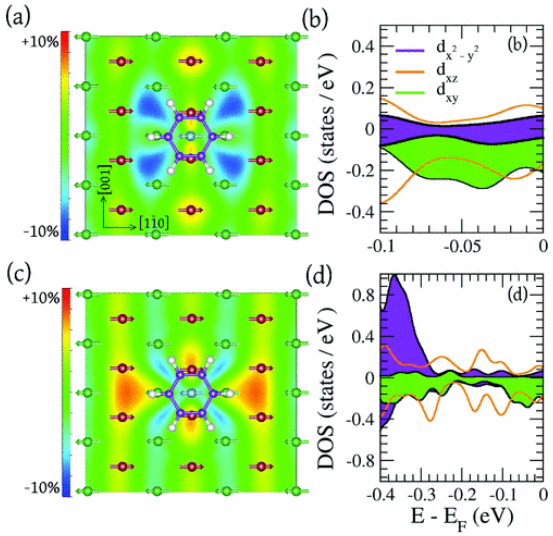

Figure 1.18: Adapted from [70]. Spin-polarisation in the vacuum 1.6 Å above a BzV molecule adsorbed on Mn/W(110), calculated for occupied energy levels [-0.1 eV, E_F] (a) and b)) [-0.4 eV, E_F] (c) and d)). The DOS are shown for the most relevant *d* orbitals of the adsorbed V atom. The z-scale refers to the sign of the polarisation. The red colour indicates positive polarisation, the green shows the absence of polarisation and the blue colour denotes a negative polarisation.

Azobenzene molecules on FM substrate illustrate further aspects of the relationship between the inversion of the spin-polarisation at the interface and the symmetry of the molecule. Azobenzene molecules are interesting because they are stimuli-

responsive materials which may undergo a conformational change from *trans* to *cis* configuration. This response is triggered by the exposure to light or temperature. Azobenzene molecule adsorbed on Fe/W(110) surfaces shows inversion of the local spin-polarisation due to the azobenzene transition from *trans* to *cis*. Fig. 1.19 shows that the *cis* conformation, due to its broken symmetry, leads to an asymmetric adsorption which in turn results in different sign of spin-polarisation for each phenyl ring. The computed charge transfer from the FM to the molecule for the *trans* (*cis*) configuration is 2.36 (2.50) electrons. Similar to previous studies, the adsorption of azobenzene leads to a reduction of the magnetic moment of the FM substrate at the interface (from 2.4 μ_B to 1.4-2.2 μ_B) and a consequent increment of the molecular magnetic moments of the *trans* and *cis* configuration (0.22 and 0.16 μ_B, respectively [71]). The sign reversal of the SP at the Fe surface in the two energy ranges is attributed to the competition between the contributions of Fe d and sp states to the SP above the surface. Although the Fe *d*-states are the dominant states and primarily spin-down around E_F, the *s* and p_z states are primarily spin-up in [E_F − 0.5 eV,E_F]. At a distance above the Fe surface, the s and pz states contribute more to the spin polarization."

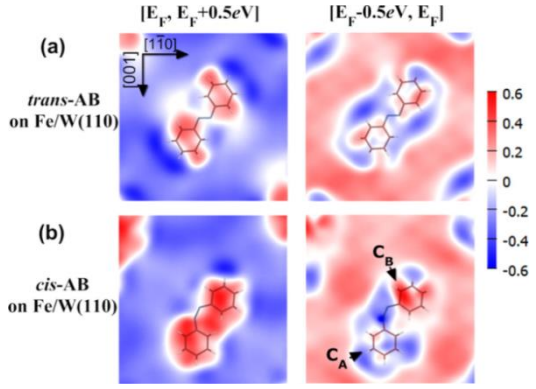

Figure 1.19: Adapted from [71]. The calculated spin-polarisation at 3.0 Å above the **a)** *trans* and **b)** *cis* azobenzene adsorbed on 1 ML Fe/W(110) surface with an area of 19×19 $Å^2$ for unoccupied [E_F, E_F + 0.5 eV] (left panels) and occupied [E_F − 0.5 eV, E_F] (right panels) energy intervals around E_F. C_A and C_B are marked as the two C atoms in the two phenyl rings in the *cis* azobenzene.

1.6.1.6 Adsorption geometries

In the case of weak interactions between the adsorbed molecule and the substrate, there is no molecular state close to E_F. However, the splitting of the interface states close to the E_F leads to a spin-filter effect i.e. the molecules are able to invert the spin-polarisation of the surface. For instance, CuPc adsorbed on Fe/Mo(110) substrate exhibits two different regions at the interface electronic structure. The first one is a small energy interval close to E_F with low density of hybrid interface states. On the other hand, the second region, away from the E_F, is dominated by the hybrid metal-organic interface and acts a spin-filter [72]. The spin filtering mechanism at the interfaces is mainly affected by the character of the hybrid interface states and their position with respect to the E_F. If the molecule has a three-dimensional structure, such as Alq3 and fullerenes, the hybrid interface states may be located away from the metal, showing longer spin lifetimes. However, if the molecule is flat such as MPc or ZMP, the molecule is closer to the metal leading to shorter spin lifetimes.

However, not just physisorbed molecules can acts as a spin-filter, the chemisorption of paracyclophane ($C_{16}H_{16,}$ PCP) on a Fe/W(111) surface results in spin-splitting of the electronic structure, suggesting a spin-filter functionality. This is due to the fact that the PCP is composed by two rings with different adsorption geometries (see Fig. 1.20a). Fig 1.20b shows that the ring closer to the surface is chemisorbed on the substrate leading to spin-polarisation at the hybrid interface and to a local enhancement of magnetic hardening on the Fe atoms underneath the molecule compared to the clean Fe surface atoms. This effect is due to an increase of the exchange interactions (by a factor of three) of the Fe atoms immediately below the molecule. On the other hand, the upper ring exhibits sharp spin-split PDOS and it acts as a spin-filter [73].

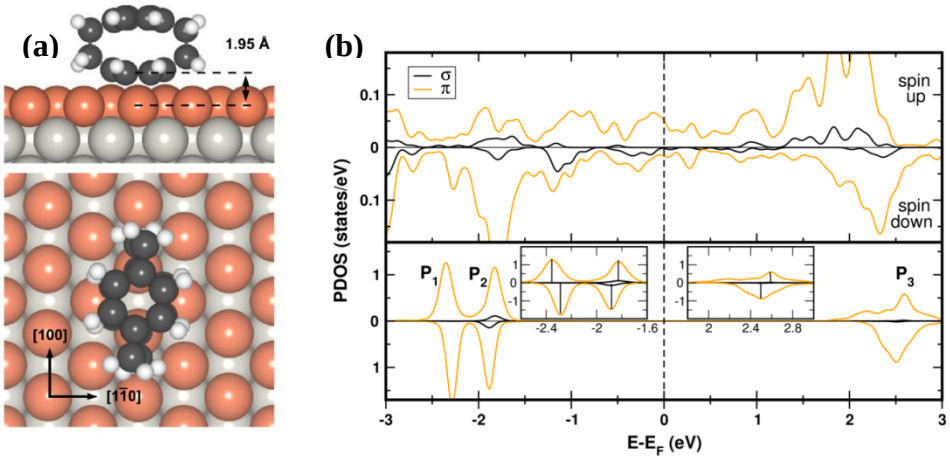

Figure 1.20: Adapted from [73]. **a)** The side and top view of the hollow site ground-state adsorption geometry of a single PCP molecule on the FM Fe/W(111) surface. **b)** σ and π resolved PDOS of the lower (top) and the upper (bottom) ring of the PCP molecule on the Fe/W(111) surface.

Similar results are found for phenalenyl molecules adsorbed into a FM substrate. Phenalenyl molecules are open–shell systems formed by benzene rings. Phenalenyl derived molecules form highly delocalised radicals that can be easily tuned to control the charge transfer and the spin-injection [74]. The adsorption of zinc methyl phenalenyl (ZMP, $C_{14}H_{10}O_2Zn$) dimer on Co(111) exhibits a peculiar electronic and magnetic structure due to the different interactions of the two molecules of the dimer (see Fig. 1.21a). The molecule closer to the substrate hybridises strongly. The charge transfer between this molecule and the substrate leads to an enhancement of the metal magnetic hardening at the interface with respect to the Co bulk layer. In contrast, the orbitals of the second molecules only weakly hybridised with the FM substrate. Fig. 1.21b indicates that the second molecule acts as spin-filter with a spin-injection barrier of 0.73 eV for spin-down electrons and 0.87 eV for spin-up electrons [4].

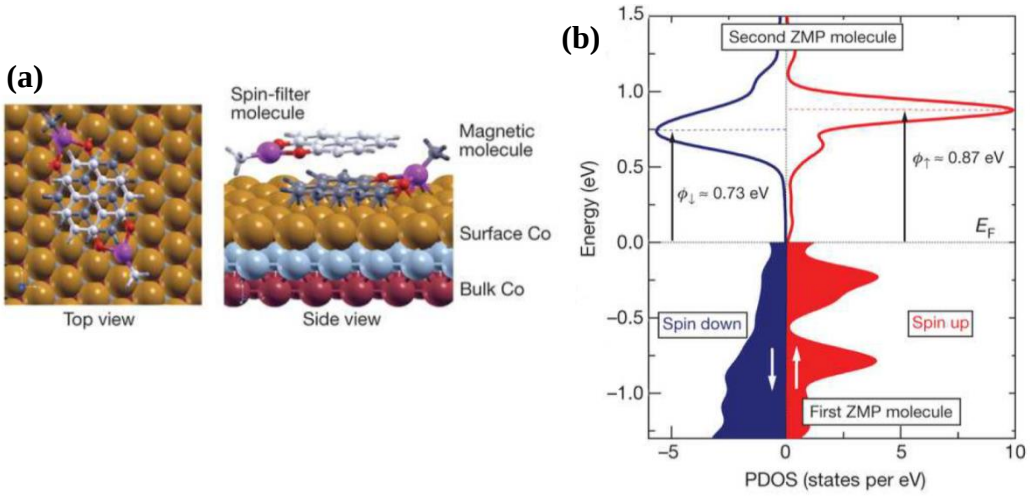

Figure 1.21: Adapted from [4]. **a)** *Ab initio* model: top view (left) and side view (right) of the relaxed molecules' configuration on the Co(111) surface; grey, carbon; red, oxygen; purple, zinc. The first-layer ZMP molecule ('magnetic molecule') absorbs flat, with six α-carbons and the central carbon of the phenalenyl sitting directly on top of Co atoms, while the β-carbons of the phenalenyl sit in a bridge position between Co atoms. The molecular plane is ~2.1–2.2 Å above the Co(111) surface (the C atoms are ~2.1 Å above, the O and Zn atoms are ~2.2 Å above). The second molecule ('spin filter molecule') sits in a staggered configuration over the first adsorbed molecule with a spacing of ~3.26 Å, forming a molecular π-dimer. **b)** PDOS of the first and second-layer ZMP molecule adsorbed on a Co surface. PDOS of the first molecule is broadened showing metal-like character, while PDOS of the second layer ZMP molecule shows discrete molecular energy levels, but with 0.14 eV spin-splitting of the lowest unoccupied molecular orbital, leading to a difference in the injection/tunnelling barrier height for the two spin channels. This process gives rise to a large spin-filtering response. Blue and red data points refer to spin-down and spin-up channels, respectively. $\phi_\downarrow$ and $\phi_\uparrow$ are the injection barrier height for spin-down and spin-up electrons, respectively.

In the case of fullerenes adsorbed on FM substrates, only a few C atoms are bonded directly to the substrate, opposite to the case of flat aromatic molecules. The hybrid interface formed by the fullerene and a FM substrate is produced by the mix of the C_{60} π-orbitals and the *d*-band of the metal. The hybrid interface increases the DOS(E_F) compared to the isolated molecule, changing the molecule from semiconductor to metallic. Experimental and theoretical studies confirm that the fullerene/FM interaction induces spin-splitting of the states close to the Fermi level. Therefore, the molecules acquire a spin-polarised DOS which is enhanced and inverted with respect to the FM surface [75-77]. Fig. 1.22a shows the inversion of the

spin-polarisation of the C atoms closer to the Cr(001) layer. The reduction of the Cr magnetic moments in comparison to the bulk (3.11 μ_B) is observed (see Fig. 1.22b). Such reduction is larger for the Cr atoms closest to the C_{60} (red dot in Fig. 1.22b) [76, 77]. It is worth noting that, due to the spin-polarised electronic transfer, even fullerenes 200 nm away from the interface play a role on decreasing the substrate magnetic moments as observed for C_{60}/Co junctions [75]. The possibility of tuning the spin polarisation in fullerenes opens a new route to engineer spin-filter effect through molecular orbitals of non-planar molecules.

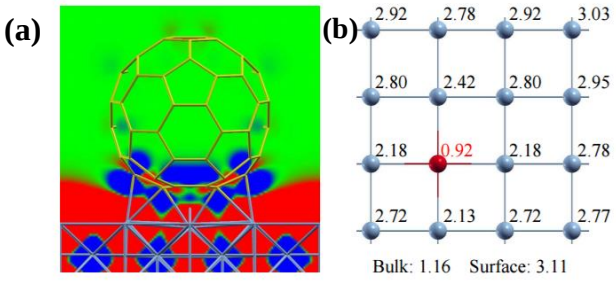

Figure 1.22: Adapted from [74]. Magnetic moments of the C_{60}/Cr(100) system. **a)** Colour map of the magnetic moments; red (blue) corresponds to positive (negative) magnetic moment. **b)** Magnetic moments of the surface Cr atoms; the Cr atom just beneath the C_{60} is shown in red. The atomic magnetic moments (μ_B) of Cr bulk and of clean Cr(100) surface are also indicated.

Furthermore, chemisorbed fullerenes on FM surface exhibit different interface electronic structure depending on the adsorption geometry, which determines the position of the hybrid state with respect to the E_F. C_{60} and C_{70} are a clear example: C_{60}/Fe(001) interface states are 0.2 eV above E_F while C_{70}/Fe(001) interface states lies at Fermi level. As a consequence, they show different MR. The larger MR of C_{70} (up to 140 %) compared to C_{60} (up to 21 %) in SV devices at small bias [78]. However, recent experimental studies in SV composed by Fe3O4/AlO/fullerenes (C_{60} or C_{70})/Co/Al junctions observed larger MR in C_{60} compared to C_{70} due to larger molecular symmetry of the C_{60}. Low symmetric structure leads to larger orientation disorder and could lead to larger energy loss during the transport of the carriers [79]. Nevertheless, the interaction between molecule and surface induces a similar

magnetic moment for C_{60} (~ 0.22 μB) and C_{70} (~ 0.26 μB) [80, 81]. Therefore, further research is required to study the influence of the adsorption site on the adsorption strength. The DFT calculations reviewed here do not account for vibronic coupling and consequently cannot capture Jahn-Teller effects and related distortions. The Jahn-Teller (JT) effect is a geometric distortion produced in non-linear molecular systems in an electronic state with orbital degeneracy. The distortion removes the pristine degeneracy leading to splitting of the originally degenerate state and lowering of the system symmetry [82]. JT effect can be found in some fullerenes [82, 83]. The interplay in these materials between the distortions and the electronic structure, through the Jahn-Teller effect can play an important role in the charge transfer [84].

Studies of graphene adsorbed on Co/Ir(111) reveal different total magnetic moment depending on the adsorption geometry. Adsorption sites fcc and hcp with shorter C-Co distances show a total magnetic moment of -1.36 μB (AFM coupling) while for top sites, where the interaction is weaker, the total magnetic moment is +0.14 μB (FM coupling). In addition, experimental studies of graphene on Fe/Ir(111) substrate indicate that the charge transfer and the MR depends on the graphene-Fe distances. Larger distances (up to 3.33 Å) show no hybridisation, while shorter distances (2.05 Å) indicate a strong hybridisation inducing a magnetic moment in graphene. Similar theoretical results were found also for MnPc adsorbed on an AFM IrMn(001) substrate. Larger charge transfer is observed to be linked to shorter distance between the organometallic and the substrate. However, it is suggested that the molecule geometrical distortion is the main cause of the enhancement of the magnetic moment of the MnPc molecule. The molecule geometrical distortion is referred to an increment of 2% of the N-Mn distance of the molecule produced by the adsorption. Moreover, this geometrical distortion tunes the spin-polarisation around the E_F from negative to positive [85]. It is thus evident that a complete understanding of the processes occurring at hybrid graphene-ferromagnetic interfaces is far from complete [50, 51].

Finally, polymers such as 11,11,12,12-tetracyanonaptho-2,6-quinodimethane (TNAP) absorbed into a FM substrate show a broadening of the DOS close to E_F

leading to a spin-polarised interface. Therefore, these polymers have been employed as spin-filter in organics devices in order to tune the spin-injection at the polymer/FM interface. The function of TNAP is increase the work-function of the interface, reducing the hole-injection barrier at the TNAP/FM interface [55]. In addition, ferroelectric polymers such as poly(vinylidene fluoride) (PVDF), offer an alternative to control the injection of spin-polarisation by modifying the ferroelectric polarisation of PVDF. The PVDF/FM interface acts as spin-filter for electron tunnelling [86].

1.6.1.7 Non-π-conjugated molecules

As mentioned in section 1.3, the spin-polarisation at the interface is due to the hybridisation of the π-orbitals from the organic molecule and the *d*-states from the FM metal. This suggests that molecules with only σ-bonds i.e. without π-orbitals, might not present highly spin-polarised interface states. However, recent experimental studies confirm that aliphatic alkanes such as pentacontane in contact with a FM metal do result in highly spin-polarised interface states due to the charge transfer between the FM metal and the molecules and the ensuing re-hybridisation. The charge transfer modifies the initial electronic structure of the molecule and of the substrate, creating the hybrid states at the interface. These results reiterate that spin-polarisation at the interface does not depends just on the molecule, it is a feature of the interface between the molecule and the substrate [87].

Magnetic hardening and/or softening of the FM atoms below the molecule depends on the binding strength of the adsorbed molecule to the FM surface. Adsorption of organic molecules on a FM surface, such as Fe/W(110), induces FM interlayer magnetic softening. Study of dioxan ($C_4O_2H_8$) that is a σ-system, i.e. all the atoms have sp^3-like hybridisation; and dioxin ($C_4O_2H_4$) that is a π-conjugated system where all the C atoms are sp^2 hybridised, indicates different binding energies, which in turn lead to different magnetic exchange interactions. The adsorption strength is related to the molecule-surface geometries adsorption. Fig. 1.23 shows that the dioxin molecule adsorbs closer to the substrate than dioxan, resulting in an accordingly larger

molecule-surface re-hybridisation. The dioxan (σ-system) is weakly chemisorbed ad interacts with the FM substrate only through the O atoms. Conversely, the dioxin (π-system) is strongly chemisorbed and interacts with the FM substrate through all the C and O atoms involved in the pristine molecular π system.

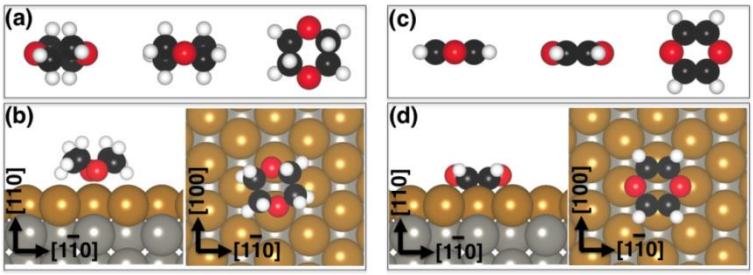

Figure 1.23: Adapted from [67]. Side and top views of the **a)** dioxin ($C_4O_2H_8$) and **c)** dioxin ($C_4O_2H_4$) molecules and the ground-state geometries for **b)** dioxan and **d)** dioxin adsorbed on the magnetic substrate. Colour code: light grey, hydrogen; black, carbon; red, oxygen; gold, iron; grey, tungsten.

It is important to note that the adsorption of dioxan and dioxin just modified the Fe substrate magnetic moments of the four atoms underneath the molecule. The magnetic moments of the Fe atoms under the dioxan are slightly reduced (< 1%) compared to the clean Fe surface. Conversely, adsorption of dioxin leads to stronger hybridisation and substantially larger changes (68%) in the magnetic moments of the Fe-atoms beneath the molecule. Furthermore, weakly chemisorbed molecules (σ system) induces magnetic softening of the 2nd topmost Fe layer (not immediately in contact with the molecule) owing to the lifting of the topmost Fe layer and ensuing reduction of the interlayer exchange interactions (see Fig. 1.24). Conversely, for strongly chemisorbed molecules (π-conjugated system), this magnetic softening is caused by the interplay between the geometrical effect and the hybridisation of π-molecular orbitals and *d*-states of the FM metal. [88]. Altogether these results indicate that, albeit through different mechanism, also non π-conjugated molecules present mechanisms and opportunities of tuning interfacial magnetic properties. In Chapter 4 I will build on these results exploring the possibility of magnetic hardening at the interfaces between Cu and non π-conjugated molecular systems.

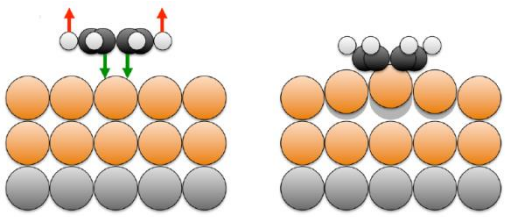

Figure 1.24: Adapted from [88]. Schematic representation of the interaction between the dioxin molecule and the Fe/W(110) substrate. Hydrogen atoms are repelled from the surface, whereas the central part of the molecule (oxygen and/or carbon atoms) interacts chemically with the surface. This induces a geometrical distortion, e.g., a lifting of the topmost Fe atoms immediately below the adsorbed molecule, which in turn leads to a decrease in interlayer magnetic exchange interactions and overall magnetic softening of the 2nd topmost Fe layers.

Finally, further recent studies of spatially extended two-dimensional graphene film adsorbed on Co(111) reveals an enhancement of the magnetic hardening of the Co atoms underneath the graphene compared to the clean Co surface. However, there is no magnetic hardening or softening for the interlayer magnetic interaction in contrast to finite π-molecular systems which exhibit magnetic interlayer softening [89]. Interlayer magnetic hardening or softening is very interesting for spintronics applications, where the magnetic ordering of the FM substrates need to be switched independently with respect to each other.

1.6.2 Interfaces between originally non-ferromagnetic metals and /organics

The adsorption of OSC on FM surface leads to a modification of the molecular states at the interface due to hybridisation which modifies the electronic and magnetic properties of the FM substrate, resulting in the formation of novel interface states with new properties. Very recently, it has been demonstrated that interface re-hybridisation can also promote magnetism when nonmagnetic metal such as Cu and Mn are employed as substrate for the adsorption of C_{60} [57]. The phenomenon is appealing because control and enhancement of emergent magnetism between cheap and non-toxic materials such as light transition-metals and organic semiconductors

may provide more eco-friendly and sustainable alternatives to conventional magnetic materials and devices [57[90].

Fig. 1.25 shows a control experiment introducing a thin Al_2O_3 layer spacer between the C_{60} and the non-magnetic metal showing that there is no magnetism when this layer is introduced. This control experiment, together with spin-polarised muon spectroscopy, confirms that the magnetic state arises from the C_{60}/Cu and C_{60}/Mn interface. Fig. 1.26 shows that the magnetisation of the Cu/C_{60} interface is more than four times larger than for Mn/C_{60} and it decays when the thickness of the fullerene is larger than 2-3nm. It is suggested that this is due to better lattice matching and larger Cu-C_{60} charge transfer. In order to study the influence of the roughness on the magnetic properties at the interface, several systems were modelled via DFT (see Fig. 1.27a-b). Fig. 1.27c shows the atom-resolved analysis of the Stoner exchange integral (I_S) of the different interfaces indicating an increment of I_S by a factor up to four with respect to the Cu bulk. Such a substantial magnetic hardening has been proposed to be the cause for the onset of ferromagnetic ordering at the hybrid interface. Recent experiments [90] demonstrate that the effect is rather general with emergent ferromagnetic ordering having being measured also for other interfaces between paramagnetic (Sc, Mn, Pt) or diamagnetic (Cu) transition-metal layers and differently π-conjugated organic substrates (fullerene C_{60} and amorphous carbon films) [90].

Overall, these results suggest new routes to produce magnetic ordering exploiting the hybrid interfaces between molecular materials and non-magnetic metals [91]. This Thesis is devoted to gather further fundamental understanding on the possibilities offered by interfacial hybridisation between non-magnetic Cu and organic systems in tuning the emergent magnetism.

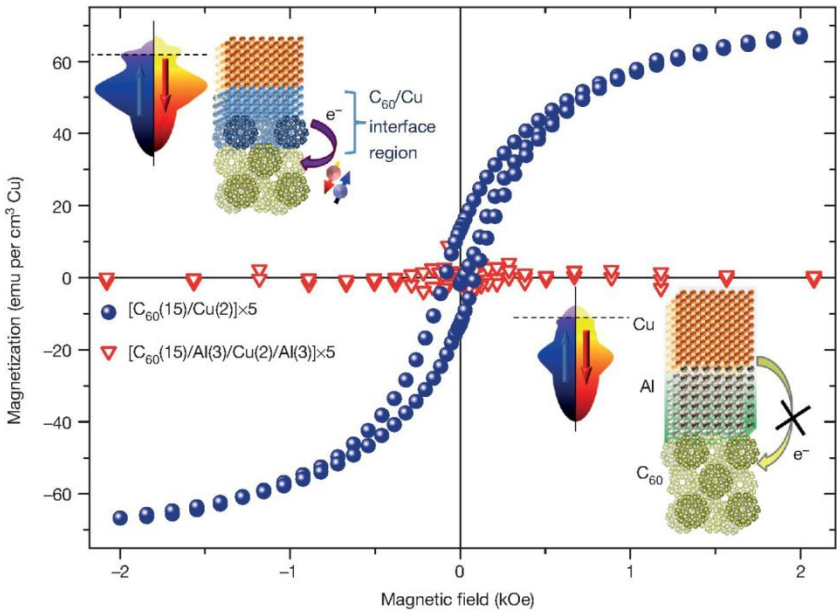

Figure 1.25: Adapted from [91]. Effect of molecular interfaces. Schematics and room-temperature magnetisation for a Ta(5)/[C_{60}(15)/Cu(2)]x5/Al(5) and a Ta(5)/[C_{60}(15)/Al(3)/Cu(2)/Al(3)]x5 sample; the numbers in parentheses are the film thicknesses in nanometres. The Cu-to-C_{60} charge transfer and interface reconstruction results in substantial changes in the DOS of the metallic film and a band splitting that leads to magnetic ordering. On the other hand, an Al spacer between both materials screens the charge transfer from the 3d transition metal and stops the band splitting. emu, electromagnetic unit.

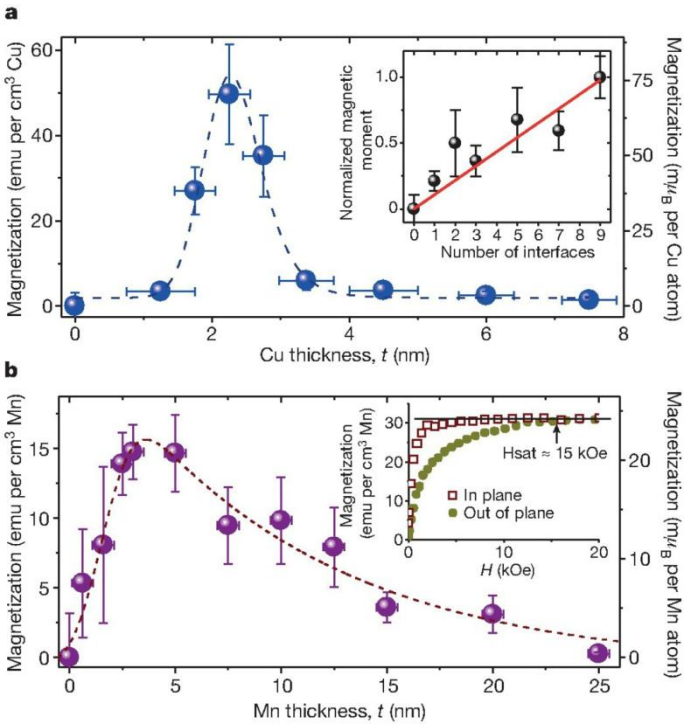

Figure 1.26: Adapted from [91]. Room-temperature magnetisation for Cu and Mn films. Dashed lines are exponentially modified Gaussian fits. Error bars in thickness quantify the film roughness. **a)** Dependence of the magnetisation on the Cu-film thickness for a total of 145 samples with the structure Ta(5)/[C_{60}(10–20)/Cu(t)/C_{60}(10–20)]x(1–5)/Al(5). Inset, magnetic moment versus the number of C_{60}(15)/Cu(2.5) interfaces: they are roughly linearly proportional. **b)** As for (a), but for Mn, with 96 samples measured. The magnetisation in Mn films is smaller than in Cu films, but propagates for a longer distance. Inset, out-of-plane and in-plane magnetisation measurements of a [C_{60}(15)/Mn(2.5)]x4 sample as a function of magnetic field strength (H). H_{sat}, magnetic field strength at which the magnetisation saturates; emu, electromagnetic unit; μ_B, Bohr magneton.

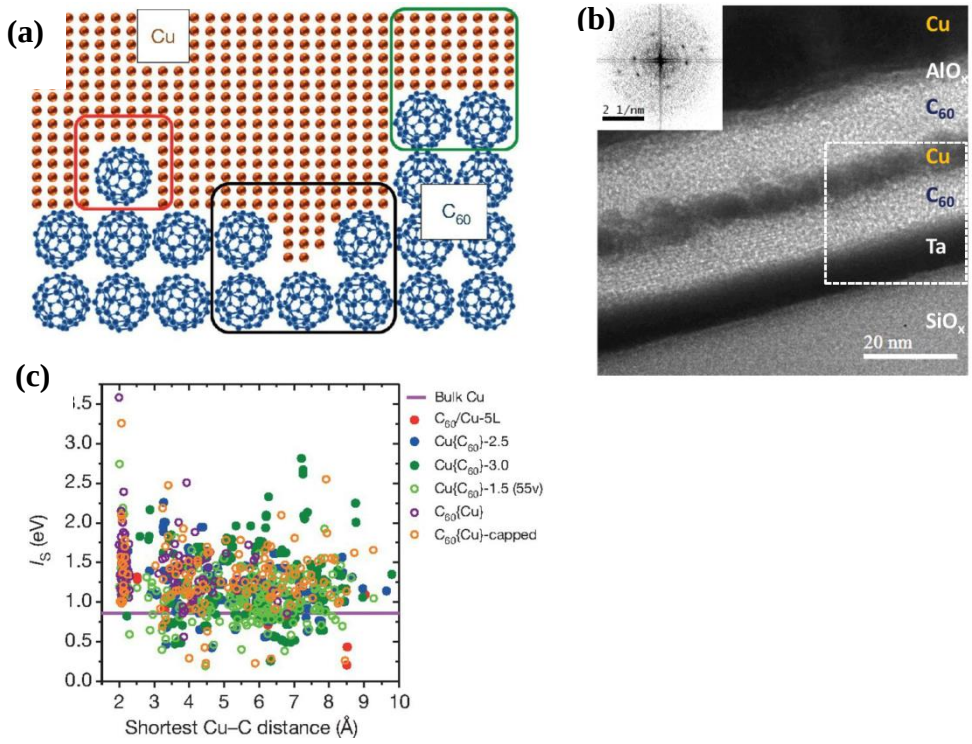

Figure 1.27: Adapted from [91]. **a)** Schematic of the molecularly rough Cu/C_{60} interface with: atomically flat C_{60}/Cu contacts (green square); C_{60} inclusion in Cu film(Cu{C_{60}}; red square); and Cu inclusion in pits of the C_{60} film (C_{60}{Cu}; black square). **b)** TEM image of a cross-section of a Si(substrate)/SiO_x/Ta/C_{60}/Cu/C_{60}/ AlO_x/Cu stack with (inset) fast Fourier transform of the region within the dotted box, indicating the crystallinity of the C_{60} layer. The polycrystalline but continuous nature of the thin Cu insertion layer is evident. **c)** Atom-resolved analysis of the DFT-approximated Stoner exchange integral I_S for the Cu atoms as a function of the shortest Cu–C_{60} distance. I_S for bulk Cu is 0.86 eV.

1.7 References

1. Dincer, I., *Renewable energy and sustainable development: a crucial review.* Renewable and Sustainable Energy Reviews, 2000. **4**(2): p. 157-175.
2. Gutfleisch, O., et al., *Magnetic materials and devices for the 21st century: stronger, lighter, and more energy efficient.* Advanced materials, 2011. **23**(7): p. 821-842.
3. Kramer, M., et al., *Prospects for non-rare earth permanent magnets for traction motors and generators.* JOM, 2012. **64**(7): p. 752-763.
4. Raman, K.V., et al., *Interface-engineered templates for molecular spin memory devices.* Nature, 2013. **493**(7433): p. 509-513.

5. Bauer, D., et al., *US Department of Energy Critical Materials Strategy.* 2010.
6. Coey, J., *Permanent magnets: Plugging the gap.* Scripta Materialia, 2012. **67**(6): p. 524-529.
7. Bruce, D.W., D. O'Hare, and R.I. Walton, *Molecular materials.* Vol. 14. 2011: John Wiley & Sons.
8. Miller, J.S., *Magnetically ordered molecule-based materials.* Chemical Society Reviews, 2011. **40**(6): p. 3266-3296.
9. Pei, Q., *Light-emitting polymers.* Material Matters, 2007. **2**(3): p. 26.
10. David, T., W. Arasho, and S.S. Sun, *Synthesis and structure-optoelectronic property relationships of a series of PPV and SFTV derived polymers.* Journal of Polymer Science Part A: Polymer Chemistry, 2015. **53**(19): p. 2202-2213.
11. Geng, R., et al., *Article type: Review Paper Title: A Review on Organic Spintronic Materials and Devices: I. Magnetic Field Effect on Organic Light Emitting Diodes.* 2016.
12. Dong, H., et al., *25th Anniversary Article: Key Points for High-Mobility Organic Field-Effect Transistors.* Advanced Materials, 2013. **25**(43): p. 6158-6183.
13. Kronemeijer, A.J., et al., *Two-Dimensional Carrier Distribution in Top-Gate Polymer Field-Effect Transistors: Correlation between Width of Density of Localized States and Urbach Energy.* Advanced Materials, 2014. **26**(5): p. 728-733.
14. Scherf, U. and E.J. List, *Semiconducting polyfluorenes—towards reliable structure–property relationships.* Advanced Materials, 2002. **14**(7): p. 477-487.
15. Chen, S., et al., *Polyacetylene,(CH) x: Photoelectrochemical solar cell.* Applied Physics Letters, 1980. **36**(1): p. 96-98.
16. Cheng, Y.-J., S.-H. Yang, and C.-S. Hsu, *Synthesis of conjugated polymers for organic solar cell applications.* Chemical reviews, 2009. **109**(11): p. 5868-5923.

17. Geng, R., et al., *A Review on Organic Spintronic Materials and Devices: I. Magnetic Field Effect on Organic Light Emitting Diodes.* Journal of Science: Advanced Materials and Devices, 2016.
18. Pei, Q., *Light emitting polymers.* Material Matters, 2007. **3**: p. 26.
19. Kaur, N., et al., *Organic materials for photovoltaic applications: Review and mechanism.* Synthetic Metals, 2014. **190**: p. 20-26.
20. Tamai, Y., et al., *Exciton diffusion in conjugated polymers: From fundamental understanding to improvement in photovoltaic conversion efficiency.* The journal of physical chemistry letters, 2015. **6**(17): p. 3417-3428.
21. Lu, L., et al., *Recent advances in bulk heterojunction polymer solar cells.* Chemical Reviews, 2015. **115**(23): p. 12666-12731.
22. Duan, C., et al., *Development of Active Materials and Interface Materials for High Performance Bulk-Heterojunction Polymer Solar Cells*, in *Progress in High-Efficient Solution Process Organic Photovoltaic Devices*. 2015, Springer. p. 191-219.
23. Thompson, B.C. and J.M. Fréchet, *Polymer–fullerene composite solar cells.* Angewandte chemie international edition, 2008. **47**(1): p. 58-77.
24. Nelson, J., et al., *Modeling charge transport in organic photovoltaic materials.* Accounts of chemical research, 2009. **42**(11): p. 1768-1778.
25. Li, G., R. Zhu, and Y. Yang, *Polymer solar cells.* Nature Photonics, 2012. **6**(3): p. 153-161.
26. Dennler, G., M.C. Scharber, and C.J. Brabec, *Polymer-Fullerene bulk-heterojunction solar cells.* Advanced Materials, 2009. **21**(13): p. 1323-1338.
27. Brabec, C.J., et al., *Polymer–fullerene bulk-heterojunction solar cells.* Advanced Materials, 2010. **22**(34): p. 3839-3856.
28. Li, C.-T., et al., *Composite films of carbon black nanoparticles and sulfonated-polythiophene as flexible counter electrodes for dye-sensitized solar cells.* Journal of Power Sources, 2016. **302**: p. 155-163.
29. Kim, B.G., K. Chung, and J. Kim, *Molecular Design Principle of All-organic Dyes for Dye-Sensitized Solar Cells.* Chemistry–A European Journal, 2013. **19**(17): p. 5220-5230.

30. Małachowski, M. and J. Żmija, *Organic field-effect transistors.* Opto-Electronics Review, 2010. **18**(2): p. 121-136.
31. Zaumseil, J. and H. Sirringhaus, *Electron and ambipolar transport in organic field-effect transistors.* Chemical reviews, 2007. **107**(4): p. 1296-1323.
32. Wang, K.L., et al. *Comparison of spintronics and nanoelectronics for information processing*. in *Solid-State and Integrated-Circuit Technology, 2008. ICSICT 2008. 9th International Conference on*. 2008. IEEE.
33. Awschalom, D.D. and M.E. Flatté, *Challenges for semiconductor spintronics.* Nature Physics, 2007. **3**(3): p. 153-159.
34. Horowitz, G., *Organic field-effect transistors.* Advanced Materials, 1998. **10**(5): p. 365-377.
35. Galbiati, M., *Molecular Spintronics: From Organic Semiconductors to Self-Assembled Monolayers*. 2015: Springer.
36. McMahon, D.P., D.L. Cheung, and A. Troisi, *Why holes and electrons separate so well in polymer/fullerene photovoltaic cells.* The Journal of Physical Chemistry Letters, 2011. **2**(21): p. 2737-2741.
37. Qin, T. and A. Troisi, *Relation between structure and electronic properties of amorphous MEH-PPV polymers.* Journal of the American Chemical Society, 2013. **135**(30): p. 11247-11256.
38. Fornari, R.P. and A. Troisi, *Theory of charge hopping along a disordered polymer chain.* Physical Chemistry Chemical Physics, 2014. **16**(21): p. 9997-10007.
39. Naber, W., S. Faez, and W. Van Der Wiel, *Organic spintronics.* Journal of Physics D: Applied Physics, 2007. **40**(12): p. R205.
40. Nguyen, T.D., et al., *Isotope effect in spin response of [pi]-conjugated polymer films and devices.* Nature materials, 2010. **9**(4): p. 345-352.
41. Huertas-Hernando, D., F. Guinea, and A. Brataas, *Spin-orbit coupling in curved graphene, fullerenes, nanotubes, and nanotube caps.* Physical Review B, 2006. **74**(15): p. 155426.
42. Devkota, J., et al., *Organic Spin Valves: A Review.* Advanced Functional Materials, 2016.

43. Niu, L., et al., *Hyperfine interaction vs. spin–orbit coupling in organic semiconductors.* RSC Advances, 2016. **6**(112): p. 111421-111426.
44. Fabian, J., et al., *Semiconductor spintronics.* arXiv preprint arXiv:0711.1461, 2007.
45. Zhan, Y. and M. Fahlman, *The study of organic semiconductor/ferromagnet interfaces in organic spintronics: A short review of recent progress.* Journal of Polymer Science Part B: Polymer Physics, 2012. **50**(21): p. 1453-1462.
46. Dediu, V., et al., *Room temperature spin polarized injection in organic semiconductor.* Solid State Communications, 2002. **122**(3): p. 181-184.
47. Xiong, Z., et al., *Giant magnetoresistance in organic spin-valves.* Nature, 2004. **427**(6977): p. 821-824.
48. Majumdar, S., et al., *Application of regioregular polythiophene in spintronic devices: effect of interface.* Applied physics letters, 2006. **89**(12): p. 122114-122114.
49. Zhang, X., et al., *Observation of a large spin-dependent transport length in organic spin valves at room temperature.* Nature communications, 2013. **4**: p. 1392.
50. Rocha, A.R., et al., *Towards molecular spintronics.* Nature materials, 2005. **4**(4): p. 335-339.
51. Barraud, C., et al., *Unravelling the role of the interface for spin injection into organic semiconductors.* Nature Physics, 2010. **6**(8): p. 615-620.
52. Sanvito, S., *Molecular spintronics: The rise of spinterface science.* Nature Physics, 2010. **6**: p. 562-564.
53. Atodiresei, N. and K.V. Raman, *Interface-assisted spintronics: Tailoring at the molecular scale.* MRS bulletin, 2014. **39**(07): p. 596-601.
54. Lazić, P., et al., *First-principles insights into the electronic and magnetic structure of hybrid organic-metal interfaces.* Journal of Physics: Condensed Matter, 2014. **26**(26): p. 263001.
55. Shi, S., et al., *Hybrid Interface States and Spin Polarization at Ferromagnetic Metal–Organic Heterojunctions: Interface Engineering for Efficient Spin Injection in Organic Spintronics.* Advanced Functional Materials, 2014. **24**(30): p. 4812-4821.

56. Moodera, J.S., T.S. Santos, and T. Nagahama, *The phenomena of spin-filter tunnelling.* Journal of Physics: Condensed Matter, 2007. **19**(16): p. 165202.
57. Brede, J. and R. Wiesendanger, *Spin-resolved characterization of single cobalt phthalocyanine molecules on a ferromagnetic support.* Physical Review B, 2012. **86**(18): p. 184423.
58. Lach, S., et al., *Metal–organic hybrid interface states of a ferromagnet/organic semiconductor hybrid junction as basis for engineering spin injection in organic spintronics.* Advanced Functional Materials, 2012. **22**(5): p. 989-997.
59. Moodera, J.S., B. Koopmans, and P.M. Oppeneer, *On the path toward organic spintronics.* MRS bulletin, 2014. **39**(07): p. 578-581.
60. Fu-Jiang, Y., H. Shi-Xuan, and X. Shi-Jie, *Progress in organic spintronics.* Chinese Physics B, 2014. **23**(5): p. 058106.
61. Majumdar, S., et al., *Comparing small molecules and polymer for future organic spin-valves.* Journal of alloys and compounds, 2006. **423**(1): p. 169-171.
62. Javaid, S., et al., *Impact on interface spin polarization of molecular bonding to metallic surfaces.* Physical review letters, 2010. **105**(7): p. 077201.
63. Yang, Z.-H., R. Pang, and X.-Q. Shi, *Engineering Magnetic Hybridization at Organic–Ferromagnetic Interfaces by C60-Adsorption-Induced Fe (001) Surface Reconstruction.* The Journal of Physical Chemistry C, 2015. **119**(19): p. 10532-10537.
64. Pang, R., X. Shi, and M.A. Van Hove, *Manipulating Magnetism at Organic/Ferromagnetic Interfaces by Molecule-Induced Surface Reconstruction.* Journal of the American Chemical Society, 2016. **138**(12): p. 4029-4035.
65. Atodiresei, N., et al., *Design of the local spin polarization at the organic-ferromagnetic interface.* Physical review letters, 2010. **105**(6): p. 066601.
66. Atodiresei, N., et al., *Engineering the magnetic properties of hybrid organic-ferromagnetic interfaces by molecular chemical functionalization.* Physical Review B, 2011. **84**(17): p. 172402.

67. Friedrich, R., et al., *Chemically functionalized magnetic exchange interactions of hybrid organic-ferromagnetic metal interfaces.* Physical Review B, 2015. **91**(11): p. 115432.
68. Brede, J., et al., *Spin-and energy-dependent tunneling through a single molecule with intramolecular spatial resolution.* Physical review letters, 2010. **105**(4): p. 047204.
69. Wang, X., et al., *Peculiarities of spin polarization inversion at a thiophene/cobalt interface.* Applied Physics Letters, 2013. **102**(11): p. 111604.
70. Caffrey, N.M., et al., *Atomic-scale inversion of spin polarization at an organic-antiferromagnetic interface.* Physical Review B, 2013. **88**(15): p. 155403.
71. Wang, Y., et al., *Reversible Spin Polarization at Hybrid Organic–Ferromagnetic Interfaces.* The Journal of Physical Chemistry Letters, 2013. **4**(20): p. 3508-3512.
72. Methfessel, T., et al., *Spin scattering and spin-polarized hybrid interface states at a metal-organic interface.* Physical Review B, 2011. **84**(22): p. 224403.
73. Callsen, M., et al., *Magnetic hardening induced by nonmagnetic organic molecules.* Physical review letters, 2013. **111**(10): p. 106805.
74. Morita, Y., et al., *Synthetic organic spin chemistry for structurally well-defined open-shell graphene fragments.* Nature chemistry, 2011. **3**(3): p. 197-204.
75. Moorsom, T., et al., *Spin-polarized electron transfer in ferromagnet/C 60 interfaces.* Physical Review B, 2014. **90**(12): p. 125311.
76. Tran, T., et al., *Hybridization-induced oscillatory magnetic polarization of C (60) orbitals at the C (60)/Fe (001) interface.* Applied Physics Letters, 2011. **98**(22): p. 222505.
77. Kawahara, S., et al., *Large magnetoresistance through a single molecule due to a spin-split hybridized orbital.* Nano letters, 2012. **12**(9): p. 4558-4563.

78. Cakır, D., D.M. Otálvaro, and G. Brocks, *Magnetoresistance in multilayer fullerene spin valves: A first-principles study.* Physical Review B, 2014. **90**(24): p. 245404.
79. Zhang, X., et al., *Spin conserved electron transport behaviors in fullerenes (C 60 and C 70) spin valves.* Carbon, 2016. **106**: p. 202-207.
80. Çakır, D., D.M. Otálvaro, and G. Brocks, *From spin-polarized interfaces to giant magnetoresistance in organic spin valves.* Physical Review B, 2014. **89**(11): p. 115407.
81. Tran, T.L.A., et al., *Magnetic Properties of bcc-Fe (001)/C60 Interfaces for Organic Spintronics.* ACS applied materials & interfaces, 2013. **5**(3): p. 837-841.
82. Borshch, S. and K. Prassides, *Fullerene Anions: Jahn− Teller or Pseudo-Jahn− Teller Effects?* The Journal of Physical Chemistry, 1996. **100**(22): p. 9348-9351.
83. Adams, G.B., et al., *Jahn-Teller distortions in solid C20 and other fullerene structures.* Chemical physics, 1993. **176**(1): p. 61-66.
84. Maurice, J.-L., et al., *Interfaces in {100} epitaxial heterostructures of perovskite oxides.* Philosophical Magazine, 2006. **86**(15): p. 2127-2146.
85. Sun, X., et al., *Magnetic moment enhancement and spin polarization switch of the manganese phthalocyanine molecule on an IrMn (100) surface.* The Journal of chemical physics, 2014. **141**(3): p. 034703.
86. Liang, S., et al., *Ferroelectric Control of Organic/Ferromagnetic Spinterface.* Advanced Materials, 2016. **28**(46): p. 10204-10210.
87. Djeghloul, F., et al., *High Spin Polarization at Ferromagnetic Metal-Organic Interfaces: a Generic Property.* The journal of physical chemistry letters, 2016.
88. Friedrich, R., et al., *Molecular induced skyhook effect for magnetic interlayer softening.* Physical Review B, 2015. **92**(19): p. 195407.
89. Friedrich, R., et al., *Exchange interactions of magnetic surfaces below two-dimensional materials.* Physical Review B, 2016. **93**(22): p. 220406.

90. Al Ma'Mari, F., et al., *Emergent magnetism at transition-metal–nanocarbon interfaces.* Proceedings of the National Academy of Sciences, 2017. **114**(22): p. 5583-5588.
91. Al Ma'Mari, F., et al., *Beating the Stoner criterion using molecular interfaces.* Nature, 2015. **524**(7563): p. 69-73.

Chapter 2

Theoretical and computational methods

Abstract

This Chapter provides an introduction to the theoretical and computational methods used in my PhD. The chapter begins with an introduction to the ground state many-body time-independent Schrödinger equation. Solving this equation is an extremely demanding task and some approximations such as the Born-Oppenheimer one and the use of the total electron density instead of the coordinates of all the electrons in the system need to be introduced for computational feasibility. The fundamentals of Density Functional Theory (DFT) and its basic mathematical ground Hohenberg-Kohn theorems are described. Then, it is explained how the Kohn-Sham (KS) equations simplify the many-body problem. Finally, all the approximations and tools employed to practically solve the KS equations such as the exchange-correlation functionals, periodic boundary conditions, plane waves and pseudopotentials are described, including several geometry optimisation methods of increasing accuracy and computational cost. In the second part of the chapter, the basic theory of magnetism, including the Stoner model for ferromagnetism and itinerant metamagnetism, is introduced.

2.1 The Schrödinger equation

The description of the properties of the matter at the atomic scale from theoretical methods is rooted on differently approximated solution to the time-independent Schrödinger equation [1]:

$$\hat{\mathrm{H}}\psi_i(\mathbf{r},\mathbf{R}) = E_i\psi_i(\mathbf{r},\mathbf{R}), \tag{2.1}$$

where $\hat{\mathrm{H}}$ is the Hamiltonian operator, ψ is the wave function, E is the ground-state energy. The Hamiltonian and the wave function depend on a set of N_n nuclear coordinates, $\mathbf{R} = \{\mathbf{R}_I,\ I = 1, \dots, N_n\}$, and a set of N_e electronic coordinates, $\mathbf{r} = \{\mathbf{r}_i,\ i = 1, \dots, N_e\}$.

The Hamiltonian is a differential operator representing the total energy of the system:

$$\hat{\mathrm{H}} = -\frac{1}{2}\sum_{i=1}^{N_e}\nabla_i^2 - \frac{1}{2}\sum_{I=1}^{N_n}\frac{1}{M_I}\nabla_I^2 - \sum_{i=1}^{N_e}\sum_{I=1}^{N_n}\frac{Z_I}{\mathbf{r}_{iI}} + \sum_{i=1}^{N_e}\sum_{j>i}^{N_e}\frac{1}{\mathbf{r}_{ij}} + \sum_{I=1}^{N_n}\sum_{J>I}^{N_n}\frac{Z_I Z_J}{\mathbf{R}_{IJ}} \tag{2.2}$$

The first two terms describe the kinetic energy of the electrons and nuclei, respectively. The following terms represent the potential energy contributions to the Hamiltonian and describe the attractive electrostatic potential due to nuclei and electrons interactions and the repulsive electron-electron and nucleus-nucleus interactions, respectively. The Laplacian operator ∇_j^2 is defined as a sum of differential operators:

$$\nabla_j^2 = \frac{\partial^2}{\partial x_j^2} + \frac{\partial^2}{\partial y_j^2} + \frac{\partial^2}{\partial z_j^2} \tag{2.3}$$

Z_I is the nuclear charge of the I$^{\text{th}}$ atom, and M_I is the mass of I$^{\text{th}}$ nucleus in atomic units. Atomic units are used here to avoid the use of physical constants, $m_e = e = \hbar = a_0 = 1$, where m_e is the mass of the electron, e is the charge of the electron, $\hbar$ is the Planck's constant/2π and a_0 is the Bohr radius.

In principle, all the properties of a system can be obtained by solving its time-independent Schrödinger equation. However, only in few cases such as hydrogenoid atoms the analytic solution is possible. One of the main difficulties in analytically solving Schrödinger equation is that the electrons interact among themselves via Coulomb interactions and the behaviour of an electron in a region of the space influences the other electrons in other regions. In other words, the electrons cannot be treated as independent particles. This is the so-called quantum many-body problem. Therefore, in order to decrease the theoretical and computational effort of solving the Schrödinger equation some approximations are needed.

2.1.1 The Born-Oppenheimer approximation

Schrödinger equation can be simplified taking advantage of the slower motion of nuclei compared to the electrons. Protons and neutrons, that constitute nuclei, have masses over 1,800 times larger than electrons and accordingly show substantially slower dynamics when coupled to electrons in atoms and molecules. As a result, electrons rapidly relax into the ground-state following the motion of the nuclei. In other words, the electrons instantaneously modify their wave function according to the nuclear wave function. This is the Born-Oppenheimer adiabatic approximation [1], which allows us to separate the motion of the nuclei from that of the electrons, $\hat{\mathrm{H}} = \hat{\mathrm{H}}_{elec} + \hat{\mathrm{H}}_{nuc}$. This approximation considers the electrons as moving in a static potential generated by frozen nuclei. If the nuclei are fixed in the space, their kinetic energy is zero and the potential energy that arises from nucleus-nucleus interactions is constant. Thus, the complete Hamiltonian can be simplified to:

$$\hat{\mathrm{H}}_{elec} = -\frac{1}{2}\sum_{i=1}^{N_e}\nabla_i^2 - \sum_{i=1}^{N_e}\sum_{I=1}^{N_n}\frac{Z_I}{\mathbf{r}_{iI}} + \sum_{i=1}^{N_e}\sum_{j>i}^{N_e}\frac{1}{\mathbf{r}_{ij}} = \hat{T} + \hat{V}_{ext} + \hat{V}_{ee}, \qquad (2.4)$$

where $\hat{T}$ is the kinetic energy operator, $\hat{V}_{ext}$ is the potential energy operator arising from the electrons and nuclei interactions and $\hat{V}_{ee}$ is the electron-electron repulsive potential energy operator. The operators $\hat{T}$ and $\hat{V}_{ee}$ are universal, they do not depend on the system, while $\hat{V}_{ext}$ is system-dependent. From now on, only the electronic

equations will be considered and the subscript $'elec'$ will be dropped. Therefore, the electronic Schrödinger equation is defined as:

$$\left[-\frac{1}{2}\sum_{i=1}^{N_e}\nabla_i^2-\sum_{i=1}^{N_e}\sum_{I=1}^{N_n}\frac{Z_I}{\mathbf{r}_{iI}}+\sum_{i=1}^{N_e}\sum_{j>i}^{N_e}\frac{1}{\mathbf{r}_{ij}}\right]\psi=E\psi\,. \tag{2.5}$$

2.1.2 The electron density

It is worth noting that the wave function of any set of particles cannot be directly observed. However, a physical interpretation is associated with the square of the wave function, as the probability that an electron *i* in the wave function $\psi(\mathbf{r})$ is located at the position **r** with an arbitrary spin, s_1. The probability, $n(\mathbf{r})$, is defined as the integral over the spin coordinates of all the electrons and over all but one of the spatial variables ($\mathbf{x}_i=\mathbf{r}_i,\mathrm{s}_i$):

$$n(\mathbf{r})=N\int\ldots\int|\,\psi\left(\mathbf{x}_{1,}\,\mathbf{x}_2,\ldots,\mathbf{x}_{N,}\right)|^2\mathrm{d}s_1,\mathrm{d}\mathbf{x}_2,\ldots,\mathrm{d}\mathbf{x}_N\,. \tag{2.6}$$

The previous equation determines the probability of finding any of the *N* electrons within the volume element d**r** but with arbitrary spin while the other *N*-1 electrons have arbitrary positions and spin in the state represented by the wave function.

The electrons are indistinguishable; hence, the probability of finding any electron at a determined position is just *N* times the probability of one electron. The electron density is a non-negative function that just depends on three variables, it integrates to the total number of electrons and it vanishes at infinity:

$$n(\mathbf{r}\to\infty)=0\,, \tag{2.7}$$

$$\int n(\mathbf{r})\,\mathrm{d}\mathbf{r}_1=N\,. \tag{2.8}$$

The advantage of using the electron density over the electronic wave function is clear by the fact that one equation that depends only on three coordinates is simpler than solve the many-body Schrödinger equation that involves $3N$ degrees of freedom. Therefore, the electron density is much more numerically and computationally effective.

2.2 Density Functional Theory

Density functional theory (DFT) provides an approach for dealing with the universal operators, $\hat{T}$ and $\hat{V}_{ee}$ in Eq. 2.4 and simplifies the many-body problem onto a single-body problem. The DFT approach can be summarized as:

$$n(\mathbf{r}) \Rightarrow \psi(\mathbf{r}_1, \dots, \mathbf{r}_N) \Rightarrow \hat{V}_{ext}. \tag{2.9}$$

That is, if we know the density of the system $n(\mathbf{r})$, we can calculate the potential of the system (V_{ext}) of wavefunction (ψ), without having to compute the wave function.

Llewellyn Thomas and Enrico Fermi developed the first DFT approach to describe quantum mechanical many-body systems in 1927 [2, 3]. They introduced the first method where the full electronic density was the fundamental variable to calculate the energy of an electronic system. This approach employs the kinetic energy of a homogeneous gas of non-interacting electrons. The nuclear-electron and electron-electron interactions are treated in a classical way, neglecting the exchange and correlation effects. However, these aggressive approximations have stark consequences on the accuracy of the method that result incapable of describing electronic bound states for systems of known stability. Furthermore, there is no physical background that establishes a one to one relationship between the ground-state wave function and the density functional. Thus, this approach was forgotten until mid-1960.

2.2.1 The Hohenberg-Kohn theorems

Hohenberg and Kohn [4] in 1964 proved two fundamental theorems, the Hohenberg-Kohn (HK) theorems, which are the basic mathematical ground of modern DFT applications. The **first theorem** postulates that the ground-state energy from Schrödinger equation is a unique functional of the electron density. In other words, there is a one-to-one relationship between the ground-state wave function and the ground-state electron density. Therefore, the ground-state wave function is obtained by solving the full many-body Schrödinger equation with the ground-state electron density

The theorem was proven by a *reduction ad absurdum* argument. We suppose that there are two different external potentials $V_{ext}^{(1)}(\mathbf{r})$ and $V_{ext}^{(2)}(\mathbf{r})$ which differ by more than a constant and correspond to the same ground-state electron density, $n_o(\mathbf{r})$. The two external potentials lead to two different Hamiltonians, $\widehat{H}^{(1)}$ and $\widehat{H}^{(2)}$, which have different ground-state wave functions, $\psi^{(1)}$ and $\psi^{(2)}$, leading to different ground-state energies $E^{(1)}$ and $E^{(2)}$. Since $\psi^{(2)}$ is not the ground-state of $\widehat{H}^{(1)}$, then:

$$E^{(1)} = \langle\psi^{(1)}|\widehat{H}^{(1)}|\psi^{(1)}\rangle < \langle\psi^{(2)}\big|\widehat{H}^{(1)}\big|\psi^{(2)}\rangle. \tag{2.10}$$

The last term in the equation can be written as:

$$\begin{aligned}\langle\psi^{(2)}\big|\hat{\mathrm{H}}^{(1)}\big|\psi^{(2)}\rangle &= \langle\psi^{(2)}\big|\widehat{H}^{(2)}\big|\psi^{(2)}\rangle + \langle\psi^{(2)}\big|\widehat{H}^{(1)} - \widehat{H}^{(2)}\big|\psi^{(2)}\rangle \\ &= E^{(2)} + \int\Big[V_{ext}^{(1)}(\mathbf{r}) - V_{ext}^{(2)}(\mathbf{r})\Big]n_o\,(\mathbf{r})\,\mathrm{d}\mathbf{r}.\end{aligned} \tag{2.11}$$

Therefore:

$$E^{(1)} < E^{(2)} + \int\Big[V_{ext}^{(1)}(\mathbf{r}) - V_{ext}^{(2)}(\mathbf{r})\Big]n_o\,(\mathbf{r})\mathrm{d}\mathbf{r}. \tag{2.12}$$

$$E^{(2)} < E^{(1)} + \int\Big[V_{ext}^{(2)}(\mathbf{r}) - V_{ext}^{(1)}(\mathbf{r})\Big]n_o\,(\mathbf{r})\mathrm{d}\mathbf{r}. \tag{2.13}$$

Adding these two inequalities, it turns out that:

$$E^{(1)} + E^{(2)} < E^{(1)} + E^{(2)}, \tag{2.14}$$

which is absurd. Hence, if $V_{ext}^{(1)}(\mathbf{r}) \neq V_{ext}^{(2)}(\mathbf{r})$, they cannot correspond to the same electronic density for the ground-state. This concludes that the ground-state density is uniquely related to the external potential V_{ext}.

Since the ground-state energy, E_0, is a functional of $n_o(\mathbf{r})$, we can split the energy into its different contributions that must be functional of $n_o(\mathbf{r})$ as well:

$$E_0[n_o] = T[n_o] + E_{ee}[n_o] + E_{Ne}[n_o] = T[n_o] + E_{ee}[n_o] + \int n_o(\mathbf{r}) E_{Ne} \mathrm{d}\mathbf{r}. \tag{2.15}$$

The potential energy due to nuclei-electron interactions is the only term in the previous equation that is system dependent, the kinetic energy and the electron-electron interactions are universally valid. We introduce here a new functional called Hohenberg-Kohn functional, $F_{HK}[n]$, that include all the system independent terms:

$$E_{HK}[n_o] = F_{HK}[n_o] + \int V_{ext}(\mathbf{r}) n_o(\mathbf{r})\, d\mathbf{r}. \tag{2.16}$$

Note that $F_{HK}[n]$ only depends on the electronic density, it does not explicitly depends on the external potential. In principle, the expectation value of the Hohenberg-Kohn functional, $\langle \psi | \hat{T} + \hat{V}_{ee} | \psi \rangle$, can be calculated using an arbitrary density, $n(\mathbf{r})$, as:

$$F_{HK}[n] = T[n] + E_{ee}[n] = \langle \psi | \hat{T} + \hat{V}_{ee} | \psi \rangle, \tag{2.17}$$

where the wave function, ψ, is the one that leads the lowest energy among all the wave functions that yield n.

The first theorem proves that an electronic density functional exists and that it can be used to solve the Schrödinger equation. However, the theorem does not provide the

analytical form of the functionals that should be employed. If these functional were known, it would be possible to solve exactly the Schrödinger equation. The electron-electron interactions term can be split in two different contributions: the classical Coulomb part, J[n], and the term E_{ncl} that includes all the non-classical contributions of the electron-electron interactions and the exchange-correlation effects.

$$E_{ee}[n] = \frac{1}{2}\int\int \frac{n(\mathbf{r})n(\mathbf{r}')}{[\mathbf{r}-\mathbf{r}']}\mathrm{d}\mathbf{r}\mathrm{d}\mathbf{r}' + E_{ncl}[n] = J[n] + E_{ncl}[n] \tag{2.18}$$

At this point, the HK theorem has proved that the properties of interest can be derived from the ground-state density. However, we still need the tools to evaluate if a certain density is the ground-state density.

The **second theorem** states that the ground-state electronic density is the one that minimises the energy functional, $E[n]$. Therefore, the full solution of Schrödinger equation should be obtained by performing a search over all the possible densities to find the one that leads to a global minimum value of $E[n]$. The variational principle states that an approximate wave function will always lead to a larger energy than the ground-state wave function. Therefore, the energy obtained by the trial density, $n^{(1)}(\mathbf{r})$, represents an upper bound to the true ground-state energy:

$$E_0[n_o] \leq E\left[n^{(1)}\right] = T\left[n^{(1)}\right] + E_{ee}\left[n^{(1)}\right] + E_{ne}\left[n^{(1)}\right]. \tag{2.19}$$

The Hohenberg-Kohn functional is equal to the expectation value of the Hamiltonian in the ground-state. Suppose that we have a system with a ground-state density $n^{(1)}(\mathbf{r})$ which corresponds to an external potential $V_{ext}^{(1)}(\mathbf{r})$, since:

$$E^{(1)}\left[n^{(1)}\right] = E_{HK}\left[n^{(1)}\right] = \langle\psi^{(1)}|\hat{H}^{(1)}|\psi^{(1)}\rangle. \tag{2.20}$$

If we consider a different density $n^{(2)}(\mathbf{r})$, it will correspond to a different wave function $\psi^{(2)}$. Therefore, the energy $E^{(2)}\left[n^{(2)}\right]$ of this state is larger than $E^{(1)}\left[n^{(1)}\right]$:

$$E^{(1)}\left[n^{(1)}\right] = \langle\psi^{(1)}|\hat{H}^{(1)}|\psi^{(1)}\rangle < \langle\psi^{(2)}|\hat{H}^{(1)}|\psi^{(2)}\rangle = E^{(2)}\left[n^{(2)}\right]. \tag{2.21}$$

In principle, HK theorems allow us to find the exact ground-state density, minimising $E_{HK}[n]$ with respect to the variation of $n(\mathbf{r})$. However, this is a difficult task, because it involves knowledge of $F_{HK}[n]$. Another main problem is that the exact kinetic energy $T[n]$ in terms of the electronic density is not known.

2.2.2 The Kohn-Sham equations

The Kohn-Sham (KS) [5] method simplifies the difficult task of solving the many-body Schrödinger equation by obtaining an exact solution of the ground-state electronic many-body problem via the electronic density. KS approach substitute the ground-state density of the original interacting system by an auxiliary set of non-interacting single-electron equations moving in an external effective potential, $V_{ext}(\mathbf{r})$. All the contributions not included in the non-interaction electron approximations such as the quantum components of the kinetic energy and the electron-electron interactions are included in a term called exchange-correlation functional $E_{xc}[n]$. The ground-state electronic density of the auxiliary system must be the same that the density of the real target system of interacting electrons:

$$n_0(\mathbf{r}) \equiv n_s(\mathbf{r}) = \sum_{i=1}^{N} f_i|\varphi_i(\mathbf{r})|^2, \tag{2.22}$$

where $\varphi_i(\mathbf{r})$ are the non-interaction one-electron orbitals and f_i are the occupation number of the KS-states. The kinetic energy $T_s[n]$ employed is the independent-electron approximation to $T[n]$ using the same density as the real interacting system:

$$T_s[n] = -\frac{1}{2}\sum_{i=1}^{N} f_i\langle\varphi_i|\nabla^2|\varphi_i\rangle. \tag{2.23}$$

This is not the exact kinetic energy for the interacting system ($T_s \neq T$), the electron correlation term must be included in the exchange and correlation energy.

The KS approach to the original full interaction many-body problem rewrites the HK expression for the ground-state energy functional in the form:

$$E_{KS}[n] = T_s[n] + \int V_{ext}(\mathbf{r})n(\mathbf{r})\,\mathrm{d}\mathbf{r} + J[n] + E_{xc}[n]. \tag{2.24}$$

The term $E_{xc}[n]$ includes all many-body effects of exchange and correlation energy:

$$E_{xc}[n] = (T[n] - T_s[n]) + (E_{ee}[n] - J[n]) = T_c[n] + E_{ncl}[n], \tag{2.25}$$

where $T_c[n]$ is the residual part of the true kinetic energy. Then, the KS functional, $F_{KS}[n]$, can be written as:

$$F_{KS}[n] = T_s[n] + J[n] + E_{xc}[n]. \tag{2.26}$$

Therefore, Eq. 2.24 may be rewritten as:

$$E_{KS}[n] = F_{KS}[n] + \int V_{ext}(\mathbf{r})n(\mathbf{r})\,\mathrm{d}\mathbf{r}. \tag{2.27}$$

The energy of the system is minimised with respect to the density, keeping N_e constant (closed system). As mentioned before, the density of the non-interacting reference system must be the same that for the real interacting system at its minimum. Therefore, the functional derivative of $E_{KS}[n]$ must vanish for the ground-state density:

$$\frac{\delta}{\delta(n(\mathbf{r}))}\left(E_{KS}[n] - \mu\int N_e(\mathbf{r})\mathrm{d}\mathbf{r}\right) = 0, \tag{2.28}$$

where μ is the chemical potential of the system, a Lagrange multiplier is introduced to enforce the system to keep N_e constant.

If we work out Eq. 2.26, we obtain the following equation for the minimised ground-state density:

$$\frac{\delta T_s[n]}{\delta(n(\mathbf{r}))} + V_{ext}(\mathbf{r}) + V_H[n] + V_{xc}[\mathrm{n}] = \mu, \tag{2.29}$$

where $V_H[n] = \int \frac{n(\mathbf{r}')}{[\mathbf{r}-\mathbf{r}']} \mathrm{d}\mathbf{r}'$ is the Hartree potential and $V_{xc}[\mathrm{n}] = \frac{\delta E_{xc}[n]}{\delta(n(\mathbf{r}))}$ is the exchange-correlation potential. Eq. 2.29 reduces to the Euler-Lagrange equation:

$$\frac{\delta T_s[n]}{\delta(n(\mathbf{r}))} + V_{KS}(\mathbf{r}) = \mu, \tag{2.30}$$

with

$$V_{KS}[\mathrm{n}] = V_{ext}(\mathbf{r}) + V_H[n] + V_{xc}[\mathrm{n}], \tag{2.31}$$

where $V_{KS}[\mathrm{n}]$ is the KS potential. The KS equations can be written as a set of N_e single particle Schrödinger-like equations:

$$\left[\hat{T}_s + \hat{V}_{KS}(\mathbf{r})\right]\varphi_i(\mathbf{r}) = \epsilon_i \varphi_i(\mathbf{r}). \tag{2.32}$$

The KS equations refer to Eqs. (2.22), (2.29) and (2.30) which simplify the problem of minimising $E[n]$ by solving Schrödinger equation for non-interacting system. Note that the exchange-correlation functional is the only part that is approximated in the KS equations. If the universal functional $E_{xc}[n]$ and its corresponding potential $V_{xc}[\mathrm{n}]$ were known, it would be possible to calculate the exact ground-state energy and density of the many-body problem by solving the KS equations for non-interacting particles. However, a good approximation of $E_{xc}[n]$ and $V_{xc}[\mathrm{n}]$ will allow us to calculate the ground-state properties of the system.

The total energy of the system must be obtained via a self-consistent iteration of the KS equations (see Fig. 2.1). First, a trial density is employed as an input for the KS equations to calculate $V_{KS}[\mathrm{n}]$ (Eq. 2.31). Then, the differential Eq. 2.32 are solved to obtain a set of single-particle wave functions, $\varphi_i(\mathbf{r})$. These orbitals are used to calculate a new electronic density using Eq. 2.22 and start again. The process is repeated until the trial density and the calculated density are the same, to within a numerical threshold. Once the solution is converged, the total energy is calculated from Eq. 2.24.

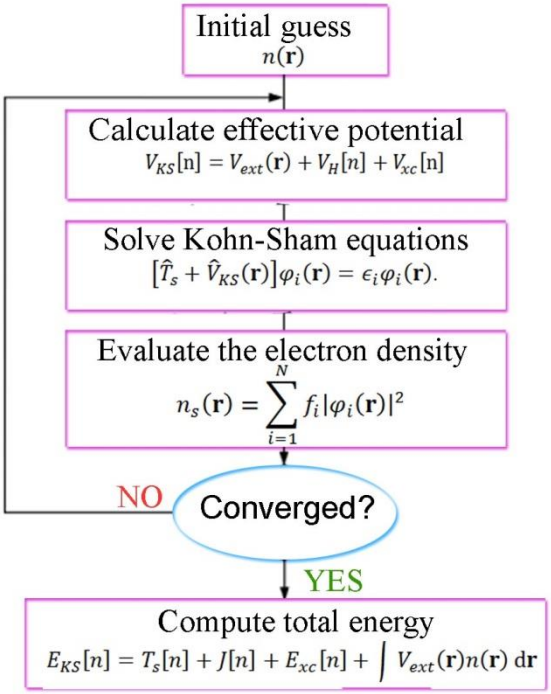

Figure 2.1: Schematic representation of the iterative Self-Consistent Field (SCF) solution of the KS DTF problem.

2.2.3 Exchange-correlation functionals

In the previous section, the many-body problem is solved by dividing the energy of an electronic system into different contributions (Eq. 2.25) which can be computed separately. As mentioned before, the exchange-correlation energy includes the kinetic energy difference between the interacting and non-interacting systems and the non-classical part of the electron-electron interactions along with the correction for the self-interaction. This is the only term that we have no information about the explicit form of the exact functional. Several exchange-correlation functional approximations have been developed using different physical models. The approaches can be classified based on their increasing complexity and computational cost, from the bottom to the top, which is known as Jacob's ladder [6]:

+ Unoccupied $\psi_i(\mathbf{r})$: Generalized random phase approximation RPA. Include the unoccupied orbitals in the calculations of the E_{xc}.

+ Exact exchange: Hybrid generalized gradient approximation. The E_{xc} is parameterised mixing the E_x of the electron independent systems and the Hartree-Fock exchange integral for fully interacting systems.

+ $\nabla^2 n(\mathbf{r})$: Meta-generalized gradient approximation. E_{xc} is computed considering a second order gradient expansion of the electronic density.

+ $\nabla n(\mathbf{r})$: Generalized gradient approximation. E_{xc} is calculated using a gradient expansion of the electronic density.

+ $n(\mathbf{r})$: Local density approximation. E_{xc} is parameterised based on the electronic density only.

In general, the exchange-correlation functional must accurately reproduce the reactions and properties of a wide range of molecules. Furthermore, it is important that the exchange-correlation functional contains the minimum number of parameters with not artificial terms introduced to satisfy physical properties. In this Thesis the local density approximation and the generalized gradient approximations will be described. The latter is the one employed in all the calculations presented, owing to

its acceptable level of compromise between accuracy for metallic interfaces (vide infra) and computational cost.

2.2.3.1 The local density approximation

The Local Density Approximation (LDA) [5] is the simplest approximation to the exchange-correlation functional according to Jacob's ladder. The form of the exchange- correlation energy functionals for the homogenous electron gas system is the only one that is known. In the uniform electron gas, the electron density is constant at all points in space. LDA uses the local density to define the approximate exchange-correlation functional. If the density $n(\mathbf{r})$ is varying slowly:

$$E_{xc}^{LDA}[n] = \int n(\mathbf{r})\epsilon_{xc}[n]\mathrm{d}\mathbf{r}, \tag{2.33}$$

where $\epsilon_{xc}[n]$ is the exchange-correlation energy per electron in a homogeneous electron gas with a density of $n(\mathbf{r})$. This energy per particle is weighed with the probability that there is an electron at this position. The term $E_{xc}^{LDA}[n]$ can be split into two contributions as:

$$E_{xc}^{LDA}[n] = E_{x}^{LDA}[n] + E_{c}^{LDA}[n]. \tag{2.34}$$

The exchange contribution, $E_{x}^{LDA}[n]$, was derived by Bloch and Dirac [7] as:

$$E_{x}^{LDA}[n] = -\frac{3}{4}\sqrt[3]{\frac{3n(\mathbf{r})}{\pi}}\int n(\mathbf{r})^{4/3}. \tag{2.35}$$

No explicit expression is known for the correlation energy density. However, several analytical expressions exist to obtain E_{c}^{LDA} [8-10].

The exchange correlation potential is derived using the product rule:

$$V_{xc}^{LDA}[n] = \frac{\delta E_{xc}^{LDA}[n]}{\delta(n(\mathbf{r}))} = n(\mathbf{r})E_{xc}^{LDA}[n] + E_{xc}^{LDA}[n]n(\mathbf{r})\frac{\delta E_{xc}^{LDA}[n]}{\delta\big(n(\mathbf{r})\big)}. \tag{2.36}$$

The exchange-correlation hole, the probability of finding an electron at $\boldsymbol{r}_2$ giving that there is an electron at $\mathbf{r}_1$, is centred in $\mathbf{r}_1$ within the LDA approach. However, the true exchange correlation hole is centred at $\mathbf{r}_2$. As a consequence, in system where the densities vary rapidly, the larger is the distance between the electrons, the worse is this assumption. Nevertheless, the results of the LDA approach are quite accurate. This is due to the fact that only the spherically averaged exchange-correlation hole is important to calculate the exchange-correlation energy and the homogeneous electron gas model provides an acceptable first approximation to the spherically averaged exchange-correlation hole of the real system. However, the LDA approach has its limitations such as the well-known overestimation of binding energies, and underestimation of the bond lengths. Such errors become larger in polar heterogeneous systems where the electronic densities are far from uniform [11].

2.2.3.2 The generalised gradient approximation

To overcome the limitations of the LDA approximation and increase the accuracy of DFT simulations, the next step in Jacob's ladder is to introduce semi-locally inhomogeneity to the density by a gradient expansion. This approach is called the General Gradient Approximation (GGA) [12] approximation to the exchange-correlation functional and it is constructed as:

$$E_{xc}^{GGA}\left[n^{\uparrow}, n^{\downarrow}\right] = \int F_{xc}\left[n^{\uparrow}, n^{\downarrow}, \nabla n^{\uparrow}, \nabla n^{\downarrow}\right] \mathrm{d}\mathbf{r}. \tag{2.37}$$

The function F_{xc} is an enhancement factor to modify LDA in order to take into account the density variation in the vicinity of the considered point. The exchange-correlation functional is usually split in the two contributions:

$$E_{xc}^{GGA}[n] = E_x^{GGA}[n] + E_c^{GGA}[n]. \tag{2.38}$$

There are different approaches to choose the explicit dependence of F_{xc} on the density and their gradients. Two popular GGA functionals are those proposed by Perdew and Wang (PW91) [9] and by Perdew, Burke, and Ernzerhof (PBE) [13, 14].

The correlation term of the GGA PBE functional is:

$$E_c^{PBE}[n] = \int n(\mathbf{r})\,\{E_c^{LDA}[n,\delta] + H[n,\delta,t]\}\mathrm{d}\mathbf{r}, \tag{2.39}$$

The gradient contribution is denoted by H. $\delta\left(=\frac{(n^{\uparrow}-n^{\downarrow})}{n}\right)$ is the local spin polarization, t is a dimensionless density gradient and the local density is defined as $n = \frac{4}{3}\pi {r_s}^3$, where r_s is the local Seitz radius.

The expression for the exchange functional reads:

$$E_x^{PBE}[n] = \int n(\mathbf{r}) E_x^{LDA}[n] {F_x}^{PBE}\,\mathrm{d}\mathbf{r}\,. \tag{2.40}$$

The ${F_x}^{PBE}$ assumes the form:

$${F_x}^{PBE} = 1 + k - \frac{k}{1 + \frac{\mu s^2}{k}}\,. \tag{2.41}$$

This functional contains only two fundamental constants: $k = 0.804$ and $\mu = 0.21951$. The local inhomogeneity parameter is $s \left(= \frac{[\nabla n(\mathbf{r})]}{2k_F n}\right)$, and $\mathrm{k_F}(= (3\pi^2 \mathrm{n})^{1/3})$ is the local Fermi wave vector. The LDA approach corresponds to the further approximation of $s = 0$.

The GGA PBE functional is constructed as:

$$E_{xc}^{GGA}[n] = \int n(\mathbf{r}) E_{xc}[n] F_x^{PBE}[n(\mathbf{r}), \nabla n(\mathbf{r}), \nabla^2 n(\mathbf{r}), \dots] \mathrm{d}\mathbf{r}, \tag{2.42}$$

The GGA PBE retains the correct features of the LDA and combines them with the density inhomogeneity. Therefore, this approach for the exchange-correlation functional improves the binging energies, bond lengths and the band gap energies, which remain however underestimates to the residual self-interaction error.

Many other approximations to the exchange-correlation functional have been developed over the years. Meta-generalized gradient approximation (meta-GGA) considers the fourth order gradient expansion of the exchange-correlation energy and the kinetic energy density. However, meta-GGA are constructed using semi-empirical parameters which normally fail for solid state calculations [15]. One of the most popular choices are the hybrid functionals such as B3LYP hybrid functional [16], the PBE0 hybrid functional [17] and the HSE hybrid functional [18]. The hybrid functionals are composed by mixing the exchange functionals of the independent electron systems and the Hartree-Fock exchange energies of the interacting system. Since the functional used in this Thesis is PBE, the theoretical and computational details of these functional will not be discussed here.

2.2.4 Solving the electronic problem via the Kohn-Sham equations

When solving the Kohn-Sham eigenvalue equations:

$$\left\{-\frac{\hbar^2}{2m}\nabla^2 + V_{ext}(\mathbf{r}) + \int \frac{n(\mathbf{r}')}{[\mathbf{r}-\mathbf{r}']}d\mathbf{r}' + V_{xc}[n]\right\}\varphi_i(\mathbf{r}) = \epsilon_i\varphi_i(\mathbf{r}), \tag{2.43}$$

with the external potential, $V_{ext}(\mathbf{r})$, given by the bare Coulomb potential as:

$$V_{ext}(\mathbf{r}) = \sum_{i=1}^{N_e}\sum_{I=1}^{N_n}\frac{Z_I}{\mathbf{r}_{iI}}, \tag{2.44}$$

one faces two important decisions: (i) the mathematical expression to represent the single-particle KS equations and solve them for extended systems such as crystalline solids or liquid and (ii) how to compute the external potential. In the following, I will provide a brief overview of, first, the most common numerical scheme to find the solution for the single-particle KS equations for periodic systems, and then, of the different approaches available to simplify the nuclei-electrons interactions to calculate the external potential.

2.2.4.1 Basis sets

The translational symmetry of the atomic structure in periodic systems can be used to reduce the computational effort of solving the KS equations. Periodic Boundary Conditions (PBC) are employed to study periodic systems such as solid to allow us to decrease the computational cost of the electronic calculations. The PBC approach makes use of a small part of an infinite system, called the unit cell, to represent an infinitely periodic lattice. The shape of the unit cell is repeated periodically in space by the reciprocal lattice vectors $\mathbf{b}_1$, $\mathbf{b}_2$ and $\mathbf{b}_3$. The reciprocal lattice vectors, such as the primitive lattice vectors in real space, are determined by the set of the three smallest independent vectors. The relation between the primitive vectors in real $\mathbf{a}_i$ and reciprocal space $\mathbf{b}_j$ is defined by the relation $\mathbf{a}_i \cdot \mathbf{b}_j = 2\pi\delta_{ij}$, $i,j = 1,2,3$. The

wave vector in the Brillouin zone (the primitive unit cell in the reciprocal space) is $\mathbf{k}$ $(= n_1\mathbf{b}_1 + n_2\mathbf{b}_2 + n_3\mathbf{b}_3)$. The volume in reciprocal space is called first Brillouin zone volume, $\Omega_R = (2\pi)^3/\Omega$, where Ω is the volume in the real space.

The solutions of the Schrödinger equations are represented by the combination of basis orbitals according to KS approach and they must verify the translational periodicity of the supercell. This is one of the Bloch's theorem statements, which are the tool to reduce the number of necessary KS equations (Eq. 2.32).

If the nuclei are arranged in a periodic lattice, their potential (experienced by the electrons) must also be periodic. Therefore, in a system of non-interacting particles moving in a periodic static potential such as the KS effective potential $V_{KS}(\mathbf{r})$, the potential has the following property:

$$V_{KS}(\mathbf{r}) = V_{KS}(\mathbf{R} + \mathbf{r}), \tag{2.45}$$

For any vector $\mathbf{R} = \mathrm{n}_1\mathbf{a}_1 + \mathrm{n}_2\mathbf{a}_2 + \mathrm{n}_3\mathbf{a}_3$ which represents the nuclei in a regular periodic array. As the Hamiltonian is periodic as well:

$$\hat{H}(\mathbf{r}) = \hat{H}(\mathbf{R} + \mathbf{r}). \tag{2.46}$$

Defining a translation operator, $\hat{T}_{\mathbf{R}}$, for each $\mathbf{R}$ which act on any position function, $f(\mathbf{r})$, as:

$$\hat{T}_{\mathbf{R}} f(\mathbf{r}) = f(\mathbf{R} + \mathbf{r}), \tag{2.47}$$

and

$$\hat{T}_{\mathbf{R}}\hat{T}_{\mathbf{R}'} f(\mathbf{r}) = f(\mathbf{R} + \mathbf{R}' + \boldsymbol{r}). \tag{2.48}$$

The $\hat{H}$ and $\hat{T}_{\mathbf{R}}$ operators have the same periodicity, thus they commute i.e. $[\hat{H}, \hat{T}_{\mathbf{R}}] = 0$ for all **R.** Furthermore, $\hat{H}$ and $\hat{T}_{\mathbf{R}}$ operators share the same set of eigenstates.

$$\hat{T}_{\mathbf{R}}\psi(\mathbf{r}) = c(\mathbf{R})\psi(\mathbf{r}) \tag{2.49}$$

From the commutation relation, it follows that the eigenvalues $c(\mathbf{R})$ can be expressed as:

$$c(\mathbf{R} + \mathbf{R}') = c(\mathbf{R})c(\mathbf{R}'). \tag{2.50}$$

This exponential identity leads to the natural representation of $c(\mathbf{R})$:

$$c(\mathbf{R}) = e^{i\mathbf{k}\cdot\mathbf{R}}. \tag{2.51}$$

To resume:

$$\hat{T}_{\mathbf{R}}\psi(\mathbf{r}) = \psi(\mathbf{R} + \mathbf{r}) = c(\mathbf{R})\psi(\mathbf{r}) = e^{i\mathbf{k}\cdot\mathbf{R}}\psi(\mathbf{r}), \tag{2.52}$$

which is one statement of Bloch's theorem. The previous equations can be written in terms of a cell periodic function with the same lattice periodicity:

$$u_{\mathbf{k}}(\mathbf{R} + \mathbf{r}) = e^{i\mathbf{k}\cdot\mathbf{R}}\psi_{\mathbf{k}}(\mathbf{r}), \tag{2.53}$$

Therefore, the wave function can be expressed as the product of a function with the same periodicity of the potential, and an imaginary phase factor arising from the translational symmetry. If the wave function is displaced by a unit vector, $\mathbf{r} + \mathbf{R}$, it follows that:

$$\psi_{\mathbf{k}}(\mathbf{R} + \mathbf{r}) = e^{i\mathbf{k}\cdot\mathbf{R}}u_{\mathbf{k}}(\mathbf{r}), \tag{2.54}$$

Bloch's theorem indicates that it is not necessary to solve the wave function over infinite space; the calculation is restricted to the wave functions within the unit cell. The only difference between neighbouring cells is the phase factor $e^{i\mathbf{k}\cdot\mathbf{R}}$. Note that the probability density $|\psi_{\mathbf{k}}(\mathbf{r})|^2$ is the same because the imaginary phase factor cancels out.

Solving the electronic structure problem within the DFT framework requires choosing a mathematical representation for the one-electron orbitals i.e. to choose a suitable basis set to represent the wave functions. If we expand the one-electron wave functions in a generic basis set described by the orbitals, ϕ_α, the KS orbitals can be expressed as a linear combination of this basis set:

$$\varphi_i = \sum_{\alpha=1}^{M} c_{i\alpha}\phi_\alpha(\mathbf{r}), \tag{2.55}$$

where the sum runs over all the basis functions up to M and $c_{i\alpha}$ are the expansion coefficient of wave function φ_i. These wave functions are the solutions of the Schrödinger equations.

2.2.4.1.1 Plane waves

The basis set of plane waves (PW) is introduced following Bloch's theorem (Eq. 2.52) and it takes advantage of the periodicity of the supercell. Since $u_{\mathbf{k}}(\mathbf{r})$ in Eq. 2.52 is periodic, it can be expressed as a Fourier series:

$$\varphi_{\mathbf{k}}(\mathbf{r}) = e^{i(\mathbf{k}+\mathbf{G})\cdot\mathbf{r}}u_{\mathbf{k}}(\mathbf{r}) = e^{i(\mathbf{k}+\mathbf{G})\cdot\mathbf{r}}\sum_{\mathbf{G}=0}^{\infty} c_G^k(\mathbf{G})\phi_{\mathbf{G}}(\mathbf{r}), \tag{2.56}$$

where **G** are reciprocal lattice vectors, which are generated by the three primitive vectors, $\mathbf{b}_1, \mathbf{b}_2, \mathbf{b}_3$. The PW basis functions $\phi_{\mathbf{G}}(\mathbf{r})$ are defined as:

$$\phi_{\mathbf{G}}(\mathbf{r}) = \frac{1}{\Omega_R} e^{i\mathbf{G}\cdot\mathbf{r}}, \tag{2.57}$$

with Ω_R being the volume of the system in reciprocal space. In principle, the summation runs over an infinite number of **G** vectors to represent the wave functions at each **k**-point. There are an infinite number of possible values for **k**. However, the coefficients of the wave function, $c_{\mathbf{k}}(\mathbf{G})$, decrease with increasing $|\mathbf{k}+\mathbf{G}|$, hence, a kinetic energy cut-off, E_{cut}, can be imposed to the plane waves expansion to truncate the sum:

$$E_{cut} = \frac{[\mathbf{k}+\mathbf{G}]^2}{2}. \tag{2.58}$$

The advantages of using PWs are: (i) the calculation of the energy and its derivatives is quite simple and (ii) the PWs represent all regions with the same accuracy. This because the PWs are not centred on any atom. However, the latter may be a disadvantage, because of the computational effort that this approach employs in representing the vacuum region. Furthermore, valence wave functions vary rapidly close to the nuclei due to the nodal structure; hence, they require many PWs of higher energy cut-off (Eq. 2.56).

2.2.4.2 The electron-nuclear interaction

In general, the electronic states of an atom can be classified in (i) those that participate in the chemical bonding, called *valence states*, (ii) *semi-core states* which are localised and polarisable, they normally do not participate in the bonding but their energy is similar to the valence states, and (iii) those tightly bound to the nuclei, named *core states*, which are highly localised and do not participate in the chemical bonding.

A large number of PWs or equivalently, large E_{cut}, is required to describe the oscillations of the valence wave functions close to the nuclei due to the strong oscillation produced by the strong attractive interaction with the nucleus and the consequent increase of the electron kinetic energy (as measured by the second derivative i.e. curvature of the wave function). Nevertheless, the core electrons are not involved in the chemical bonding and they are slightly perturbed by the formation of chemical bonds, which makes use of computation for their explicit description avoidable in most cases.

There are different strategies to numerically deal with (semi-)core and valence electrons within the KS equations: (i) to expand the one-electron KS wave function in terms of atomic orbitals. The wave functions of the semi-core and core states are described with fewer basis functions of minimal or no overlap, while the valence states are represented by more basis functions and their overlap. (ii) As mentioned before, the distribution of the core electrons is almost the same when a chemical bond occurs. Therefore, the number of required electronic states ant the size of the basis set can be reduced by assuming the core electrons to be "frozen". This is the idea behind the pseudopotentials methods. Calculations that include this approximation are called frozen-core calculations otherwise, are all-electron calculations. (iii) The Augmented Plane Wave (APW) method is an all-electron approach. This method divides the space into atom-centred spheres and interstitial region between them. Therefore, it employs atom-centred basis functions for the spheres and floating functions (not linked to atomic nuclei) such as PWs for the interstitial regions.

The Projector Augmented Wave (PAW) method is a combination of the pseudopotential and the APW approach. The PAW method is used in this Thesis; hence, I will briefly describe the pseudopotential approximation and the augmented wave methods to finally introduce the PAW method.

2.2.4.2.1 Pseudopotential approximation

In the KS equations, the effective potential (Eq. 2.31) is calculated using the total electronic density and the self-consistent calculated solutions are single-particle orbitals with the same density. The pseudopotential approach removes the core electrons from the calculations while the valence electrons-nucleus interactions is substituted by softer pseudopotential that depends on the angular momentum of the valence electrons to accomplish the orthogonally conditions. For each angular momentum, *l*, the pseudopotential must has the valence *l*-state as the ground state. Therefore, in the pseudopotential approximation, $V_H[\mathrm{n}]$ and $V_{xc}[\mathrm{n}]$ are evaluated for the valence density, and the external potential is substituted by a pseudopotential that accounts for the core electrons. There are numerous ways of constructing the pseudopotentials such as norm-conserving pseudopotential, ultra-soft pseudopotential [19] and others [20-23].

The radial pseudo-wave function (and potential), $R_{PS}(r)$, used to substitute the valence wave functions must meet some requirements:

$$R_{PS}(r) = \begin{cases} \tilde{R}_{PS}(r), & r < r_c \\ R_{AE}(r), & r \geq r_c \end{cases} \tag{2.59}$$

where $\tilde{R}_{PS}(r)$ represents the radial wave function inside the core region, r_c, and $R_{AE}(r)$ corresponds to the pseudo wave function outside r_c. Outside r_c, the pseudo-wave function must be the same that the actual valence wave function, i.e. beyond the augmentation sphere the potential decays as the all-electron potential. The solution of the atomic Schrödinger equation for the pseudopotential conserves the scattering properties of the all-electron potential, although the radial pseudo-wave function is nodeless inside the core region. Inside r_c, the pseudo-wave function is not the same than the actual wave functions. However, the norm is constrained to be the same in order to guarantee that both wave functions generate the same electron densities inside the core regions:

$$\int_0^{r_c} \left|r\tilde{R}_{PS}(r)\right|^2 \mathrm{d}r = \int_0^{r_c} |rR_{AE}(r)|^2 \mathrm{d}r. \tag{2.60}$$

The transferability is one of the most important characteristics of this methods, the transferability is defined by the range of energies over which the logarithmic derivatives of $\tilde{R}_{PS}$ and R_{AE} outside the core region holds adequately. This method is called norm-conserving pseudopotentials.

The general procedure for obtaining pseudo-wave functions involves solving the radial Schrödinger equation which is a second-order linear differential equation:

$$\left\{-\frac{1}{2}\frac{\mathrm{d}^2}{\mathrm{d}r^2}+\frac{l(l+1)}{2r^2}+v[n](r)\right\}rR_{AE}^{l}(r)=\varepsilon_l rR_{AE}^{l}(r), \tag{2.61}$$

where

$$v[n](r)=-\frac{Z}{r}+\int\frac{n(r')}{[r-r']}\mathrm{d}r'+V_{xc}[\mathrm{n}]. \tag{2.62}$$

However, within the frozen-core approximation, the core states are not included in the calculations. Once that the pseudo-wave function is constructed, it is used to invert the radial Schrödinger equation for the screened pseudopotential:

$$v_{PS}^{(sc)l}(r)=\varepsilon_l-\frac{l(l+1)}{2r^2}+\frac{1}{2rR_{PS}^{l}(r)}\frac{\mathrm{d}^2}{\mathrm{d}r^2}\left[rR_{AE}^{l}(r)\right], \tag{2.63}$$

where $R_{AE}^{nl}(r)$ is the value of the wave function at a given point r_0 when the energy, ε, is fixed. This equation is solved for a chosen atomic configuration called reference configuration.

The pseudopotential is obtained by:

$$v_{PS}^{l}(r)=v_{PS}^{(sc)l}(r)-\int\frac{n_v(r')}{[r-r']}\mathrm{d}r'-V_{xc}[n_v]. \tag{2.64}$$

Note that the Coulomb interactions and the exchange-correlation potential are the one calculated with the electronic density of the valence electrons:

$$n_v(r) = \sum_{l=0}^{l_{max}} \sum_{m=-l}^{l} \left| rR_{PS}^{l}(r) \right|^2, \tag{2.65}$$

where l_{max} is the largest angular momentum of the isolated atom in the reference configuration.

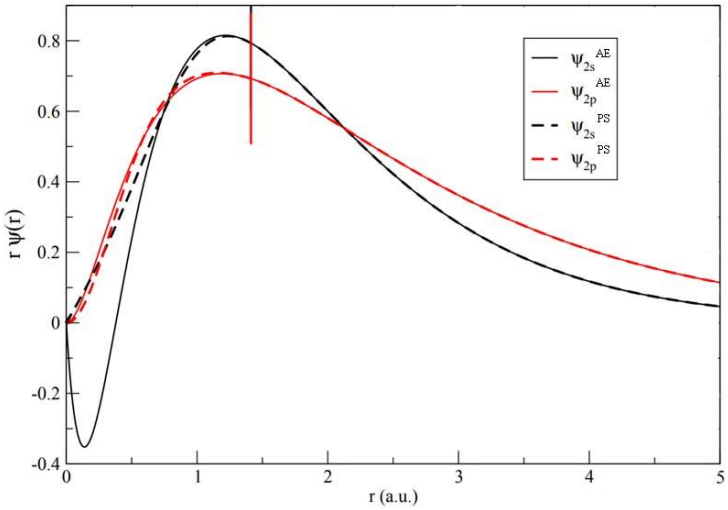

Figure 2.2: Example of pseudopotential for C generated by Opium code [24]. The probability amplitudes of all-electrons (AE) wave functions ($\boldsymbol{\psi}$) are compared to the pseudo (PS) wave functions. The core cutoff ($\boldsymbol{r_c}$) is indicated by the vertical red line. As evident for the $\boldsymbol{\psi_{2s}}$ case, the PS wave functions do not have nodes (zero amplitude) within $\boldsymbol{r_c}$, contrary to the AE solutions.

An example of the pseudopotential method for C is shown in Fig. 2.2. The pseudopotential method is not useful if we are interested on the information contained in the region close to the nuclei. An alternative is to use the APW method which is an all-electrons approach.

2.2.4.2.2 Augmented plane wave method

The APW method was originally developed by Slater in 1937 [25]. As mentioned before, augmented wave methods divide the system into atomic spheres called muffin-tin spheres (if the spheres of neighbouring atoms touch) with radius (R_{MT}) and interstation regions. A schematic representation is shown in Fig. 2.3.

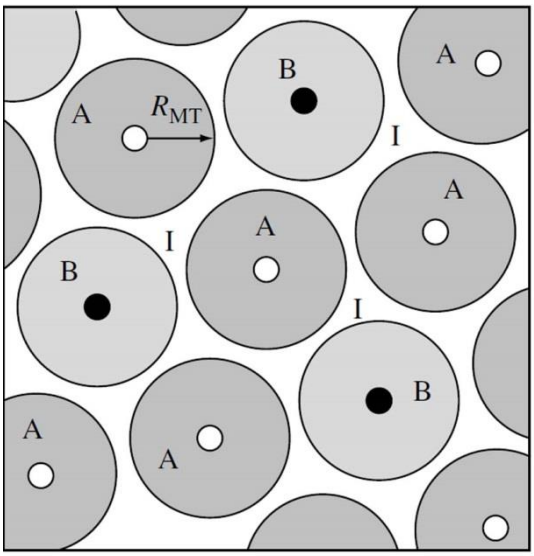

Figure 2.3: Adapted from [26]. Schematic representation of the volume of the unit cell partitioned into atomic spheres (shaded areas) of radii $\boldsymbol{R_{MT}}$ and interstitial regions (I). Two different types of atoms, A and B, are shown.

In the atomic regions, the electrons approximately behave as in an isolated atom and they are described by atomic-like wave functions generated by integrating the radial Schrödinger equation. On the other hand, in the interstitial regions the electrons are almost free; hence, the wave functions are described using a regular basis set such as plane waves.

The Linear Augmented Plane Wave (LAPW) method [27] is introduced to fulfil the continuity of the atomic function and the interstitial basis set at the sphere boundary. The LAPW basis wave functions are constructed by connecting the PW functions in the interstitial region with the linear combination of atomic-wave functions of the muffin-tin spheres. The main advantage of the APW methods over the

pseudopotential approach is that core and semi-core electrons are treated explicitly i.e. the APW method is an all-electron approach.

2.2.4.2.3 Projector augmented wave method

The PAW method unifies all-electron character and pseudopotential methods. The all-electron wave function is obtained from the pseudo-wave function by a linear transformation:

$$|\varphi_{AE}^{n}\rangle = |\varphi_{PS}^{n}\rangle + \sum_{I=1}^{P}\sum_{l,m}\sum_{i}\left(|\phi_{AE}^{iIlm}\rangle - |\phi_{PS}^{iIlm}\rangle\right)\langle\tilde{p}_{i}^{Ilm}|\varphi_{PS}^{n}\rangle. \quad (2.66)$$

There are three key terms that determines the transformation: (i) ϕ_{AE}^{iIlm} that corresponds to all-electron partial waves centred on atom *I*, (ii) ϕ_{PS}^{iIlm} which are the pseudo-atomic partial waves that coincide with the all-electron one outside R_M and (iii) the projector functions $\tilde{p}_{i}^{Ilm}$ for each pseudo-wave function located within the augmentation region and which must verify the relation $\langle\tilde{p}_{i}^{Ilm}|\phi_{PS}^{jIlm}\rangle = \delta_{ij}$. The sums run over all the atomic sites, angular momenta (l, m) and projector functions i. According to this, the electron density and the total energy are split in three different contributions as well: the plane wave part and the two radial function expansions per atom ϕ_{AE}^{iIlm} and ϕ_{PS}^{iIlm}. A schematic representation of the PAW method is shown in Fig. 2.4.

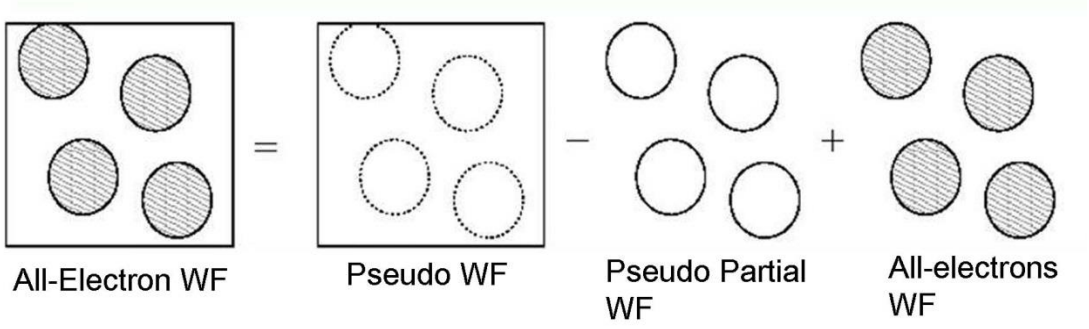

Figure 2.4: Schematic representation of the PAW scheme.

The expressions which involves localized quantities are evaluated using radial grids while the pseudo-terms are evaluates on a Cartesian grid using PW. The pseudo-wave function is constructed as in the pseudopotential methods following the frozen-core approximation.

The advantage of the PAW scheme lies on the ability to expand the core region as the difference between a density from the (all-electrons) atomic orbitals and from a set of node-less pseudo-atomic orbitals which allows the core region to respond to changes in the valence states which leads to a very efficiency description of the wavefunction with minimal computational cost.

2.2.5 Geometry optimisation

The aim of first principles calculations of electronic structures is to obtain the physical properties of specific systems. In order to do that, the first step is to calculate the correct relaxed configuration of the system as this will be the most populated one at low temperature. The optimisation process consists in subsequently evaluate the electronic potential energy for different ionic positions. Those points in the electronic potential energy surface where the first derivative of the electronic potential energy with respect to the nuclear coordinates is zero and the second derivative is positive are minimum stationary points. However, a multidimensional function (such as the electronic potential energy for a systems of several atoms) may contain many different stationary points, leading to the occurrence of both local and global minima Furthermore, non-linear functions (such as the electronic potential energy) require iterative methods for locating the stationary points where the target function and its derivatives are calculated with finite precision. In the iterative methods, a threshold value is implemented and consecutively compare with the energy difference between the two last iterations. The most popular methods to obtain the lowest-energy conformation are steepest descent method [28], conjugate gradient methods [29] and the quasi-Newton method. For the research in this Thesis, I used the quasi-Newton scheme [30] implemented in the Vienna Ab initio

Simulation Package (VASP) code [31]. VASP is a computer program for atomic scale materials modelling from first principles.

2.2.5.1 Hellman-Feynman Theorem

The forces acting on the atoms can be computed by the application of the Hellmann-Feynman theorem [32]. This theorem states that considering a system with a Hamiltonian H(λ) that depends on a parameter λ:

$$\frac{\mathrm{d}E}{\mathrm{d}\lambda} = \left\langle \psi(\lambda) \middle| \frac{\mathrm{d}H}{\mathrm{d}\lambda} \middle| \psi(\lambda) \right\rangle. \tag{2.67}$$

Thus, provided one can compute the DFT Hamiltonian, the corresponding forces acting on the nuclei can be obtained as:

$$-\frac{\partial E}{\partial \mathbf{R}_I} = \left\langle \psi \middle| \frac{\partial H}{\partial \mathbf{R}_I} \middle| \psi \right\rangle = \int n(\mathbf{r}) \frac{Z_I(\mathbf{r} - \mathbf{R}_I)}{\left|\mathbf{r} - \mathbf{R}_J\right|^3} \mathrm{d}^3\mathbf{r} + \sum_{J \neq I} \frac{Z_I Z_J (\mathbf{R}_I - \mathbf{R}_J)}{\left|\mathbf{R}_I - \mathbf{R}_J\right|^3}, \tag{2.68}$$

where $\mathbf{R}_I$ is the position of the nucleus I with atomic number Z_I. The Hellmann–Feynman theorem can be used to calculate atomic forces and find the equilibrium structures by varying $\mathbf{R}_I$ until the energy is a minimum and $-\frac{\partial E}{\partial \mathbf{R}_I} = 0$.

2.2.5.2 Newton method

Given a multidimensional function $f(\mathbf{x})$, we can expand it into a second order Taylor expansion:

$$f(\mathbf{x_{i+1}}) = f(\mathbf{x}_i) + (\mathbf{x_{i+1}} - \mathbf{x}_i)\nabla f(\mathbf{x}_i) + \frac{1}{2}(\mathbf{x_{i+1}} - \mathbf{x}_i)^2 \nabla^2 f(\mathbf{x}_i). \tag{2.69}$$

If we apply the condition to find an extreme, $\nabla f(\mathbf{x}) = 0$, and we rearrange the equation, it follows that:

$$\mathbf{x_{i+1}} = \mathbf{x}_i - \frac{\nabla f(\mathbf{x}_i)}{\nabla^2 f(\mathbf{x}_i)} = \mathbf{x}_i - A_i^{-1}\nabla f(\mathbf{x}_i) = \mathbf{x}_i - H_i \nabla f(\mathbf{x}_i), \tag{2.70}$$

where A is the Hessian matrix, the square matrix whose elements are the second derivatives of the function, $f(\mathbf{x})$, H is the inverse of the Hessian matrix. This iterative method consists in solving Eq. 2.70 and update $\mathbf{x}_i$. The main disadvantage of using this method for electronic calculations is that in most of the cases the Hessian matrix, is not available [33].

2.2.5.3 Quasi-Newton method

Quasi-Newton scheme do not compute the exact inverse Hessian matrix. Defining the vectors,

$$\boldsymbol{\delta}_i = \mathbf{x}_{i+1} - \mathbf{x}_i, \qquad \boldsymbol{\gamma}_i = \nabla f(\mathbf{x}_{i+1}) - \nabla f(\mathbf{x}_i). \tag{2.71}$$

The Quasi-Newton scheme must satisfy the secant equation:

$$\boldsymbol{\delta}_i = H_{i+1}\boldsymbol{\gamma}_i. \tag{2.72}$$

There are different approaches to calculate the approximation and update the Hessian matrix such as the Davidon-Fletcher-Powell (DFP) [34, 35] method, Broyden-Fletcher-Goldfarb-Shanno (BFGS) [36-39] update and Residual minimisation method-direct inversion in the iterative subspace (RMM-DIIS) [30].

The DFP method updates the inverse of the Hessian matrix by:

$$H_{i+1} = H_i - \frac{(H_i\boldsymbol{\delta}_i)(H_i\boldsymbol{\delta}_i)^T}{\boldsymbol{\delta}_i^T H_i \boldsymbol{\delta}_i} + \frac{\boldsymbol{\gamma}_i\boldsymbol{\gamma}_i^T}{\boldsymbol{\gamma}_i^T\boldsymbol{\delta}_i}. \tag{2.73}$$

Nowadays, one of the most employed methods is the BFGS method which update formula is obtained as:

$$H_{i+1} = H_i - \frac{\boldsymbol{\delta}_i\boldsymbol{\gamma}_i^T H_i + H_i\boldsymbol{\gamma}_i\boldsymbol{\delta}_i^T}{\boldsymbol{\delta}_i^T\boldsymbol{\gamma}_i} + \left(1 + \frac{\boldsymbol{\gamma}_i^T H_i \boldsymbol{\gamma}_i}{\boldsymbol{\delta}_i^T\boldsymbol{\gamma}_i}\right)\frac{\boldsymbol{\delta}_i\boldsymbol{\delta}_i^T}{\boldsymbol{\delta}_i^T\boldsymbol{\gamma}_i}. \tag{2.74}$$

The RMM-DIIS method is implemented in VASP. This method calculates the approximation of the inverse Hessian matrix by taking into account information from previous iterations. Therefore, the inverse of the Hessian matrix is improved in each step. This approach is very effective for electronic optimisation. However, for structural optimisation this scheme always a find a vector close to the trial vector which can generate problems if the starting geometry is far from the minimum. If this situation occurs, best practice suggests initially optimising the structure by using a conjugated gradients method [28] within a coarse tolerance criterion, and then refining the structural optimisation by applying the quasi-Newton method on the pre-optimised structure.

2.3. Magnetism

There are three main types of magnetism: diamagnetism, paramagnetism and ferromagnetism. Diamagnetic materials have all the orbital shells filled and there are no unpaired electrons, when they are placed in a magnetic field they show a weak magnetization opposite to the applied magnetic field producing a negative magnetization and a negative susceptibility, this quantity describes the response of the system to an applied magnetic field. Paramagnetic materials have unpaired electrons in partially filled orbitals, when an external field is applied dipoles line-up with the field, resulting in a positive magnetization and small positive susceptibility

with temperature dependence. Ferromagnetic materials atomic moments exhibit very strong interactions. These interactions are produced by electronic exchange forces and result in a line-up of the dipoles permanently upon application of an external field with a very high positive susceptibility. There are only three elements that are ferromagnetic at room temperature: iron, cobalt and nickel.

2.3.1 The Stoner model for ferromagnetism

The Stoner model [40, 41] is useful to describe the ground-state magnetic properties of correlated itinerant electrons systems. It explains why Fe, Co and Ni are magnetic by deriving a simple relation known as the Stoner criterion. Moreover, this model calculates the value of the magnetic moments by the relationship between the magnetic moments and the number of holes in the *d*-band. However, the Stoner approach overestimates Curie temperatures, temperature at which the systems lose their permanent magnetic properties, by nearly one order of magnitude.

Most of the systems are non-magnetic, since the gain in exchange energy (interactions between electrons with parallel spin) of magnetic solution is not sufficient to compensate for the loss of kinetic energy, which is higher for systems with delocalised electrons (such as metals). Usually, the width of a metallic band is inversely proportional to the degree of localisation of the atomic states. Localised states lead to narrow bands with high values of the Density of States (DOS) showing lower kinetic energy. On the other hand, delocalized states in broader bands with low DOS leads to larger kinetic energy. Therefore, to obtain magnetism, a certain degree of localisation is needed.

At surfaces, due to the lower number of neighbour atoms, the electrons have lower possibilities to jump to another lattice site. Therefore, the lowering of the bandwidth leads to an increment of the DOS which compensate the lowered exchange interaction due to the reduced number of neighbour atoms. Thus, the Stoner product I_SxDOS at surfaces and thin-films can be larger than in the bulk.

The magnetism in transition metals is difficult to describe due to the d electrons which are neither completely localised nor completely delocalised (itinerant). Electronic localisation can be quantified, as in this thesis, by projecting the states on the atom core region. Higher electronic localisation will result in larger atom-projection of the electronic states describing such electrons. The Stoner theory of itinerant magnetism treats the systems as an average field with indistinguishable electrons in order to reduce the many-body problem of interacting electrons to an effective single-electron. It describes electrons which move freely in the periodic potential of the solid under the effect of a mean (time-independent) field. This field is the average effect of one electron of all the other electrons and nuclei of the system.

In the Stoner model, the electron states overlap and form bands, where the number of electronic states at each energy level is described by the DOS formed by these bands [42, 43]. The electron density, $n(\mathbf{r})$, can be split into its two contributions: spin-up and spin-down:

$$n(\mathbf{r}) = n^{+}(\mathbf{r}) + n^{-}(\mathbf{r}), \tag{2.75}$$

and the magnetization density:

$$m(\mathbf{r}) = n^{+}(\mathbf{r}) - n^{-}(\mathbf{r})\,. \tag{2.76}$$

The exchange correlation potential in the Stoner model is:

$$V_{xc}^{\pm}(\mathrm{r}) = V_{xc}^{o}(\mathrm{r}) \pm \frac{1}{2} I_S M, \tag{2.77}$$

where $V_{xc}^{o}(\mathbf{r})$ is the exchange correlation potential for non-spin polarized electrons, I_S is the Stoner exchange parameter and M is the local moment defined as the integral of the magnetization density over the unit cell, Ω:

$$M = \int_0^{\Omega} m(\mathbf{r})\,\mathrm{d}\mathrm{r}\,. \tag{2.78}$$

The constant changes of the $V_{xc}^{\pm}(\mathbf{r})$ do not affect the wavefunction. However, the eigenvalues are shifted by a constant which describes an exchange or band splitting between the spin-up and down:

$$\Delta E = I_S M\,. \tag{2.79}$$

The electron density can be represented as:

$$n(\mathrm{E}) = n^o(E \pm \frac{1}{2} I_S M), \tag{2.80}$$

Where n^o is referred to the DOS of the non-spin polarized system. Therefore, the number of electrons N and the moment M can be obtained by integrating over all the occupied states below the Fermi energy, E_F:

$$N = \int_0^{E_F} \left[n^o\left(E + \frac{1}{2} I_S M\right) + n^o\left(E - \frac{1}{2} I_S M\right)\right] \mathrm{d}E, \tag{2.81}$$

$$M = \int_0^{E_F} \left[n^o\left(E + \frac{1}{2} I_S M\right) - n^o\left(E - \frac{1}{2} I_S M\right)\right] \mathrm{d}E. \tag{2.82}$$

Equation (2.82) implicitly defines $M = F(M)$, then:

$$M = F(M) = \int_0^{E_F(M)} \left[n^o\left(E + \frac{1}{2} I_S M\right) - n^o\left(E - \frac{1}{2} I_S M\right)\right] \mathrm{d}E. \tag{2.83}$$

The previous equations satisfy the following conditions:

$$F(M) = -F(-M),$$

$$F(0) = 0,$$

$$F(\pm\infty) = \pm M_{\infty},$$

$$F'(M) > 0. \tag{2.84}$$

The term M_{∞} is the saturation magnetization for full spin-polarized systems, when all majority states are occupied and the minorities are empty. The last condition is because the density is always positive. The function $F(M)$ has two possibilities as is shown in Fig. 2.5. The first one is the trivial non-magnetic solution, $M = 0$, that corresponds to function (A). On the other hand, function (B) has three solutions, $M = \pm M_S$ which corresponds to a finite spontaneous magnetization and $M = 0$.

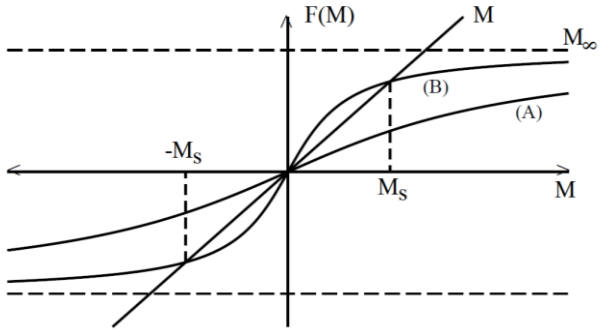

Figure 2.5: Adapted from [43]. Graphical solution for the Stoner model. The intersection of $\boldsymbol{F(M)}$ with the straight line $\boldsymbol{M}$ determines the solutions $\boldsymbol{\pm M_S}$.

If the slope of $F(M)$ at $M = 0$ is larger than one, the spontaneous magnetizations exits. Therefore, a system is magnetic if $F'(0) > 1$. The derivative $F'(M)$ can be calculated as:

$$\begin{aligned} F'(M) = \frac{I_S}{2}\left[n^o\left(E + \frac{1}{2}I_S M\right) + n^o\left(E - \frac{1}{2}I_S M\right)\right] \\ + \left[n^o\left(E + \frac{1}{2}I_S M\right) - n^o\left(E - \frac{1}{2}I_S M\right)\right]\frac{\mathrm{d}E_F}{\mathrm{d}M}. \end{aligned} \tag{2.85}$$

When there is not magnetization:

$$F'(0) = I_S n^o(E_F). \tag{2.86}$$

As mentioned before, the sufficient conditions for a system to be magnetic is $F'(0) > 1$ then, the Stoner criterion for spontaneous magnetic order of a system of itinerant electrons at T = 0 is:

$$I_S N(E_F) > 1. \tag{2.87}$$

Therefore, for a system to be ferromagnetic, a sufficiently high I_S and a large DOS at the Fermi level is required. How to increase both I_S and $N(E_F)$ via molecular interfaces of light transition metals is the subject of the fundamental research reported in this Thesis.

2.3.2 Evaluation of I_S within a PAW-DFT approach

Within the PAW-DFT approach the I_S parameter can be computed from the net magnetization per atom, m, and the band splitting, ΔE, as:

$$I_S\left(E_{\boldsymbol{k},n}\right) = \frac{\Delta E_{\boldsymbol{k},n}}{m}. \tag{2.88}$$

The magnetization is obtained from the atomic magnetic moment inside the PAW core regions. Therefore, the band splitting is calculated as the different between the spin-up (↑) and spin-down (↓) Kohn-Sham states at the wave vector **k**:

$$\Delta E_{\boldsymbol{k},n} = \uparrow \Delta E_{\boldsymbol{k},n} - \downarrow \Delta E_{\boldsymbol{k},n}. \tag{2.89}$$

However, I_S is almost **k**-independent [44]. Therefore, the band splitting is computed at the stationary points (maxima and minima) of the PAW-core projected density of states (PDOS).

Being based on a mean-field approximation to exchange interactions (as approximately parameterized in the adopted XC-functional) Eq. 2.88 cannot intrinsically account for spin-fluctuations that may be responsible for the measured ferromagnetic ordering at the interfaces between originally non-magnetic systems [45-47]. Quantitative description of these effects requires more sophisticated methods capable of describing dynamical aspects of local magnetic susceptibilities [48-50]. In spite of these intrinsic limitations, the approach is nevertheless capable of producing trends in magnetic hardening that semi-quantitatively match the measured magnetizations of Cu-C_{60} and Cu-aC interfaces [45, 46]. Based on these results, this approach (Eq. 2.88) is adequate to model these interfaces and provide first estimates to trends in magnetic hardening between different Cu-molecule interfaces. The unsolved challenges in atomically resolved characterization of the Cu-organic interfaces in Refs [45] and [46], and the possible risk of the model being poorly representative of the real system, call for cautious in the use of more accurate (computationally more expensive) methods for preliminary study these systems, which is the target of this Thesis. This consideration, and the overall very light computational cost of the approach, enabling fast and convenient simulation of systems up to over 200 atoms as considered in this study, justify its use for exploratory screening of novel strategies towards molecule-induced magnetic hardening and possible emergent magnetism.

2.3.3 Itinerant metamagnetism

The possibility of ferromagnetism in an itinerant paramagnet under the influence of a magnetic field was theoretical studied first by Wohlfarth and Rhodes [51] who demonstrate that a paramagnetic system under an applied magnetic field may experiment a sudden phase-transition into a ferromagnetic state. If the system is tuned in a way that the Fermi level is moved through the peak in the DOS with an enhancement of the exchange interactions, the system will show ferromagnetic ordering. On the other hand, if the Fermi level is slightly away from the DOS peak then, the Stoner criterion is not fulfilled and the system is paramagnetic.

Paramagnetic DOS are split into two identical bands for spin-up and down. When the DOS of spin-up and spin-down are identical, the magnetization is zero. If an external field (H_{ext}) is applied, the band energy is shifted as shown in Fig. 2.6. The E_F must be equal for spin-up and spin-down channels then, a redistribution of the electrons yields different occupation for spin-up and spin-down electrons. If the Fermi level gets close enough to the DOS peak, a magnetization is produced. Therefore, a metamagnetic transition may arise when an external field is applied into the system.

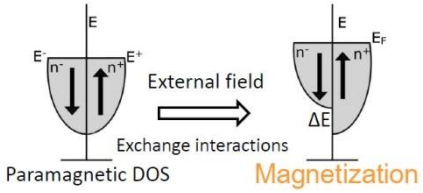

Figure 2.6: Representation of electron redistribution at the E_F in the presence of an external field (H). **a)** Paramagnetic density of states. **b)**Ferromagnetic equilibrium state. The occupation numbers $\mathbf{n}^+$ ($\mathbf{n}^-$) is the DOS for spin-up (down) and $\mathbf{\Delta E}$ is referred to the molecular field energy or band splitting: $\mathbf{\Delta E} = \varepsilon^+ - \varepsilon^-$.

The behaviour of a paramagnet is controlled by the curvature of the density of states, i.e. $N''(E_F)$. Depending on the curvature of the DOS at the Fermi level, the positive (negative) curvature may results in an increment (decrease) of the DOS at the Fermi level as is shown in Fig. 2.7.

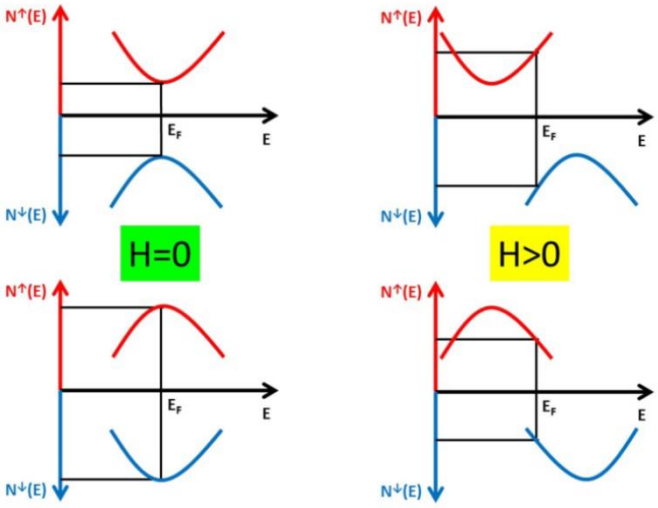

Figure 2.7: Adapted from [42]. Schematic diagrams of the effect of the curvature of the $N(E_F)$ when a magnetic field (H) is applied. Positive (negative) curvatures lead to an increment (decrement) of the DOS at the Fermi level when a magnetic field is applied.

The applied magnetic field leads to inequalities between spin-up and spin-down electrons which produce a magnetization defined as:

$$M = 2{\mu_B}^2 N(E_F) S H (1 + \frac{1}{6} c' S^3 {\mu_B}^2 H^2) \,, \tag{2.90}$$

where μ_B is the Bohr magneton and S is the Stoner enhancement:

$$S = \frac{1}{1 - I_S N(E_F)}. \tag{2.91}$$

The coefficient c' is related to the curvature of the density of states at Fermi energy as:

$$c' = \frac{N''(E_F)}{N(E_F)} - 3\frac{{N'^{(E_F)}}^2}{N(E_F)} \,. \tag{2.92}$$

Fig. 2.8 shows how the sign of c' determines the behaviour of the paramagnet. There are two possible cases: (i) $c' > 0$, the magnetization shows saturation behaviour.

(ii) $c' < 0$, the system shows a divergent behaviour and it can undergo to a metamagnetic transition if the applied external field is large enough.

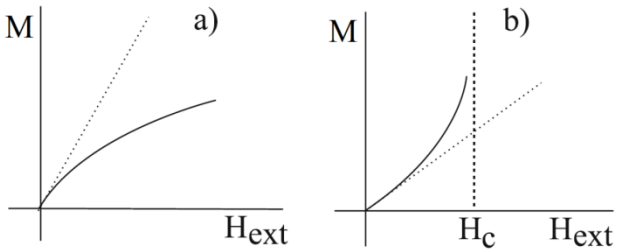

Figure 2.8: Adapted from [52]. The magnetism can experiment **a**) saturation behaviour or **b**) a divergent behaviour depending on the sign of $\boldsymbol{c'}$.

The critical field, H_c, needed for the transition from a paramagnetic state into a magnetic ordered one is defined as:

$$H_c = \frac{1}{3N(E_F)\sqrt{\frac{1}{8}\frac{N''(E_F)}{N(E_F)} - 3\frac{N'(E_F)^2}{N(E_F)}}}. \tag{2.93}$$

The critical field can be reduced by bringing $I_S N(E_F)$ closer to unity or by increasing the curvature of $N(E_F)$. Induced magnetic hardening of the metal modifies these parameters, decreasing the critical field.

2.4 References

1. Born, M. and R. Oppenheimer, *Zur quantentheorie der molekeln.* Annalen der Physik, 1927. **389**(20): p. 457-484.
2. Fermi, E., *Eine statistische Methode zur Bestimmung einiger Eigenschaften des Atoms und ihre Anwendung auf die Theorie des periodischen Systems der Elemente.* Zeitschrift für Physik, 1928. **48**(1-2): p. 73-79.
3. Thomas, L.H. *The calculation of atomic fields*. in *Mathematical Proceedings of the Cambridge Philosophical Society*. 1927. Cambridge Univ Press.

4. Hohenberg, P. and W. Kohn, *Inhomogeneous electron gas.* Physical review, 1964. **136**(3B): p. B864.
5. Kohn, W. and L.J. Sham, *Self-consistent equations including exchange and correlation effects.* Physical review, 1965. **140**(4A): p. A1133.
6. Perdew, J.P., et al. *Jacob's ladder of density functional approximations for the exchange-correlation energy*. in *AIP Conference Proceedings*. 2001. AIP.
7. Dirac, P.A. *Note on exchange phenomena in the Thomas atom*. in *Mathematical Proceedings of the Cambridge Philosophical Society*. 1930. Cambridge Univ Press.
8. Vosko, S.H., L. Wilk, and M. Nusair, *Accurate spin-dependent electron liquid correlation energies for local spin density calculations: a critical analysis.* Canadian Journal of physics, 1980. **58**(8): p. 1200-1211.
9. Perdew, J.P. and Y. Wang, *Accurate and simple analytic representation of the electron-gas correlation energy.* Physical Review B, 1992. **45**(23): p. 13244.
10. Ceperley, D.M. and B. Alder, *Ground state of the electron gas by a stochastic method.* Physical Review Letters, 1980. **45**(7): p. 566.
11. Kohn, W., *Density-functional theory for excited states in a quasi-local-density approximation.* Physical Review A, 1986. **34**(2): p. 737.
12. Perdew, J.P., K. Burke, and Y. Wang, *Generalized gradient approximation for the exchange-correlation hole of a many-electron system.* Physical Review B, 1996. **54**(23): p. 16533.
13. Perdew, J.P., K. Burke, and M. Ernzerhof, *Generalized gradient approximation made simple.* Physical review letters, 1996. **77**(18): p. 3865.
14. Perdew, J.P., et al., *Atoms, molecules, solids, and surfaces: Applications of the generalized gradient approximation for exchange and correlation.* Physical Review B, 1992. **46**(11): p. 6671.
15. Perdew, J.P., et al., *Accurate density functional with correct formal properties: A step beyond the generalized gradient approximation.* Physical Review Letters, 1999. **82**(12): p. 2544.
16. Becke, A.D., *Density-functional thermochemistry. III. The role of exact exchange.* The Journal of chemical physics, 1993. **98**(7): p. 5648-5652.

17. Adamo, C. and V. Barone, *Toward reliable density functional methods without adjustable parameters: The PBE0 model.* The Journal of chemical physics, 1999. **110**(13): p. 6158-6170.
18. Heyd, J., G.E. Scuseria, and M. Ernzerhof, *Hybrid functionals based on a screened Coulomb potential.* The Journal of Chemical Physics, 2003. **118**(18): p. 8207-8215.
19. Vanderbilt, D., *Soft self-consistent pseudopotentials in a generalized eigenvalue formalism.* Physical Review B, 1990. **41**(11): p. 7892.
20. Kerker, G., *Non-singular atomic pseudopotentials for solid state applications.* Journal of Physics C: Solid State Physics, 1980. **13**(9): p. L189.
21. Bachelet, G., D. Hamann, and M. Schlüter, *Pseudopotentials that work: From H to Pu.* Physical Review B, 1982. **26**(8): p. 4199.
22. Troullier, N. and J.L. Martins, *Efficient pseudopotentials for plane-wave calculations.* Physical review B, 1991. **43**(3): p. 1993.
23. Lin, J., et al., *Optimized and transferable nonlocal separable ab initio pseudopotentials.* Physical Review B, 1993. **47**(8): p. 4174.
24. http://opium.sourceforge.net/index.html
25. Slater, J., *Wave functions in a periodic potential.* Physical Review, 1937. **51**(10): p. 846.
26. Kohanoff, J., *Electronic structure calculations for solids and molecules: theory and computational methods*. 2006: Cambridge University Press.
27. Andersen, O.K., *Linear methods in band theory.* Physical Review B, 1975. **12**(8): p. 3060.
28. Dennis Jr, J.E. and R.B. Schnabel, *Numerical methods for unconstrained optimization and nonlinear equations*. 1996: SIAM.
29. Fletcher, R. and C.M. Reeves, *Function minimization by conjugate gradients.* The computer journal, 1964. **7**(2): p. 149-154.
30. Pulay, P., *Convergence acceleration of iterative sequences. The case of SCF iteration.* Chemical Physics Letters, 1980. **73**(2): p. 393-398.
31. https://www.vasp.at
32. Feynman, R.P., *Forces in molecules.* Physical Review, 1939. **56**(4): p. 340.

33. Saad, Y., J.R. Chelikowsky, and S.M. Shontz, *Numerical methods for electronic structure calculations of materials.* SIAM review, 2010. **52**(1): p. 3-54.
34. Davidon, W.C., *Variable metric method for minimization.* SIAM Journal on Optimization, 1991. **1**(1): p. 1-17.
35. Fletcher, R. and M.J. Powell, *A rapidly convergent descent method for minimization.* The computer journal, 1963. **6**(2): p. 163-168.
36. Broyden, C.G., *The convergence of a class of double-rank minimization algorithms 1. general considerations.* IMA Journal of Applied Mathematics, 1970. **6**(1): p. 76-90.
37. Fletcher, R., *A new approach to variable metric algorithms.* The computer journal, 1970. **13**(3): p. 317-322.
38. Goldfarb, D., *A family of variable-metric methods derived by variational means.* Mathematics of computation, 1970. **24**(109): p. 23-26.
39. Shanno, D.F., *Conditioning of quasi-Newton methods for function minimization.* Mathematics of computation, 1970. **24**(111): p. 647-656.
40. Stoner, E.C., *Collective electron specific heat and spin paramagnetism in metals.* Proc. R. Soc. A, 1936. **154**(883): p. 656-678.
41. Stoner, E.C., *Collective electron ferromagnetism.* Proc. R. Soc. A, 1938: p. 372-414.
42. Levitin, R. and A.S. Markosyan, *Itinerant metamagnetism.* Physics-Uspekhi, 1988. **31**(8): p. 730-749.
43. Zeller, R., *Spin-polarized dft calculations and magnetism.* Computational Nanoscience: Do It Yourself, 2006. **31**: p. 419-445.
44. Gunnarsson, O., *Band model for magnetism of transition metals in the spin-density-functional formalism.* Journal of Physics F: Metal Physics, 1976. **6**(4): p. 587.
45. Al Ma'Mari, F., et al., *Beating the Stoner criterion using molecular interfaces.* Nature, 2015. **524**(7563): p. 69-73.
46. Al Ma'Mari, F., et al., *Emergent magnetism at transition-metal–nanocarbon interfaces.* Proceedings of the National Academy of Sciences, 2017. **114**(22): p. 5583-5588.

47. Raman, K.V. and J.S. Moodera, *Materials chemistry: A magnetic facelift for non-magnetic metals.* Nature, 2015. **524**(7563): p. 42-43.
48. Lounis, S., et al., *Dynamical magnetic excitations of nanostructures from first principles.* Physical review letters, 2010. **105**(18): p. 187205.
49. Lounis, S., et al., *Theory of local dynamical magnetic susceptibilities from the Korringa-Kohn-Rostoker Green function method.* Physical Review B, 2011. **83**(3): p. 035109.
50. Ibañez-Azpiroz, J., et al., *Tuning paramagnetic spin-excitations of single adatoms.* arXiv preprint arXiv:1706.02085, 2017.
51. Wohlfarth, E. and P. Rhodes, *Collective electron metamagnetism.* Philosophical Magazine, 1962. **7**(83): p. 1817-1824.
52. Mohn, P., *Magnetism in the solid state: an introduction*. Vol. 134. 2006: Springer Science & Business Media.

Chapter 3

The role of lattice distortion for the magnetic properties of bulk Cu

Abstract

Towards quantification of the relative importance of lattice distortion and metal-organic charge-transfer for the magnetic hardening of Cu, in this Chapter I investigate the role of lattice distortion for the electronic and magnetic properties of bulk Cu. Analysis of different distortions maintaining and breaking the original face centred cubic (FCC) symmetry for bulk Cu indicates that expansion of the FCC lattice increases the average exchange interactions and magnetic hardening of Cu. The computed hardening (up to 30% for 15-20% expansion of the lattice) is comparable with what obtained –at the same level of theory− for Cu-amorphous carbon (aC) interfaces measured to develop ferromagnetic ordering. Conversely, compression of the FCC lattice leads to reduction to average exchange interactions and overall magnetic softening. Study of several tetragonal, orthorhombic and monoclinic distortions of the optimised bulk FCC Cu cell indicates that rupture of the FCC symmetry, besides being strongly disfavoured energetically in the absence of any charge enrichment or depletion, invariably leads to either negligible magnetic hardening or substantial magnetic softening.

3.1 Introduction

As overviewed in Chapter 1 (Section 1.6.1.8), experimental characterisation of the interfaces between paramagnetic (Sc, Mn, Pt) or diamagnetic (Cu) transition-metal layers and differently π-conjugated organic substrates (fullerene C_{60} and aC) provides evidence of the emergence of interfacial room-temperature ferromagnetic ordering [1, 2]. The compelling experimental evidence of ferromagnetic ordering has been complemented by DFT simulation of some of the interfaces considered. The available DFT insights point to both charge-transfer between the metal and the organics, and interface-relaxation induced distortions at the metal substrates as the two key drivers for the magnetic hardening of the metal substrate and consequent emergence of magnetic ordering [1, 2]. To date, the relative importance of charge transfer between the metal and (π-conjugated) organic, and distortion of the metal lattice for the emergence of interfacial magnetic ordering remains unquantified, which is the knowledge gap I first target in my Thesis.

With the final aim of disentangling the role of charge-transfer and lattice distortion for the magnetic hardening of Cu, this Chapter starts by considering the dependence of the magnetic properties on the local geometry and coordination of Cu atoms in the bulk phase. To quantify the relative importance of both the Cu-Cu distance and coordination symmetry for the magnetic properties of bulk Cu, Section 3.3 initially explores the effect of isotropic expansion and compression of bulk face-centred cubic (FCC) Cu i.e. distortions that alter the Cu-Cu distance without affecting the local coordination symmetry of the Cu atoms. The results of this study are then used as a reference to explore the effects of FCC-symmetry breaking distortions on the electronic and magnetic properties of bulk Cu both in volume-conserving cases (Section 3.4) and after optimisation of the cell volume (Section 3.5).

3.2 Computational details

3.2.1 Parameters of the DFT simulations

Standard and fixed spin-moment [3], DFT simulations were executed via the Projected Augmented Wave (PAW) method as implemented in the VASP program [4] with the PBE exchange-correlation (XC) functional [5], a 400 eV plane-wave energy cut-off, (0.2 eV, 1st order) Methfessel-Paxton electronic smearing [6]. k-point sampling grids were defined on the basis of convergence tests on the magnetic properties of bulk Cu in the FCC structure (see Section 3.2.3).

Due to the modelled non-magnetic ground-state for all the models studied, atom-resolved approximations to the Stoner exchange integral (I_S, see Section 2.3.2) were computed by enforcing a magnetic moment of 0.1 μ_B/Cu-atom via fixed spin-moment DFT [3]. Following Refs. [1, 2, 7, 8], increase (decrease) of I_S with respect to the reference bulk value is taken as indication of magnetic hardening (softening).

Magneto-crystalline anisotropy Energies (MAEs) were computed via fixed-spin moment (0.1 μ_B/Cu-atom), non-collinear DFT simulations with inclusion of spin-orbit coupling as available in VASP [4]. The simulations were carried out non-self-consistently, that is, keeping the charge density (from a collinear run) fixed. The magnetic field was selectively oriented perpendicularly to high-symmetry directions of the considered system.

3.2.2 Numerical errors in the DFT-approximation to I_S

As explained in Chapter 2 (Eq. 2.88), the DFT approximation to the Stoner exchange integral (I_S) is computed as the ratio between the band-splitting (ΔE) and the magnetic moment for the atoms in a given system.

In his seminal papers on a band model for magnetism in transition metals based on the spin-density formalism, Gunnarsson [9] showed that the ΔE is relatively **k** independent by comparing the values obtained from spin polarised band calculations [10] for bulk body-centred cubic (BCC) Fe at different symmetry points in the Brillouin zone (triangles in Fig. 3.1) with the full Brillouin zone integrated results

(continuous line in Fig. 3.1). On the other hand, it can also be observed in Fig. 3.1 that the dependence of ΔE on the band-energy is stronger, with (more delocalised) lower-energy bands yielding smaller ΔE by comparison to (less delocalised) bands of closer in energy to E_F. As analysed in detail in Ref. [9], more localised amplitudes of the bands (KS states) corresponds to larger changes of the local Kohn-Sham potential between the up and down spin-channels, leading to larger computed values for ΔE.

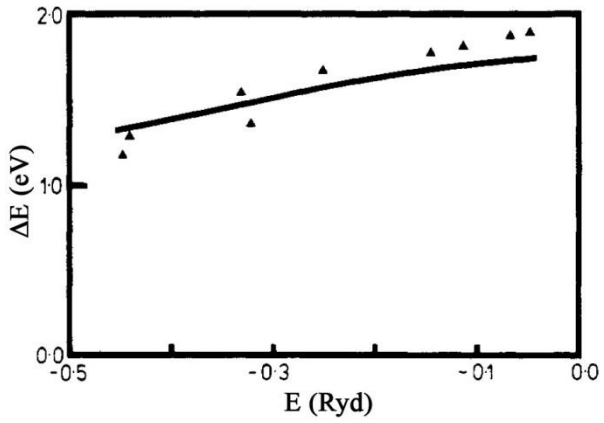

Figure 3.1: Adapted from Ref. [9]. Band-splitting (ΔE) of bulk BCC Fe as a function of the Kohn-Sham states energy (E). The triangles show the band-splitting for individual high-symmetry **k**-points in in the Brillouin zone from a full band calculation from Ref. [10], while the continuous line show the results after integration over the full Brillouin zone.

The non-negligible dependence of ΔE on the energy of the Kohn-Sham states, and the consideration that systems different from bulk BCC Fe may have different (atom dependent) inter-dependencies between these parameters, prompts for definition of a procedure to quantify and compare the error of ΔE, thence I_S (Chapter 2, Eq. 2.88).

To this end, I applied Eq. 2.88 (Chapter 2) to all the stationary points (maxima and minima) of the PAW-core PDOS in the energy interval between the Fermi energy (E_F) and E_F-3eV. This interval was decided, following numerical tests, to have at least three stationary points (maxima or minima) of the PDOS used in the computation of an average value and corresponding standard deviation for I_S. The standard deviation was then taken as error-bar of the computed I_S. Fig 3.2 illustrates application of the procedure to bulk FCC Cu isotropically deformed in the range

between 15% contraction (0.85 scaling) and 20% expansion (1.20 scaling). For simplicity, the maxima (minima) points in the PDOS where located, by mean of an ad hoc FORTRAN program, as those point having the largest (lowest) PDOS value in a 0.14 eV energy-window and a consistently negative (positive) first derivative in the same energy range. As shown in Fig. 3.2, it was graphically checked that the procedure could correctly identify stationary minima for all the systems considered in this and the following Chapters.

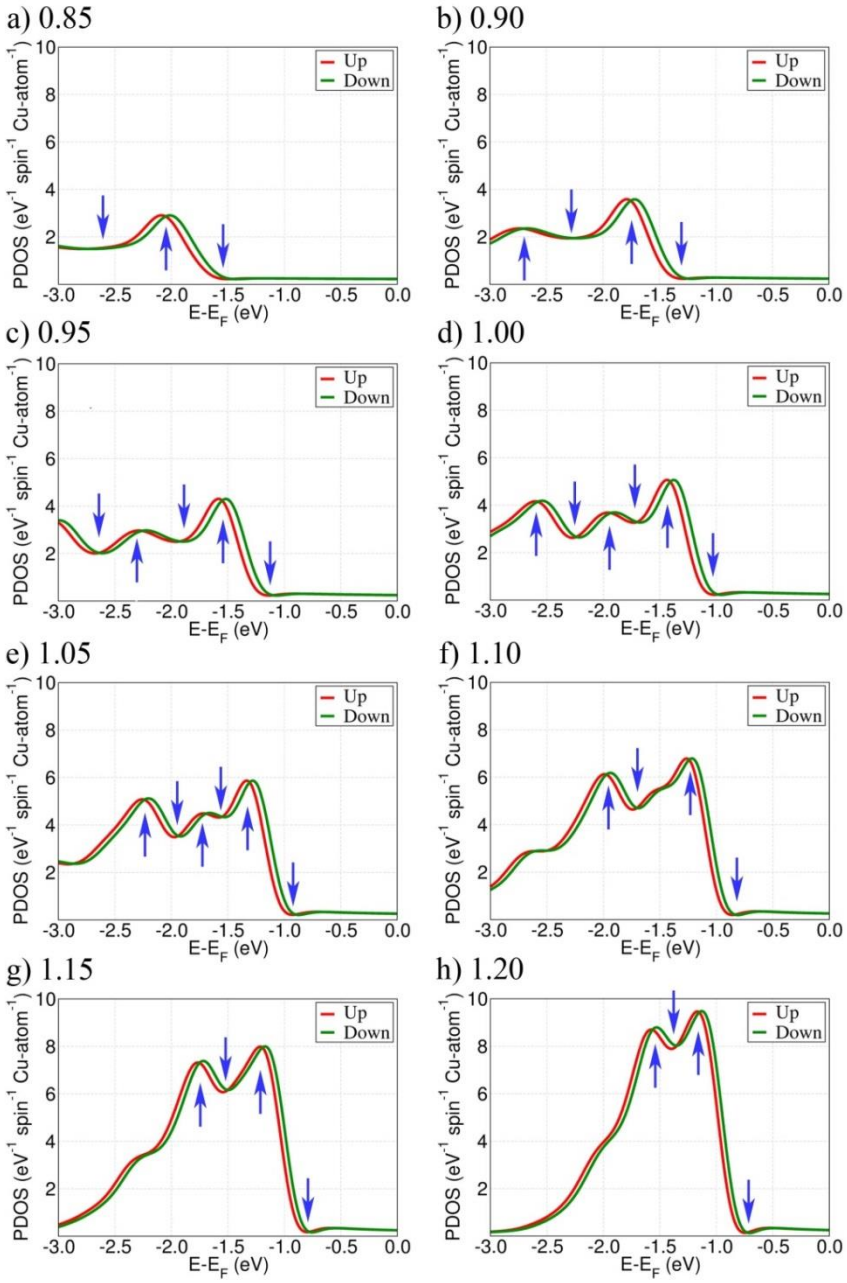

Figure 3.2: Spin-resolved Cu-PDOS for bulk FCC Cu isotropically deformed in the range between 15% contraction [0.85 scaling in panel **a)**] and 20% expansion [1.20 scaling in panel **h)**]. The blue arrows mark the stationary (maxima and minima) points identified with the procedure described in the text.

3.2.3 Dependence of bulk FCC Cu magnetic properties on the adopted k-point sampling

In the interest of both computational accuracy and convenience, it is crucial to determine the smallest number of symmetry irreducible k-points needed to provide a sufficiently well-converged description of the magnetic properties (not just the total energy) for the systems studied. Since the systems to be studied have different volume, they consequently have differently sized reciprocal lattices, thence Brillouin zone (Section 2.2.4.1). The target of this Section is to determine numerically what is the least dense k-point sampling (grid) needed to ensure acceptable convergence of the computed atomic magnetic moments (m) and band-splittings (ΔE) (thence I_S in Eq. 2.88) for bulk Cu in the FCC structure for the range of volume changes considered.

To this end, I first quantify of the convergence of the computed m and ΔE for bulk Cu in the FCC structure as a function of both the k-point grid sampling and the volume of the FCC cell, varied between compressions of 15% and expansion of 20% around the computed energy minimum (3.649 Å lattice parameter, see Fig. 3.3). It is found that a spacing of at least 0.0079 $Å^{-1}$ between k-point is sufficiently dense to yield computed values of m, ΔE and I_S converged, over the range of volume changes considered, to within $<10^{-3}$ μ_B, 6 meV and 2 meV, respectively. Based on these results, a spacing of at least 0.0079 $Å^{-1}$ is used for all the simulations of bulk Cu in this Chapter.

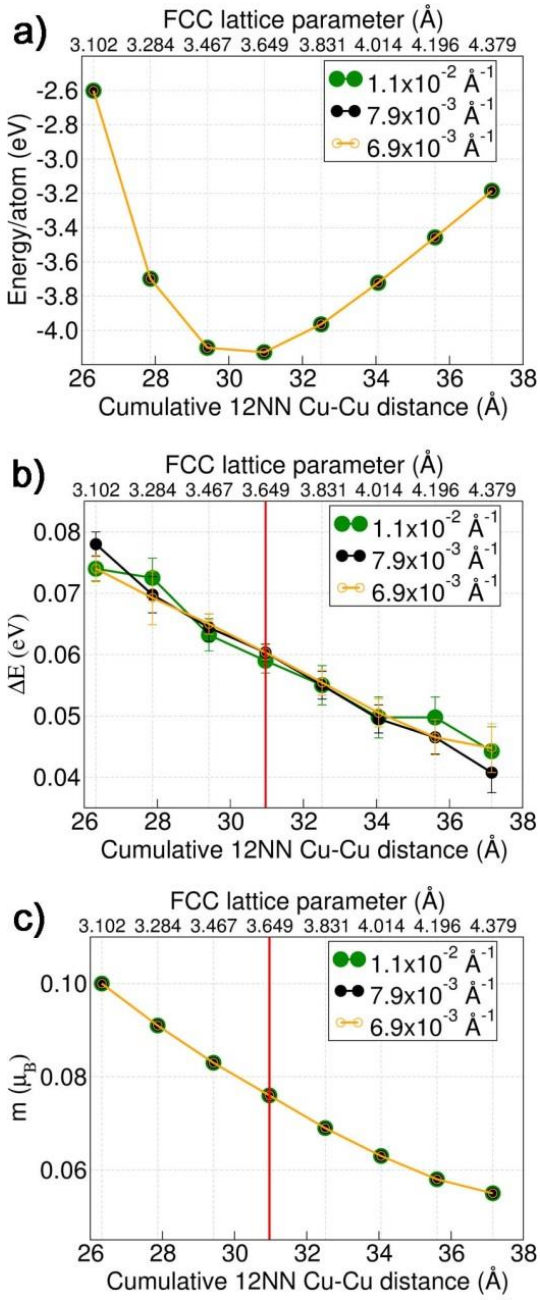

Figure 3.3: Computed **a)** energy per Cu-atom, **b)** band-splitting (ΔE), and **c)** atomic magnetic moment (m) as a function of the lattice parameter for bulk Cu in the FCC structure for different k-point samplings. For each structure considered, the sum of the 12 shortest nearest-neighbours (NN) Cu-Cu distances is also indicated. The vertical red line marks the value of the cumulative 12 NN Cu-Cu distance (30.962 Å) in bulk FCC Cu for the optimised lattice parameter (3.649 Å).

3.3 Isotropic deformation of bulk FCC Cu

I start by studying the effects of FCC-symmetry conserving compression and expansion on the magnetic properties of bulk Cu, specifically on the computed stoner exchange integral (I_S), Density of States at the Fermi level [$DOS(E_F)$], and Stoner product [$I_S \times DOS(E_F)$].

Although it is experimentally known that the maximum epitaxial lattice expansion for FCC Cu is 8% [11, 12], Cu-lattice relaxation in interfaces with C_{60} is computed to be as large as 15% [2] owing to the large interfacial charge transfer (clearly absent for systems constituted only by Cu). This result prompts for extensive scan of the magnetic properties of Cu for such large volume variation. I recall that the objective of this Chapter is to provide a reference term for the effects of Cu-lattice distortion alone on the magnetic properties of Cu, ahead of exploration of other hybrid Cu-molecule system and expectedly large [2] interface relaxation.

For the range of volumes considered, the computed values of I_S for bulk FCC Cu as a function of the lattice parameter (Fig. 3.4a) show a small variation (<0.05 eV or, equivalently, <6%) from the optimised reference value. Compression (expansion) of the Cu FCC lattice results in decrease (increase) of I_S, with larger changes (up to 6%, that is 0.05 eV) upon compression. The computed magnetic hardening for expanded Cu lattices agrees qualitatively, but not quantitatively, with results for C_{60}-perturbed FCC Cu substrates, where increases up to a factor of over three in I_S were computed for 15% expansion of the local Cu FCC coordination [1]. This result provides a first indication that increase of Cu-Cu distances without changes of the local coordination symmetry for Cu-atoms and depletion of the electronic charge by the organics is not exceedingly effective in inducing magnetic hardening of Cu substrates. . However, given the close match between the maximum change of I_S as a function of the volume change (<0.07 eV) and its computed error (up to nearly 0.06 eV for the most deformed cases in Fig. 3.4a), this analysis should be considered at a qualitative level and further work is needed to explore the dependence of the error of I_S on the projection scheme used to compute band splitting and atomic magnetic moment (Section 2.3.2)However, the increase of I_S with the lattice parameter is accompanied

by a parallel rise in the Density of States at the Fermi Energy [DOS(E_F), Fig. 3.4b-c], leading to up to 30% larger I_S×DOS(E_F) products (Fig. 3.4 d), closer to comply with the Stoner criterion for spontaneous onset of ferromagnetic ordering in *3d*-metals (I_S×DOS(E_F) > 1 [13, 14]). Conversely, compression of bulk FCC Cu, and the ensuing reduction in both I_S and DOS(E_F), leads to up to over 30% reduction of I_S×DOS(E_F). Overall, these results indicate that expansions maintaining the FCC symmetry are more effective than analogous symmetry conserving compression in inducing magnetic hardening of Cu. The one order difference between the maximum computed changes in I_SxDOS(E_F) values (~0.08 eV) and errors (<0.01 eV) provides at least semi-quantitative value to this conclusion.

Notably, the largest increase in of I_S×DOS(E_F) for 20% expanded bulk Cu FCC, leading to a value of roughly 0.16 spin^{-1} atom^{-1} is substantially smaller (-30%) than what computed, at the same level of theory, for Cu-C_{60} interfaces (up to 0.23 spin^{-1} atom^{-1} [1], confirming that isotropic FCC expansion may not be the most effective strategy towards magnetic hardening of Cu substrates. On the other hand, it also worth noting that for the as prepared Cu-aC interfaces measured to develop ferromagnetic ordering [2], the computed I_S×DOS(E_F) products are close to 0.15 spin^{-1} atom^{-1}. This result suggests that exploration of Cu FCC lattice expansion, possibly by epitaxial growth of ultra-thin films on suitable substrates, could be a potentially alternative route towards magnetic hardening of Cu and the ensuing emergence of ferromagnetic ordering *without* the use of molecular interfaces. Clearly, epitaxial Cu films grown on substrates of expanded periodicity with respect to FCC Cu are expected to manifest, in the absence of charge-transfer with the underlying substrate, out of plane lattice contraction, which may alter the magnetic properties from what computed in Fig. 3.4d for expanded FCC lattices. The effects of such (tetragonal or orthorhombic) distortion are investigated in the following sections and discussed with respect to these preliminary suggestions.

Non-collinear fixed-spin DFT simulations for all the compressed and expanded bulk FCC systems indicate minimal changes (<10^{-7} eV/atom) in the MAEs, that remain consistently in the order of 10^{-6} eV/atom, in line with the weak shape anisotropies measured for ferromagnetic Cu-C_{60} interfaces (~10^{-6} eV/Cu-atom [1]). The

anisotropy found in the compressed and expanded Cu bulk FCC systems is comparable with soft magnetic materials such as permalloys [15], nickel iron alloy, which show low or vanishing magnetic anisotropies of a few J/m^3 [16, 17]. Although the computed differences in MAEs are clearly substantially below the (meV range, see Methods section) convergence of the simulations, the computed sub-meV values can be nevertheless taken as an indication that the isotropic deformations studied are not capable of substantially increasing MAEs for Cu-substrates to the meV range, as desirable for practical applications [8].

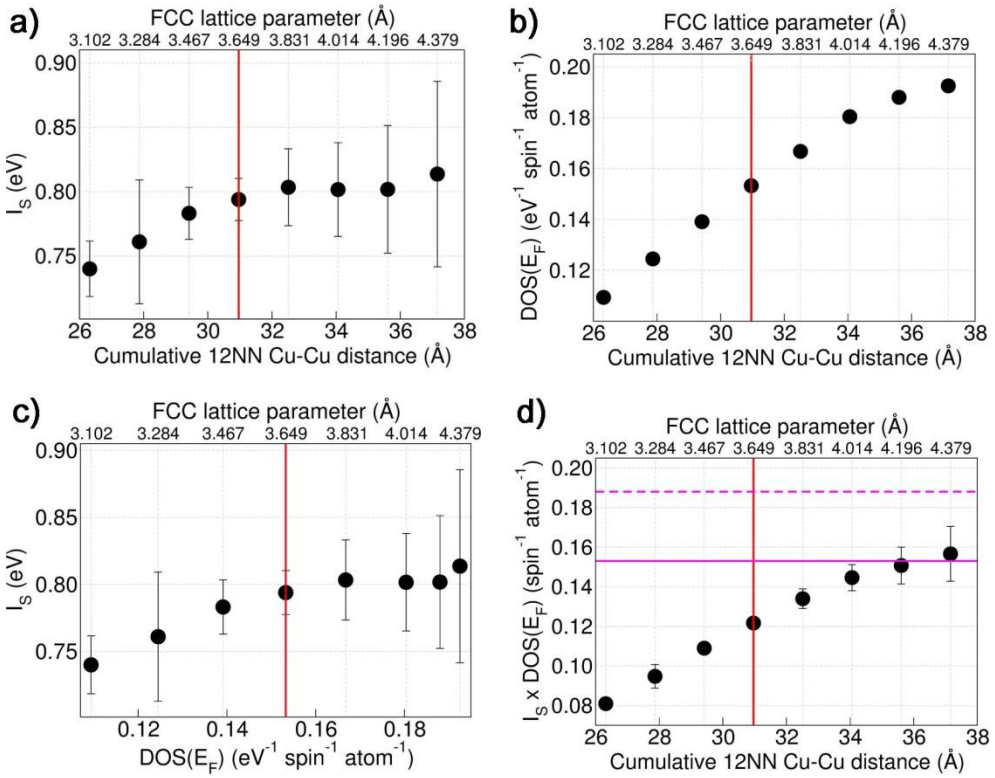

Figure 3.4: Computed **a)** Stoner exchange integral (I_s), and **b)** Density of States at the Fermi level [DOS(E_F)] as a function of both the lattice parameter for bulk FCC Cu and the sum of the 12 shortest nearest-neighbours (NN) Cu-Cu distances. **c)** Computed I_S as a function of DOS(E_F). **d)** Change of I_S×DOS(E_F) as a function of the lattice parameter. The vertical red line marks the values for the optimised lattice parameter (3.649 Å). The horizontal continuous (0.15 spin^{-1} atom^{-1}) and dashed (0.19 spin^{-1} atom^{-1}) magenta lines in d) mark the largest computed I_S×DOS(E_F) product at the same level of theory for the interfaces between Cu and as deposited (1.7 gr/cm^3) and annealed (2.3 gr/cm^3) aC measured to be ferromagnetic in Ref. [2].

3.4 Volume-conserving distortions of bulk FCC Cu

To disentangle the role of both the Cu-Cu distances and the local coordination symmetry for the magnetic properties of bulk Cu, I next turn to the study of different crystal distortions breaking the FCC symmetry. The response of bulk FCC Cu under different kinds of load has been extensively studied in the literature [18-21] to screen alloying strategies towards creation of innovative structural materials based on light transition metals for aerospace, aircraft and automobile applications. Unfortunately for the focus of this Thesis, all these elasticity-theory studies have investigated (one-, bi- and tri-axial) loading of the substrate in the absence of charge accumulation or depletion, which is instead understood to be critical for magnetic hardening at Cu-organic interfaces [1, 2] and may well alter the computed lower-energy phase transformation paths from what previously computed for neutral bulk FCC Cu substrates.

Given the (unsolved) challenges in determining via periodic DFT simulations the energy of bulk systems in the presence of extra (delocalised) charge [22-24], which prevents energy-based approaches to screening the energy favourable distortion pathways for charge enriched or depleted bulk FCC Cu, here I adopt a pragmatic exploratory strategy based on screening of the change in magnetic properties of Cu for distortions that increase or decrease the Cu-Cu bond distances while simultaneously breaking the FCC coordination for the atoms. The final aim of this work is to provide a comparison term to the results in Section 3.3 (FCC-symmetry maintaining expansion and compression of bulk Cu) and disentangle the role of lattice Cu-Cu distances and FCC symmetry breaking for the magnetic properties of Cu.

Fig. 3.5 and Table 3.1 summarise the distortions considered. In all cases, the lattice parameters were varied according to the symmetry of the crystal distortion studied, while maintaining the cell volume equal to the optimised FCC value (3.649^3 $Å^3$, Fig. 3.3). Due to the very steep increase of the energy of the systems upon changing one lattice angle of the FCC system −quickly over 1 eV/atom for the monoclinic distortions (Fig. 3.6)− and the overall magnetic softening found for FCC-symmetry

breaking distortions (vide infra), it was decided not to consider rhombohedral and triclinic distortions, as they involve change of two or more lattice angles in the pristine FCC system. The distortions resulting in positive electron energy (unbound electrons) were discarded from the analysis of magnetic properties.

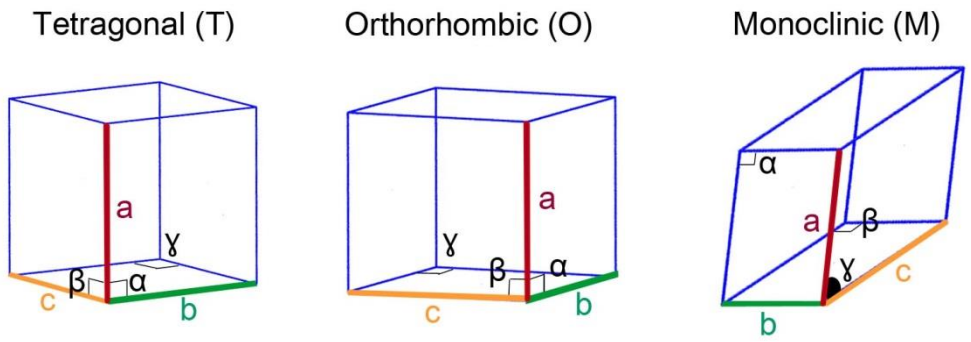

Figure 3.5: Schematic representation of the FCC Cu-bulk distortions studied: tetragonal (T), orthorhombic (O) and monoclinic (M) systems where **a**, **b** and **c** correspond to the lattice vectors and α, β, γ are the lattice angles.

Table 3.1: Summary of the volume-conserving distortions from the FCC crystal structure studied.

Distortion	**Lattice vectors**	**Lattice angles**	**Applied changes to lattice vectors and angles**
Tetragonal (T)	a=b=3.649 Å≠c	α=β=γ=90º	a=b: ±5, ±10, ±15, ±20% change. c compressed or expanded to maintain FCC optimised volume
Orthorhombic (O)	a=3.649 Å≠b≠c	α=β=γ=90º	a=3.649 Å. b: ±5, ±10, ±15, ±20% change. c compressed or expanded to maintain FCC optimised volume
Monoclinic (M)	a=3.649 Å≠b≠c	α=β=90º≠γ	a=3.649 Å. b: ±5, ±10, ±15, ±20% change. c compressed or expanded to maintain FCC optimised volume. γ=81º, 72º, 60º,50º

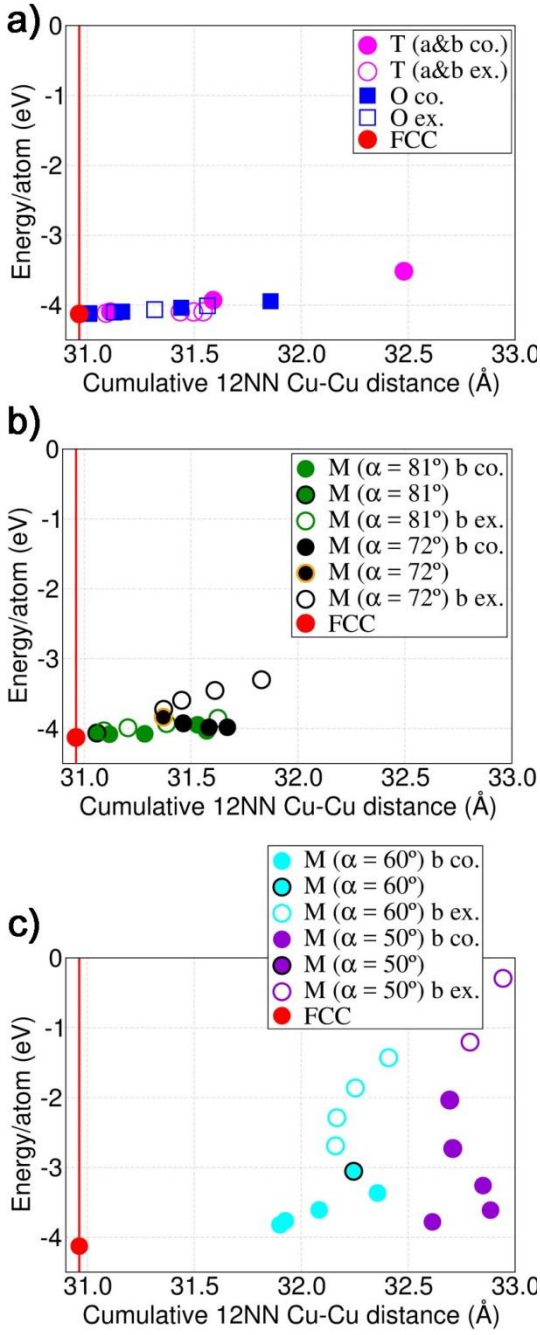

Figure 3.6: Computed energy per Cu-atom for the considered **a)** tetragonal and orthorhombic, **b-c)** monoclinic volume-conserving distortions of the bulk FCC Cu lattice. Computed values are reported as a function of the sum of the 12 shortest nearest-neighbours (NN) Cu-Cu distances for the given structure. The vertical red line marks the value of the cumulative 12 NN Cu-Cu distance (30.962 Å) in bulk FCC Cu for the optimised lattice parameter (3.649 Å). Expansion ("ex.", empty symbols) or compression ("co.", filled symbols) of the lattice vectors is indicated in the legends. Unless stated otherwise, the *a* (*b*) lattice vector(s) were maintained to the FCC optimised value. See also Table 3.1 for complete listing of the geometrical details of each distortion studied.

The volume-conserving distortions studied lead to smaller changes in the computed atomic magnetic moment (< 0.006 μ_B in Fig. 3.7) and band-splitting (< 0.01 eV in Fig. 3.8) than the isotropic FCC cell expansion or compression shown in Fig. 3.3. The joint-contribution of these two quantities to Eq. 2.88 (Chapter 2) results in a limited increase in I_S (< 0.05 eV) for those tetragonal or orthorhombic distortions with a smaller (< 1.5 Å) increase of the sum of 12 shortest Cu-Cu distances (Fig. 3.9a), indicative of a more contained loosening of the Cu lattice. Conversely, increased loosening of the lattice, or reduction of the γ-angle below 72º in monoclinic systems, results in more significant lowering (up to -0.15 eV in Fig. 3.9c) of I_S. These results are in contrast with the computed increase of I_S with loosening of the FCC lattice shown in Fig. 3.4 and found in [1] for Cu-C_{60} interfaces, and reveal a magnetic softening effect on Cu for FCC-symmetry breaking distortions that expand the Cu lattice.

Contrary to the computed correlated increase of I_S and DOS(E_F) for isotropic deformation of bulk FCC Cu, the correlation between I_S and DOS(E_F) for the distortions considered is weaker. However, a general trend is present in that the monoclinic distortion, changing one lattice angle from 90º, is consistently modelled to reduce both I_S and DOS(E_F). As a result of these effects on I_S and DOS(E_F), the I_S×DOS(E_F) product for the tetragonal and orthorhombic cases is minimally altered from the optimised bulk FCC Cu case (Fig. 3.9g). Conversely, and owing the simultaneous decrease of both I_S and DOS(E_F), the computed I_s×DOS(E_F) products are lowest for the monoclinic distortions (up to -33% of the bulk Cu value in Fig. 3.9i), revealing a substantial softening effects of monoclinic symmetry coordination for the Cu atoms.

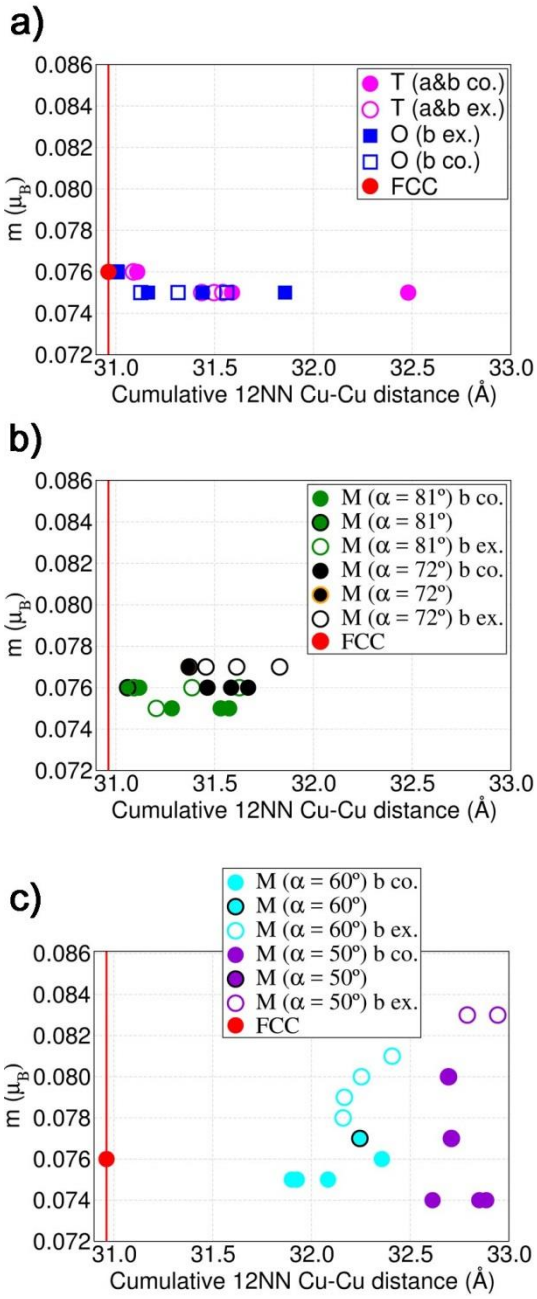

Figure 3.7: Computed atomic magnetic moment (m) for the considered **a)** tetragonal and orthorhombic, **b-c)** monoclinic volume-conserving distortions of the bulk FCC Cu lattice. Computed values are reported as a function of the sum of the 12 shortest nearest-neighbours (NN) Cu-Cu distances for the given structure. The vertical red line marks the value of the cumulative 12 NN Cu-Cu distance (30.962 Å) in bulk FCC Cu for the optimised lattice parameter (3.649 Å). Expansion ("ex.", empty symbols) or compression ("co.", filled symbols) of the lattice vectors is indicated in the legends. Unless stated otherwise, the *a* (b) lattice vector(s) were maintained to the FCC optimised value. See also Table 3.1 for complete listing of the geometrical details of each distortion studied.

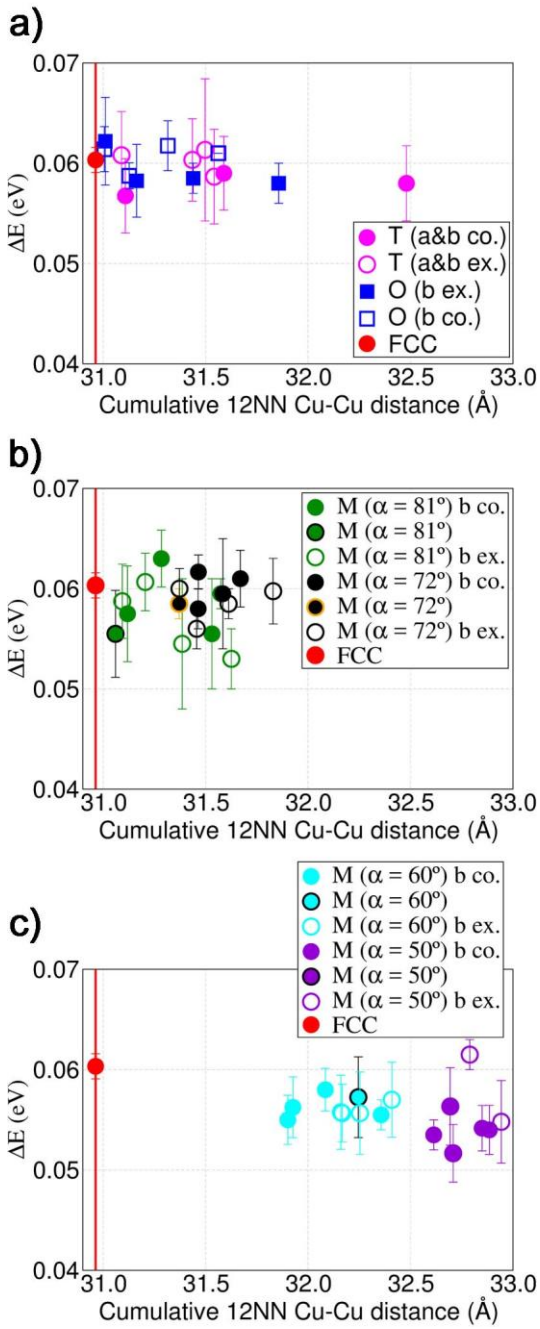

Figure 3.8: Computed band-splitting (ΔE) for the considered **a)** tetragonal and orthorhombic, **b-c)** monoclinic volume-conserving distortions of the bulk FCC Cu lattice. Computed values are reported as a function of the sum of the 12 shortest nearest-neighbours (NN) Cu-Cu distances for the given structure. The vertical red line marks the value of the cumulative 12 NN Cu-Cu distance (30.962 Å) in bulk FCC Cu for the optimised lattice parameter (3.649 Å). Expansion ("ex.", empty symbols) or compression ("co.", filled symbols) of the lattice vectors is indicated in the legends. Unless stated otherwise, the *a* (*b*) lattice vector(s) were maintained to the FCC optimised value. See also Table 3.1 for complete listing of the geometrical details of each distortion studied.

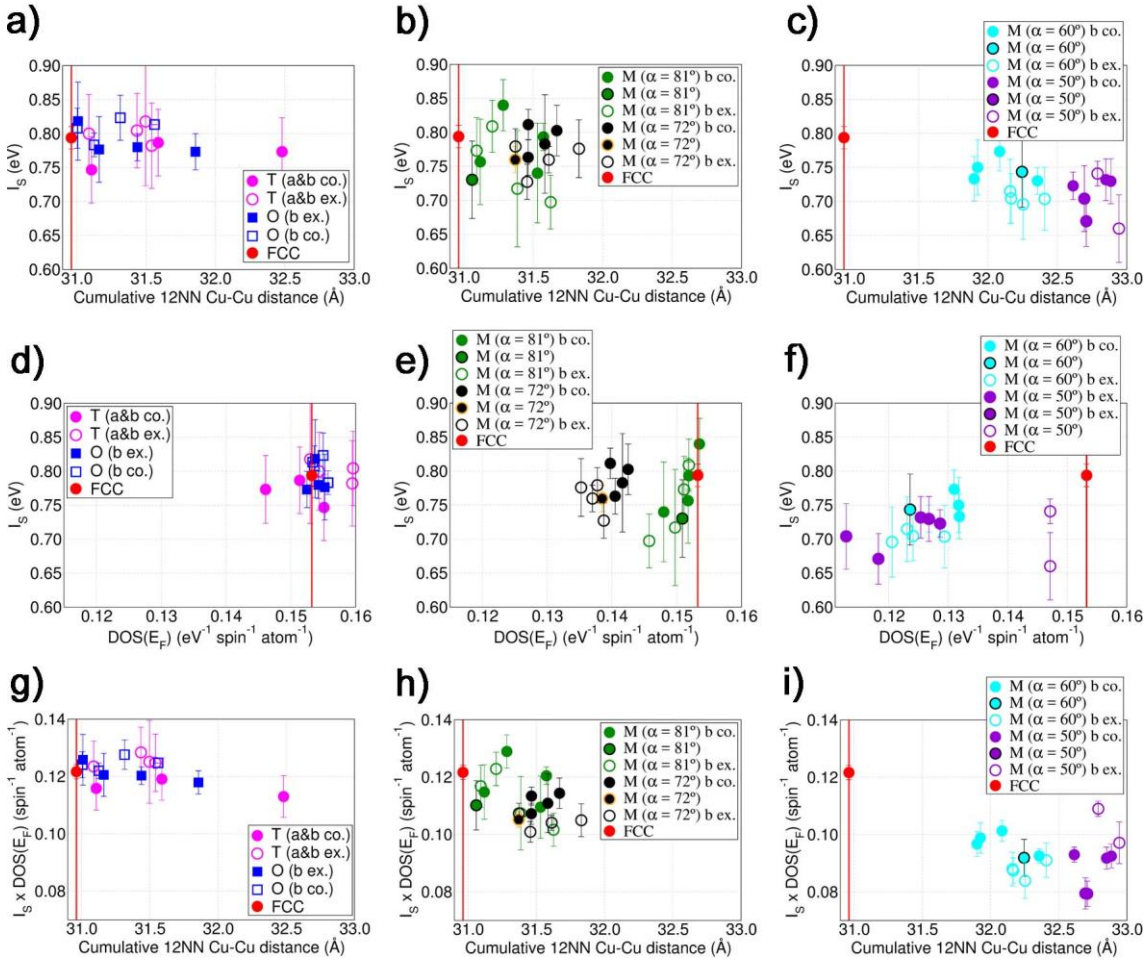

Figure 3.9: a-c) Computed Stoner exchange integral, I_S, for the considered volume-conserving distortions of bulk FCC Cu as a function of the sum of the 12 shortest nearest-neighbours (NN) Cu-Cu distances. **d-f)** Computed I_S as a function of $DOS(E_F)$ for the systems considered. **g-i)** Change of $I_S \times DOS(E_F)$ as a function of the cumulative 12 NN Cu-Cu distance. The vertical red line marks the value corresponding to optimised bulk FCC Cu. Expansion ("ex.", empty symbols) or compression ("co.", filled symbols) of the lattice vectors is indicated in the legends. Unless stated otherwise, the *a* (*b*) lattice vector(s) were maintained to the FCC optimised value. See also Table 3.1 for complete listing of the geometrical details of each distortion studied. The $I_S \times DOS(E_F)$ product show negligible changes for the tetragonal and orthorhombic systems compared to the Cu bulk. On the other hand, Cu magnetic softening, i.e. reduction of the $I_S \times DOS(E_F)$ product, is observed for the monoclinic distorted structures.

3.5 Volume-optimised distortions of bulk FCC Cu

While informative on the response of Cu magnetic properties on changes of the crystal structure, and despite atomic forces being zero by symmetry, most of the distortions explored in the previous section entail substantial increase of the energy per Cu atom (Fig. 3.6) pointing to an unlikely realisation in reality, even in the presence of charge-transfer from suitable deposition substrates.

This Chapter is accordingly extended by optimising the cell energy of selected distortions with respect to the cell volume maintaining the cell shape and symmetry. For this study I focus on the distortions in Table 3.1 characterised by ±10% change of the *a and b* (tetragonal cell) or *only b* (orthorhombic and monoclinic cells) lattice vectors, and optimise the energy of the system maintaining the lattice angles, ratio between the modules of the lattice vectors, and the direct coordinates of the atoms in the cell fixed.

As shown in Fig. 3.10, minimisation of the energy of the system as a function of its volume leads to changes in the sum of the 12 nearest-neighbour Cu-Cu distances for the same cell shape, which enables independent analysis of the role of the Cu-Cu distances for fixed coordination symmetries in tuning the magnetic properties of Cu for tetragonal, orthorhombic and monoclinic cells.

In spite of deviations in the computed magnetic moments (m, Fig. 3.11) and band-splittings (ΔE, Fig. 3.12) due to the optimisation of the cell volume and the ensuing changes in the Cu-Cu distances, the computed I_S for the volume-optimised orthorhombic and tetragonal distortions remains close (to within 0.05 eV) to the bulk FCC Cu value (Fig. 3.13). Also in this case, the monoclinic distortions with smaller γ-angles (50º and 60º) are computed to lead to substantially lowered I_S values (up to -0.15 eV in Fig. 3.13c). Similar to the fixed-volume cases (Fig. 3.9), also for the volume-optimised systems the correlation between I_S and DOS(E_F) remains weaker (Fig. 3.13d-f) than for the FCC case (Fig. 3.4c) and the computed $I_S \times DOS(E_F)$ products (Fig. 3.13g-i) are either minimally increased (up to no more than 0.01 $spin^{-1}$ $atom^{-1}$) or decreased with respect to the bulk FCC Cu value. The only exception to this trend is presented by the volume-optimised monoclinic distortion with an α angle

of 60 degrees and *b* lattice vector initially increased by 10%, that results in a Stoner product of 0.14 $spin^{-1}$ $atom^{-1}$ [Fig. 3.13i], noticeable larger than the FCC value (0.12 $spin^{-1}$ $atom^{-1}$). However, given the substantial energy increase (over 1 eV/atom) with respect to the bulk FCC case, this geometry could be hardly populated, even in the absence in substantial charge transfer and its experimental design should not be prioritised.

Finally, I return to the previous proposition (Section 3.3) of developing magnetically harder Cu films by epitaxial growth on substrates with an in-plane lattice constant larger than bulk FCC Cu. On the basis of the negligible increase in magnetic hardening computed for the volume-optimised tetragonal distortions considered (Fig 3.13a and Fig. 3.13g), the simulations suggest that growth of epitaxial Cu films tetragonally distorted (expansion of *a* and *b* lattice vectors, compression of the *c* vector) may not be a very effective strategy to enhancement of magnetism in Cu, at least in the absence of charge transfer from the growth substrate (neglected in the present simulations). As the present results do not allow any comment on whether a tetragonal distortion of Cu in the presence of substantial charge-transfer may or may not lead to viable magnetic hardening of Cu, and owing to the time constraints of my PhD project, this aspect is left to future research in the field.

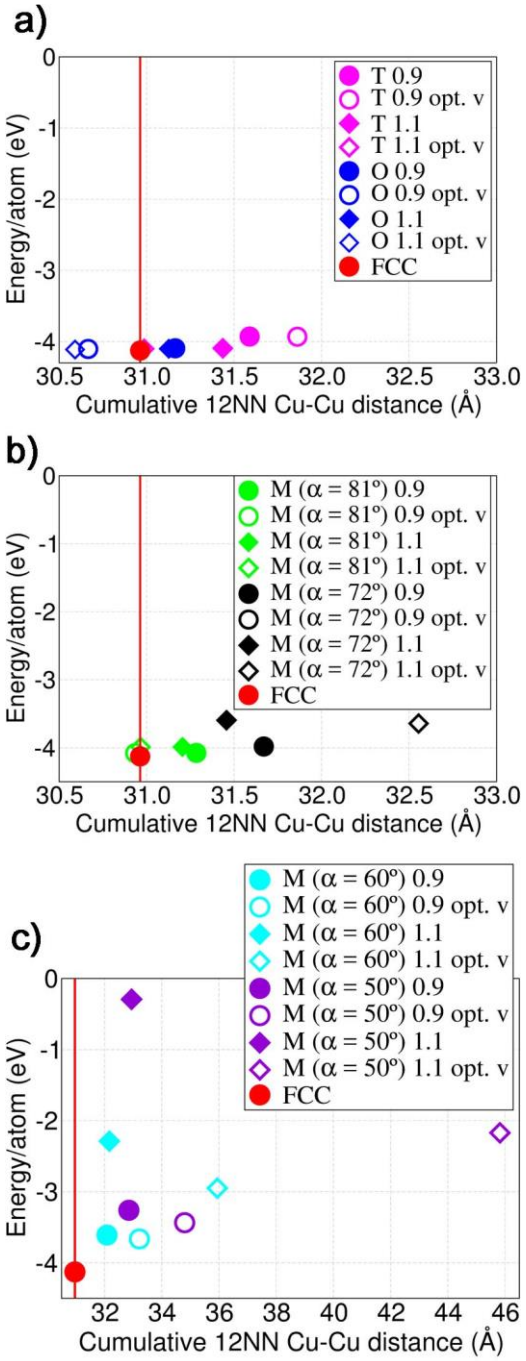

Figure 3.10: Comparison between the computed energy per Cu-atom for the considered volume-conserving (filled symbols) and volume-optimised ("opt. v", empty symbols) distortions of the bulk FCC lattice. **a)** tetragonal and orthorhombic case, **b-c)** monoclinic cases. The initial 10% reduction or increase of the lattice vector(s) is marked by the "0.9" and "1.1" label, respectively. The computed values are reported as a function of the sum of the 12 shortest nearest-neighbours (NN) Cu-Cu distances for the given structure. The vertical red line marks the values for bulk FCC Cu at the optimised lattice parameter (3.649 Å). The minimisation of the energy of the considered structures as a function of its volume results in a change in the sum of the 12 nearest-neighbour Cu-Cu distances for the same cell shape.

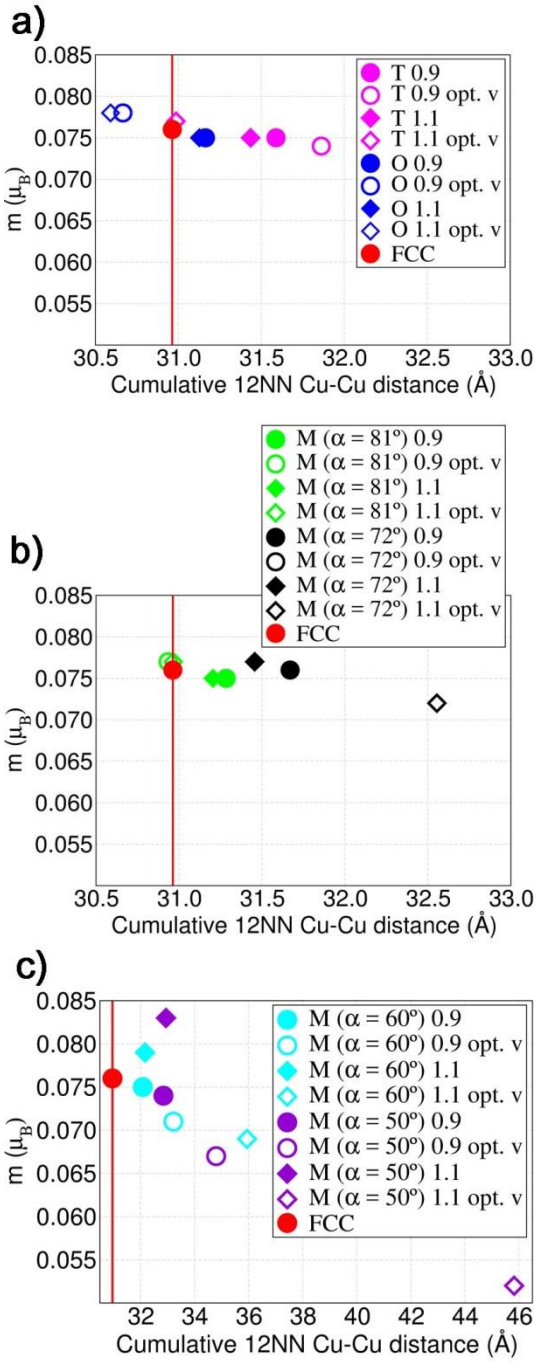

Figure 3.11: Comparison between the computed magnetic moment (m) for the considered volume-conserving (filled symbols) and volume-optimised ("opt. v", empty symbols) distortions of the bulk FCC lattice. **a)** tetragonal and orthorhombic case, **b-c)** monoclinic cases. The initial 10% reduction or increase of the lattice vector(s) is marked by the "0.9" and "1.1" label, respectively. The computed values are reported as a function of the sum of the 12 shortest nearest-neighbours (NN) Cu-Cu distances for the given structure. The vertical red line marks the values for bulk FCC Cu at the optimised lattice parameter (3.649 Å). A weak correlation between the loosening of the Cu lattice and the decrease of the computed magnetic moment is observed.

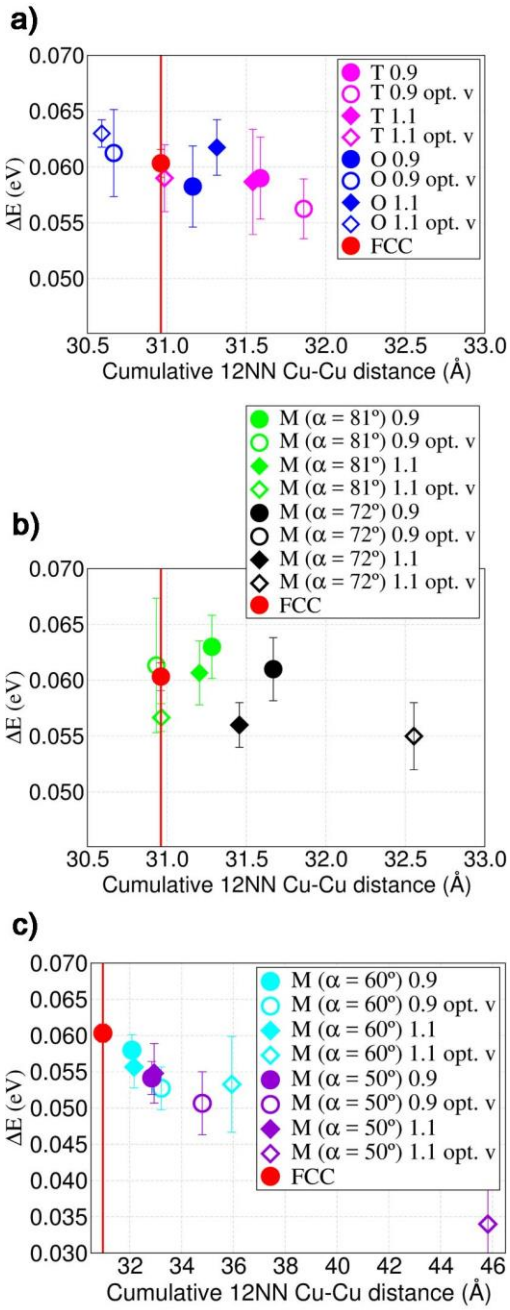

Figure 3.12: Comparison between the computed band-splitting (ΔE) for the considered volume-conserving (filled symbols) and volume-optimised ("opt. v", empty symbols) distortions of the bulk FCC lattice. **a)** tetragonal and orthorhombic case, **b-c)** monoclinic cases. The initial 10% reduction or increase of the lattice vector(s) is marked by the "0.9" and "1.1" label, respectively. The computed values are reported as a function of the sum of the 12 shortest nearest-neighbours (NN) Cu-Cu distances for the given structure. The vertical red line marks the values for bulk FCC Cu at the optimised lattice parameter (3.649 Å). A weak correlation between the loosening of the Cu lattice and the decrease of the band-splitting moment is observed.

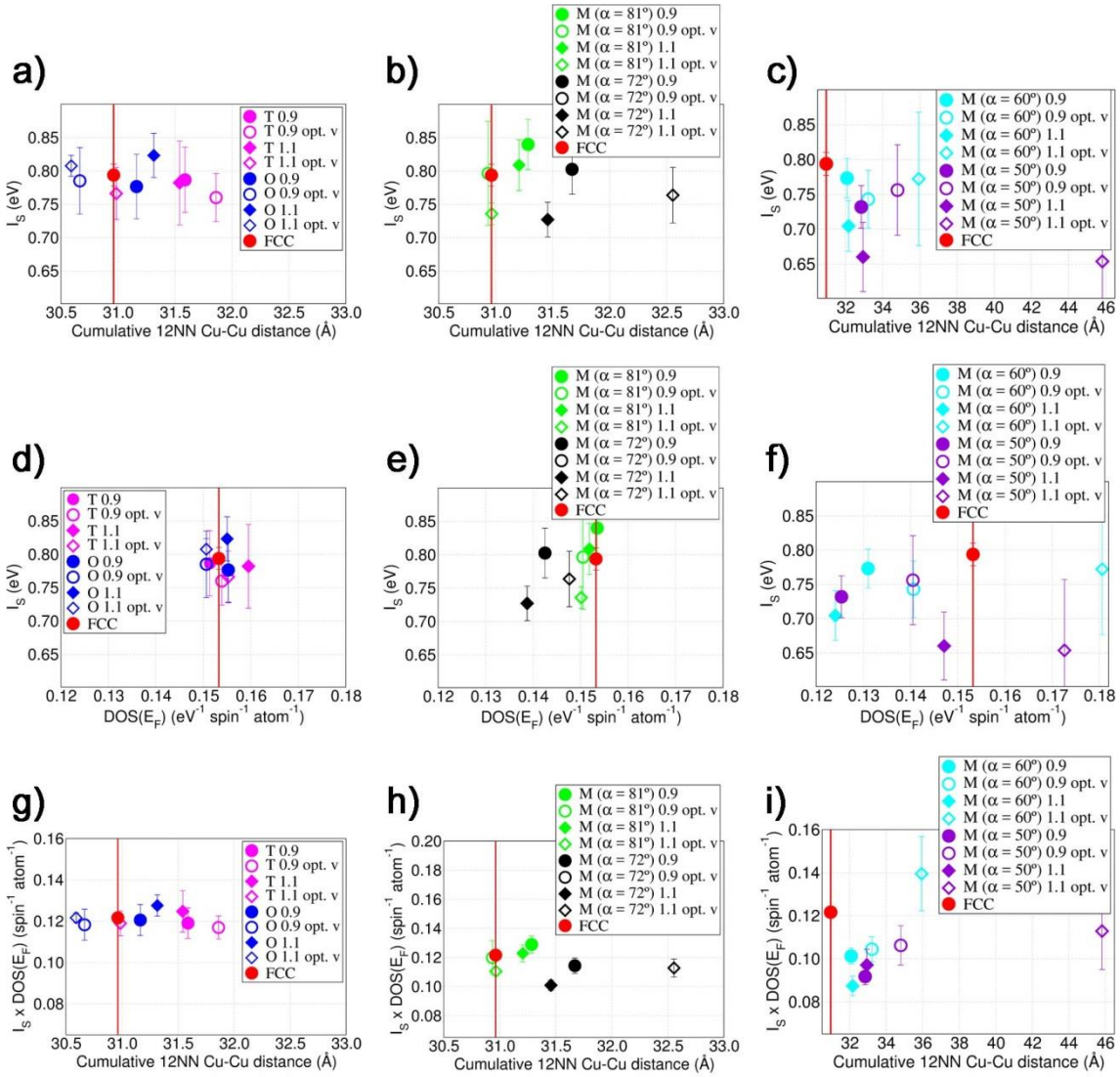

Figure 3.13: a-c) Computed Stoner exchange integral, I_S, for the considered volume conserving (filled symbols) and volume-optimised ("opt. v", empty symbols) distortions of bulk FCC Cu as a function of the sum of the 12 shortest nearest-neighbours (NN) Cu-Cu distances. **d-f)** Computed I_S as a function of DOS(E_F) for the systems considered. **g-i)** Change of I_S×DOS(E_F) as a function of the cumulative 12 NN Cu-Cu distance. The initial 10% reduction or increase of the lattice vector(s) is marked by the "0.9" and "1.1" label, respectively. Negligible increase of the magnetic hardening is observed for all the considered systems suggesting that growth of epitaxial distorted Cu films may not be an effective strategy for the enhancement of the Cu magnetic hardening.

3.6 Conclusion

Summarising this Section, simulations of different distortions of bulk Cu indicate that, whereas FCC-symmetry maintaining expansion of the Cu lattice leads to increase of I_S and $I_S \times DOS(E_F)$ products to values previously computed for systems measured to be ferromagnetic (the Cu-aC interfaces in [2]), rupture of the FCC symmetry invariably leads to either negligible magnetic hardening or substantial magnetic softening of Cu with up to 30% reduction from bulk FCC Cu. It thus emerges that protection of a local FCC coordination, as observed to be present by small-angle X-rays measurements of magnetic Cu-organics interfaces [1, 2], accompanied by extension of the Cu-Cu bonds, is a necessary element to magnetically harden Cu. In the next Chapters, we disentangle the interplay of FCC-preserving expansions of the Cu lattice and electronic-charge depletion by investigating systems capable of different Cu-organics charge-transfer and deformation of the FCC Cu lattice.

3.7 References

1. Al Ma'Mari, F., et al., *Beating the Stoner criterion using molecular interfaces.* Nature, 2015. **524**(7563): p. 69-73.
2. Al Ma'Mari, F., et al., *Emergent magnetism at transition-metal–nanocarbon interfaces.* Proceedings of the National Academy of Sciences, 2017. **114**(22): p. 5583-5588.
3. Schwarz, K. and P. Mohn, *Itinerant metamagnetism in YCO2.* Journal of Physics F: Metal Physics, 1984. **14**(7): p. L129.
4. Kresse, G. and J. Furthmüller, *Efficient iterative schemes for ab initio total-energy calculations using a plane-wave basis set.* Physical Review B, 1996. **54**(16): p. 11169.
5. Perdew, J.P., K. Burke, and M. Ernzerhof, *Generalized gradient approximation made simple.* Physical Review letters, 1996. **77**(18): p. 3865.
6. Methfessel, M. and A. Paxton, *High-precision sampling for Brillouin-zone integration in metals.* Physical Review B, 1989. **40**(6): p. 3616.

7. Raman, K.V., et al., *Interface-engineered templates for molecular spin memory devices.* Nature, 2013. **493**(7433): p. 509.
8. Callsen, M., et al., *Magnetic hardening induced by nonmagnetic organic molecules.* Physical Review letters, 2013. **111**(10): p. 106805.
9. Gunnarsson, O., *Band model for magnetism of transition metals in the spin-density-functional formalism.* Journal of Physics F: Metal Physics, 1976. **6**(4): p. 587.
10. Wakoh, S. and J. Yamashita, *Band structure of ferromagnetic iron self-consistent procedure.* Journal of the Physical Society of Japan, 1966. **21**(9): p. 1712-1726.
11. Yue, Y., et al., *Approaching the theoretical elastic strain limit in copper nanowires.* Nano letters, 2011. **11**(8): p. 3151-3155.
12. Xie, Y.-Q., et al., *Electronic structure and properties of Cu metal.* Science in China Series A-Mathematics, Physics, Astronomy & Technological Science, 1993. **36**(4): p. 487-494.
13. Stoner, E.C., *Collective electron ferromagnetism.* Proceedings of the Royal Society of London. Series A, Mathematical and Physical Sciences, 1938: p. 372-414.
14. Stoner, E.C., *Collective electron ferromagnetism. II. Energy and specific heat.* Proceedings of the Royal Society of London. Series A, Mathematical and Physical Sciences, 1939: p. 339-371.
15. Yin, L., et al., *Magnetocrystalline anisotropy in permalloy revisited.* Physical Review letters, 2006. **97**(6): p. 067203.
16. Herzer, G., *Nanocrystalline soft magnetic materials.* Journal of Magnetism and Magnetic Materials, 1992. **112**(1-3): p. 258-262.
17. Cullity, B.D. and C.D. Graham, *Introduction to magnetic materials*. 2011: John Wiley & Sons.
18. Milstein, F. and B. Farber, *Theoretical fcc→ bcc transition under [100] tensile loading.* Physical Review Letters, 1980. **44**(4): p. 277.
19. Cerny, M., et al., *Ab initio calculations of ideal tensile strength and mechanical stability in copper.* Journal of Physics: Condensed Matter, 2004. **16**(7): p. 1045.

20. Jahnatek, M., M. Krajčí, and J. Hafner, *Response of fcc metals and L 12 and D 022 type trialuminides to uniaxial loading along [100] and [001]: ab initio DFT calculations.* Philosophical Magazine, 2011. **91**(4): p. 491-516.
21. Černý, M. and J. Pokluda, *Ideal tensile strength of cubic crystals under superimposed transverse biaxial stresses from first principles.* Physical Review B, 2010. **82**(17): p. 174106.
22. Neugebauer, J. and M. Scheffler, *Adsorbate-substrate and adsorbate-adsorbate interactions of Na and K adlayers on Al (111).* Physical Review B, 1992. **46**(24): p. 16067.
23. Makov, G. and M. Payne, *Periodic boundary conditions in ab initio calculations.* Physical Review B, 1995. **51**(7): p. 4014.
24. Komsa, H.-P., T.T. Rantala, and A. Pasquarello, *Finite-size supercell correction schemes for charged defect calculations.* Physical Review B, 2012. **86**(4): p. 045112.

Chapter 4

The role of molecular π-conjugation for the magnetic hardening at Cu-organics interfaces

Abstract

This Chapter investigates the role of molecular π-conjugation for the magnetic hardening at Cu-organics interfaces by exploring several models of interfaces between Cu and polymers of different steric hindrance, π-conjugation and electron-accepting properties: polyethylene, polyacetylene, polyethylene terephthalate and polyurethane. Contrary to expectations based on the extent of π-conjugation on the organic and resulting charge-transfer, the computed magnetic hardening is largest for Cu interfaced with polyethylene, and smallest for the Cu-polyacetylene systems as a result of a differently favourable re-hybridisation leading to different enhancement of exchange interactions and Density of States at the Fermi level. These results suggest that neither the presence of molecular π-conjugation nor substantial charge-transfer may be strictly needed for magnetic hardening of Cu-substrates, widening the range of organics of potential interest for enhancement of emergent magnetism at metal-organic interfaces.

4.1 Introduction

As recently observed (see also Chapter 1, Section 1.6.1.8), hybridisation between a metal substrate and an organic material can be used to promote magnetism and ferromagnetic ordering between originally non-magnetic components [1-8]. The phenomenon is appealing because control and enhancement of emergent magnetism between cheap and non-toxic materials such as light transition-metals and organic semiconductors may provide more eco-friendly and sustainable alternatives to conventional magnetic materials and devices [6-8].

The compelling experimental evidence on the emergence of ferromagnetic ordering has been complemented by Density Functional Theory (DFT) modelling of some of the interfaces considered. The available DFT modelling points to both charge-transfer between the metal and the organics, and interface-relaxation induced distortions at the metal substrates as the two key drivers for the magnetic hardening of the metal substrate and consequent emergence of magnetic ordering [7]. To date, the relative importance of charge-transfer between the metal and (π-conjugated) organic, and distortion of the metal lattice for the emergence of interfacial magnetic ordering remains unquantified, with the immediate consequence of interfaces between metal and non π-conjugated molecules having being overlooked in recent investigations of emergent magnetism [6-8].

However, recent spin-resolved photoemission spectroscopy measurements on a linear alkane, pentacontane $C_{50}H_{102}$, on Co(001) have unambiguously shown that π-conjugation on the organic is not necessary for emergence of strongly spin-polarized interface states between ferromagnetic metals such as Co and an adsorbed organic molecule or layer [9]. Furthermore, this study reveals that a full spin-polarization of the *d*-states at E_F is not required. These results inevitably rise the question as to whether π-conjugation is actually necessary (or not) also for the magnetic hardening and emergence of magnetism at the interface between originally non-magnetic transition metals and molecular systems.

To answer this question, in this Chapter I disentangle the role of metal distortion, metal-organics charge-transfer, and organic π-conjugation for the magnetic

hardening at metal-organic interfaces. Specifically, I screen via DFT the electronic and magnetic properties of several models of interfaces between Cu (known to originate ferromagnetic ordering when contacted with C_{60} and aC films) [6, 7] and four polymeric systems of different steric hindrance, π-conjugation and electron-accepting properties, disentangling the relative importance and interplay between these factors and the resultant interface magnetic hardening or softening.

4.2 Computational details

Standard and fixed spin-moment [10], van der Waals (vdW) corrected [11], Density Functional Theory (DFT) simulations were executed via the Projected Augmented Wave (PAW) method as implemented in the VASP program [12] with the PBE exchange-correlation (XC) functional [13], a 400 eV plane-wave energy cut-off, and (0.2 eV, 1st order) Methfessel-Paxton electronic smearing [14]. The grids for k-point sampling were defined on the basis of convergence tests on the magnetic properties of bulk Cu in the face-centered cubic (FCC) structure (see Fig. 3.3 in Chapter 3) and scaled according to the size of the reciprocal lattice of the system under consideration. The atomic-force threshold for geometry optimisation was 0.02 eV Å^{-1}. All the atoms in the Cu slabs and in the polymers were fully relaxed in all the directions. A vacuum separation of at least 15 Å was present between replicated images of the 5-layer Cu(111) slab models for the in-plane interface models (Fig. 4.1). Bader charge analyses [15] were computed on the total charge density i.e. accounting for both the electronic and ionic core charges.

Due to the computed non-magnetic ground-state for all the models studied, atom-resolved approximations to the Stoner exchange integral (I_s, see Chapter 2, Section 2.3.2) were calculated by enforcing a magnetic moment of 0.1 μ_B/Cu-atom via fixed spin-moment DFT [10]. Errors on the approximated I_S were computed averaging over the stationary point of the Density of States closest to the Fermi Energy (E_F) following the procedure explained in Chapter 3 (Section 3.2.2). Following Refs. [6, 7, 16, 17], increase (decrease) of I_S with respect to the reference bulk value is taken as indication of *magnetic hardening* (*softening*) for a given substrate.

Magneto-crystalline anisotropy Energies (MAEs) were computed via fixed-spin moment (0.1 μ_B/Cu-atom), non-collinear DFT simulations with inclusion of spin-orbit coupling as available in VASP [12]. The simulations were carried out non-self-consistently, that is, keeping the charge density (from a collinear run) fixed. The magnetic field was selectively oriented perpendicularly to the high-symmetry directions of the considered system and the corresponding energy subtracted to quantify the MAEs. These non-collinear DFT simulations were performed with the same number of symmetry irreducible k-points tested to yield PAW-integrated I_S values converged to within 2 meV i.e. 8436 and 25 for bulk FCC Cu and the Cu-polyethylene interfaces, respectively.

4.3 The Cu-polymer interface models

To disentangle the role of Cu-lattice expansion and charge-depletion for the observed magnetic hardening of Cu at molecular interfaces [6, 7], this Chapter considers several models of interfaces between FCC Cu and organic systems with different electron-accepting properties, steric hindrance or excluded volume and, owing to a different extent of π-conjugation, conformational flexibility and relaxation possibilities when interfaced with the Cu-substrate. The Chapter focuses on four different polymeric systems, namely polyethylene (PE), polyacetylene (PAC), polyethylene terephthalate (PET) and polyurethane (PUR), whose monomeric units are shown in Fig. 4.1. These systems have been chosen on the basis of their different electron affinities (EA), thence expected electron-accepting properties neglecting interface-relaxation effects to be quantified in the following. The measured or computed EA for the considered systems range from negative for PE (experimentally derived value: -0.5±0.5 eV [18-22]) to increasingly positive values going from PUR (B3LYP computed vertical value, neglecting electronic and atomic relaxation: 0.63 eV [23]) to PET (experimental value: 2.85±0.05 eV [24]) and PAC (extrapolated – adiabatic- value for infinite chain at B3LYP level: 5.5 eV [25]). Based on these values, the expectation, to be verified against the results for the relaxed interface models, is that the charge-transfer from Cu to the polymer should increase following the series PE < PUR < PET < PAC.

In addition, the systems examined have different torsional flexibility owing to either the lack (PE) or different extent of π-conjugation (PET ~ PUR < PAC), and different steric hindrance due to the presence (PET and PUR) or absence (PE and PAC) of bulkier phenyl groups. Both these elements are anticipated to affect the relaxation at the interface with Cu, enabling quantification of the role of both the polymer-induced distortion of the Cu lattice and the polymer-relaxation for the emerging magnetic properties at the interfaces.

Before proceeding, it is worth recalling that all the Cu-organics interfaces capable of emergent magnetism measured to date have been prepared by alternated magnetron sputtering deposition of Cu (metal) and thermally evaporated organics (C_{60} molecules or C-atoms) films. The sample preparation protocol leads to creation of films with nm-range roughness [6, 7]. Since, in principle, alternative routes to preparation of single Cu-organics interfaces could be realized via chemical or electrochemical deposition of Cu on a polymeric-film, practical creation of the Cu-polymer interfaces studied below cannot be excluded a priori, motivating out interest in exploring computationally emergent magnetism at suitably treated interfaces of polymer substrates.

In analogy to the molecular films in Refs. [6, 7], ordinary noncrystalline films of the polymers considered are not atomically flat, with roughness in the nm-range [22] or above. Since such molecular roughness would inevitably result in growth of the deposited Cu inside pits of the polymer film or around “self-passivating” protruding polymer loops present at the surfaces of polymer-films [26], I bracket the possible interface geometries by the two extreme cases shown in Fig. 4.1: in the first one, the polymer chain is placed parallel to the Cu(111) planes of a five-layer slab (in-plane model). In the second one, the polymer chain is perpendicular to the slab plane (perpendicular model).

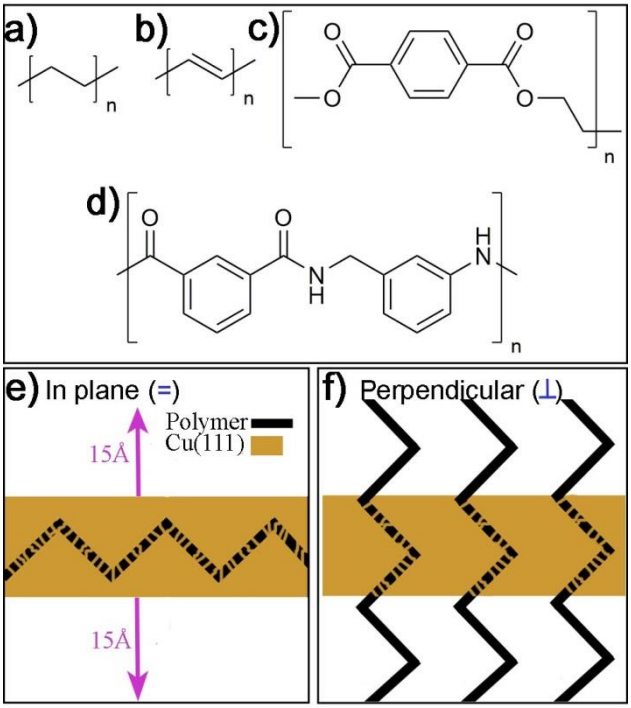

Figure 4.1: Monomer atomic structure for the polymers considered. **a)** polyethylene (PE), **b)** polyacetylene (PAC), **c)** polyethylene terephthalate (PET) and d) polyurethane (PUR). Schematic representation of the two interface models used: **e)** in-plane (=) geometry with the polymer chain inserted parallel to the Cu(111) plane, **f)** perpendicular (⊥) geometry with the polymer chain inserted perpendicular to the Cu(111) plane.

Here, it is also worth noting that magnetron sputtering preparation of the metal-organic interfaces is *not* a thermodynamic-driven process based on chemical equilibrium. Metastable systems can be initially formed. Indeed, the magnetron-sputtering prepared metal-molecule interfaces are experimentally observed to relax, following thermal treatment or ageing, into lower (free) energy systems of partially or strongly modified magnetic properties [6, 7]. These considerations motivate the neglect of thermodynamics-related parameters such as the formation energy (always positive for the considered interface models and progressively less favourable as the number of Cu atoms in the models increases) in favour of an exploratory focus on screening the electronic and magnetic properties of model Cu-polymer interface forcing different degree of interface geometric relaxation. As in Ref. [6], to include the effects of differently constrained optimisation of the Cu-polymer interface on the emerging magnetic properties, different models were prepared for each interface

geometry and polymer using several cut-off's (1.5, 2.0, 2.5 and 3.0 Å) on the initial Cu-polymer distance. Fig. 4.2 contains images of a selection of the initial geometries prepared with an initial cut-off of 1.5 Å. The value of the initial cut-off's were chosen in order to start the interface structural relaxation both in repulsive and attractive regimes, as estimated from the shortest Cu-C distances measured by I-V LEED for an archetypal interface between Cu and a π-conjugated system: the 7-vacancy C_{60}/Cu(111)-4x4 reconstruction (shortest interfacial Cu-C distance: 1.98 Å, longest interfacial Cu-C distance: 2.20 Å) [27]. Since the interface properties depend on the details of the interface re-hybridisation, which may change depending on the relaxation freedom available in the system, this strategy offers the possibility to quantify the role of differently constrained relaxations, as likely present in real samples of limited crystallinity [6, 7], on the emerging electronic and magnetic properties of the models studied.

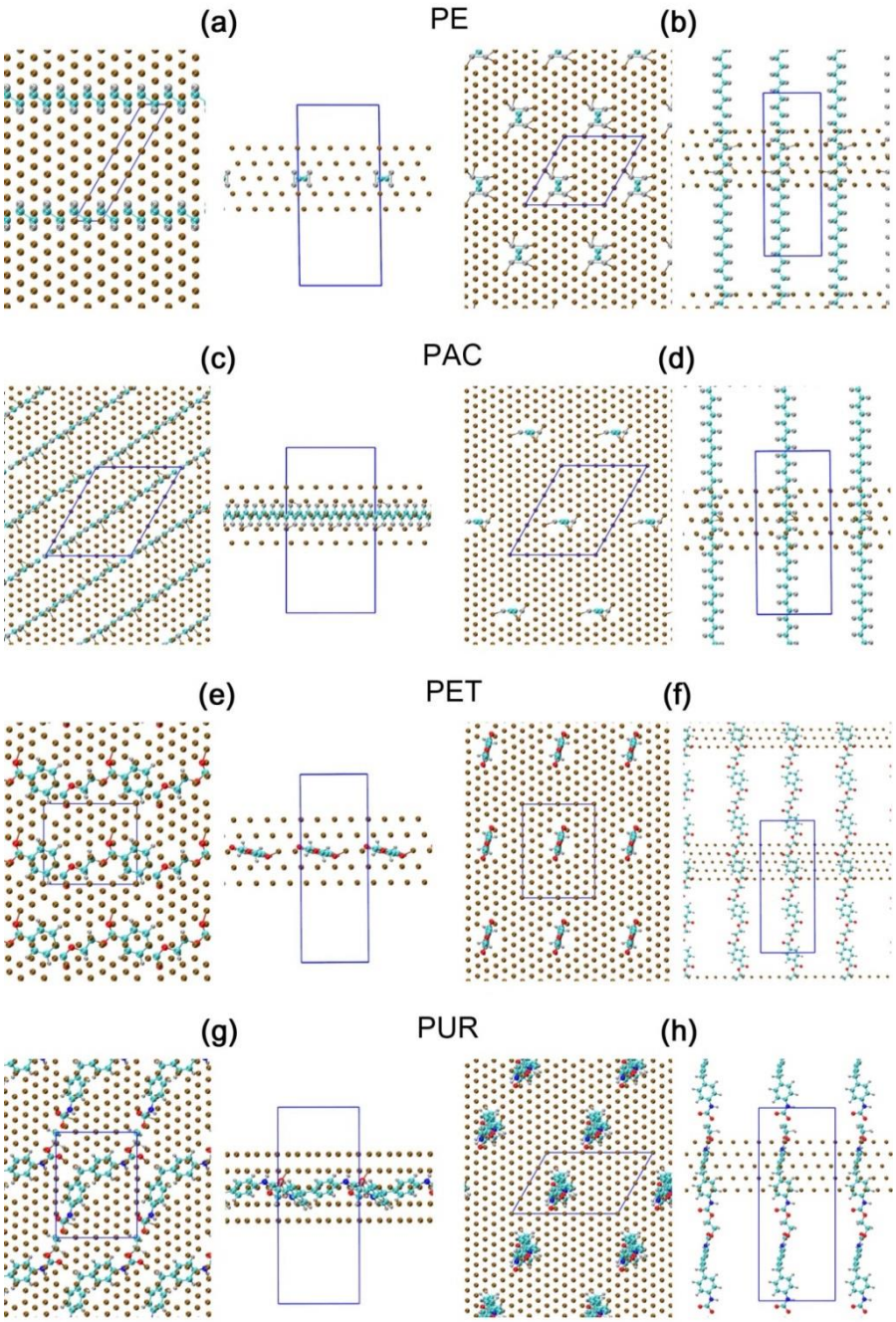

Figure 4.2: Top (left) and side (right) view of the initial geometries (1.5 Å cut-off) for the in-plane (=) and perpendicular (⊥) models of the Cu interfaces with PE (**a-b**), PAC (**c-d**), PET (**e-f**) and PUR (**g-h**). The periodic simulation cell is marked by blue continued lines. C: cyan, O: red, N: blue, H: silver, Cu: brown.

For the in-plane (=) interface models, commensurability between the Cu(111) slab and the polymer chains was achieved by modelling the smallest Cu(111) slab, in either a hexagonal or orthorhombic cell, capable of minimising the lattice mismatch with the given periodic polymer chain. Compromising between reduction of the periodicity mismatch and size of the simulation cell, I chose lattice mismatches <1.2% for PE, PAC and PUR and roughly 3% for PET. The positive lattice mismatch values indicate that the polymer chain was stretched to match the Cu(111) slab one. Table 1 reports a summary of the geometric parameters for the simulation cells used for the different Cu-polymer interface models. For the perpendicular (⊥) interface models, the size of the simulation cell along the direction perpendicular to the Cu(111) was based on the optimised period of the given polymer chain.

Table 4.1: Geometric parameters of the simulations cell for the different Cu(111)-polymer interface models studied. l_0 (Å): length of the monomer unit. N_p: number of monomer units in the Cu-polymer interface model. h: hexagonal cell. o: orthorhombic cell. The positive lattice mismatch values indicate that the polymer chain was stretched to match the Cu(111) slab one.

	l_0 (Å)	N_p	Model	Cu(111) super-cell	In-plane periodicity (Å^2)	Lattice mismatch (%)
PE	2.55	1	=	$(1x5)_h$	2.58x12.90	1.19
		10	⊥	$(4x4)_h$	10.32x10.32	
PAC	2.45	10	=	$(5x6)_h$	12.90x15.48	0.46
		10	⊥	$(5x6)_h$	12.90x15.48	
PET	10.90	1	=	$(4x2)_o$	10.32x8.94	3.09
		3	⊥	$(4x3)_o$	10.32x13.41	
PUR	16.90	1	=	$(4x3)_o$	10.32x13.41	0.12
		2	⊥	$(6x4)_h$	15.48x10.32	

4.4 Geometric relaxation of the interface models

Depending on the polymer, and in-plane or perpendicular interface, geometry optimisation of the Cu-polymer models (Fig. 4.3) leads to different relaxation of the Cu slab and loosening of the Cu lattice as quantified by the average cumulative 12 nearest-neighbors (NN) Cu-Cu distances for the Cu atoms in the slab (Fig. 4.4). In all cases, no barrier-less breaking of the bonds of the polymer chain and atom-transfer to interface Cu-atom during the geometry optimisation was observed.

In general, all the interface models considered induce loosening of the FCC Cu lattice. Not unexpectedly, the distortions for the in-plane models are larger than for the perpendicular ones. In line with expectations based on the larger hindrance of the phenyl group (in PUR and PET) with respect to $–CH_2–CH_2–$ (PE) and –CH=CH– (PAC) fragments, the computed loosening of the Cu lattice is largest for PUR and PET. Interestingly, the PAC-induced loosening of the Cu lattice is closer to PUR values than PE results. This result suggests a predominant role of the presence (or absence) of molecular π-conjugation (and ensuing Cu-organics charge-transfer) for the relaxation of the metal substrate. In the following I quantify the extent to which such an enhanced geometric relaxation directly correlates (or not) with the interface electronic and magnetic properties.

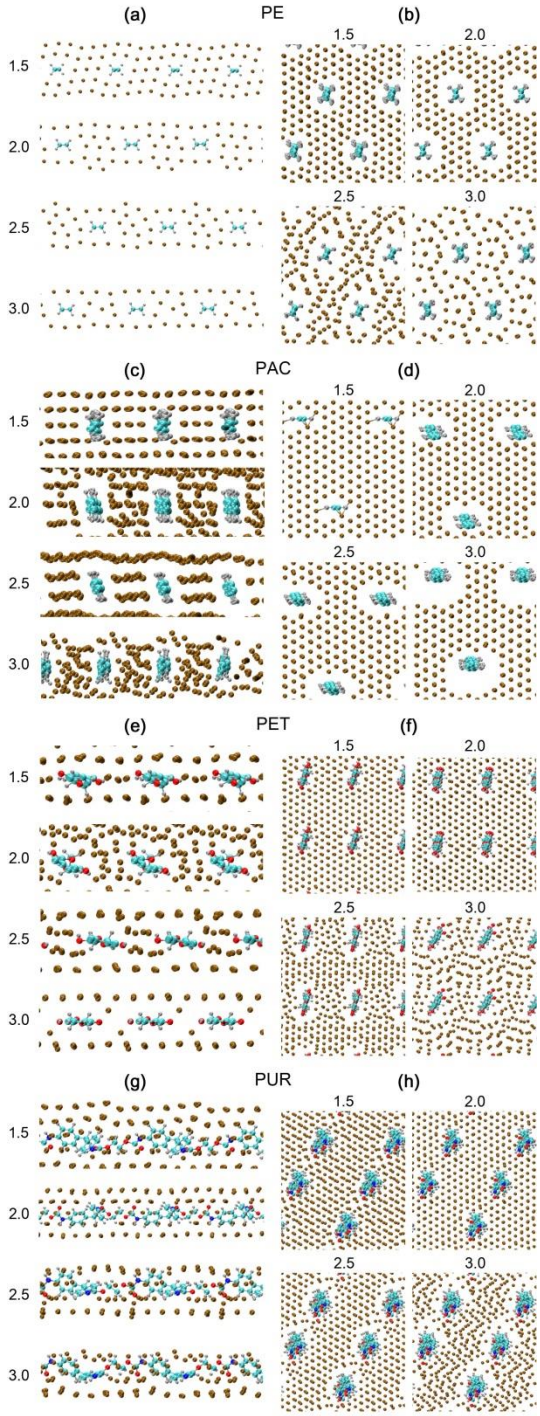

Figure 4.3: Optimised geometries for the considered in-plane (a, c, e, g) and perpendicular (b, d, f, h) models for the interface between Cu and PE (a, b), PAC (c, d), PET (e, f) and PUR (g, h) as a function of the initial Cu-polymer distance cut-off used. C: cyan, O: red, N: blue, H: silver, Cu: brown

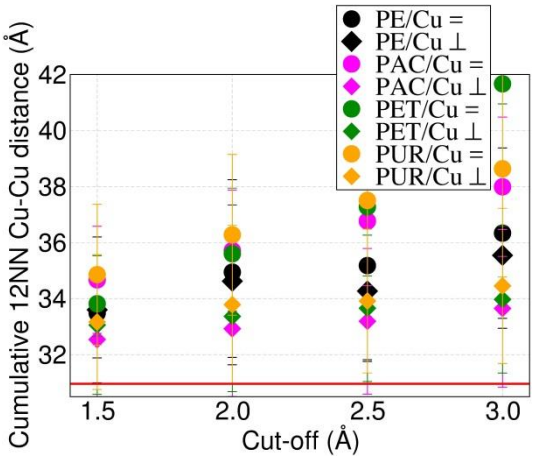

Figure 4.4: Polymer-induced loosening of the Cu lattice for the Cu-polymer interfaces considered as quantified by the sum of the 12 NN Cu-Cu distances in the optimised slabs. The horizontal red line marks the value of cumulative 12 NN Cu-Cu distances (30.962 Å) for optimised bulk FCC Cu (lattice parameter: 3.649 Å).

4.5 Electronic properties of the interface models

In spite of the substantial relaxation induced on the Cu-substrate by the polymer chain, all the interfaces are computed to be metallic and characterized by a well-defined *3d* band with an absolute Density of States (DOS) maximum at about 1.5 eV below E_F, as present for bulk FCC Cu (Fig. 4.5). Comparison between Cu and polymer-resolved PAW-projected DOS (PDOS), shown in Fig.4.6 and Fig. 4.7, indicates that the DOS at E_F [DOS(E_F)] is dominated by Cu states and that the interface relaxation leads to metallization (non-zero PDOS at E_F) for all the polymers. These findings are in qualitative agreement with the results for other interfaces between Cu and differently conjugated systems such as C_{60} [6], aC [7] and linear alkanes [28], suggesting that π-conjugation of the organics is not necessary for the creation of hybrid Cu-polymer delocalised metallic-states at the interface.

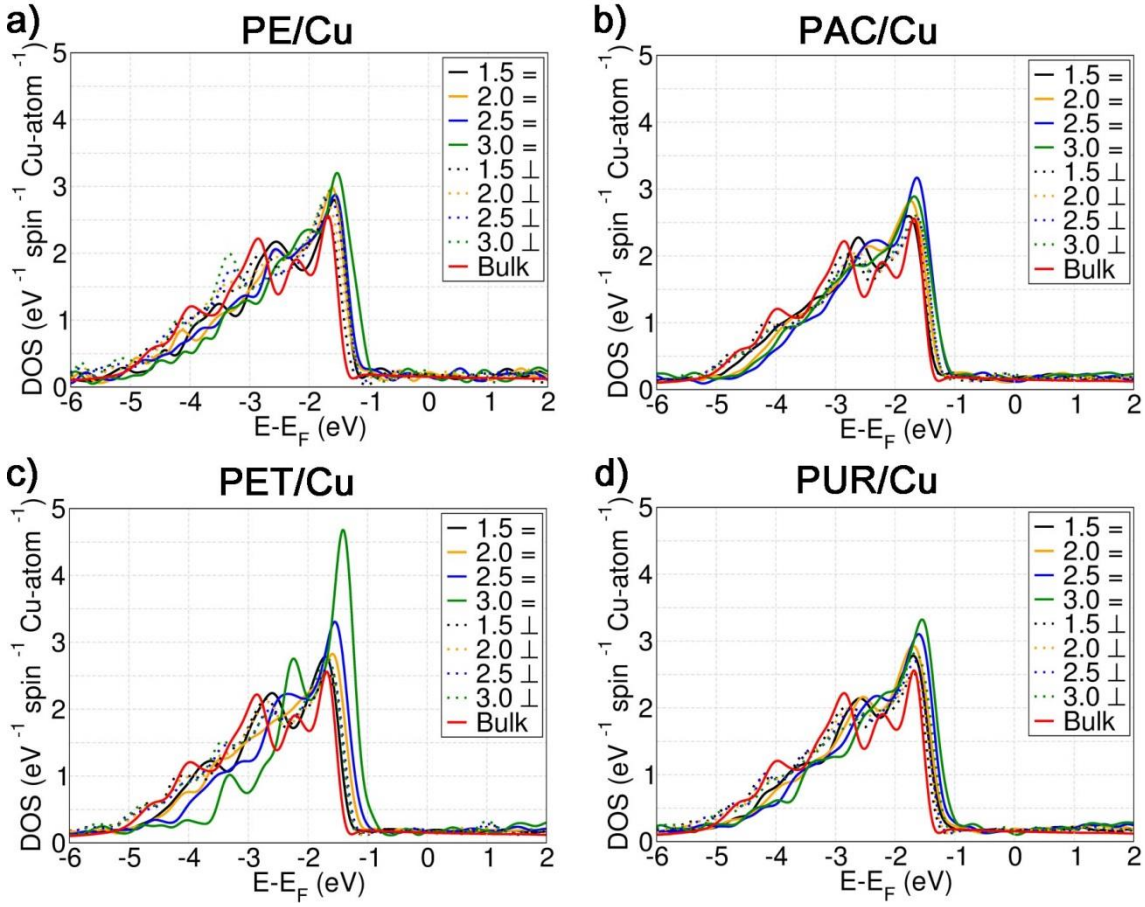

Figure 4.5: Computed Density of States (DOS) for the Cu-polymer interface models studied. All the systems present a well-defined *3d* band with an absolute Density of States (DOS) maximum at about 1.5 eV below E_F, as present for bulk FCC Cu. Furthermore, all the interfaces show a non-zero DOS at the Fermi level. Thus, all the interfaces are computed to be metallic.

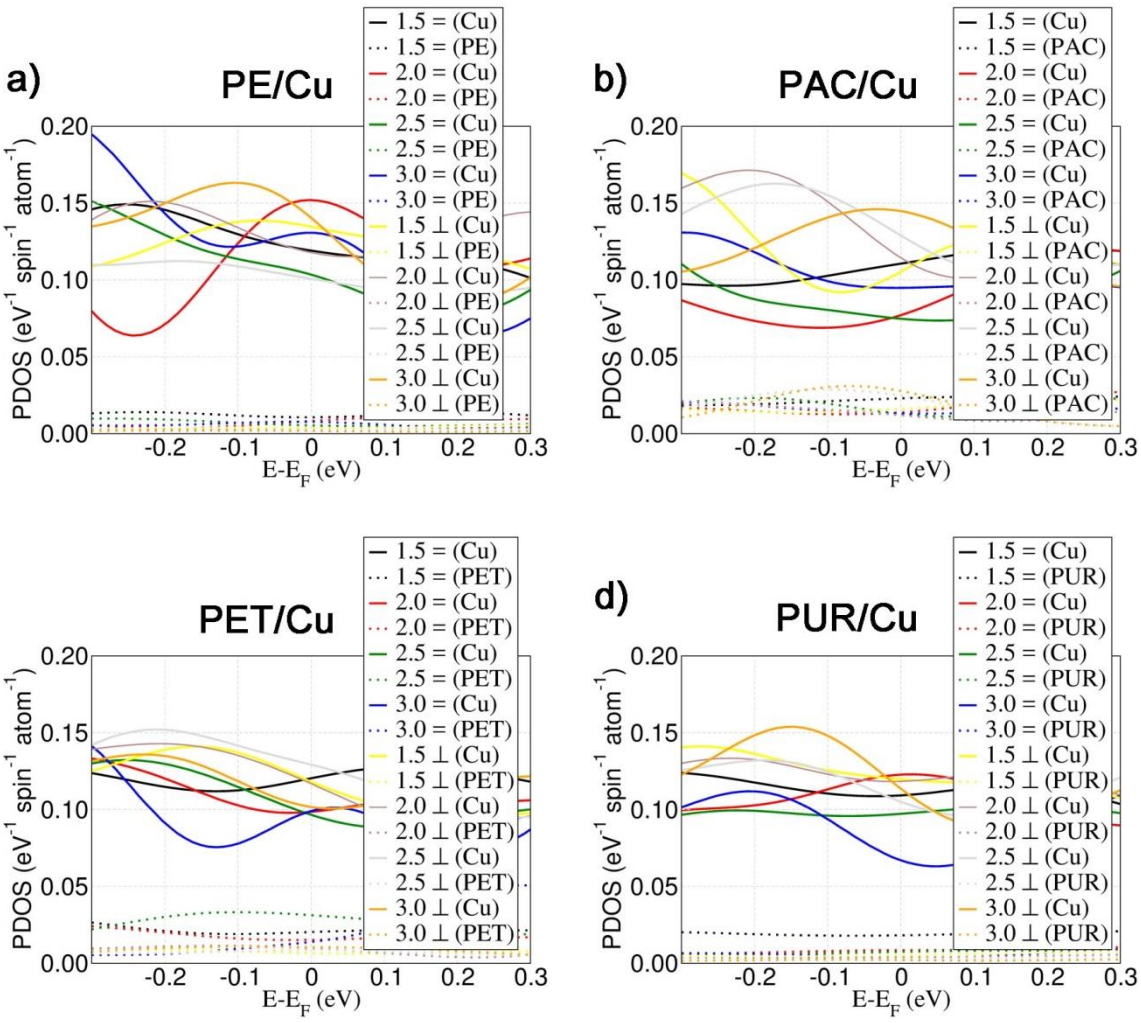

Figure 4.6: Cu (continuous) and organic (dotted) resolved atom-projected DOS (PDOS) for the Cu-polymer interface models considered. Larger polymer-projected PDOS(E_F) is observed for PAC, PET and PUR interfaces indicative of larger hybridisation between the Cu and these polymers in comparison to PE.

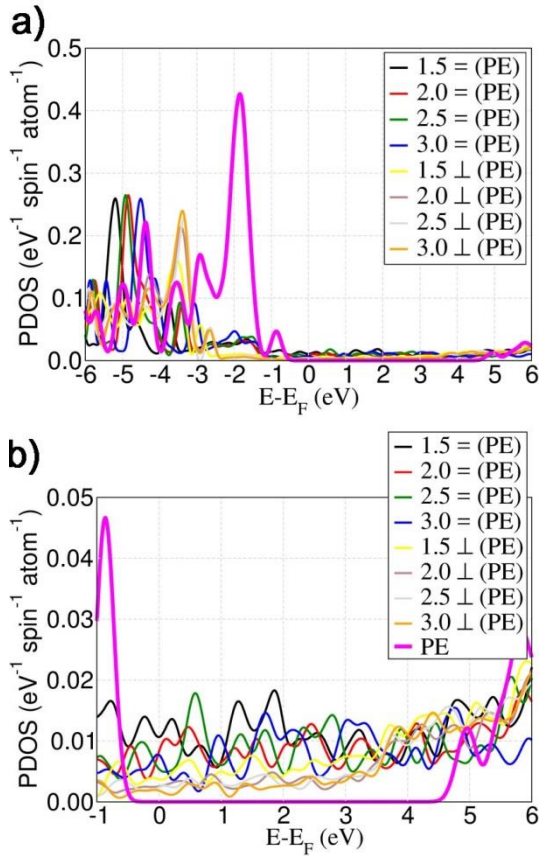

Figure 4.7: a) PE-resolved PDOS for one isolated PE chain (with a well-defined HOMO-LUMO gap) and the different Cu/PE interface models considered. **b)** Close up of the PDOS around the Fermi level (E-E_F=0 eV). In all cases, and regardless of the initial Cu-PE distance cut-off used to prepare the starting geometry, re-hybridisation and metallization [non-zero PDOS(E_F)] of the PE interfaced to Cu is evident.

Consistent with the larger hybridisation between the Cu and polymer modelled for PAC, PET and PUR by comparison to PE, leading to larger polymer-projected PDOS(E_F) for the former systems (Fig. 4.6). Bader charge analysis for the optimised models reveals a larger Cu → polymer electron transfer for the systems with π-conjugation (PAC, PET and PUR in Fig. 4.8).

Notably, the interfacial charge-transfer turns out to qualitatively correlate with the vertical electron affinity (EA) of the polymer chains, as first approximated by the position of the LUMO for the isolated chain with respect to the vacuum level. Thus, it appears the energy of the unrelaxed electron-acceptor level (as quantified by the vertical EA), rather than the relaxation of the system's electronic and nuclear degrees

of freedom after the electronic addition (adiabatic EA) is the dominant factor for the Cu-polymer interfaces considered here. With the exception of the in-plane PUR/Cu(=) interface-model prepared with the shortest initial cut-off (1.5 Å, Fig. 4.3h), the trend in Bader charge-transfer (PE < PUR < PET < PAC) follows qualitatively what expected on the basis of the vertical EA as first approximated by minus the energy of the LUMO level with respect to the vacuum (again PE < PUR < PET < PAC from Table 4.2). These results suggest that, at least for the Cu-polymer interfaces studied, trends in interfacial charge-transfer between different molecular systems may be effectively estimated based on the position of the LUMO level for the isolated organic. It consequently follows, again at least for the systems considered, that the different interface relaxation (PE < PAC < PUR ~ PET in Fig. 4.4) plays a secondary role with respect to the organic EA for the overall interface charge-transfer: larger interface relaxation (Fig. 4.4) does not directly correlate with larger charge-transfer at the interface.

Table 4.2: Computed vacuum-aligned LUMO energy for the isolated chains of the polymer considered (at their optimised periodicity).

System	**E_{LUMO} (eV)**
PE	-0.85
PAC	-3.68
PET	-3.28
PUR	-1.68

Before proceeding, it is worth nothing that, in spite of the substantial re-hybridisation leading to metallization of PE interfaced to Cu, the overall charge-transfer from the Cu substrate to PE in the in-plane models is less than 0.14 e in Fig. 4.8 (0.07 e per PE unit in the simulation cell). This result stems from the competition between Cu → organic donation and organic → Cu back-donation previously discussed for alkanes on metallic substrates such as Cu [28] or Co [9]. Here, it has to be noted that empty (Kohn-Sham) states for PE chains, as typically other saturated aliphatic molecules

(alkanes), tend to be localised mostly outside the molecular backbone, leading to accumulation of excess charge in the interstitial regions around the PE chain [21, 22, 29-31], an aspect that may have affected Bader partitioning [15] of the electronic charge at the Cu-PE interfaces.

In previous studies, the C–H bond weakening is shown to correlate with new adsorption-induced features in the unoccupied DOS [32]. In order to compute the changes in the geometric structure due to the interaction of PE upon adsorption on the Cu surface, the average computed C-H, C-C bond distances and C-C-C angles for PE in the Cu-PE interface models are shown in Table 4.3. In line with previous results in the literature [28], in spite of the minimal net charge-transfer, and the additional constraints induced by the use of infinitely periodic interface models, the Cu-PE re-hybridisation and ensuing metallization of the organic system is accompanied by an increase up to 1.5% (decrease up to 4%) of C-H (C-C) bond-distances and a parallel increase up to 3% in the C-C-C bond angles in PE (Table 4.3). These results are indicative of a partial $sp^3 \rightarrow sp^2$ re-hybridisation of the aliphatic chain upon interaction with Cu, as also evident by the dramatic change in PE-resolved DOS for all the Cu-PE interface models (Fig. 4.7).

Table 4.3: Average computed C-H (d_{CH}, Å), C-C (d_{CC}, Å) bond distances and C-C-C angles (θ_{CCC}, degrees) for PE in the Cu-PE interface models with standard deviation. Values for one isolated PE chain at the optimised periodicity are also reported for comparison.

		Average over all the PE atoms in the system		
Interface geometry	**Cut-off (Å)**	**d_{CC} (Å)**	**d_{CH} (Å)**	**θ_{CCC} (º)**
=	1.5	1.52 ± 0.00	1.12 ± 0.00	116.33 ± 0.00
	2.0	1.52 ± 0.00	1.12 ± 0.00	115.65 ± 0.00
	2.5	1.52 ± 0.00	1.12 ± 0.00	115.95 ± 0.00
	3.0	1.53 ± 0.00	1.12 ± 0.00	115.45 ± 0.00
⊥	1.5	1.52 ± 0.01	1.11 ± 0.01	114.46 ± 1.92
	2.0	1.52 ± 0.01	1.11 ± 0.01	113.65 ± 0.74
	2.5	1.52 ± 0.01	1.11 ± 0.01	113.85 ± 1.27
	3.0	1.53 ± 0.01	1.11 ± 0.01	113.69 ± 1.14
		Average over all the PE atoms in the Cu-slab		
⊥	1.5	1.51 ± 0.01	1.12 ± 0.01	114.89 ± 2.51
	2.0	1.52 ± 0.01	1.12 ± 0.01	114.09 ± 1.02
	2.5	1.51 ± 0.01	1.12 ± 0.01	114.17 ± 1.41
	3.0	1.51 ± 0.01	1.12 ± 0.01	114.33 ± 2.52
		Isolated PE chain at the optimised periodicity		
		1.53 ± 0.00	1.11 ± 0.00	113.18 ± 0.00

Finally, analysis of the computed Bader charge-transfer as a function of the loosening of the Cu lattice (Fig. 4.8b) reveals another correlation potentially useful when designing Cu-organic interfaces. For all the interface models considered, the Cu → organic charge-transfer decreases as the local coordination environment of the Cu atoms is expanded. Thus, contrary to the Cu-C_{60} case [6], increased interface relaxation and loosening of the Cu-lattice is found to hinder, rather than enhance, depletion of electronic charge at the Cu-substrate by the considered organics. This result indirectly suggests that strain on the π-system (larger for C_{60} than the considered, originally planar, PAC, PET and PUR) may play an important role for the interface relaxation and charge-transfer, an aspect worth of detailed investigation

in the future. In the following, I quantify to extent to which such a quantitatively different charge-transfer affects the emerging magnetic properties of the Cu-polymer interfaces.

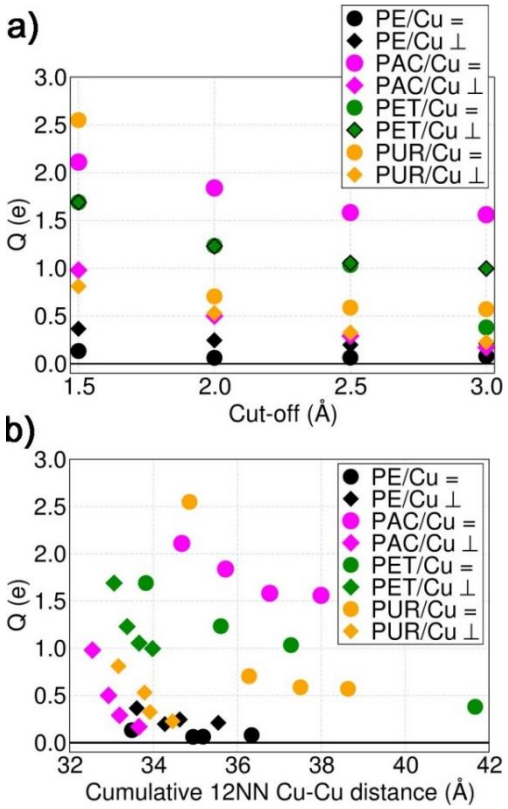

Figure 4.8: Computed Cu → polymer Bader charge transferred (Q, e) as a function of **a)** the initial Cu-polymer cut-off distance, and **b)** the cumulative 12 NN Cu-Cu distance in the optimized Cu-polymer interface models.

4.6 Magnetic properties of the interface models

The relaxed Cu-polymer interfaces are characterized by generally smaller band splitting (ΔE) and magnetic moments (m) with respect to bulk FCC Cu (Fig. A.1). The direct (inverse) contribution of these parameters to the approximated Stoner exchange integral (I_s, Chapter 2, Eq. 2.88) leads to scattering of the computed Cu-resolved I_S both above and below the bulk FCC Cu value, with largest values in the 1.1-1.3 eV range for all the different polymer considered, close and in cases above the largest value computed for as deposited ferromagnetic Cu-aC systems (I_s=1.25 eV) [7]. In line with results for Cu-C_{60} interfaces [6], the increase in I_S is not

localised at the immediate Cu-polymer interface but spread over the whole Cu-substrate. Contrary to results for Cu-C_{60} hybrids [6], but in agreement with simulations of the Cu-aC interfaces [7], no immediate correlation is found between the increase in I_S and the loosening of the Cu lattice as measured by the sum of the 12 NN Cu-Cu distances (Fig. A.2).

In general, Cu-substrate averaged I_S values turn out to be either minimally larger (less than 0.1 eV increase) or smaller than for bulk FCC Cu (Fig. 4.10a). An exception to this trend is the parallel Cu-PE interface prepared with an initial cut-off distance of 2.0 Å. For this system the average I_S value is nearly 0.2 eV higher than bulk FCC Cu, first revealing that, pending favourable interface relaxation, significant increase in I_S can be also produced by interfacing Cu with non π-conjugated organics such as PE. The non-monotonic, system-dependent change of the computed I_S as a function of initial cut-off (Fig. 4.10a) clearly indicates that relaxation of the interface under different geometrical constraints, as expected for Cu-samples of different crystallinity and homogeneity, can majorly affect the interfacial magnetic properties, answering one of the research questions behind the choice of the models.

With the exception of the in-plane (=) Cu-PAC (2.0 and 2.5 Å cut-off) and Cu-PUR (3.0 Å) systems, all the other interfaces result in a substantial increase (from over 20% to up to a factor of two) of the computed DOS(E_F) with respect to the bulk FCC value (Fig. 4.10b). Notably, among the in-plane models, the largest DOS(E_F) values are computed for Cu interfaced with PE, that completely lacks π-conjugation. These results clearly demonstrate that the presence of a π-system, and ensuing enhancement of the Cu → organics charge-transfer (Fig. 4.8) is not strictly necessary for enhancing the interfacial DOS(E_F): suitable interface relaxation and composition can also be effective to this end. It thus emerges that I_S and DOS(E_F), key quantities of the Stoner model of ferromagnetism (Chapter 2, Section 2.3.1), are i) differently sensitive to the composition and structure of the interface, and ii) not directly correlated at least for the systems considered (see also Fig. 4.9). The changes in the I_S are small compared to the Cu-bulk. On the other hand, as the value of the DOS(E_F) is substantial larger than the Cu-bulk for most of the considered system, there is an enhancement of the Cu magnetic hardening. Due to the simultaneous increase in both

I_S and DOS(E_F) the in-plane Cu-PE interface with a cut-off distance of 2.0 Å is found to lead to the largest I_S×DOS(E_F) product.

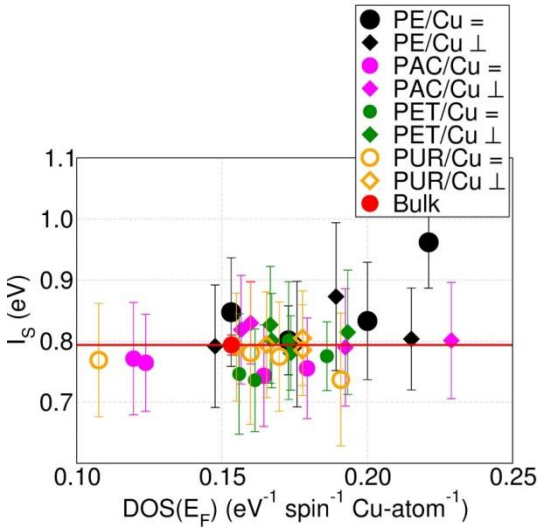

Figure 4.9: System-averaged I_S as a function of DOS(E_F) for the interface model considered. I_S and DOS(E_F) are evidently uncorrelated.

Notably, in spite of the reduced interface relaxation (Fig. 4.4) and charge-transfer (Fig. 4.8), the computed DOS(E_F) for the perpendicular (⊥) interface models turns out to be comparable (or noticeable larger in the case of PAC) with the value obtained for the parallel (=) system. It thus turns out that substantial increase of DOS(E_F) can be achieved also by relatively localised contacts between the Cu-substrate and the organic.

As shown in Fig. 4.10d, the combination of the differently altered I_S and DOS(E_F) leads to I_S×DOS(E_F) products generally larger than for bulk FCC Cu, indicative of magnetic hardening. The only exception to trend is represented by the in-plane interface between Cu and PAC, the system with the most extended π-conjugated system and the largest Cu → organic charge-transfer (Fig. 4.8). Further evidence of the non-immediate correlation between interface magnetic hardening and charge-transfer is provided by the fact that the I_S×DOS(E_F) products for the Cu-PE interface are comparable to those for π-conjugated polymers such as PET and PUR, in spite of the substantially different interfacial charge-transfer (Fig. 4.8).

Contrary to what was found in Ref. [6] for Cu-C_{60} interfaces, the largest computed $I_S \times DOS(E_F)$ does not appear to correlate with increased loosening of the Cu-lattice as measured by the cumulative 12 NN Cu-Cu distance (Fig. 4.10d). Additionally, for the Cu-PUR interface, the computed $I_S \times DOS(E_F)$ is found to actually decrease as the Cu lattice is loosened.

Perhaps surprisingly, due to the simultaneous increase in both I_S (Fig. 4.10a) and $DOS(E_F)$ (Fig. 4.10b) the in-plane Cu-PE interface with a cut-off distance of 2.0 Å is found to lead to the largest $I_S \times DOS(E_F)$ product (0.21 $spin^{-1}$ $atom^{-1}$), larger than what computed at the same level of theory for the annealed Cu-aC interface (0.19 $spin^{-1}$ $atom^{-1}$) measured to be ferromagnetic in Ref. [7]. Non-collinear fixed-spin DFT simulations of this Cu-PE interface points out minimal changes ($<10^{-7}$ eV/atom) in the computed MAEs, that remain consistently in the order of 10^{-6} eV/atom, in line with the weak shape anisotropies measured for ferromagnetic Cu-C_{60} interfaces (~10^{-6} eV/Cu-atom) [6].

It thus transpires that, in spite of the negligible charge-transfer (Fig. 4.8), the PE chain is nevertheless capable, via interface relaxation and the ensuing re-hybridisation with the metal (Fig. 4.6 and Fig. 4.7), of inducing magnetic hardening of Cu competitive to that observed for interfaces with substantially larger electron-depletion of Cu. Analysis of the computed Cu-resolved I_S values as a function of the atomic Bader charges (Fig. A.3) rules out any direct correlation between atomic charges on Cu atoms and ensuing magnetic hardness as quantified by the I_S parameter, strengthening the conclusion that rather than charge-transfer, it is the Cu-organic re-hybridisation to be crucial for the interface magnetic hardening. As the data for the Cu-PE interface (Fig. 4.8) and published result for alkanes on transition metals [9, 28] indicate, important interfacial re-hybridisation, leading to emergence of interface electronic states of desirable properties [in the present case an increased $I_S \times DOS(E_F)$ due to joint or separate enhancement of I_S and $DOS(E_F)$], may take place also without substantial net charge-transfer between the metal and the organic. The computed strong magnetic hardening for the planar (2.0 Å cut-off) and perpendicular (3.0 Å) Cu-PE interface models in Fig. 4.10d, together with the presence of empty “surface” states (amenable to PBE simulation [22] as done here)

with a typical vacuum decay length of 3.0 Å for periodic PE chains [22, 33], altogether suggest that re-hybridisation of molecular (empty) surface states with a metal can also be effective in tuning the interface magnetic properties.

These results, if not contrast, at least significantly add to existing suggestions that charge-transfer from the metal to the π-conjugated molecule is necessary for magnetic hardening and the emergence of ferromagnetic ordering at Cu-organics interfaces [6-8]. Although results about the unnecessity of π-conjugation for the creation of highly spin-polarized states at the interface between a ferromagnetic metal and an organic molecule have been previously published [9], to the best of my knowledge, these are the very first insights into i) negligible magnetic hardening at the interface between Cu and a completely π-conjugated substrate (PAC), and ii) the possibility of magnetic hardening at the interface between a transition metal and a non π-conjugated molecule. The comparable magnetic hardening between the Cu-aC (measured to be ferromagnetic in Ref. [7]) and Cu-PE interfaces prompts further research in the overlooked possibilities offered by (non π-conjugated) aliphatic molecules for promoting emergent magnetism at metal-organic interfaces.

The computed decrease in Cu magnetic hardening going from C_{60} to aC [6-8], to the π-conjugated polymers considered here inevitably raises the question as to whether optimal re-hybridisation between Cu and π-conjugated organics towards enhancement of interfacial magnetism requires fine-tuning of the strain of the π-system on the organics. Research to answer to this question is presented in Chapter 5 and 6.

Finally, the computed substantial increase of the $I_S \times DOS(E_F)$ products for discontinuous contact between the organic and the Cu (the largest cut-off perpendicular PE and PAC interfaces in Fig. 4.10c) is also worth of mention. The results for these systems suggest that, depending on the nature of the organic, non-homogenous interfaces (as in the perpendicular models) may also be effective in inducing interface re-hybridisation and emergence of magnetic hardening, opening up for the study of less regular or more complex multi-layer depositions than pursued so far.

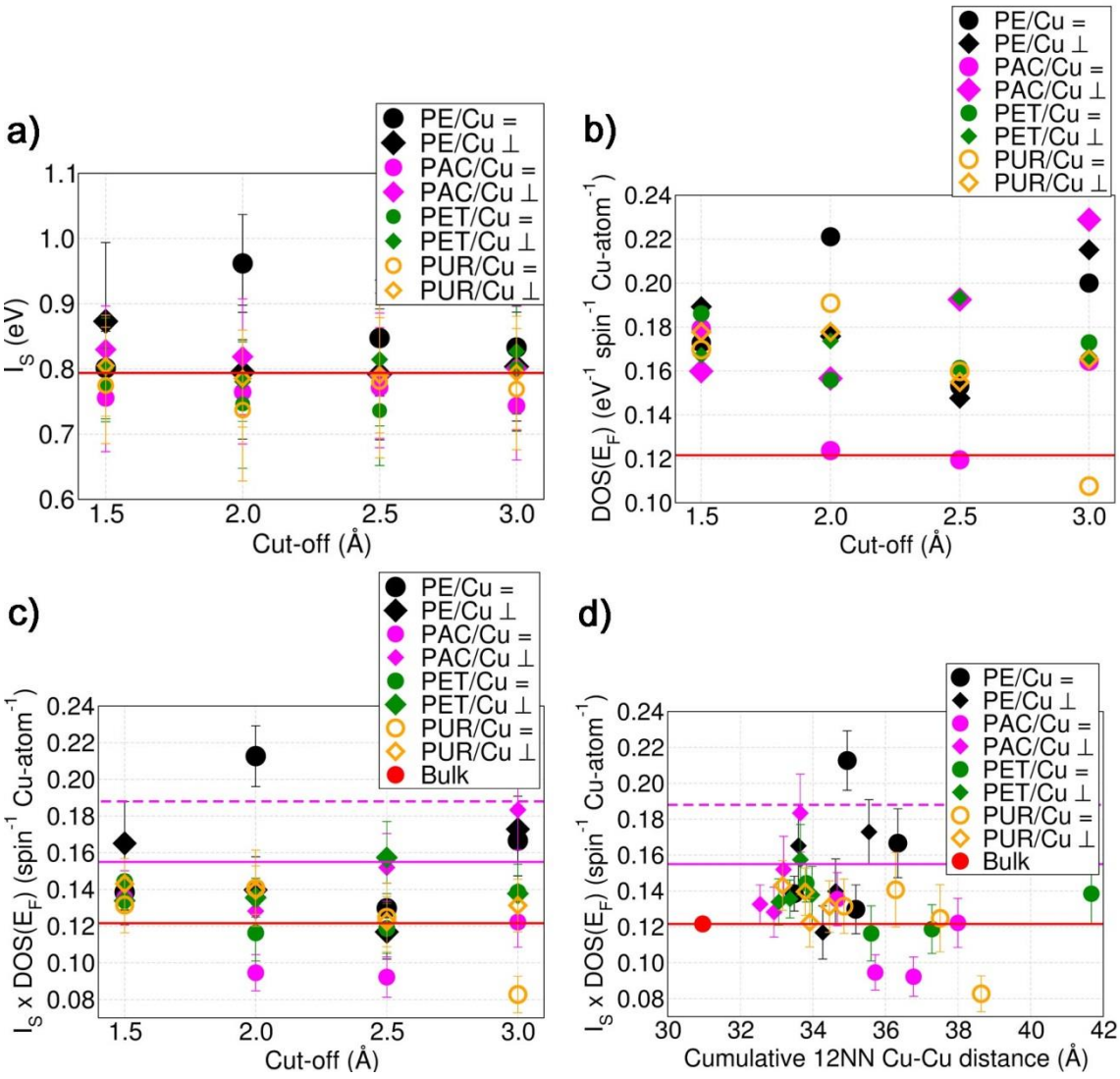

Figure 4.10: Average **a)** Stoner exchange integral (I_s), **b)** Density of States at the Fermi level [$DOS(E_F)$] and **c)** $I_S \times DOS(E_F)$ product for the Cu-polymer interface models as a function of the initial cut-off used. **d)** Average $I_S \times DOS(E_F)$ product as a function of the average cumulative 12 NN Cu-Cu distance in the optimised models. The horizontal red line marks the values for optimised bulk FCC Cu. The horizontal continuous (0.15 $spin^{-1}$ $atom^{-1}$) and dashed (0.19 $spin^{-1}$ $atom^{-1}$) magenta lines in c)-d) mark the largest computed $I_S \times DOS(E_F)$ product at the same level of theory for interfaces between Cu and as deposited (1.7 gr/cm^3) and annealed (2.3 gr/cm^3) aC measured to be ferromagnetic in Ref. [7].

As shown in Fig. 4.11 no direct correlation is found between the $I_S \times DOS(E_F)$ product and the ratio between the Projected Density of States at the Fermi level of carbon atoms [$PDOS_c(E_F)$] over the PDOS of Cu atoms [$PDOS_{Cu}(E_F)$]. The larger charge-transfer for systems composed by PAC and in-plane PET (Fig. 4.8) result in larger $PDOS_c(E_F)$ / $PDOS_{Cu}(E_F)$ ratio. Thus, although larger charge-transfer leads to increase of $PDOS_{Cu}(E_F)$, and of $PDOS_c(E_F)$ / $PDOS_{Cu}(E_F)$, it is found not directly enhance the magnetic properties of the interface, consistent with the results shown in Appendix A Fig. A.3.

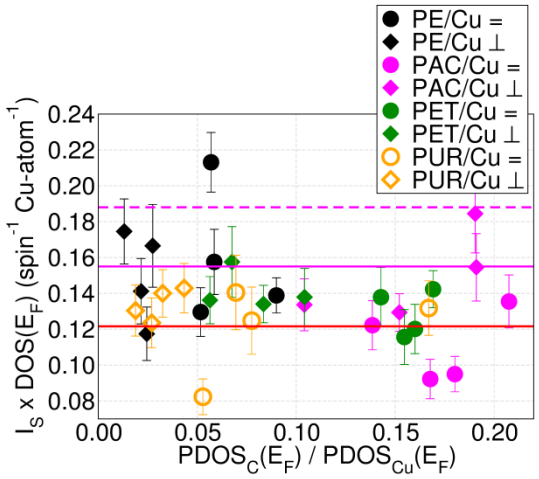

Figure 4. 11: Average $I_S \times DOS(E_F)$ product as a function of the ratio between the Projected Density of States at the Fermi level for the carbon [$PDOS_C(E_F)$] and Cu [$PDOS_{Cu}(E_F)$] atoms. The horizontal red line marks the values for optimised bulk FCC Cu. The horizontal continuous (0.15 $spin^{-1}$ $atom^{-1}$) and dashed (0.19 $spin^{-1}$ $atom^{-1}$) magenta lines mark the largest computed $I_S \times DOS(E_F)$ product at the same level of theory for interfaces between Cu and as deposited (1.7 gr/cm^3) and annealed (2.3 gr/cm^3) aC measured to be ferromagnetic in Ref. [7].

4.7 Conclusion

In summary, DFT simulations have been used to investigate the role molecular π-conjugation for the magnetic hardening of Cu-organics interfaces. Analysis of the simulations for several models of the interfaces between Cu and differently π-conjugated polymers, namely polyethylene (PE), polyacetylene (PAC), polyethylene terephthalate (PET) and polyurethane (PUR) indicate that:

i) In spite of the substantially different, polymer-dependent, geometry relaxation, all the interfaces studied lead to metallization of the organic system.

ii) Organics with larger vertical electron affinity (EA) leads to larger charge-transfer when interfaced with Cu. This result suggests a secondary role for the interface relaxation and, pending further validation on a more extended set of systems, that the EA of the isolated molecule may be conveniently used in designing of charge-transfer at Cu-organics interfaces. The Cu → organic charge-transfer is found to be consistently suppressed by increase in the interfacial relaxation or loosening of the Cu lattice.

iii) At least for the systems studied, charge-transfer is found *not* to directly correlate with the interfacial magnetic hardening. The system with the most extended π-conjugation and largest interfacial charge-transfer (PAC) leads to the smallest magnetic hardening. Magnetic hardening appears to be governed by the details of the electronic re-hybridisation with the metal. The precise role of strain in the π-system of the organic for such re-hybridisation remains to be quantified and will be investigated in Chapter 5 and 6.

iv) Depending on the interfacial relaxation, re-hybridisation between Cu and vacuum decaying empty states of the organic, as present in PE, are found to be effective in inducing interfacial magnetic hardening comparable with or larger than Cu-amorphous carbon systems recently measured to develop room-temperature ferromagnetic ordering [7].

It thus turns out the neither the presence of the organic interface, molecular π-conjugation nor substantial charge-transfer may be strictly needed for magnetic hardening of Cu-substrates, albeit combination of the present results and available experimental data suggests that maximization of the effect does require both (strained) π-conjugation and substantial charge-transfer [6, 7]. These results prompt for further research in the, to date overlooked, possibilities of non π-conjugated molecules with empty surface states and maximally strained π-systems for magnetic hardening and emergent magnetism at transition-metal-organic interfaces. In the

remaining of the Thesis I will focus on the role of strain in the π-conjugated organic for the magnetic hardening of molecular interfaces with Cu.

4.8 Reference

1. Carmeli, I., et al., *Magnetism induced by the organization of self-assembled monolayers.* The Journal of Chemical Physics, 2003. **118**(23): p. 10372-10375.
2. Vager, Z. and R. Naaman, *Bosons as the origin for giant magnetic properties of organic monolayers.* Physical Review letters, 2004. **92**(8): p. 087205.
3. Crespo, P., et al., *Permanent magnetism, magnetic anisotropy, and hysteresis of thiol-capped gold nanoparticles.* Physical Review letters, 2004. **93**(8): p. 087204.
4. Hernando, A., P. Crespo, and M. Garcia, *Origin of orbital ferromagnetism and giant magnetic anisotropy at the nanoscale.* Physical Review letters, 2006. **96**(5): p. 057206.
5. Naaman, R. and Z. Vager, *Cooperative electronic and magnetic properties of self-assembled monolayers.* MRS bulletin, 2010. **35**(6): p. 429-434.
6. Al Ma'Mari, F., et al., *Beating the Stoner criterion using molecular interfaces.* Nature, 2015. **524**(7563): p. 69-73.
7. Al Ma'Mari, F., et al., *Emergent magnetism at transition-metal–nanocarbon interfaces.* Proceedings of the National Academy of Sciences, 2017. **114**(22): p. 5583-5588.
8. Raman, K.V. and J.S. Moodera, *Materials chemistry: A magnetic facelift for non-magnetic metals.* Nature, 2015. **524**(7563): p. 42-43.
9. Djeghloul, F., et al., *High Spin Polarization at Ferromagnetic Metal–Organic Interfaces: A Generic Property.* The journal of physical chemistry letters, 2016. **7**(13): p. 2310-2315.
10. Schwarz, K. and P. Mohn, *Itinerant metamagnetism in YCO2.* Journal of Physics F: Metal Physics, 1984. **14**(7): p. L129.

11. Grimme, S., et al., *A consistent and accurate ab initio parametrization of density functional dispersion correction (DFT-D) for the 94 elements H-Pu.* The Journal of Chemical Physics, 2010. **132**(15): p. 154104.
12. Kresse, G. and J. Furthmüller, *Efficient iterative schemes for ab initio total-energy calculations using a plane-wave basis set.* Physical Review B, 1996. **54**(16): p. 11169.
13. Perdew, J.P., K. Burke, and M. Ernzerhof, *Generalized gradient approximation made simple.* Physical Review letters, 1996. **77**(18): p. 3865.
14. Methfessel, M. and A. Paxton, *High-precision sampling for Brillouin-zone integration in metals.* Physical Review B, 1989. **40**(6): p. 3616.
15. Henkelman, G., A. Arnaldsson, and H. Jónsson, *A fast and robust algorithm for Bader decomposition of charge density.* Computational Materials Science, 2006. **36**(3): p. 354-360.
16. Raman, K.V., et al., *Interface-engineered templates for molecular spin memory devices.* Nature, 2013. **493**(7433): p. 509.
17. Callsen, M., et al., *Magnetic hardening induced by nonmagnetic organic molecules.* Physical Review letters, 2013. **111**(10): p. 106805.
18. Ueno, N., et al., *Low-energy electron transmission and secondary-electron emission experiments on crystalline and molten long-chain alkanes.* Physical Review B, 1986. **34**(9): p. 6386.
19. Dudde, R. and B. Reihl, *Complete electronic structure of oriented films of hexatriacontane.* Chemical Physics letters, 1992. **196**(1): p. 91-96.
20. Bloor, D., *Correlation of experimental and theoretical electron band energies of polyethylene.* Chemical Physics Letters, 1976. **40**(2): p. 323-325.
21. Serra, S., et al., *Interchain electron states in polyethylene.* Physical Review B, 2000. **62**(7): p. 4389.
22. Righi, M., et al., *Surface states and negative electron affinity in polyethylene.* Physical Review letters, 2001. **87**(7): p. 076802.
23. Demir, P. and F. Akman, *Molecular structure, spectroscopic characterization, HOMO and LUMO analysis of PU and PCL grafted onto PEMA-co-PHEMA with DFT quantum chemical calculations.* J. Mol. Struct., 2017. **1134**: p. 404-415.

24. Rajopadhye, N. and S. Bhoraskar, *Ionization potential and work function measurements of PP, PET and FEP using low-energy electron beam.* J. Mater. Sci. Lett., 1986. **5**(6): p. 603-605.
25. Horný, L.u., et al., *What Is the Nature of Polyacetylene Neutral and Anionic Chains HC2 n H and HC2 n H-(n= 6− 12) That Have Recently Been Observed?* Journal of the American Chemical Society, 2002. **124**(20): p. 5861-5864.
26. Dissado, L.A. and J.C. Fothergill, *Electrical degradation and breakdown in polymers*. Vol. 9. 1992: IET.
27. Pai, W.W., et al., *Optimal electron doping of a C 60 monolayer on Cu (111) via interface reconstruction.* Physical Review letters, 2010. **104**(3): p. 036103.
28. Öström, H., et al., *Orbital rehybridization in n-octane adsorbed on Cu (110).* The Journal of Chemical Physics, 2003. **118**(8): p. 3782-3789.
29. Cubero, D., N. Quirke, and D.F. Coker, *Electronic transport in disordered n-alkanes: From fluid methane to amorphous polyethylene.* The Journal of Chemical Physics, 2003. **119**(5): p. 2669-2679.
30. Cubero, D., N. Quirke, and D.F. Coker, *Electronic states for excess electrons in polyethylene compared to long-chain alkanes.* Chemical physics letters, 2003. **370**(1): p. 21-25.
31. Wang, Y., et al., *Single electron states in polyethylene.* The Journal of Chemical Physics, 2014. **140**(15): p. 154902.
32. Witte, G., et al., *Damping of molecular motion on a solid substrate: evidence for electron-hole pair creation.* Physical Review letters, 1998. **80**(1): p. 121.
33. Echenique, P. and J. Pendry, *Theory of image states at metal surfaces.* Prog. Surf. Sci., 1989. **32**(2): p. 111-159.

Chapter 5

The role of fullerene-curvature and strain of the π-system for the magnetic hardening at Cu-fullerene interfaces

Abstract

This Chapter investigates the role of the fullerene-curvature, and ensuing strain on the molecular π-system, for the magnetic hardening at Cu-fullerene interfaces. Different models of interfaces between Cu(111) slabs and several fullerenes of different curvature and electron-accepting properties (C_{20}, C_{30}, C_{60}) are investigated to establish the link, if any, between curvature of the molecular system and interfacial magnetic hardening as well as the dependence of the computed results on the initial geometry of the interface model. Contrary to earlier suggestions, the simulations indicate that maximisation of the Cu → fullerene charge-transfer does not maximise the interfacial magnetic hardening. The largest magnetic hardening is computed for those Cu-C_{60} interfaces with reduced charge-transfer. Analysis of the role of the fullerene curvature for the emergent interfacial magnetic properties indicates that slightly strained π-systems, as present on C_{60}, are to be preferred to strongly strained ones (as present in C_{20} and C_{30}) in order to maximise the interfacial magnetic hardening. Finally, comparison of the results for interface-models prepared with the same fullerene in initial different geometry indicates that fine details in the atomic structure of the intimate Cu-fullerene interface can non-negligibly affect the interface re-hybridisation and emerging magnetic properties.

5.1. Introduction

Molecular interfaces offer the possibility of tuning the magnetic properties of transition metals, potentially enabling creation of low-cost alternative magnetic system. As summarised in Chapter 1, the charge-transfer between C_{60} and ferromagnetic metals can modify the spin-polarisation and the magnetic properties of the interface [1, 2]. The additional interactions between the metallic surface and the molecule alter the electronic structure of the molecule-substrate interface compared to their isolated electronic structure (see Fig. 1.7), causing electronic re-hybridisation. Moreover, re-hybridisation between metals and molecules can also be used to promote magnetism from systems originally non-magnetic [2, 3].

Available experimental data indicate a (over 40%) stronger magnetization of Cu-C_{60} interfaces [4] with respect to those between Cu and amorphous carbon (aC) [1]. However, the results presented in Chapter 4 for π-conjugated system of different vertical EA and electron-accepting propensity, suggest that interfacial magnetic hardening is not directly correlated with the Cu → organic charge transfer. Combination of these results indirectly suggests that the strain of the π-system may play a critical role in tuning the interfacial re-hybridization and the resulting magnetic hardening. This aspect is investigated in the present Chapter by studying the interfaces with Cu of different fullerenes (C_{20}, C_{30} and C_{60}) with different curvature, thence strain of the π-system.

In addition, as the key parameters of the Stoner theory of itinerant magnetism (see Chapter 2, Section 2.3), namely the Density of States at the Fermi Energy [DOS(E_F)] and the Stoner exchange parameter (I_S), can strongly depend on the interface structure [5, 6], this Chapter explores also the role of the initial geometry and fullerene adsorption site for the magnetic hardening at Cu-interfaces. To this end, an exhaustive screening of all the possible high-symmetry adsorption sites on a Cu(111) slab for the considered fullerenes is presented. The dependence of the computed magnetic hardening on the initial geometry is analysed and discussed.

5.2 Computational details

The calculations were performed within the framework of Projected-Augmented Wave (PAW) Density Functional Theory (DFT) as implemented in the VASP package [7]. A generalized gradient approximation, as parameterized in the PBE functional [8], was used as for the exchange-correlation (XC) functional. The plane wave cut-off was set to 400 eV.

Structural relaxation of the different interfaces was carried out using a convergence criterion of 0.03 eV $Å^{-1}$ on the atomic forces. The k-point sampling grid for surface Brillouin zone sampling was defined based on the convergence test for bulk FCC Cu presented in Chapter 3, Section 3.2.3, and scaled according to the in-plane size of the fullerenes/Cu(111)-4x4 interface systems. The simulation cell was periodic along the x and y directions, with a 15 Å vacuum buffer along the z-direction. The total charge density was computed using Bader charge scheme [9].

Due to the computed non-magnetic ground-state for all the models studied, atom-resolved approximations to the Stoner exchange integral (I_s, see Chapter 2, Section 2.3) were calculated by enforcing a magnetic moment of 0.1 μ_B/Cu-atom via fixed spin-moment DFT [10].

5.3 Interface models

To investigate the influence of the Cu-lattice loosening, charger transfer and strain of the π-system, as quantified by the fullerene pyramidalization angle, on the interfacial magnetic properties, different interfaces made of FCC Cu and fullerenes with different volume and electron-accepting properties were prepared. The fullerenes examined are the C_{60} Buckminsterfullerene, the most studied fullerene since it was discovered in 1985 [11], and the two smallest fullerenes reported in the literature: C_{20} [12] with I_h symmetry, and C_{30} with C_{2v} symmetry [13] whose structures are shown in Fig. 5.1. Since both the C_{20} and C_{30} present several isomers, to contain the computational cost, I focussed on the lowest energy ones only i.e. C_{20} in the I_h symmetry and C_{30} in the C_{2v} symmetry [14].

The experimental electron affinity (EA), inclusive of structural and electronic relaxation after the electron addition, for C_{20} and C_{60} is 2.25 [12] and 2.7 eV [15], respectively. To the best of my knowledge, no experimental EA has been reported for C_{30} fullerenes. Based on these results and on the evidenced correlation between (vertical) EA of the organic and Cu → organics charge-transfer (Ref. [16] and Chapter 3, Section 3.5), the expectation, to be verified against the results for the relaxed interface models, is that the charge-transfer from Cu to the C_{20} should be smaller than for the C_{60}.

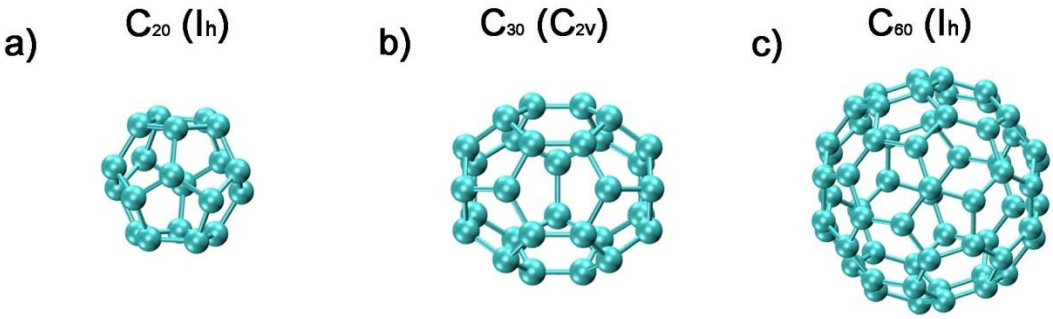

Figure 5.1: Molecular structure for the considered fullerenes. **a)** C_{20} (I_h), **b)** C_{30} (C_{2v}) and **c)** C_{60} (I_h).

To study the influence of the fullerene adsorption geometry on the magnetic properties of Cu-fullerene interfaces, all the four high-symmetry adsorption sites on a model five–layer Cu(111)-4x4 slab (10.32×10.32 $Å^2$ in-plane periodicity) were accounted for: top, bridge, hcp and fcc (see Fig. 5.2a). In each case, the in-plane (xy) projection of the centre of mass (CM) of the molecule was placed on these different high-symmetry adsorption sites. Given the different volume of the fullerenes considered, and for more straightforward comparison of the results, in all cases only half of the fullerene was inserted into the Cu(111) slab. Thus, the interface-models were initially prepared by placing the fullerene CM at the xy coordinates of the (top, bridge, hcp, fcc) site and at the z-coordinate of the topmost Cu layer (see Fig. 5.2b).

As for the polymer interface considered in Chapter 4, to include the effects of differently constrained optimisation of the Cu-fullerene interfaces on the emerging

magnetic properties, different models were prepared for each interface geometry and fullerene using several cut-off's (1.5, 2.0 and 2.5 Å) on the initial shortest Cu-fullerene distance. No Cu atom was present inside the fullerenes.

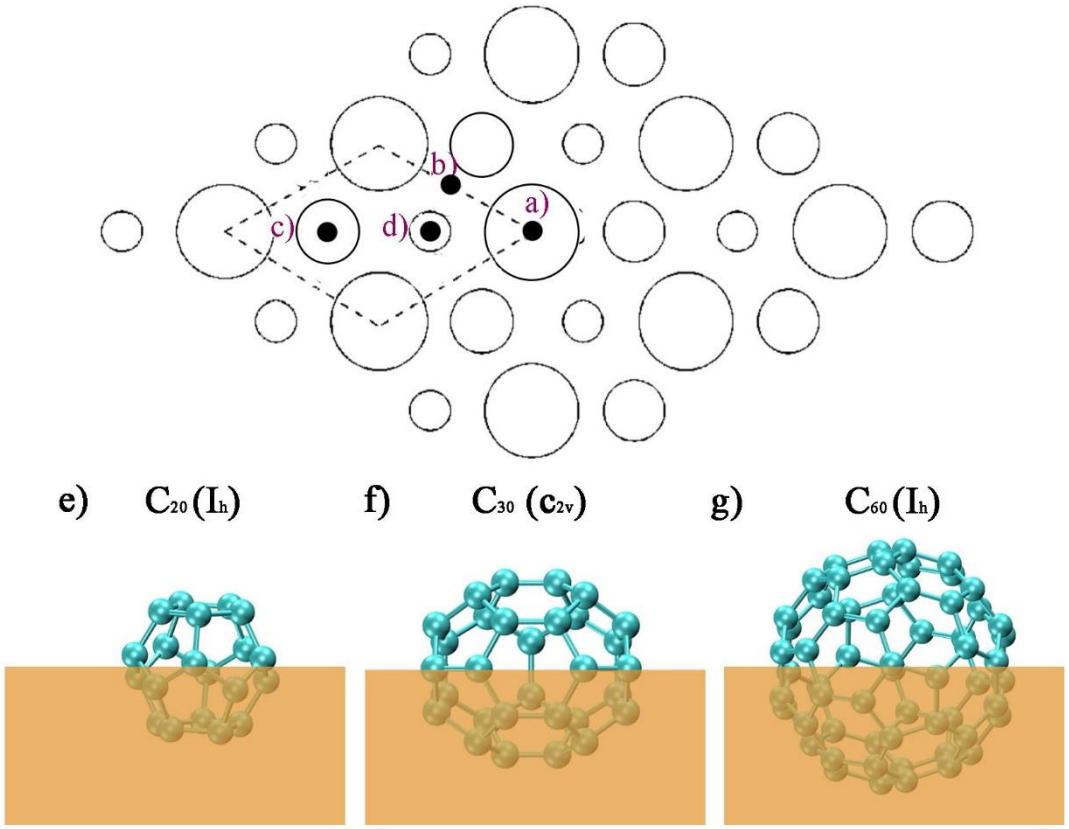

Figure 5.2: Top: schematic top view of the FCC Cu(111) surface. The first, second and third layer of Cu atoms are indicated by large, middle and small circles, respectively. The full black circles denote the initial adsorption geometries screened for each considered fullerene: a) top, b) bridge, c) hcp and d) fcc sites. **Bottom**: scheme of partial insertion of the fullerenes into the Cu(111)-4x4 slab.

5.4. Geometric relaxation of the interface models

The optimised structure for the different Cu-fullerene interface-models considered is shown in Fig. 5.3. It is found that the interface relaxation and loosening of the Cu lattice, as quantified by the by the average cumulative 12 nearest-neighbours (NN) Cu-Cu distances for the Cu atoms in the slab (Fig. 5.4), is larger for insertion of C_{60}, probably due to a too small extent of the Cu(111)-4x4 slab, leading to an excessively

constrained system. We leave computation demanding clarification of this aspect to future work.

For the smallest fullerene studied (C_{20} and C_{30}), the dependence of the Cu-lattice loosening on the initial adsorption site result to be smaller than on the initial cut-off distance used to prepared the models. Conversely, for C_{60} the trend is less clear with the two factors (initial cut-off and adsorption sites) being more closely related. Depending on the initial adsorption site for C_{60}, comparable Cu-lattice loosening is recovered in systems prepared with different initial Cu-C_{60} cut-off.

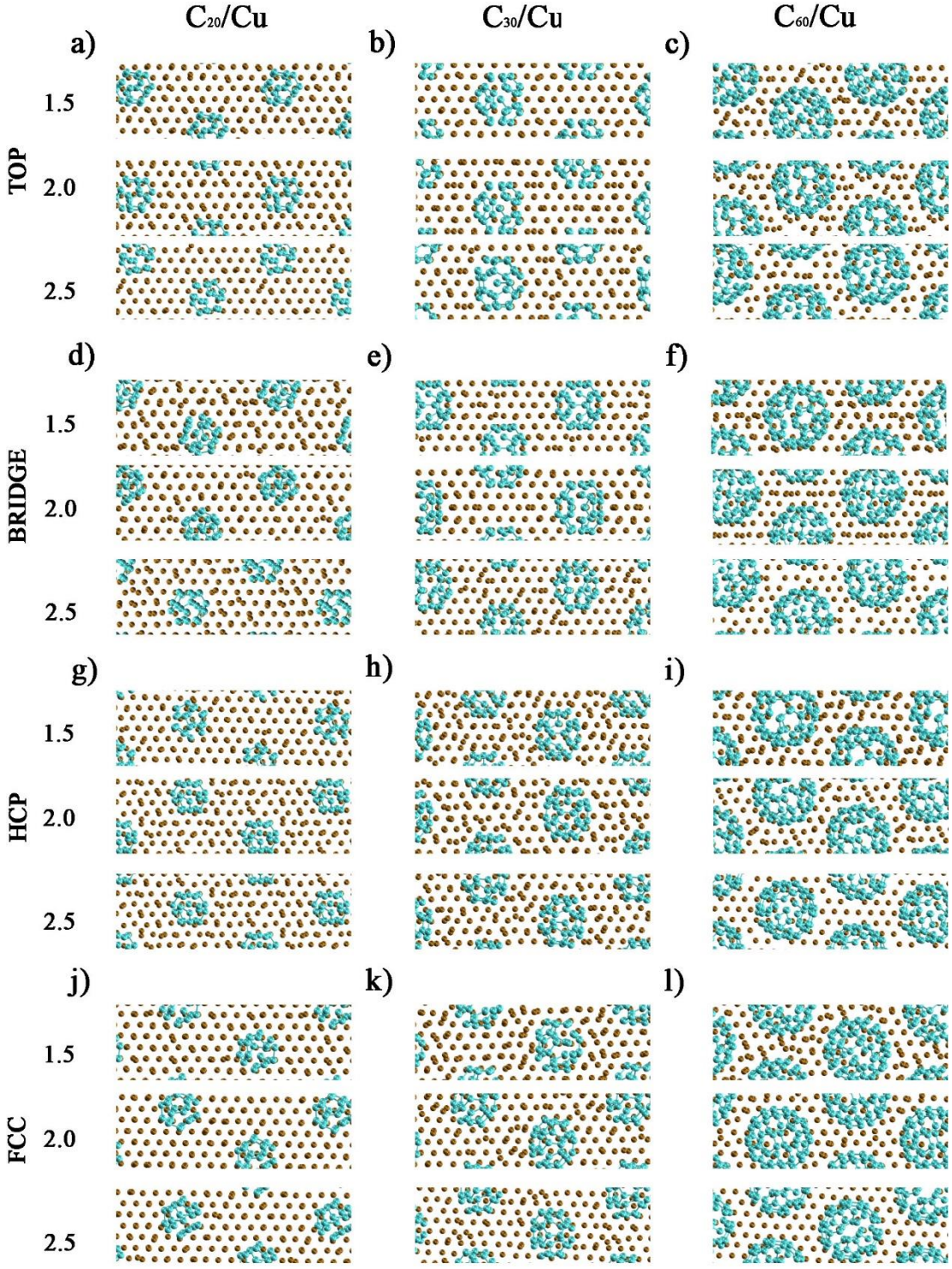

Figure 5.3: Top view of the optimised atomic structure of the considered interfaces models between C_{20} (top: **a**, bridge: **d**, hcp: **g**, fcc: **j**), C_{30} (top: **b**, bridge: **e**, hcp: **h**, fcc: **k**) and C_{60} (top: **c**, bridge: **f**, hcp: **i**, fcc: **l**) and Cu(111)-4x4 as a function of the initial Cu-fullerene cut-off distance (1.5, 2.0, and 2.5 Å) and adsorption site.

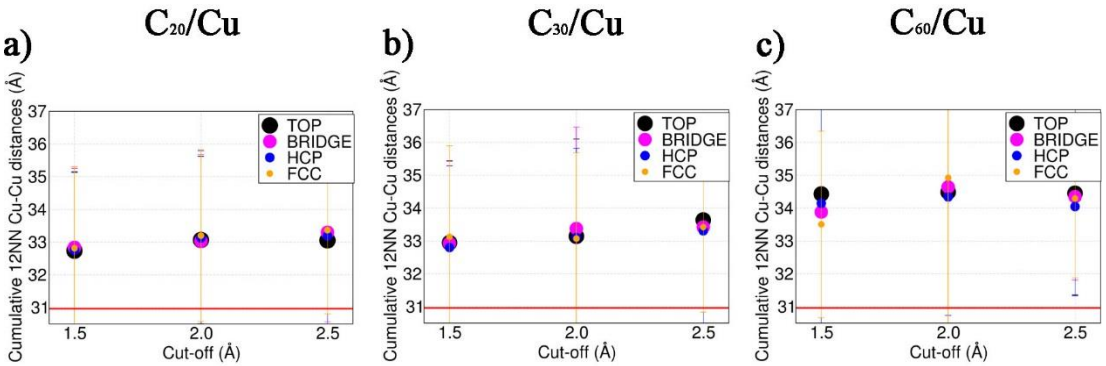

Figure 5.4: Fullerene-induced loosening of the Cu lattice for the Cu-fullerene interfaces considered as quantified by the sum of the 12 NN Cu-Cu distances in the optimised slabs. The horizontal red line marks the value of cumulative 12 NN Cu-Cu distance (30.962 Å) for the optimised bulk FCC Cu cell (lattice parameter: 3.649 Å).

5.5 Electronic Structure of the interface models

As previously found for the Cu-polymer interfaces in Chapter 4 (Section 4.5) and different models of the Cu-C_{60} interface [10], regardless of the interface relaxation and ensuing loosening of the Cu lattice (Fig. 5.4), all the Cu-fullerene interface models result in a well-defined *3d* band with an absolute Density of States (DOS) maximum at about 1.5 eV below E_F, as present for bulk FCC Cu (Fig. 5.5). Consistent with the results of previous experimental and theoretical studies on C_{60}/Cu(111) interfaces [17], also the present models are computed to have a non-zero Density of States at the Fermi energy [DOS(E_F)] and, consequently, to be metallic.

Analysis of the Cu- and fullerene-resolved PAW-projected DOS (PDOS), shown in Fig. 5.6, offer elements to first appreciate subtle differences in the re-hybridisation between Cu and the different fullerenes considered. For the Cu-C_{60} interfaces, more than the 87% of the total PDOS at the Fermi level [PDOS(E_F)] are due to Cu, with the remaining 13% from the C_{60}. Conversely, for the C_{20}-Cu systems, up to 40% of the total PDOS(E_F) is due to the fullerene. Thus, as the size of the fullerene decrease, its contribution of the fullerene PDOS at the Fermi level increases.

The larger (smaller) differences between Cu-resolved (fullerene-resolved) PDOS in Fig. 5.6 suggest that the dependence on the initial adsorption site of the interfacial re-

hybridisation is larger for Cu than for the fullerene. Consequently, the changes in total DOS(E_F) in Fig. 5.5 stem mainly from the different re-hybridization of the interfacial Cu-atoms.

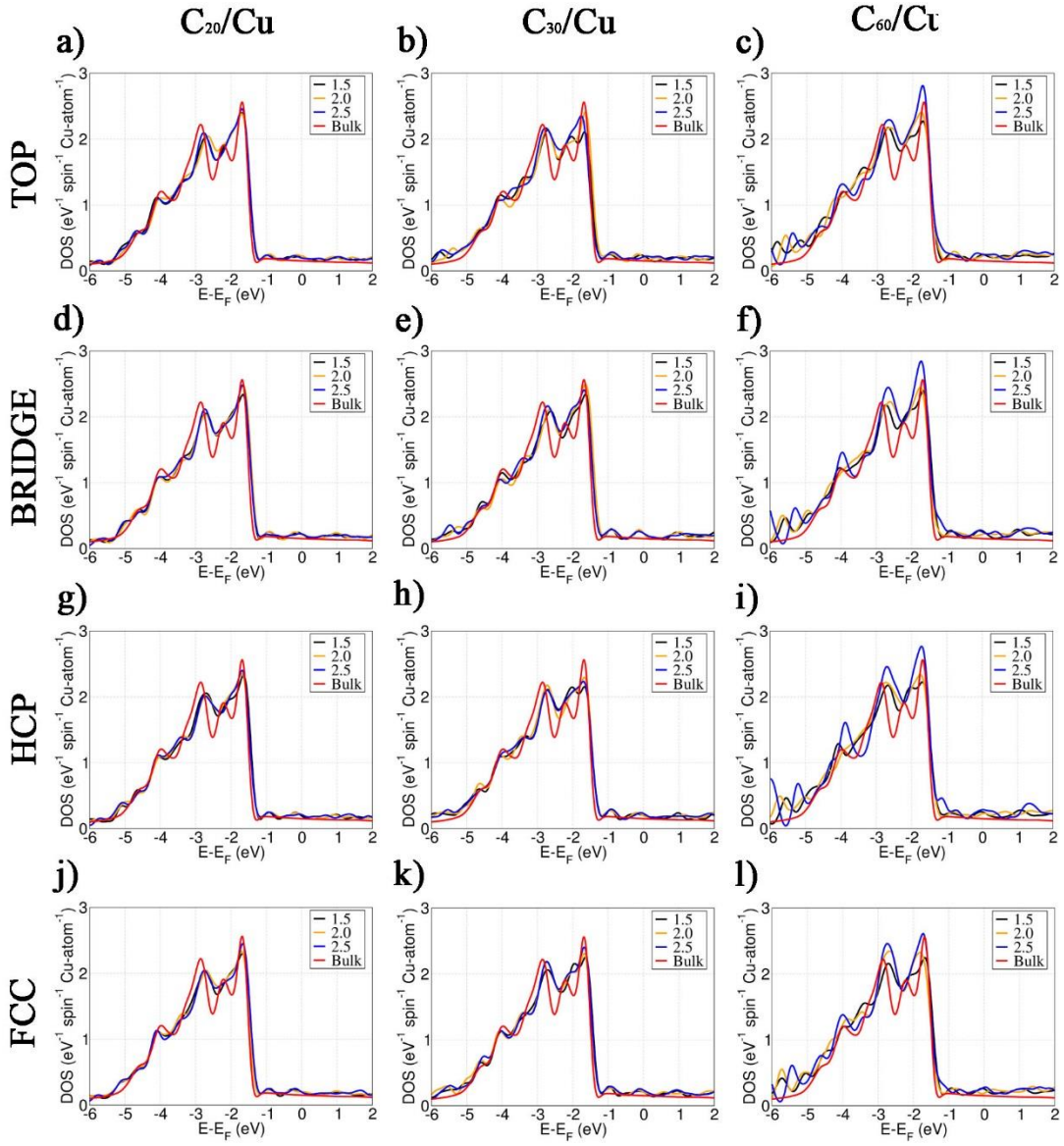

Figure 5.5: Computed density of states (DOS) for the Cu-fullerenes interface models considered. The computed DOS for bulk FCC Cu is also shown for comparison. All the interface models show a well-defined *3d*-band with an absolute DOS maximum at about 1.5 eV below E_F. Moreover, the non-zero DOS at the Fermi level indicate the metal character of the interface systems.

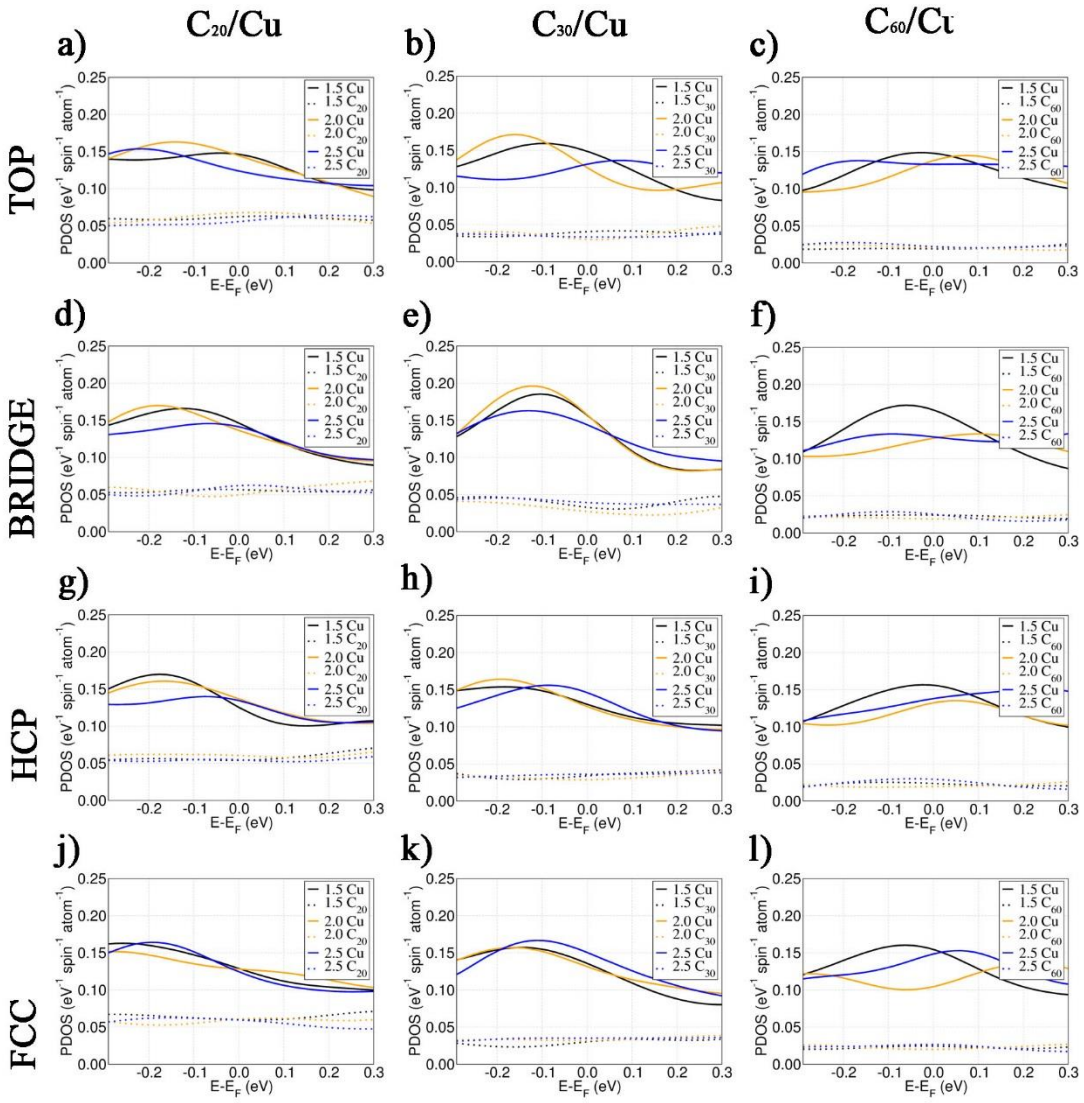

Figure 5.6: Cu (continuous lines) and fullerene (dotted lines) projected Density of States (PDOS) for the interface models considered. The contribution of the fullerene PDOS at the Fermi level is directly correlated to the decrease of the fullerene size, i.e. for the Cu-C_{60} interfaces, more than the 87% of the total PDOS at the Fermi level [PDOS(E_F)] are due to Cu, with the remaining 13% from the C_{60}. Conversely, for the C_{20}-Cu systems, up to 40% of the total PDOS(E_F) is due to the fullerene. Furthermore, the dependence on the initial adsorption site of the interfacial re-hybridisation is larger for Cu than for the fullerene as observed in this figure.

5.6 Magnetic properties of the interface models

5.6.1 Interface-averaged magnetic properties

I now turn to analyse the role of the fullerene size, curvature and initial adsorption site for the interface-averaged magnetic properties. Fig. 5.7 reports the interface-averaged band-splitting (ΔE) and magnetic moments (m) for the considered Cu-fullerene interface models. Both ΔE and m turn out to be lower than for the bulk FCC Cu. For the Cu-C_{20} and Cu-C_{30} interfaces, the computed ΔE and m show weak dependence on both the initial cut-off and adsorption site used to prepare the interface model. Conversely, while still showing a small dependence on the initial adsorption site, the results for the Cu-C_{60} interface-models turn out to be more sensitive to the initial cut-off, owing to the larger relaxation induced by the larger C_{60} with respect to the smaller fullerenes (Fig. 5.4).

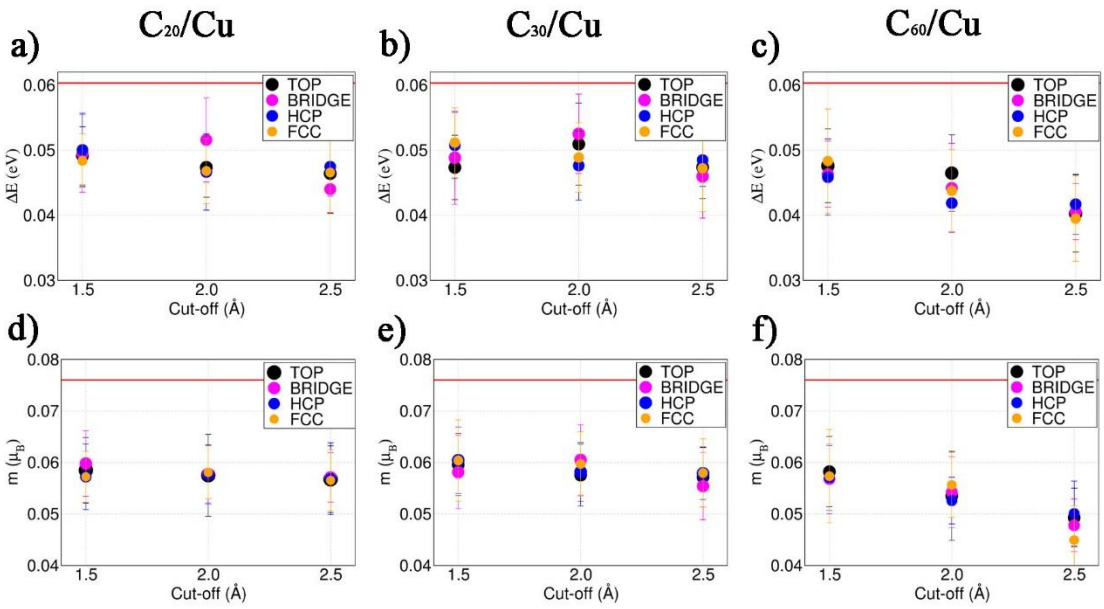

Figure 5.7: Average band-splitting (ΔE) and magnetic moments (m) as a function of the initial cut-off distance for the Cu-fullerene interfaces. The horizontal red marks the values for bulk FCC Cu at the optimised lattice parameter (3.649 Å).

As shown in Fig. 5.8a-c, owing to the definition of I_S (Chapter 2, Eq. 2.88), the computed values for m and ΔE (Fig. 5.7) lead to an overall increase of I_S for all the Cu-fullerene interface models with respect to bulk FCC Cu. The computed $DOS(E_F)$ is also increased with respect to bulk FCC Cu, up to 88% in Fig. 5.8d-f, leading to an overall increase of the $I_S \times DOS(E_F)$ product for all the Cu-fullerene interface models (Fig. 5.8g-i). The increase is largest (up to 60% the bulk FCC Cu value) for the interfaces between Cu and C_{60}, suggesting that C_{60} is more effective than smaller fullerenes such as C_{20} and C_{30} in inducing magnetic hardening of interfacial Cu atoms.

Analysis of the computed $I_S \times DOS(E_F)$ products between interfaces prepared with the same fullerene but different initial cut-off and adsorption site reveals the largest (smallest) deviations for the largest (smallest) C_{60} (C_{20}) fullerene. These results suggest that for small fullerenes, the interface magnetic properties are not extremely sensitive to the initial geometry at the interface that becomes progressively more important as the size of the fullerene increases.

It is worth noting that the $I_S \times DOS(E_F)$ product for the Cu-C_{60} interface turns out to be larger than for Cu-aC interface models (Fig. 5.8g-l), in line with the experiment [3]. Conversely, the Cu-C_{20} and Cu-C_{30} interfaces result in computed $I_S \times DOS(E_F)$ products comparable with those previously calculated for Cu-aC models [3]. Thus, use of fullerene smaller than C_{60} is predicted not to be effective in enhancing the interfacial magnetism with respect to what observed for Cu-C_{60} interfaces [16]. In the next Chapter we explore whether the use of fullerenes larger than C_{60} may provide more rewarding alternatives.

Contrary to results for C_{60} completely inserted in the Cu lattice [16], the computed $I_S \times DOS(E_F)$ products for the partially inserted fullerene considered here does not support any strong correlation between increase of the magnetic hardening and loosening of the Cu lattice as quantified by the sum of the 12 NN Cu-Cu distances (Fig. 5.8j-l). However, although only for the C_{60} case, a weak correlation between $DOS(E_F)$ and the loosening of the Cu lattice is nevertheless found in Fig. 5.9. Altogether, these results demonstrate that the hybridisation and emergence of

magnetic properties at Cu-fullerene interface can be tuned by changing the fullerene used in the interface. Notably, as shown by the dependence of the computed results for the same fullerene on the initial adsorption geometry (Fig. 5.8), fine details in the atomic structure of the intimate Cu-fullerene interface can non-negligibly affect the interface re-hybridisation, making it inevitable to try to extend as much as possible the set of interface models screened (and the computational efforts) when modelling this kind of molecular interfaces. In the following Sections of this Chapter I further analyse the present results in terms of Cu → fullerene charge transfer and strain of the molecular π-system as quantified by the average fullerene pyramidalization angle.

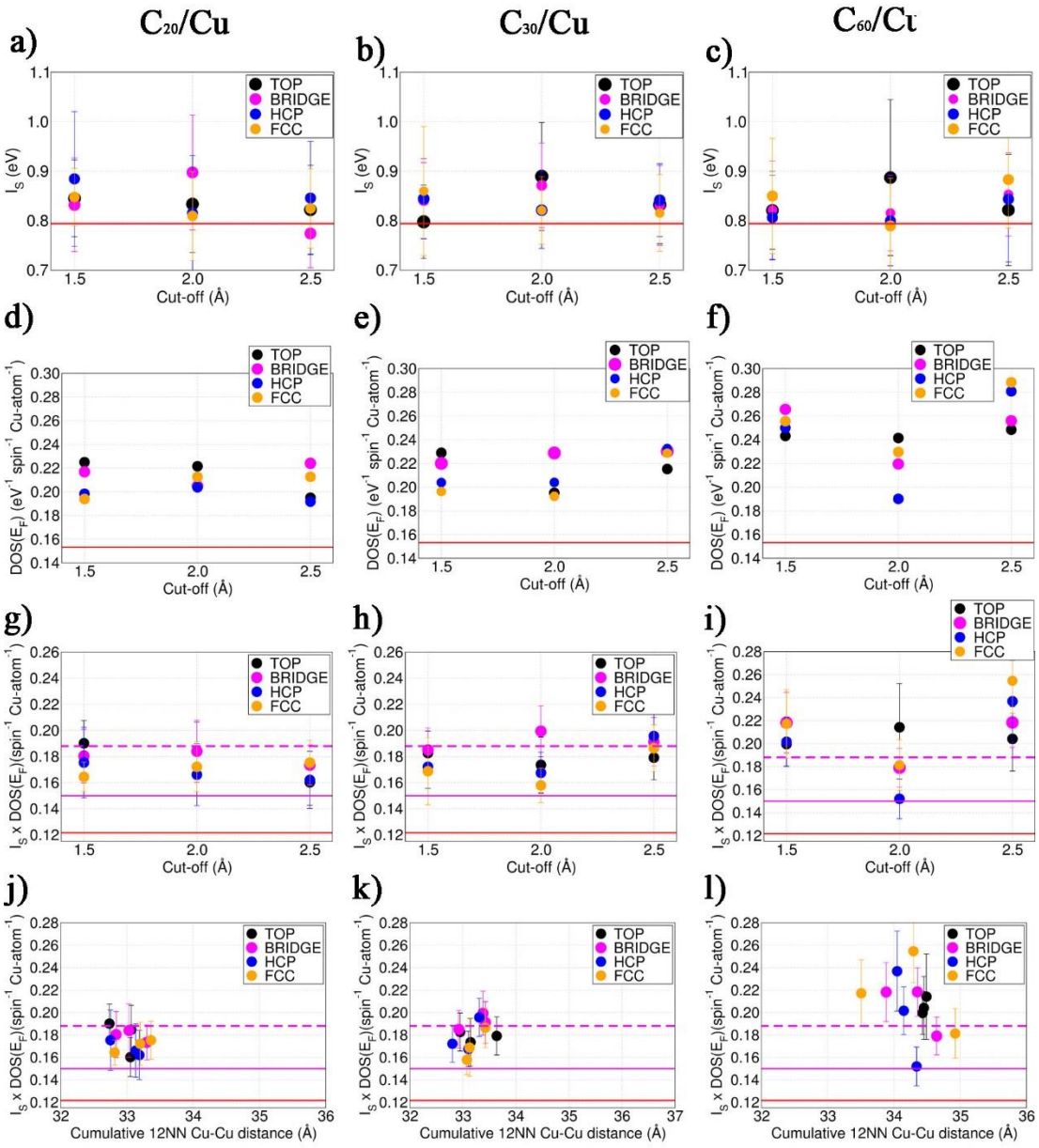

Figure 5.8: a-c) Computed average Stoner exchange integral (I_S) and **d-f)** density of states at the Fermi level [$DOS(E_F)$] as a function of the initial Cu-C cut-off distance. $I_S \times DOS(E_F)$ product as a function of **g-i**) the initial cut-off, and **j-l**) sum of the shortest 12 NN Cu-Cu distances. The horizontal red line marks the value of for bulk FCC Cu at the optimised lattice parameter (3.649 Å). The horizontal continuous (0.15 $spin^{-1}$ $atom^{-1}$) and dashed (0.19 $spin^{-1}$ $atom^{-1}$) magenta lines in g-l) indicate the largest computed $I_S \times DOS(E_F)$ product at the same level of theory for the interfaces between Cu and as deposited (1.7 gr/cm^3) and annealed (2.3 gr/cm^3) amorphous carbon [3].

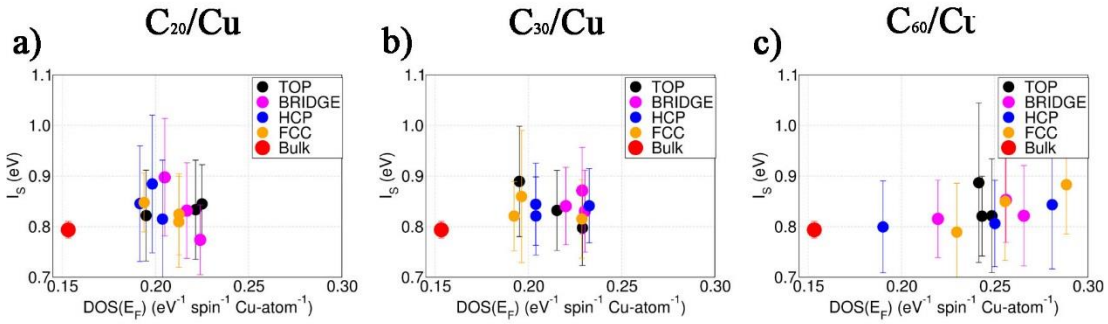

Figure 5.9: Computed average Stoner exchange integral (I_S) as a function of the Density of States at the Fermi energy [$DOS(E_F)$] for the Cu-fullerene interface considered.

As show in Fig. 5.10, there is an inverse relationship between the $I_S \times DOS(E_F)$ product and the ratio between the Projected Density of States at the Fermi level of carbon atoms [$PDOS_C(E_F)$] over the PDOS of Cu atoms [$PDOS_{Cu}(E_F)$]. Fullerenes of larger size (C_{60}) show a lower $PDOS_C(E_F)$ / $PDOS_{Cu}(E_F)$ ratio and larger values of the average $I_S \times DOS(E_F)$ product. Larger charge-transfer leads to a decrease of $PDOS_{Cu}(E_F)$ for the Cu-C_{60} interfaces and to an increment on the $PDOS_c(E_F)$ / $PDOS_{Cu}(E_F)$ ratio which does not directly enhance the magnetic properties of the interface as shown in Fig. 5.10. On the other hand, negligible changes on the charge transfer are found for Cu-C_{20} and Cu-C_{30} systems (see Fig. 5.12) with not direct correlation with the $PDOS_c(E_F)$ / $PDOS_{Cu}(E_F)$ ratio.

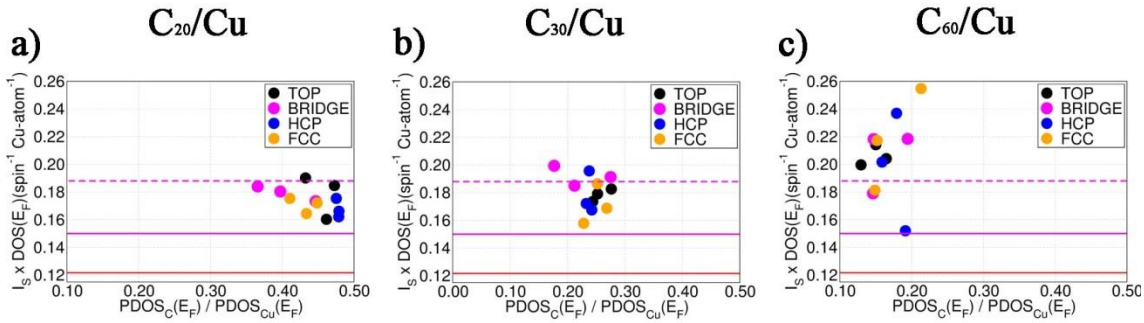

Figure 5.10: Average $I_S \times DOS(E_F)$ product as a function of the ratio between the Projected Density of States at the Fermi level for the carbon [$PDOS_C(E_F)$] and Cu [$PDOS_{Cu}(E_F)$] atoms. The horizontal red line marks the values for optimised bulk FCC Cu. The horizontal continuous (0.15 $spin^{-1}$ $atom^{-1}$) and dashed (0.19 $spin^{-1}$ $atom^{-1}$) magenta lines mark the largest computed $I_S \times DOS(E_F)$ product at the same level of theory for interfaces between Cu and as deposited (1.7 gr/cm^3) and annealed (2.3 gr/cm^3) aC measured to be ferromagnetic in Ref. [3].

5.6.2 The role of the interfacial Cu → fullerene charge-transfer

This Section investigates the role of the Cu → fullerene charge-transfer for the emerging magnetic properties of the interfaces. The larger experimental electronic affinity (EA) for C_{60} (2.7 eV [13]) with respect to C_{20} (2.25 eV [10]) anticipate, in the presence of negligible relaxation effects, larger charge-transfer at the Cu-C_{60} interface. Given the absence of experimental value for the EA of C_{30} in the literature, this is approximated (crudely by neglecting ionic and electronic relaxation effect following addition of the extra electron) as minus the energy of the molecular LUMO with respect to the vacuum level. Based on the vacuum-aligned energy of the LUMO for the considered fullerenes (Table 5.1), and again neglecting any interface relaxation effects, C_{30} is expected to extract more electronic charge than C_{60}, with the smallest charge-transfer for the Cu-C_{20} interface.

Table 5.1: Computed vacuum-aligned LUMO energy for the considered fullerenes optimised in vacuum.

Fullerene	**E_{LUMO} (eV)**
C_{20}	-4.07
C_{30}	-4.60
C_{60}	-4.20

Contrary to expectations based on the vacuum-aligned energy for the molecular LUMO in Table 5.1 (C_{30} < C_{60} < C_{20}), and the results for the conjugated polymers studied in Chapter 4, the computed Cu → fullerene charge-transfer do not correlate with E_{LUMO} for the isolated molecules (Fig. 5.11a-c). Thus, the deviations in the computed charge-transfer between different fullerenes turn out to be determined mostly by the adsorption site and initial cut-off of the system, rather than by E_{LUMO} for the isolated fullerene. These results reiterate that, at least for the considered fullerenes, the relaxation of the interface plays a dominant role in tuning the Cu → organic interfacial charge-transfer.

Notably, on average the charge-transfer increases going from C_{20} and C_{30} to C_{60}, suggesting that, regardless of the computed E_{LUMO}, the interfacial charge-transfer

(largest for the Cu-C_{60} interfaces) does not directly correlate with the strain in the molecular π-system (smallest for C_{60}, see also next Section).

The computed transfer of up to 3 electrons at the Cu-C_{60} interfaces (Fig. 5.11c) is in good agreement with previous experimental studies of C_{60}-induced reconstructions of Cu(111), resulting in substantially larger metal→C_{60} charge-transfer than for C_{60} adsorbed on Cr(100) (0.5 e [18]), Ag(100) (0.15 e [19]) or Au(111) (0.01 e [19]).

As shown in Fig. 5.11d-f, in general the computed Cu → fullerene charge-transfer appear to be enhanced by loosening of the Cu-lattice, although depending on the fullerene and adsorption site, small deviations from the main trend are nevertheless present.

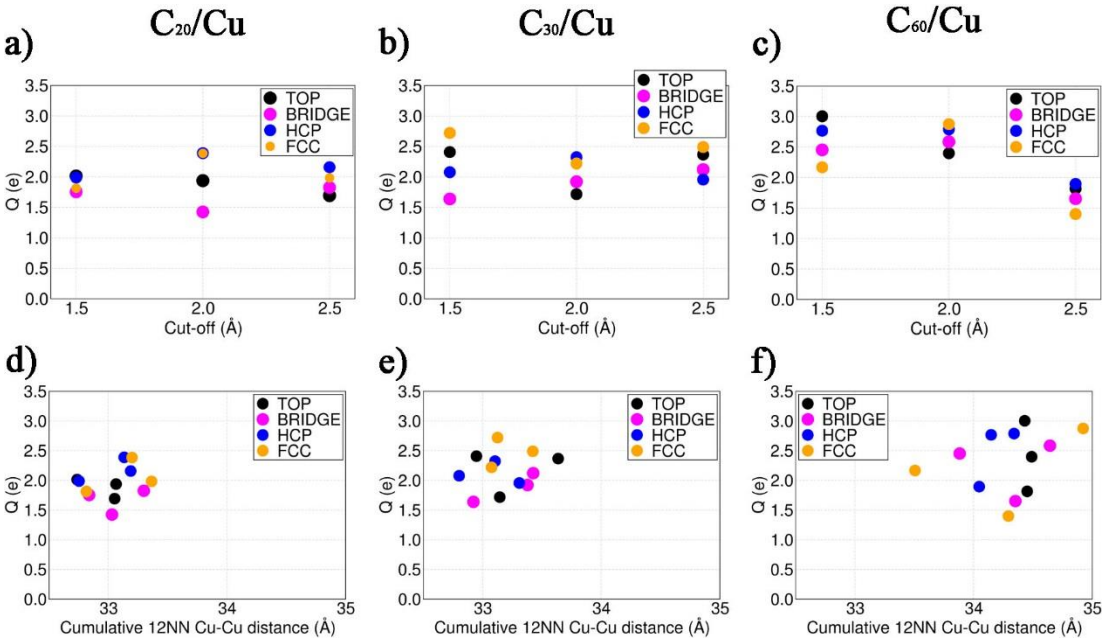

Figure 5.11: Computed Cu → fullerene Bader charge transferred (Q, e) as a function of **a-c)** the initial Cu-fullerene cut-off distance, and **d-f)** the average cumulative 12 NN Cu-Cu distance in the optimised Cu-polymer interface models.

Turning to the dependence of the computed magnetic hardening on the interfacial charge-transfer, the correlation between these two quantities is illustrated in Fig. 5.12 and Fig. 5.13. As previously found for the planar π-conjugated polymers investigated

in Chapter 4, the interface-averaged Stoner exchange integral (I_s) is found not to directly correlate with the interfacial charge-transfer. As shown in Fig. 5.12a-c, for most of the interface modelled, I_S turns out to be inversely dependent on the Cu → fullerene charge-transfer, re-iterating that interfacial re-hybridisation, rather than the total charge-transfer, is critical for enhancing the magnetic hardening at the molecular interface. These results prompt for direct experimental consideration of this issue by experimentally investigating interfaces with other available fullerenes (e.g. C_{20}, C_{70} and larger ones [20-22]), that have not been studied yet, so to provide a direct validation term.

As shown in Fig. 5.12d-f, increased charge-transfer can lead to both suppression of DOS(E_F) for the Cu-C_{60} interfaces and negligible changes in DOS(E_F) for the Cu-C_{20} and Cu-C_{30} systems. These results strengthen the conclusion that re-hybridisation between Cu and the different fullerene is both quantitatively and qualitatively different.

The different dependence of I_S and DOS(E_F) on the interfacial charge-transfer for the fullerene studied results in the trends displayed in Fig. 5.12g-f. Whereas the computed I_S×DOS(E_F) product for the Cu-C_{20} and Cu-C_{30} is found to be negligibly affected by the (geometry-dependent) interfacial charge-transfer, for the C_{60} interfaces the magnetic hardening turns out to be enhanced for those geometries with overall smaller charge-transfer. These results clearly indicate that maximisation of the charge-transfer for C_{60} interfaces, as previously suggested in Ref. [16], may not be the most effective strategy towards enhancement of magnetic hardening at Cu-fullerene interfaces. More rewarding strategies should aim at maximising the I_S×DOS(E_F) product, which may be achieved also without maximising the interfacial charge-transfer.

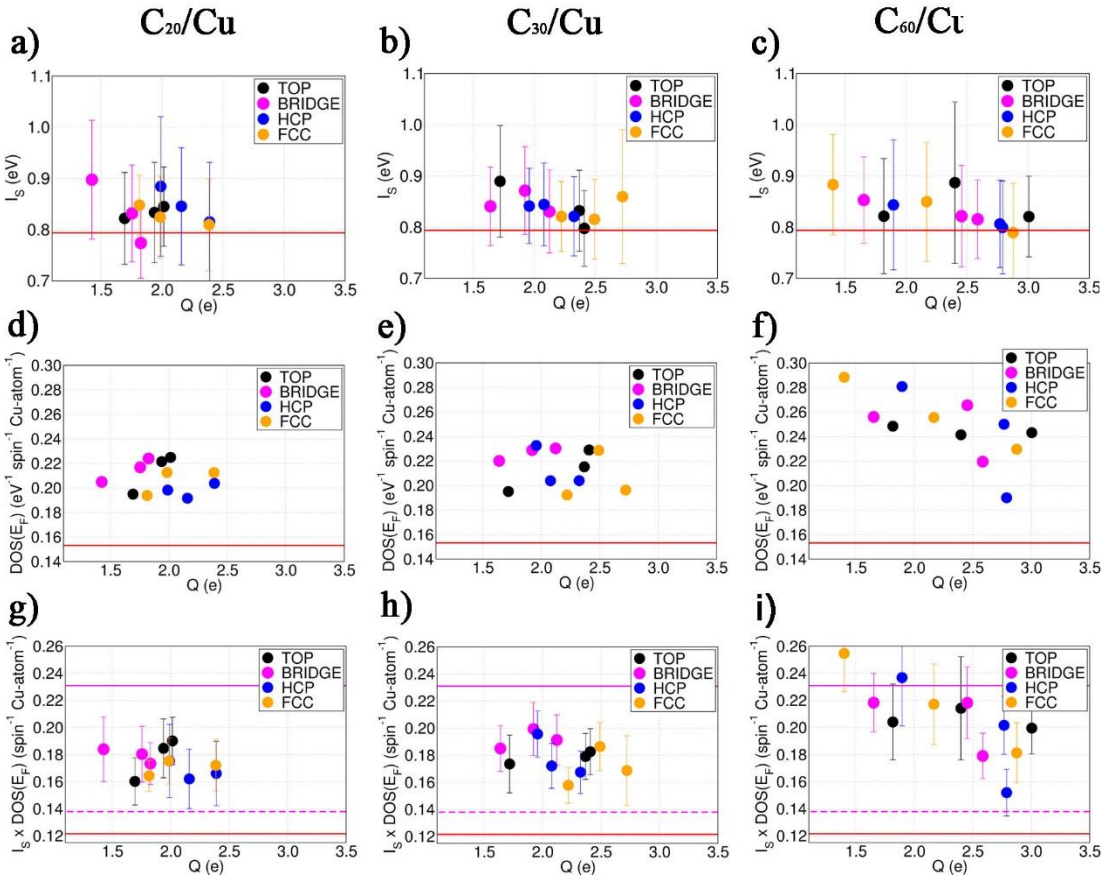

Figure 5.12: a-c) Average Stoner exchange integral (I_S), **d-f)** density of states at the Fermi level [$DOS(E_F)$] and **g-i)** $I_S \times DOS(E_F)$ product as function of the total Cu → fullerene Bader charge transferred. The horizontal red marks the values for bulk FCC Cu at the optimised lattice parameter (3.649 Å). The horizontal continues (dashed) magenta lines marks the maximum (minimum) $I_S \times DOS(E_F)$ product computed for the models in Ref. [4].

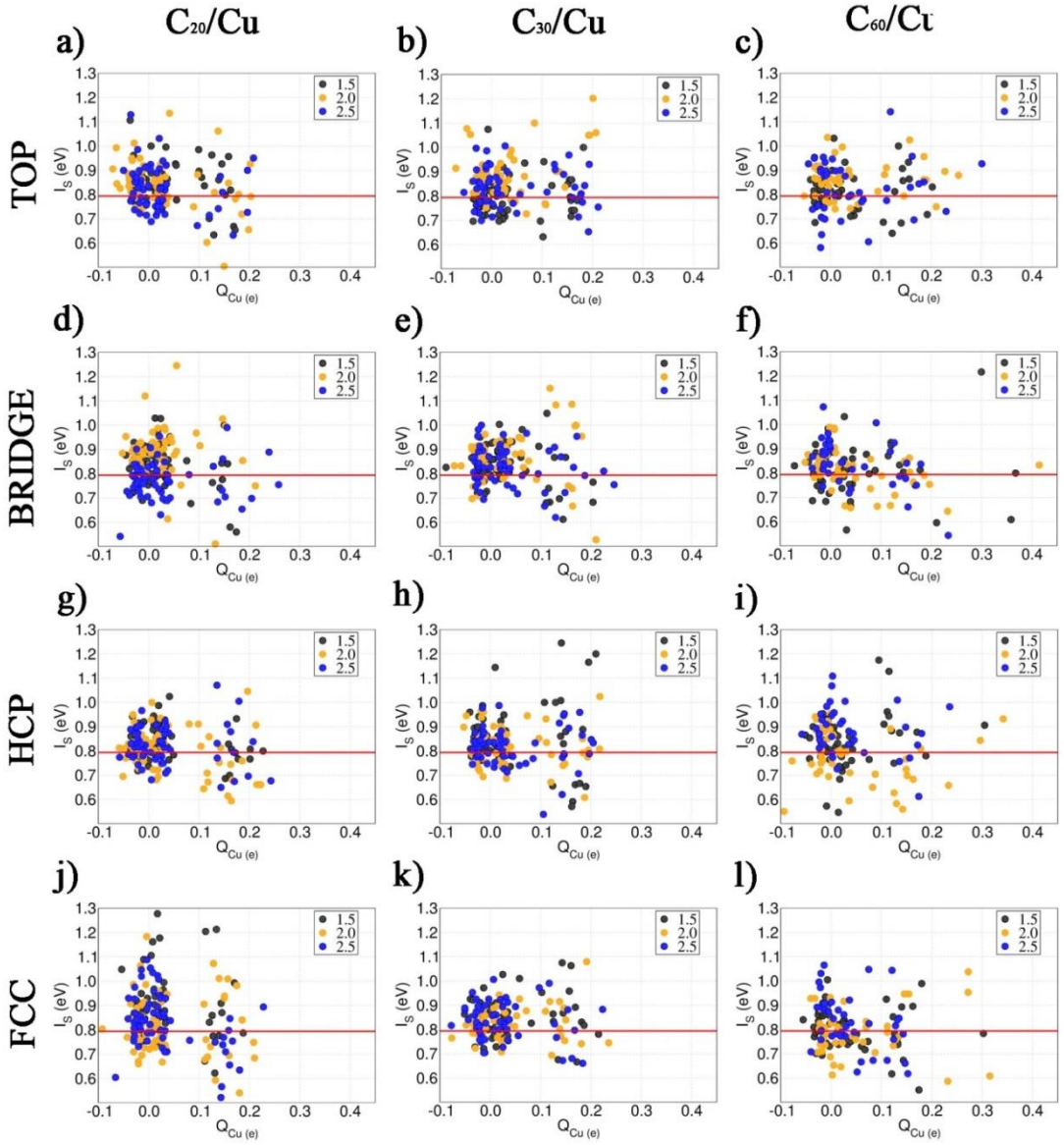

Figure 5.13: Atom-resolved magnetic hardening as a function of the computed Bader charge transfer (Cu → fullerene) per Cu-atom for the simulated fullerenes/Cu interfaces at the different adsorption geometries. The horizontal red line marks the value of the magnetic hardening for the reference FCC-cubic system.

5.6.3 The role of strain on the molecular π-system

I conclude this Chapter by analysing the role of strain on the π-system of the fullerene, as quantified by the corresponding pyramidalisation angle (θ_p), for the interfacial magnetic properties.

Following existing literature [23], θ_p is defined as the angle measuring the deviation from co-planarity for the three bonds of the sp^2 C-atoms in the fullerene molecules (see Fig. 5.14). From this definition it follows that the smaller the curvature of the fullerene, the larger θ_p and, consequently, the larger the strain on the molecular π-system.

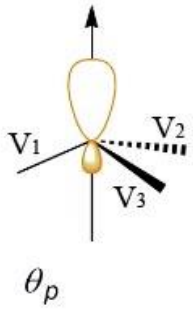

Figure 5.14: Schematic representation of the pyramidalization angle (θ_p) where the vectors V_1, V_2, V_3, are the bond-directions to the adjacent atoms 1, 2, and 3.

As shown in Fig. 5.15a-c, θ_p is found to (unsurprisingly) decrease going from the more strained C_{20} to the less strained C_{60}. Following optimisation of the interface geometry, the computed θ_p values turn out to be minimally affected by both the initial adsorption site and cut-off, resulting in effectively constant values for each of the considered fullerenes.

Analysis of the dependence of both I_S and the $I_S \times DOS(E_F)$ product on the fullerene pyramidalization indicate that, whereas I_S is rather insensitive to the θ_p values for the fullerenes optimised at the interface (Fig. 5.15d-f), in general the $I_S \times DOS(E_F)$ product decreases with increasing θ_p. Thus, the less strained C_{60} ($\theta_p \sim 12°$) is more effective in promoting interfacial magnetic hardening than the more strained C_{30} ($\theta_p \sim 17°$) and C_{20} ($\theta_p \sim 21°$) fullerenes. Together with the results for the planar π-

conjugated systems presented in Chapter 4, these findings indicate that mildly strained π-systems (as present in C_{60}) are beneficial for enhancing the magnetic hardening of its interfaces with Cu. The next Chapter explores whether interfacial re-hybridisation with less strained fullerenes (C_{100} and C_{180}) is capable (or not) of enhanced magnetic hardening with respect to the Cu-C_{60} interfaces.

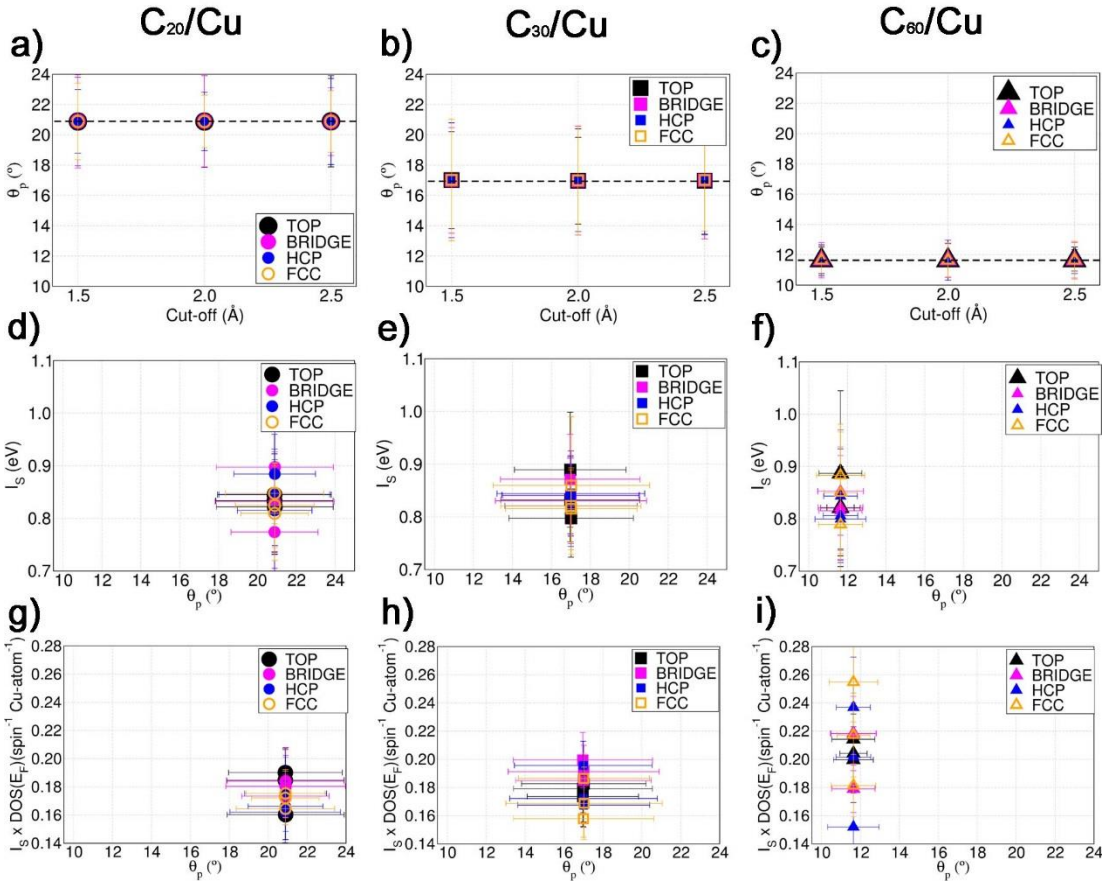

Figure 5.15: a-c) Average pyramidalization angle (θ_p) and associated standard deviation as a function of the initial Cu-fullerene cut-off for the optimised interface models. **d-f)** Average computed Stoner exchange integral (I_S), and **g-i)** $I_S \times DOS(E_F)$ product as a function of θ_p for the Cu-fullerene interfaces considered. The black dashed line presented in a-c marks the θ_p of the isolated fullerenes optimised in vacuum.

5.6.4 Fullerene and Cu contribution to the interfacial magnetism

Experimental measurements on ferromagnetic Cu-C_{60} [16] and Cu-aC [3] interfaces indicate a stronger (weaker) dependence of the interfacial magnetism on the metal thickness for the C_{60} (aC) case. Whereas ferromagnetism in Cu-C_{60} interfaces is quenched if the metal layer is more than 5 nm thick [16], this is not the case for Cu-aC junctions that instead present ferromagnetic ordering also for thicker (>5nm) metal layers. These results and DFT simulations, supported by spin-polarised muon spectroscopy [3,16] altogether suggest that the contributions from the carbon substrate to the interfacial ferromagnetic order are larger for aC than for C_{60}. I next analyse whether the size and curvature of the smaller fullerene leads to deviations or not from these reported trends.

Fig. 5.16 shows the computed ratio between fullerene-localised and total magnetic moment for the interfaces studied. In line with earlier results for Cu-C_{60} interfaces suggesting contributions lower than 23% to the total interface magnetic moment [16], the C_{60} contribution to the magnetisation is relatively small, ranging between 16% and 29%. Interestingly given the C_{20} and C_{30} larger contribution to the total interface Density of States at the Fermi energy [DOS(E_F)] with respect to C_{60} (Fig. 5.6), for the Cu-C_{20} and Cu-C_{30} interfaces localisation of the magnetic moment on the carbon-substrates is further suppressed (to 12-20%) by comparison to the Cu-C_{60} cases.

Altogether, these results lead to the prediction that, at least in terms of localisation of the magnetism, smaller fullerenes such as C_{20} and C_{30} should be closer to C_{60} than aC, and lead to a metal-thickness dependence of the emergent ferromagnetism. Finally, based on the observed lack of strong correlation between the fullerene contribution to DOS(E_F) and the ensuing contribution to the interface magnetism, it transpires that, at least for the C_{20}, C_{30} and C_{60} studied, larger fullerene-contributions to DOS(E_F) do not directly lead to larger contributions to the interface magnetisation.

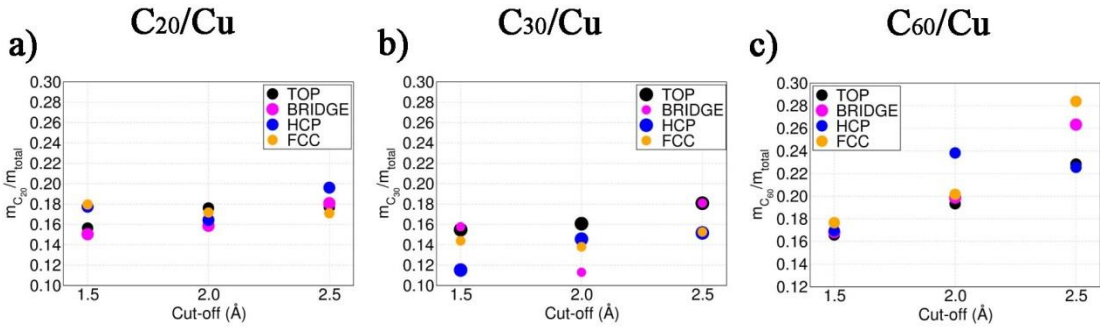

Figure 5.16: Computed contribution of the fullerenes ($m_{C20,30,60}$) to the total magnetic moment (m_{total}) for the interface models considered.

5.7 Conclusions

DFT simulations have been used to investigate the role fullerene curvature and adsorption sites for the magnetic hardening of Cu-fullerene interfaces. Analysis of the simulations for several models of the interfaces between Cu and fullerenes of different size, curvature and strain of the molecular π-system, namely C_{20}, C_{30} and C_{60} indicate that:

i) Regardless of the fullerene and adsorption sites, relaxation of the interface consistently leads to metallization of the fullerene. The computed fullerene resolved Density of States at the Fermi energy [PDOS(EF)] is largest (smallest) for C_{20} (C_{60}), suggesting an increased hybridization for C_{20} with respect to C_{60}.

ii) At least for cases considered, the computed Cu → fullerene charge-transfer is found not to be correlated with the vacuum-aligned energy of the LUMO for the isolated fullerene. In general, enhancement of the Cu-lattice loosening suppresses interfacial charge transfer. These results contrast what found previously (Chapter 4) for planar π-conjugated polymers, suggesting a non-negligible role of the strain of the molecular π-system in tuning the interfacial relaxation and ensuing charge transfer.

iii) Owing to larger increases in the interface-averaged I_S and DOS(E_F), the computed I_S×DOS(E_F) products are largest for the Cu-C_{60} interfaces. C_{60} is therefore

predicted to be more effective than C_{20} and C_{30} in maximising the magnetic hardening of Cu-fullerene interfaces.

iv) The largest magnetic hardening among Cu-C_{60} interfaces is computed for the interface-models characterised by the smallest charge-transfer. This result reiterates that the details of the metal-organic re-hybridisation, rather than the net charge-transfer, are critical for enhancing the magnetic hardening at Cu-organic interfaces.

v) Analysis of the interplay between curvature of the fullerene and resultant strain on the molecular π-system on the hand, and emergent magnetic properties on the other suggests that mildly strained π-systems, as present in C_{60}, are more effective in promoting interfacial magnetic hardening than strongly strained (as present in C_{30} and C_{20}) or planar (as present in the systems analysed in Chapter 4) ones. Given the not immediate correlation between magnetic hardening and interfacial charge transfer, thence electron-accepting properties of the fullerenes [point ii) above], this result is in my view very interesting and prompts for further experimental investigation to fullerenes different from C_{60}. As for the polymers in Chapter 4, the simulations presented here clearly suggest that interfacial re-hybridisation (related to the fullerene curvature and ensuing strain on the π system) may be dominant over the overall charge-transfer for the interfacial magnetic hardening.

vi) Comparison of the results for interface-models prepared with the same fullerene in different initial adsorption geometries indicates that fine details in the atomic structure of the intimate Cu-fullerene interface can non-negligibly affect the interface re-hybridisation and emerging magnetic properties, calling for extra care (read extensive screening) when modelling this kind of molecular interfaces. While the absolute value for the $I_S \times DOS(E_F)$ may not be totally accurate, differences between computed $I_S \times DOS(E_F)$, due to different interface relaxation and re-hybridisation should be meaningful as computed at the same level of theory.

vii) Regardless of the quantitative differences in induced magnetic hardening of Cu, for all the fullerene considered the interface magnetism is computed to be mostly localised on the Cu-substrate and, as a result, potentially sensible to the thickness of the metal layers as previously experimentally observed for Cu-C_{60} interfaces. The

present results also indicate that larger fullerene-contributions to DOS(E_F) do not directly lead to larger contributions to the interface magnetisation

Overall, the results in this Chapter prompt the question as to whether enhanced magnetic hardening with respect to Cu-C_{60} interfaces can be achieved by using fullerene of smaller curvature (reduced strain on the molecular π-system), which is one of the objective of the final Chapter of this Thesis.

5.8 References

1. Wong, P.J., et al., *Electronic and magnetic structure of C 60/Fe 3 O 4 (001): a hybrid interface for organic spintronics.* Journal of materials chemistry C, 2013. **1**(6): p. 1197-1202.
2. Cakır, D., D.M. Otálvaro, and G. Brocks, *Magnetoresistance in multilayer fullerene spin valves: a first-principles study.* Physical Review B, 2014. **90**(24): p. 245404.
3. Al Ma'Mari, F., et al., *Emergent magnetism at transition-metal–nanocarbon interfaces.* Proceedings of the National Academy of Sciences, 2017. **114**(22): p. 5583-5588.
4. Al Ma'Mari, F., et al., *Beating the Stoner criterion using molecular interfaces.* Nature, 2015. **524**(7563): p. 69-73.
5. Warner, M., et al., *Potential for spin-based information processing in a thin-film molecular semiconductor.* Nature, 2013. **503**(7477): p. 504.
6. Serri, M., et al., *High-temperature antiferromagnetism in molecular semiconductor thin films and nanostructures.* Nature communications, 2014. **5**: p. 3079.
7. Kresse, G. and J. Furthmüller, *Efficient iterative schemes for ab initio total-energy calculations using a plane-wave basis set.* Physical Review B, 1996. **54**(16): p. 11169.
8. Perdew, J.P., K. Burke, and M. Ernzerhof, *Generalized gradient approximation made simple.* Physical Review letters, 1996. **77**(18): p. 3865.

9. Henkelman, G., A. Arnaldsson, and H. Jónsson, *A fast and robust algorithm for Bader decomposition of charge density.* Computational Materials Science, 2006. **36**(3): p. 354-360.
10. Schwarz, K. and P. Mohn, *Itinerant metamagnetism in YCO2.* Journal of Physics F: Metal Physics, 1984. **14**(7): p. L129.
11. Kroto, H.W., et al., *C60: Buckminsterfullerene.* Nature, 1985. **318**(6042): p. 162-163.
12. Prinzbach, H., et al., *Gas-phase production and photoelectron spectroscopy of the smallest fullerene, C20.* Nature, 2000. **407**(6800): p. 60.
13. Song, J., et al., *A study on the electronic and structural properties of fullerene C 30 and azafullerene C 18 N 12.* Journal of Molecular Structure: THEOCHEM, 2010. **942**(1): p. 71-76.
14. Zhang, B., et al., *The geometry of small fullerene cages: C 20 to C 70.* The Journal of Chemical Physics, 1992. **97**(7): p. 5007-5011.
15. Wang, L.-S., et al., *Threshold photodetachment of cold C− 60.* Chemical Physics letters, 1991. **182**(1): p. 5-11.
16. Modesti, S., S. Cerasari, and P. Rudolf, *Determination of charge states of C 60 adsorbed on metal surfaces.* Physical Review letters, 1993. **71**(15): p. 2469.
17. Tamai, A., et al., *Electronic structure at the C 60/metal interface: an angle-resolved photoemission and first-principles study.* Physical Review B, 2008. **77**(7): p. 075134.
18. Kawahara, S., et al., *Large magnetoresistance through a single molecule due to a spin-split hybridized orbital.* Nano letters, 2012. **12**(9): p. 4558-4563.
19. Lu, X., et al., *Charge transfer and screening in individual C 60 molecules on metal substrates: A scanning tunneling spectroscopy and theoretical study.* Physical Review B, 2004. **70**(11): p. 115418.
20. Prinzbach, H., et al., *Gas-phase production and photoelectron spectroscopy of the smallest fullerene, C 20.* Nature, 2000. **407**(6800): p. 60.
21. Deguchi, S., R.G. Alargova, and K. Tsujii, *Stable dispersions of fullerenes, C60 and C70, in water. Preparation and characterization.* Langmuir, 2001. **17**(19): p. 6013-6017.

22. Parker, D.H., et al., *High-yield synthesis, separation, and mass-spectrometric characterization of fullerenes C60 to C266.* Journal of the American Chemical Society, 1991. **113**(20): p. 7499-7503.
23. Haddon, R., *Comment on the relationship of the pyramidalization angle at a conjugated carbon atom to the σ bond angles.* The Journal of Physical Chemistry A, 2001. **105**(16): p. 4164-4165.

Chapter 6

The role of fullerene-encapsulation for the magnetic hardening at Cu-fullerene interfaces

Abstract

This Chapter investigates the role of the fullerene-encapsulation and interplay between the strain of the π-system of the inner and outer fullerenes for the magnetic hardening at the interfaces between Cu and carbon onions. Different models of interface between Cu(111) slabs and fullerenes larger than C_{60} such as C_{100} and C_{180}, and related $C_{20}@C_{100}$ and $C_{20}@C_{180}$ onions, are investigated to explore whether use of encapsulated fullerenes (carbon onions) can be beneficial for enhancing the magnetic hardening at molecular interfaces of Cu with respect to the Cu-C_{60}. The results for the systems considered suggest this not to be the case. Analysis of the results for the Cu-$C_{20}@C_{100}$ and Cu-$C_{20}@C_{180}$ interfaces strengthens the conclusion that the interfacial magnetic hardening is not maximised by enhancement of Cu → molecule charge-transfer. Analysis of the results for the Cu-$C_{20}@C_{100}$ and Cu-$C_{20}@C_{180}$ interfaces strengthens the conclusion that the interfacial magnetic hardening is not maximised by enhancement of Cu → molecule charge-transfer, thence not immediately correlated with the electron-accepting properties of the molecular substrate. Based on the computed lower magnetic hardening for the considered Cu-$C_{20}@C_{100}$ and Cu-$C_{20}@C_{180}$ interfaces with respect to Cu-C_{60} ones, it is inevitably to note that, as per the isolated fullerenes, it appears that the curvature of interfaced fullerene plays a predominant role in tuning interfacial re-hybridisation and ensuing magnetic hardening.

6.1 Introduction

The computed results for the interfaces between Cu and C_{60} (Ref. [1] and Chapter 5), fullerenes with curvature larger than C_{60} (C_{20} and C_{30} in Chapter 5), and organic substrates with planar π-system (Chapter 4) altogether point to C_{60} as the most effective molecule, out of those considered, in enhancing the magnetic hardening of its interfaces with Cu. Together with the presented evidence on the (not direct) correlation between interfacial magnetic hardening and Cu → organic charge-transfer, these results also suggest that moderate strain of the π-system (as present in C_{60} and increased in C_{20} and C_{30}) is beneficial to maximise emergent magnetism at Cu-organic interfaces.

To conclude the assessment of the role of curvature, and ensuing strain, of the molecular π-system for the magnetic properties of the interfaces with Cu and carbon-based organic substrates, this Chapter investigates the effects induced on Cu by fullerenes of reduced curvature (strain on the π-system) with respect to C_{60}, namely C_{100} and C_{180}.

In addition, the progress in synthesis, separation and characterisation of encapsulated fullerenes (*carbon nano-onions*) as well as the increasing interest in their appealing properties for opto-electro-chemical applications [2-15], make these systems amenable also to investigation of their properties for molecular spintronics and emergent magnetism. Motivated by these considerations, this Chapter investigate also whether nano-encapsulation of fullerenes can lead to enhancement of the magnetic hardening at their interfaces with Cu by comparison to what computed (and measured [1]) for Cu-C_{60} systems.

6.2 Computational details

All the simulations were performed within the framework of Projected-Augmented Wave (PAW) Density Functional Theory (DFT) as implemented in the VASP package [16]. A generalized gradient approximation, as parameterized in the PBE functional [17], was used as for the exchange-correlation (XC) functional. The plane wave cut-off was set to 400 eV.

Structural relaxation of the different interfaces was carried out using a convergence criterion of 0.03 eV $Å^{-1}$ on the atomic forces. The k-point sampling grid for surface Brillouin zone sampling was defined based on the convergence test for bulk FCC Cu presented in Chapter 3, Section 3.2.3, and scaled according to the in-plane size of the fullerenes/Cu(111)-6x6 interface systems. The simulation cell was periodic along the x and y directions, with a 15 Å vacuum buffer along the z-direction. The total charge density was computed using the Bader charge-partitioning scheme [18].

Due to the computed non-magnetic ground-state for all the models studied, atom-resolved approximations to the Stoner exchange integral (I_s, see Chapter 2, Section 2.3) were calculated by enforcing a magnetic moment of 0.1 μ_B/Cu-atom via fixed spin-moment DFT [19].

6.3 Interface models

To compromise between computational cost and size of the interface models, I focus on encapsulation of the smallest fullerene C_{20} into two larger fullerenes, namely C_{100} and C_{180}, leading to creation of systems with smaller ($C_{20}@C_{100}$) and larger ($C_{20}@C_{180}$) separation between the encapsulated fullerenes. Table 6.1 reports the computed shortest (R_{min}) and largest (R_{max}) radii for the considered molecules optimised in vacuum. Based on these results, the smallest (largest) inter-layer separations between encapsulated fullerenes are 1.99 Å (3.22 Å) and 3.94 Å (4.37 Å) for the $C_{20}@C_{100}$ and $C_{20}@C_{180}$ onions, respectively.

Table 6.1: Computed shortest (R_{min}, Å) and largest (R_{max}, Å) radius for the considered fullerenes optimised in vacuum.

	r_{min} (Å)	r_{max} (Å)
C_{20} (I_h)	1.94	2.09
C_{30} (C_{2v})	2.25	2.70
C_{60} (I_h)	3.55	3.55
C_{100} (D_5)	4.08	5.16
C_{180} (I_h)	6.03	6.31

In analogy with the procedure followed for the fullerenes considered in Chapter 5 (C_{20}, C_{30} and C_{60}), the centre of mass (CM) of the molecule, or the outer fullerene for the nano-onions, was placed in a top position of a five-layer Cu(111)-6x6 slab inserting only half of the fullerene (onion) inside the Cu-slab (Fig. 6.1). Depending on the shape of the outer fullerene (C_{100} is prolate whereas C_{180} is more spherical, see also the difference between shortest and longest radii in Table 6.1), different asymmetric initial position for the inner C_{20} were considered (Fig. 6.1) in order to quantify the effects of the relative position of the inner and outer systems in the onion for the emerging magnetic properties of its interfaces with Cu.

Following Refs. [1, 20], and the same procedure used for the Cu-polymer and Cu-fullerene interfaces in Chapters 4 and 5, to include the effects of differently constrained optimisation of the Cu-fullerene interfaces on the emerging magnetic properties, different models were prepared for each interface geometry and fullerene using several cut-off's (1.5, 2.0 and 2.5 Å) on the initial shortest Cu-fullerene distance. No Cu atom was present inside the fullerenes.

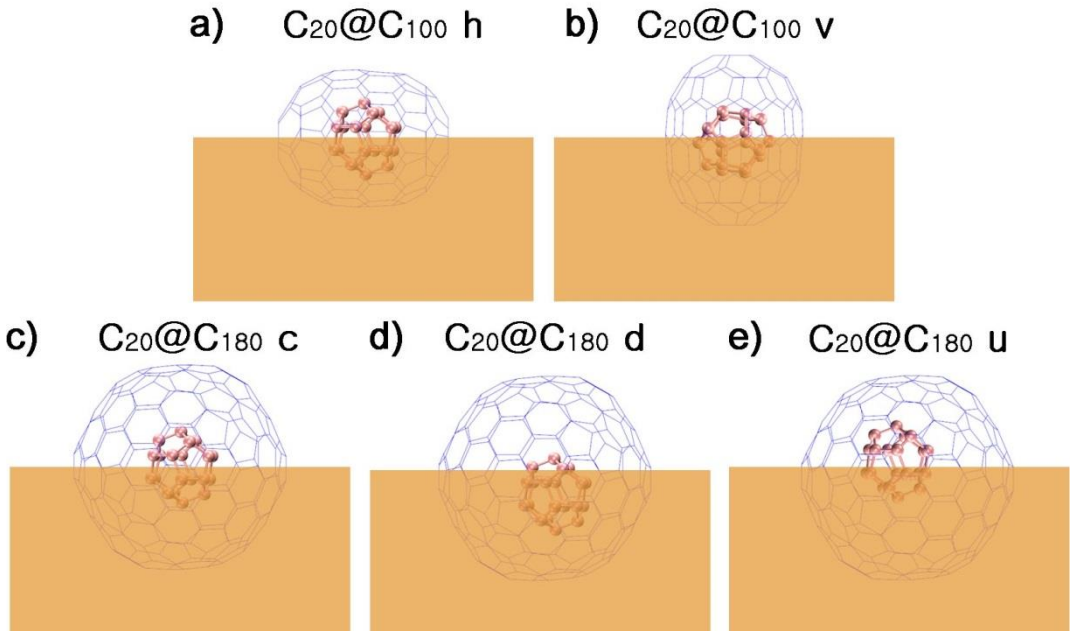

Figure 6.1: Schematic representation of the models studied for the Cu-onion interfaces. **a)** $C_{20}@C_{100}$ with the C_{20}'s centre of mass (CM) displaced 0.1 Å from the C_{100}'s CM, and the C_{100}'s longest axis **a)** parallel to the Cu(111) plane (horizontal, **h**, geometry) or **b)** perpendicular to the Cu(111) plane (vertical, **v**, geometry). **c)** $C_{20}@C_{180}$ with the C_{20}'s CM displaced 0.1 Å from the C_{180}'s CM. $C_{20}@C_{180}$ with the C_{20}'s CM displaced 3 Å from the C_{180}'s CM **d)** towards the slab (down **d** geometry) or **e)** away from the slab (up **u** geometry). Cu slab: transparent orange rectangle, C_{20}: pink, C_{100} and C_{180}: cyan.

6.4 Cu-C_{100} and Cu-C_{180} interfaces

Before analysing the interfaces between Cu and the $C_{20}@C_{100}$ and $C_{20}@C_{180}$ onions, we introduce, as future term of comparison, the changes induced on Cu by outer fullerenes alone. Given the more prolate shape of C_{100} with respect to C_{180}, also for the isolated C_{100} two geometries were studied: a vertical (v) one, where the C100's longest axis was initially placed perpendicular to the Cu(111) plane, and an horizontal (h) one for which the C_{100}'s longest axis was initially parallel to the Cu(111) plane (see also Fig. 6.1).

Fig. 6.2 summarises the main results for these systems. Regardless of the initial Cu-fullerene cut-off used to prepare the interface models, and the substantial Cu → fullerene charge-transfer (3-4.5 electrons depending on the fullerene and initial interface geometry, Fig. 6.2b) optimisation of the interface geometry leads to

minimal deviations of the C_{100} and C_{180}'s average pyramidalisation angle (θ_p) with respect to the values computed for the isolated molecules optimised in vacuum (Fig. 6.2a).

The larger Cu → fullerene charge-transfer for C_{100} and C_{180} (> 3 e) with respect to C_{60} (between 1.5 and 3 e, see Fig. 5.11 in Chapter 5), together with the decrease of θ_p (strain of the π-system) from ~12° (C_{60}, Fig. 5.15c in Chapter 5) following the C_{60} < C_{100} < C_{180} series, demonstrate that no direct correlation exists between the strain of the π-system and the effectiveness of the molecule in subtracting charge from the Cu-substrate. When analysed against the computed vacuum-aligned energy of the LUMO level (E_{LUMO} in Table 6.2) for the isolated fullerenes, the results for the interfacial Cu → fullerene charge-transfer confirm the findings of Chapter 5 (Fig. 5.11): the interfacial charge-transfer (substantially larger for C_{180} than for C_{60}) does not directly correlate with E_{LUMO} for the isolated molecule (-4.2 eV for both C_{180} and C_{60} in Table 6.2): it thus emerges that interfacial relaxation is the dominant factor governing the metal → molecule charge-transfer for the cases studied.

Table 6.2: Computed vacuum-aligned LUMO energy (E_{LUMO}, eV) and charge transfer per C atom (Q/C atom, e) for the considered fullerenes and onions optimised in vacuum.

System	E_{LUMO} (eV)	Q/C atom (e)
C_{20}	-4.07	0.101
C_{30}	-4.60	0.065
C_{60}	-4.20	0.023
C_{100}	-4.83	0.034
C_{180}	-4.20	0.019
$C_{20}@C_{100}$	-4.91	0.032
$C_{20}@C_{180}$	-4.47	0.015

Comparison between the results for the Cu-$C_{100/C180}$ (Fig. 6.2c-d) and Cu-C_{60} (Chapter 5, Figs. 5.8cf) interfaces reveal that besides being less effective than C_{60} in increasing the Stoner exchange integral (I_S) with respect to the FCC Cu bulk value, both C_{100} and C_{180} lead to smaller (by comparison to C_{60}) rise of the Density of States

at the Fermi level [DOS(E_F)], which turns out to be the smallest for C_{100}. As a result of the limited increase of both I_S and DOS(E_F), the I_S×DOS(E_F) products for the Cu-C_{100} and Cu-C_{180} interfaces are lower than for the analogous Cu-C_{60} (top) models (Fig. 6.2e). Thus, reductions of θ_p and of the strain on the molecular π-system as present for C_{100} and C_{180} turns out not to be effective in increasing the interfacial magnetic hardening with respect to C_{60}, that consequently remain the most performing fullerene out of the systems considered. In the next Sections I explore whether encapsulation of C_{20} inside C_{100} and C_{180} alter this conclusion.

Finally, as shown in Fig. 6.2f, and in analogy with what found for the partially inserted C_{60} in Chapter 5 (Fig. 5.8l), no immediate correlation appears to exist between the computed magnetic hardening of the Cu-fullerene interfaces, as quantified by the I_S×DOS(E_F) product, and the loosening of the Cu-lattice as quantified by the average sum of the 12 nearest-neighbour (NN) distances for the Cu(111)-6x6 slab.

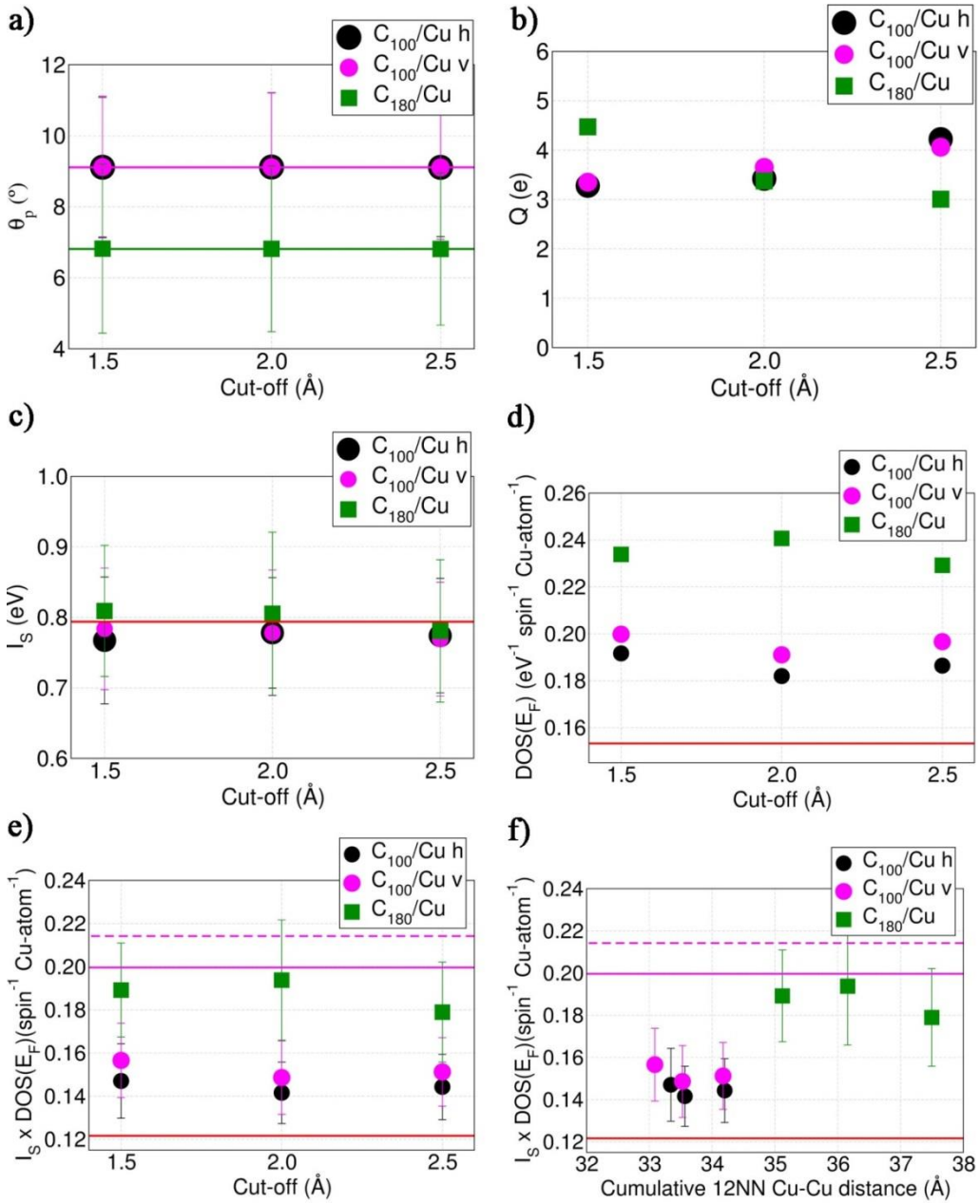

Figure 6.2: a) Average pyramidalisation angle (θ_p) for the C_{100} and C_{180} relaxed in the interface models studied. The values for the isolated fullerenes optimised in vacuum are marked by the magenta (C_{100}) and green (C_{180}) horizontal lines. **b)** Cu → fullerene Bader charge transferred (Q, e), **c)** Stoner exchange integral (I_S), **d)** Density of States at the Fermi level [$DOS(E_F)$], and **e)** $I_S \times DOS(E_F)$ product as a function of the initial Cu-fullerene cut-off distance. **f)** $I_S \times DOS(E_F)$ product as a function of the average cumulative 12 NN Cu-Cu distance in the optimised Cu-polymer interface models. The red line marks the value of for bulk FCC Cu at the optimised lattice parameter (3.649 Å). The continuous (dashed) magenta lines mark the minimum (maximum) $I_S \times DOS(E_F)$ value for the (top) Cu-C_{60} interfaces, see also Chapter 5, Fig.5.8i.

6.5 Geometric relaxation of the Cu-C_{20}@C_{100} and Cu-C_{20}@C_{180} interfaces

The optimised structures for the different Cu-onion interface-models considered is shown in Fig. 6.3. Unsurprisingly given the larger size of the C_{180} with respect to the C_{100} (Table 6.1 and Fig. 6.1), it is found that interface relaxation and loosening of the Cu lattice, as quantified by the by the average cumulative 12 nearest-neighbours (NN) Cu-Cu distances for the Cu atoms in the slab (Fig. 6.4), is larger for the C_{20}@C_{180} onion than for the C_{20}@C_{100} system.

Interestingly, both the v and h (Fig. 6.1) insertion geometries of the C_{20}@C_{100} in the Cu(111) slab lead to nearly identical loosening of the Cu-lattice, suggesting that it is the volume excluded by the fullerene, rather than the geometrical details of the interface to be key for the geometrical relaxation of the interface. Regardless of the different initial positions of the C_{20} inside the C_{180} and the resulting different optimised geometries (Fig. 6.3), all the C_{20}@C_{180} interfaces prepared with the same initial cut-off lead to minimally different loosening of the Cu-lattice (Fig. 6.4). This result strengthens the conclusion that it is the volume excluded by the outer fullerene to be of predominant importance for the geometrical relaxation of the interfaces between Cu and carbon-onions.

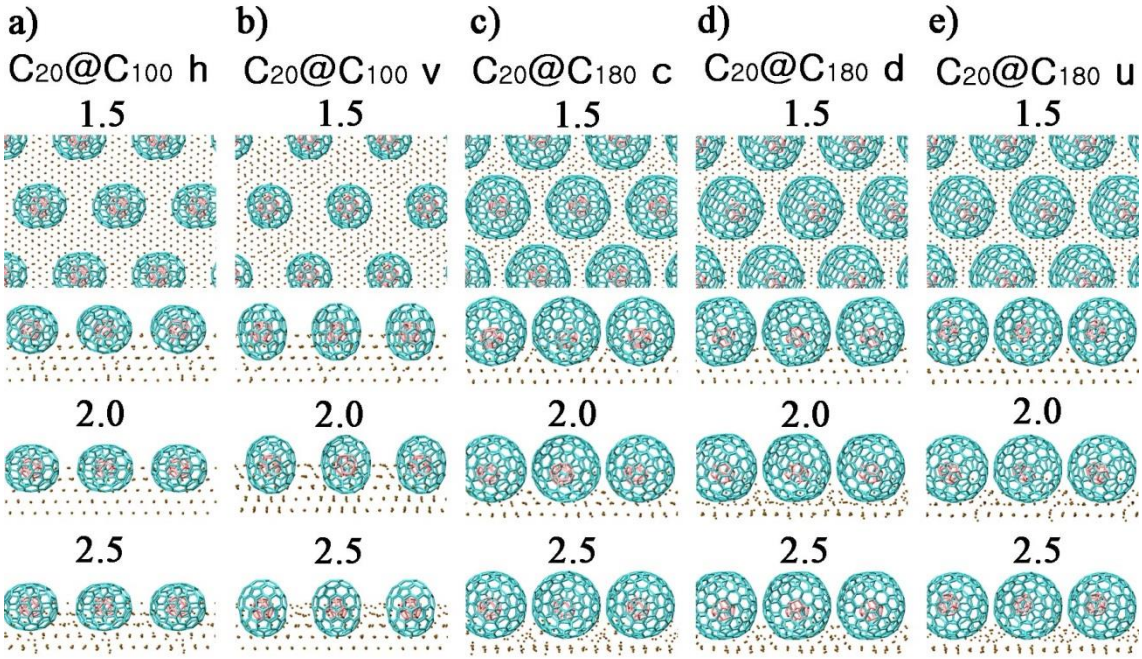

Figure 6.3: Top and side view of the optimised geometry as a function of the initial Cu-fullerene cut-off distances for the Cu-onions interface-models studied. Same labelling as in Fig. 6.1. Outer fullerenes: cyan, inner fullerene C_{20}: pink. Cu: brown.

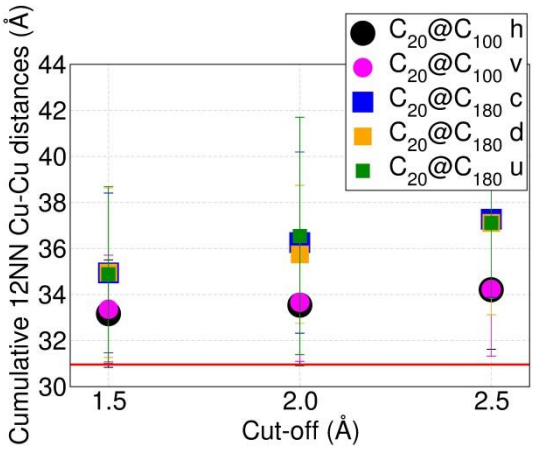

Figure 6.4: Onion-induced loosening of the Cu-lattice for the Cu-onion interfaces studied as quantified by the average sum of the 12 NN Cu-Cu distances in the optimised slabs. The horizontal red line marks the value of the cumulative 12 NN Cu-Cu distance (30.962 Å) for bulk FCC Cu at the optimised lattice parameter (3.649 Å).

6.6 Electronic structure of the Cu-C_{20}@C_{100} and Cu-C_{20}@C_{180} interfaces

In line with published results for Cu-C_{60} interfaces [1], and findings for the larger curvature fullerenes in Chapter 5 (Fig. 5.15), regardless of the interface relaxation and ensuing loosening of the Cu lattice (Fig. 6.4), all the Cu-onion interface models result in a well-defined *3d*-band with an absolute Density of States (DOS) maximum at about 1.5 eV below E_F, as present for bulk FCC Cu (Fig. 6.5). Consistent with the results of previous experimental and theoretical studies on C_{60}/Cu(111) interfaces [1, 21], and what found for C_{20} and C_{30} in Chapter 5 (Fig 5.5), also the present models are computed to have a non-zero Density of States at the Fermi energy [DOS(E_F)] and, consequently, to be metallic.

Analysis of the Cu- and fullerene-resolved PAW-projected DOS (PDOS), shown in Fig. 6.6, reveal over 80% larger contributions from the Cu atoms with respect to C-atoms at E_F. As previously found for π-conjugated polymers in Chapter 4 (Fig. 4.5) and individual fullerenes in Chapter 5 (Fig. 5.6), DOS(E_F) is evidently dominated by Cu-states also for the considered C_{20}@C_{100} and C_{20}@C_{180} onions.

Comparison between the contributions to the total onion-resolved PDOS from the inner and outer fullerenes, shown in Fig. 6.7, indicates that both for C_{20}@C_{100} and C_{20}@C_{180} the outer (C_{100} and C_{180}) fullerenes have a lower PDOS at the Fermi-level than C_{20}, revealing that the inner fullerene too is evidently coupled to Cu and involved in the ensuing metal-organic interfacial re-hybridisation. The appearance of a small gap at energies 0.1-0.2 eV below E_F for C_{20} in the Cu-C_{20}@C_{180} interfaces (but not in the C_{20}@C_{100} systems) indicate that, owing to the larger distances between fullerenes in this onion (Table 6.1 and Fig. 6.3) the coupling between C_{20}-Cu coupling is larger in the Cu-C_{20}@C_{100} interfaces than in the Cu-C_{20}@C_{180} ones. These results suggests that future consideration of endohedral fullerenes with an inorganic guest (atoms, ions or clusters) may be a rewarding strategy to explore for tuning and enhancement of interfacial magnetism.

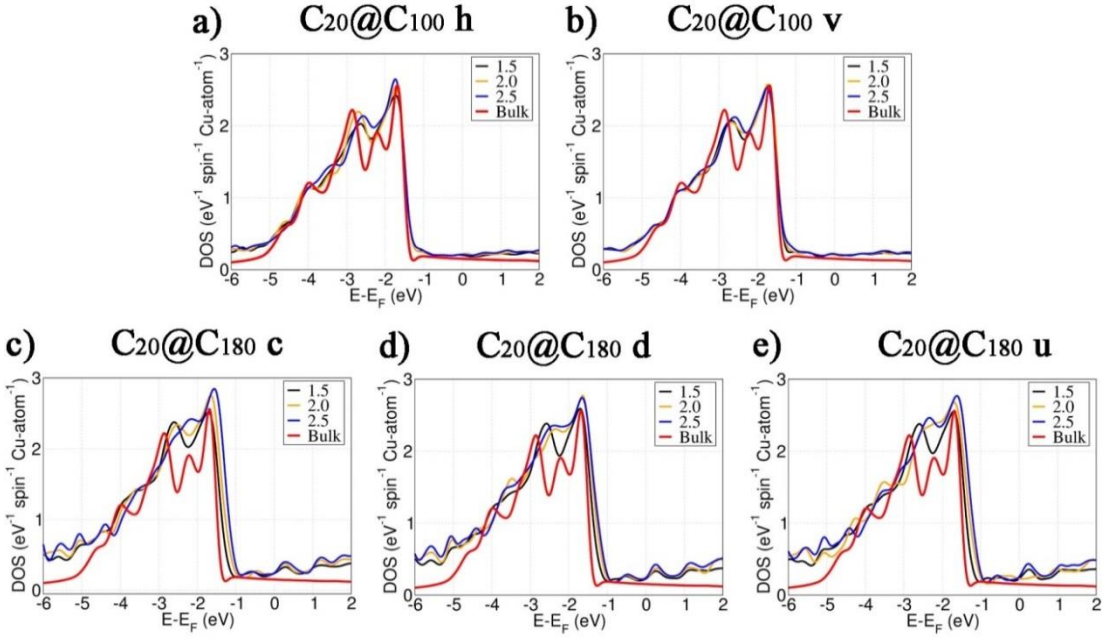

Figure 6.5: Computed density of states (DOS) for the Cu-onions interface models considered. The computed DOS for bulk FCC Cu is also shown for comparison. All the Cu-onion interface systems show a well-defined 3*d*-band with a maximum DOS around 1.5 eV below E_F, as present for bulk FCC Cu.

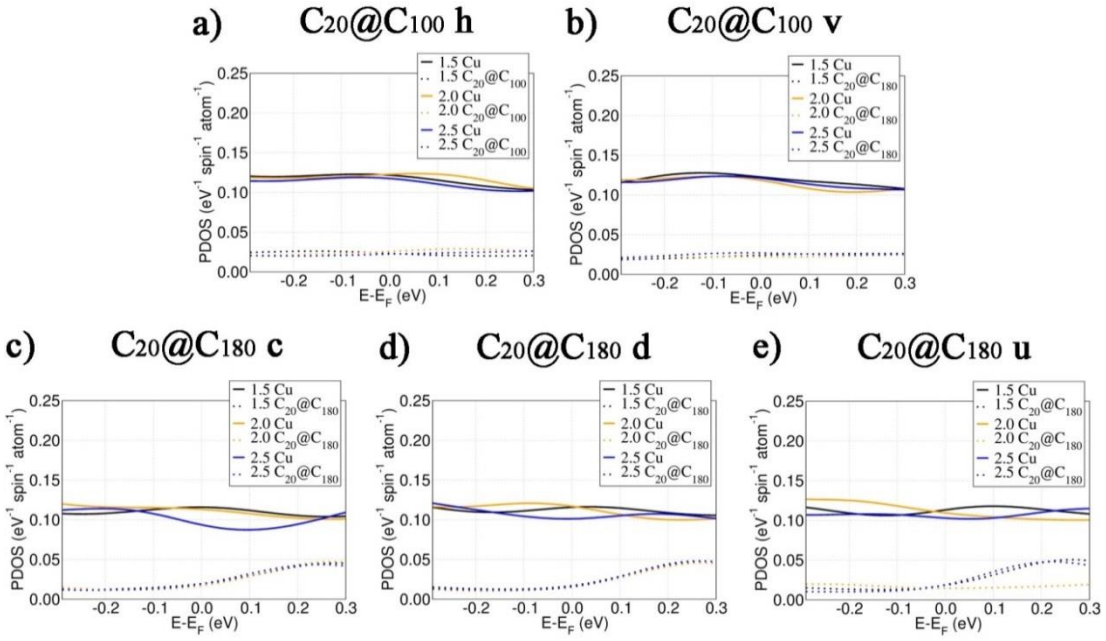

Figure 6.6: Cu (continuous lines) and onion (dotted lines) projected Density of States (PDOS) for the interface models considered. The contribution of the Cu atoms to the PDOS at E_F is 80% larger compared to the C atoms, i.e. the PDOS(E_F) is dominated by Cu-states.

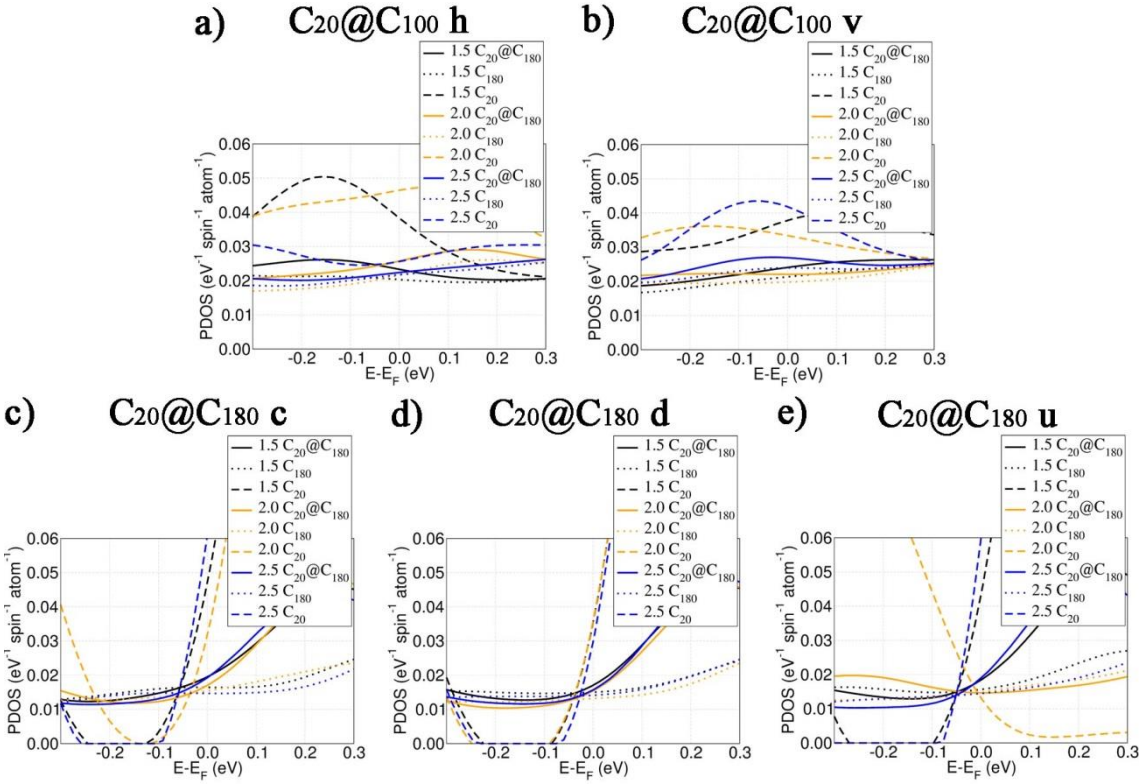

Figure 6.7: Total (continuous lines), inner fullerene (dashed) and outer fullerene (dotted) projected Density of States (PDOS) for the interface models considered. For all the considered systems, the outer (C_{100} and C_{180}) fullerenes have a lower PDOS(E_F) than C_{20}, indicating that the inner fullerene is involved in the metal-organic interfacial re-hybridisation as well. Cu-C_{20}@C_{180} interface systems show a small gap at energies 0.1-0.2 eV below E_F for C_{20} that is not present in the C_{20}@C_{100} systems. This indicates that the C_{20}-Cu coupling is larger for in the Cu-C_{20}@C_{100} interfaces than in the Cu-C_{20}@C_{180} ones.

6.7 Magnetic properties of the Cu-C_{20}@C_{100} and Cu-C_{20}@C_{180} interfaces

6.7.1 Interface-averaged magnetic properties

This Section investigates the effect of the different onion composition and geometry, as well insertion-geometry in the Cu slab, for the interface averaged magnetic properties. Fig. 6.8 shows the interface-averaged, band-splitting (ΔE) and atomic magnetic moment (m) for the considered Cu-onion systems. Unsurprisingly given the computed atom-resolved values in Appendix C Fig. C.1. and Fig. C.2, both the interface-averaged ΔE and m turn out to be lower than for the bulk FCC Cu. Both for C_{20}@C_{100} and C_{20}@$_{C180}$, a weak correlation emerges in that the systems prepared

with the largest (2.5 Å) Cu-C cut-off result in lower average values for both ΔE and m with respect to the interface-models prepared with the smallest (1.5 Å) cut-off.

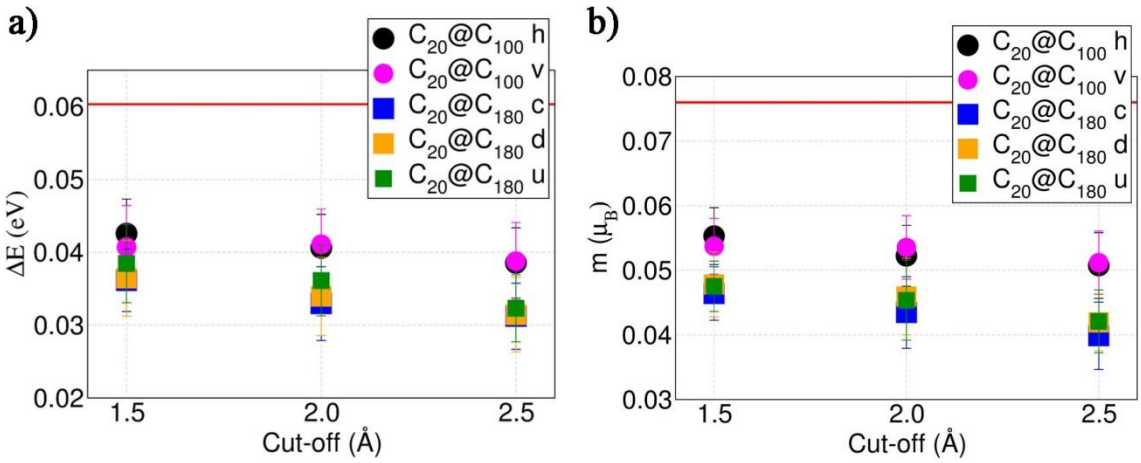

Figure 6.8: Interface-averaged **a)** band-splitting (ΔE) and **b)** atomic magnetic moment (m) as a function of the initial cut-off distance for the models considered. The horizontal red line marks the values for FCC bulk Cu at the optimised lattice parameter (3.649 Å).

In analogy with what found for the individual C_{100} and C_{180} fullerenes interfaced with Cu (Fig. 6.2), when averaged over the whole interface, the computed I_S values result to be minimally different from bulk FCC Cu, with deviations smaller than 0.05 eV (Fig. 6.9a). Conversely, the average Density of States at the Fermi energy [DOS(E_F)] is substantially larger (from 25% to up to over 60%) than for bulk FCC Cu (Fig. 6.9b). Combination of these two trends leads to interface-averaged I_S×DOS(E_F) products that, although substantially (at least 30%) larger than for bulk FCC Cu, remain consistently lower than for the (top) Cu-C_{60} interfaces (Fig. 6.9c below and Fig. 5.8i in Chapter 5). Based on these results, the Cu-C_{20}@C_{100} and Cu-C_{20}@C_{180} interfaces considered here are predicted not to be effective in enhancing the magnetic hardening of interfaces Cu with respect to what obtained (Fig. 6.9c) and measured for Cu-C_{60} systems [1].

In line with results for C_{60} completely inserted in the Cu slabs [1], thence in contrast with what found for partially inserted C_{20}, C_{30} and C_{60} in Chapter 5 (Fig. 5.8j-l), analysis of the dependence of the interface-averaged I_S×DOS(E_F) products on the

loosening of the Cu lattice, as quantified by the sum of the 12 NN Cu-Cu distances, indicate that. fullerenes onions of larger excluded volume half inserted on the Cu slab, leading to larger loosening of the Cu lattice (Fig. 6.4) result also in larger I_Sx$DOS(E_F)$, thence magnetic hardening, although of lower magnitude that for half-inserted C_{60} (Fig. 5.8), indicating that loosening of the Cu-lattice is not the driving factor in emergence of magnetic hardening at the interface.

In line with what found for C_{60} partially inserted into the Cu(111) slab in a top geometry (Chapter 5, Fig. 5.9), analysis of the dependence of the computed interface averaged I_S value on the total $DOS(E_F)$ of the interface does not result in any strong correlation (Fig. 6.10). These results indicate that the interface-averaged exchange interactions, as approximated by I_S, do not depend on the total $DOS(E_F)$. Therefore, it transpires that strategies to maximise $DOS(E_F)$ are not guaranteed to maximise also I_S (exchange interactions), as requested for maximum enhancement of the resulting interfacial magnetic hardening. Based on the result presented here and in Chapters 4 and 5, C_{60} appears to offer the best interfacial re-hybridisation with Cu (due to its excluded volume, curvature and the strain of its π-system) to simultaneously increase both I_S and $DOS(E_F)$, thence the $I_S \times DOS(E_F)$ product and the overall interfacial magnetic hardening. In the following Sections of this Chapter I further elaborate this statement by including in the analysis the result for the Cu → onion charge transfer and strain of the molecular π-system as quantified by the average fullerene pyramidalisation angle of the onion.

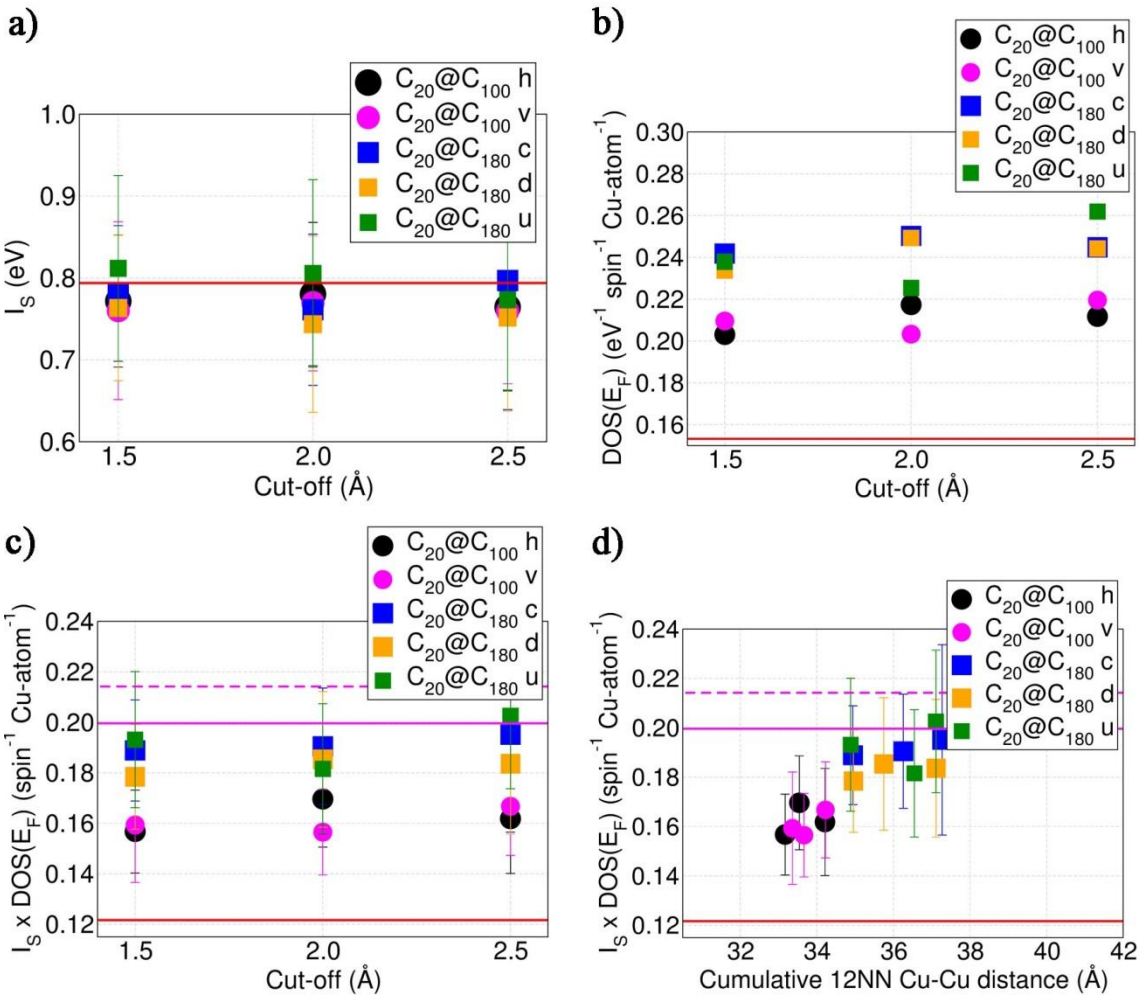

Figure 6.9: Interface-averaged **a)** Stoner exchange integral (I_s), **b)** Density of States at the Fermi level [DOS(E_F)] and **c)** I_s×DOS(E_F) product as a function of the initial cut-off used to prepare the Cu-onions systems considered. **d)** Average I_s×DOS(E_F) product as a function of the slab-averaged cumulative 12 NN Cu-Cu distance in the optimised models. The horizontal red line marks the values for optimised bulk FCC Cu. The horizontal continuous (dashed) magenta lines in (c)-(d) mark the smallest (largest) computed I_s×DOS(E_F) value for the top Cu-C_{60} interfaces in Appendix B (Fig. B.6.).

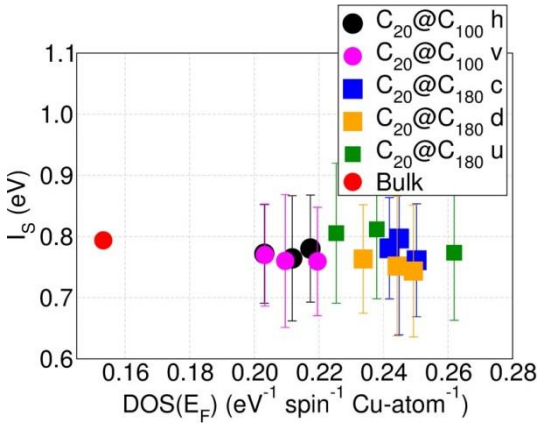

Figure 6.10: Interface-averaged Stoner exchange integral (I_S) as a function of the Density of States at the Fermi energy [DOS(E_F)] for the Cu-onion interface considered.

6.7.2 The role of the interfacial Cu → onion charge-transfer

This Section investigates the role of the Cu → onion charge-transfer for the emerging magnetic properties of the interfaces. Based on its lower computed vacuum-aligned E_{LUMO} (Table 6.2), neglecting interface atomic and electronic effects, the $C_{20}@C_{100}$ onion (E_{LUMO} = −4.91 eV) would be expected to subtract more electronic charge from Cu than the $C_{20}@C_{180}$ (E_{LUMO} = −4.47 eV). The comparable (~4 e) Cu → onion charge transferred onto $C_{20}@C_{100}$ and $C_{20}@C_{180}$ in the interface models prepared with the smaller cut-offs (1.5 and 2.0 Å) contradicts such expectation (Fig. 6.11a). However, for the models prepared with the largest (2.5 Å) cut-off, the computed charge-transfer for the $C_{20}@C_{100}$ system (still ~4 e) does become larger than for the $C_{20}@C_{180}$ onion (~3 e) as expected based on the higher E_{LUMO} of the latter. Inspection of the computed charge-transfer (Fig. 6.11a) and Cu-loosening (Fig. 6.4) reiterates that conclusion, the increased loosening of the Cu-lattice does not directly lead to enhancement of the Cu → onion charge transfer.

In line with what computed for smaller C_{20}, C_{30} and C_{60} fullerenes in Chapter 5 (Fig. 5.12), no direct correlation is found between the interfacial charge-transfer and the resulting interface-averaged DOS(E_F) (Fig. 6.11b), m (Fig. 6.12), ΔE (Fig. 6.12), I_S (Fig.6.11c and 6.12), and I_S×DOS(EF) product (Fig. 6.11d). These results strengthen the conclusion of Chapter 5 that maximisation of the I_S×DOS(E_F) product or,

equivalently of the interface magnetic hardening, cannot be guaranteed by maximisation of the interfacial charge-transfer. The structural and electronic details of the interfacial re-hybridisation, leading to simultaneous increase of the I_S and $DOS(E_F)$, thence of the $I_S \times DOS(E_F)$ product, appear to be more important.

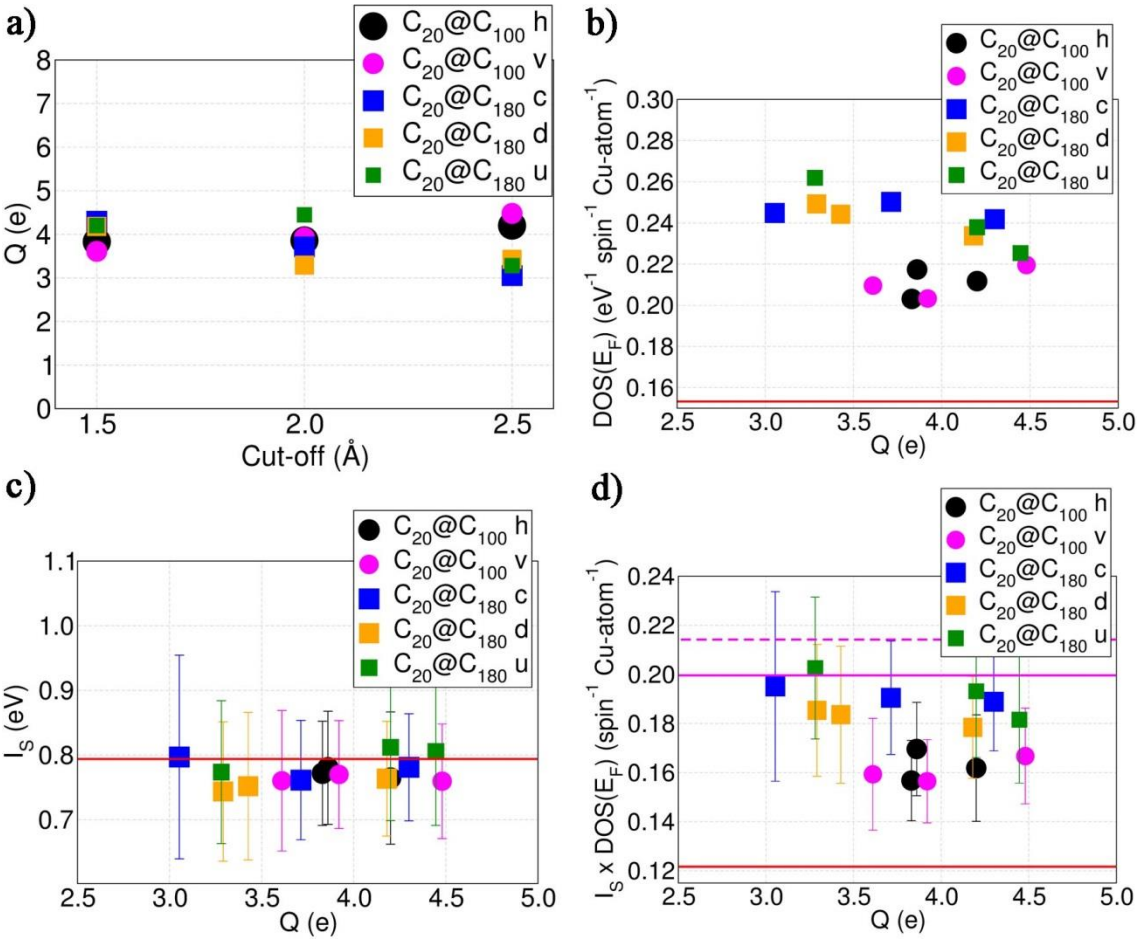

Figure 6.11: a) Computed Cu → onion Bader charge transferred (Q, e) as a function of the initial Cu-onion cut-off distance. Interface-averaged **b)** $DOS(E_F)$, **c)** I_S and **d)** $I_s \times DOS(E_F)$ product as a function of Q.

I conclude this Section by investigating the redistribution of the Cu → onion charge-transferred inside the onion between the different constituting fullerenes. As shown in appendix C Fig. C.3, in all cases most of the electronic charge subtracted to the Cu substrate result localised on the outer C_{100} and C_{180} fullerenes (from over 60% to nearly 98%). The localisation of excess charge from the Cu-slab on the inner C_{20} fullerene (from nearly 0 to 1 e) appears to be more sensitive to the details of the interface relaxation than the presence of an outer C_{100} or C_{180}. Based on the limited number of systems considered here (only $C_{20}@C_{100}$ and $C_{20}@C_{180}$) further simulations are needed to assess whether these conclusion can be transferred across the many carbon onion that are nowadays available [2-15].

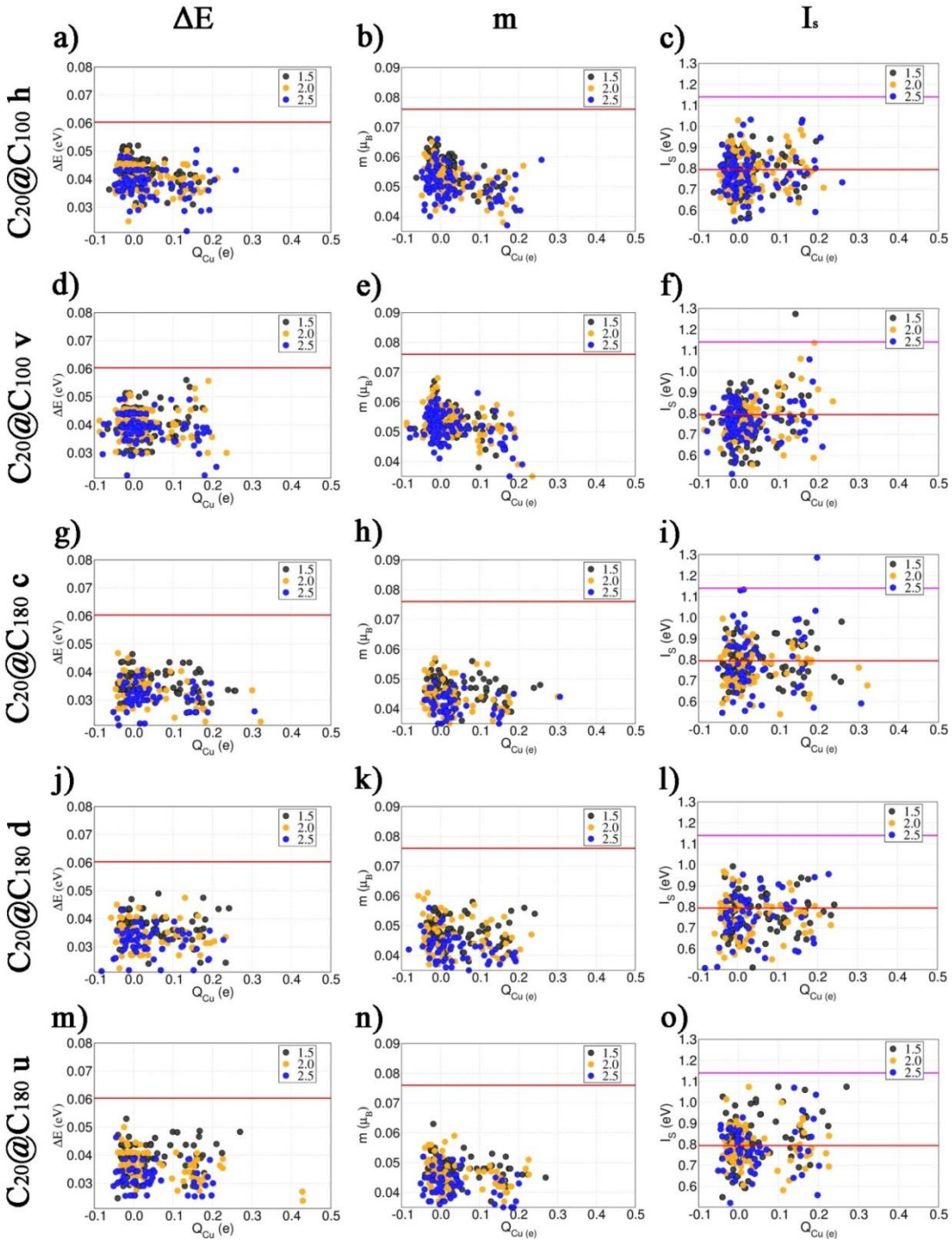

Figure 6.12: Cu-atom resolved band-splitting (ΔE), atomic magnetic moment (m) and Stoner exchange integral (I_S) for the fullerene-onions/Cu interface models studied as a function of the Cu atomic Bader charge. The horizontal red line marks the values for FCC bulk Cu at the optimised lattice parameter (3.649 Å). The horizontal continuous magenta line indicates the maximum I_S value (1.25 eV) computed for the interface between Cu and as deposited (1.7 gr/cm^3) amorphous carbon, measured to be ferromagnetic [20].

In line with results for single fullerenes (Fig. 5.10 in Chapter 5), analysis of the dependence of the interface-averaged $I_S \times DOS(E_F)$ products on the ratio between the Projected Density of States at the Fermi level of carbon atoms [$PDOS_C(E_F)$] over the PDOS of Cu atoms [$PDOS_{Cu}(E_F)$] indicate that interfaces composed by smaller fullerene onions ($C_{20}@C_{100}$) and Cu are more hybridised, i.e. the $PDOS_C(E_F)$ / $PDOS_{Cu}(E_F)$ ratio is larger. As shown in Fig. 6.11, the charge-transfer is not correlated to the $PDOS_{Cu}(E_F)$. Larger charge-transfer leads to increase of $PDOS_c(E_F)$ / $PDOS_{Cu}(E_F)$ ratio which does not directly enhance the magnetic properties of the system as shown in Fig. 6.13.

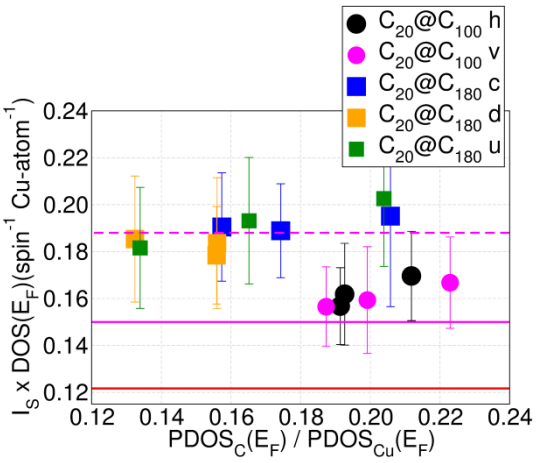

Figure 6.13: Average $I_S \times DOS(E_F)$ product as a function of the ratio between the Projected Density of States at the Fermi level for the carbon [$PDOS_C(E_F)$] and Cu [$PDOS_{Cu}(E_F)$] atoms. The horizontal red line marks the values for optimised bulk FCC Cu. The horizontal continuous (0.15 $spin^{-1}$ $atom^{-1}$) and dashed (0.19 $spin^{-1}$ $atom^{-1}$) magenta lines mark the largest computed $Is \times DOS(E_F)$ product at the same level of theory for interfaces between Cu and as deposited (1.7 gr/cm^3) and annealed (2.3 gr/cm^3) aC measured to be ferromagnetic in Ref. [20].

6.7.3 The role of strain on the molecular π-system

I conclude this Chapter by analysing the role of strain on the π-system of the carbon onions, as quantified by the corresponding average pyramidalisation angle (θ_p), for the interfacial magnetic properties.

As previously done in Chapter 5 (Section 5.6.3) and for the isolated C_{100} and C_{180} fullerenes (Fig. 6.2), θ_p is defined as the angle measuring the deviation from co-planarity for the three bonds of the sp^2 C-atoms in the molecules. From this definition it follows that the smaller the curvature of the fullerene, the larger the average θ_p and, consequently, the larger the strain on the molecular π-system. For the following analysis I computed both onion-averaged and fullerene-resolved θ_p values.

Comparison between θ_p for the $C_{20}@C_{100}$ and $C_{20}@C_{180}$ onions relaxed in vacuum and at the interface with Cu (Fig. 6.14a, 6.14d, 6.14g, 6.14j and 6.14m) reveals negligible effects on θ_p of the relaxation of the Cu-$C_{20}@C_{180}$ interface. Conversely, for $C_{20}@C_{100}$, the C_{100} (C_{20}) resolved θ_p is larger (smaller) than computed for the analogous systems in vacuum, leading to an overall increase of θ_p also for the whole onion with respect to the vacuo results. Thus, the interface relaxation for $C_{20}@C_{100}$ and $C_{20}@C_{180}$ turns out to be qualitative different, being the changes on the Cu-substrate (Fig. 6.4) and onion largest for $C_{20}@C_{180}$ and $C_{20}@C_{100}$, respectively.

Analysis of the relationship between θ_p for the onions and the resulting interface-averaged Stoner exchange integral (I_s) does not reveal any strong correlation, being the I_S values scattered between 0.75 eV and 0.80 eV for both the $C_{20}@C_{180}$ and $C_{20}@C_{180}$ systems (Fig. 6.14b, 6.14e, 6.14h, 6.14k and 6.14n). Conversely, comparison between the computed $I_S \times DOS(E_F)$ products for the $C_{20}@C_{100}$ and $C_{20}@C_{180}$ systems (Fig. 6.14c, 6.14f, 6.14i, 6.14l and 6.14o) clearly indicates that the reduced average θ_p for the outer C_{180} (~7°) with respect to C_{100} (~10°) result in enhanced magnetic hardening for the interface with Cu. When compared against the θ_p values for Cu-C_{60} (~12°), Cu-C_{30} (~17°) and Cu-C_{20} (~21°) interfaces (Chapter 5, Fig. 5.15) and resulting $I_S \times DOS(E_F)$ products (largest for C_{60}, Fig. 6.9) it is inevitable to note that the C_{60}, with its intermediate θ_p (larger than ~7° for C_{180} and ~10° for C_{100} yet smaller than ~17° for C_{30}) and resulting strain on the molecular π-

system offers, out of the systems considered, the most effective interfacial re-hybridisation towards magnetic hardening of Cu. Based on these results, it remains to be assessed by future work whether fullerenes of similar curvature but different symmetry and electron-accepting properties from C_{60} (e.g. C_{70} not considered in this Thesis), can lead to substantial differences (or not) in the interfacial magnetic hardening of Cu.

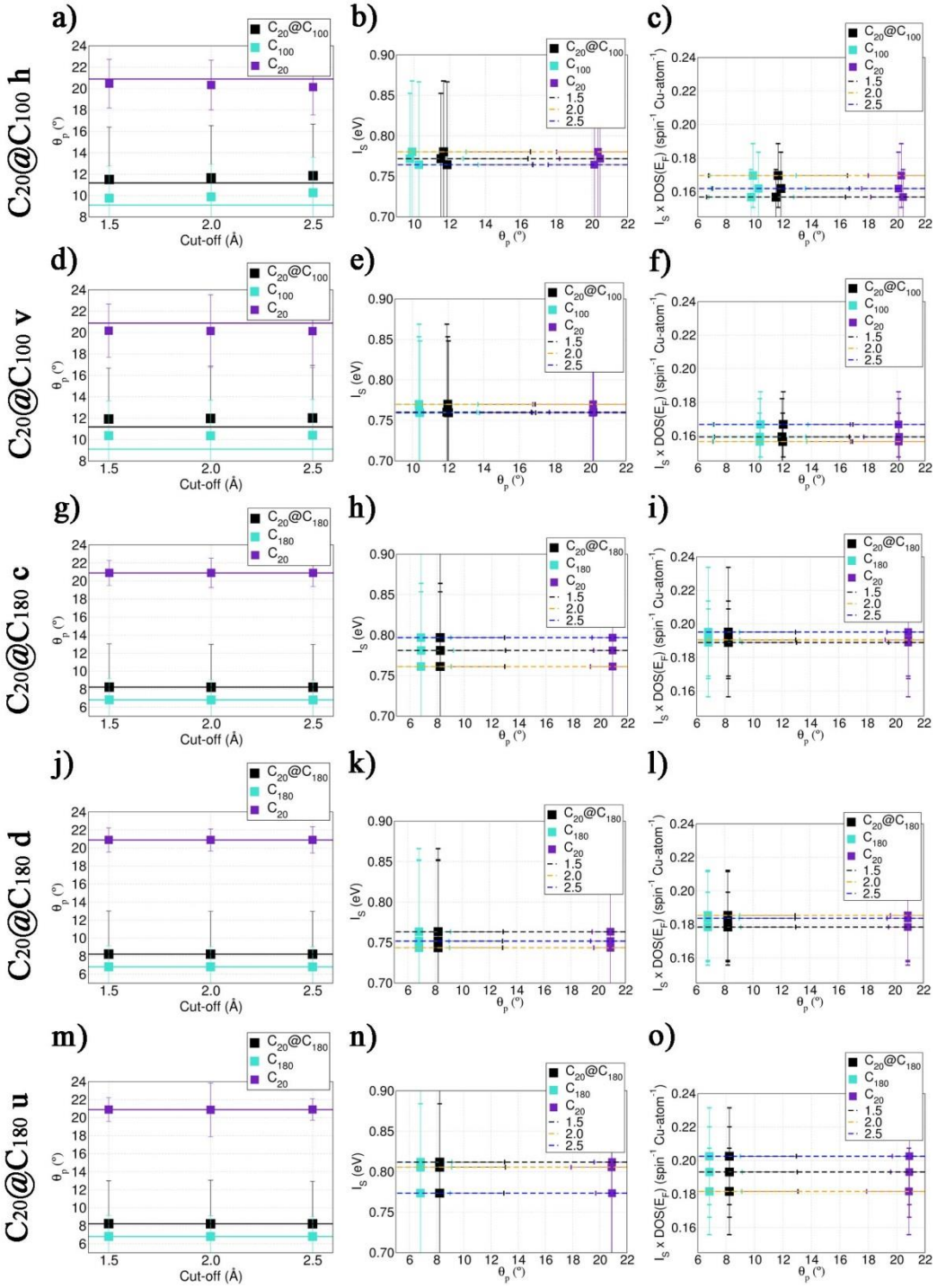

Figure 6.14: a, d, g, j, m) Average pyramidalisation angle (θ_p) and associated standard deviation as a function of the initial Cu-onion cut-off for the optimised interface models. **b, e, h, k, n)** Interface-averaged Stoner exchange integral (I_S), and **c, f, i, l, o)** $I_S \times DOS(E_F)$ product as a function of θ_p for the Cu-onion interfaces considered.

6.8 Conclusions

DFT simulations have been used to investigate the role of larger than C_{60} fullerenes and fullerene-encapsulation for the magnetic hardening of interfaced Cu-substrates. Analysis of the simulations for several models of the interfaces between Cu and C_{100} and C_{180} fullerenes as well as $C_{20}@C_{100}$ and $C_{20}@C_{180}$ onions indicate that:

i) Regardless of the use of the individual C_{100} and C_{180} fullerene or their carbon onions, and the initial geometry of the models, relaxation of the interface consistently leads to metallization of the organic systems. Notably, the simulations suggest metallization also for the inner C_{20} fullerene in $C_{20}@C_{100}$ and $C_{20}@C_{180}$, indicating that metal molecule re-hybridisation is not limited to the outer fullerene only but substantially extends to the inner system too. This result suggests that future consideration of endohedral fullerenes with an inorganic guest (atoms, ions or clusters) may be a rewarding strategy to explore towards tuning and enhancement of interfacial magnetism.

ii) At least for the cases considered, the computed Cu → onion charge-transfer is found not to be generally correlated with the vacuum-aligned energy of the LUMO for the isolated onion or constituting fullerenes. In general, enhancement of the Cu-lattice loosening does not majorly enhance interfacial charge transfer that results instead suppressed for $C_{20}@C_{180}$ (but not for $C_{20}@C_{100}$). These results are in qualitative agreement with what found for smaller C_{20}, C_{30} and C_{60} fullerenes (Chapter 5), and for planar π-conjugated polymers (Chapter 4), suggesting a non-negligible role of the strain of the molecular π-system in tuning the interfacial charge transfer.

iii) Owing to the substantial increase in DOS(E_F) and a more limited increase in I_S the considered interfaces between Cu and individual C_{100} and C_{180} as well as $C_{20}@C_{100}$ and $C_{20}@C_{180}$ onions are predicted not to increase the interfacial magnetic hardening with respect to the Cu-C_{60} cases. Consequently, C_{60} emerges as the most effective systems, out of those explored in this Thesis, in inducing magnetic hardening at its interfaces with Cu-substrates.

iv) In spite of a comparable interfacial charge-transfer, the magnetic hardening induced by $C_{20}@C_{180}$ is larger than what computed for $C_{20}@C_{100}$. This result reiterates the conclusion of Chapters 4 and 5 that the details of the metal-organic re-hybridisation, rather than the net charge-transfer, are critical for enhancing the magnetic hardening at Cu-fullerene and Cu-onions interfaces.

v) Analysis of the interplay between curvature of the fullerene in the onions and resultant strain on the molecular π-systems on the hand, and emergent magnetic properties on the other confirms that mildly strained π-systems, as present in C_{60}, are more effective in promoting interfacial magnetic hardening than more strained (as present in C_{30} and C_{20}) or less strained (as present in the individual C_{100} and C_{180} or the $C_{20}@C_{100}$ and $C_{20}@C_{180}$ onions) ones.

When considered with the findings presented in the rest of the Thesis, the results of this Chapter enable the conclusion that out of the all the systems studies (polymers with planar π-systems, non π-conjugated polymers, highly strained fullerenes, low-strain fullerenes and related carbon-onions), C_{60} emerges as the most effective system in inducing magnetic hardening of its interfaces with Cu. Based on the evidenced strong electron coupling and re-hybridisation between the inner fullerene and the Cu-substrate for the considered carbon-onions, exploration of the use of an inorganic core (atoms, ions, clusters) as possible for endohedral fullerenes (starting from the C_{60} itself) could be meaningfully pursued in the development of further strategies to tune and enhance interfacial magnetic hardening for Cu (or other light transition metal) substrates.

6.9 References

1. Al Ma'Mari, F., et al., *Beating the Stoner criterion using molecular interfaces.* Nature, 2015. **524**(7563): p. 69-73.
2. Subramoney, S., *Novel nanocarbons—structure, properties, and potential applications.* Advanced Materials, 1998. **10**(15): p. 1157-1171.
3. Sano, N., et al., *Nanotechnology: Synthesis of carbon'onions' in water.* Nature, 2001. **414**(6863): p. 506.

4. Caiulo, N., et al., *Carbon-Decorated FePt Nanoparticles.* Advanced Functional Materials, 2007. **17**(8): p. 1392-1396.
5. Che, R., et al., *Microwave absorption enhancement and complex permittivity and permeability of Fe encapsulated within carbon nanotubes.* Advanced Materials, 2004. **16**(5): p. 401-405.
6. Ugarte, D., *Canonical structure of large carbon clusters: Cn, n> 100.* EPL (Europhysics Letters), 1993. **22**(1): p. 45.
7. Ugarte, D., *Onion-like graphitic particles.* Carbon, 1995. **33**(7): p. 989-993.
8. Mordkovich, V., *The observation of large concentric shell fullerenes and fullerene-like nanoparticles in laser pyrolysis carbon blacks.* Chemistry of materials, 2000. **12**(9): p. 2813-2818.
9. Oku, T., I. Narita, and A. Nishiwaki, *Formation, atomic structural optimization and electronic structures of tetrahedral carbon onion.* Diamond and related materials, 2004. **13**(4): p. 1337-1341.
10. Verkhovtsev, A., A.V. Korol, and A.V. Solov'yov, *Photoionization of multishell fullerenes studied by ab initio and model approaches.* The European Physical Journal D, 2016. **70**(10): p. 221.
11. Türker, L., *A bucky onion from C 20 and C 60—an AM1 treatment.* Journal of Molecular Structure: THEOCHEM, 2001. **545**(1): p. 207-214.
12. Dolgonos, G., *Which Fullerene Is Appropriate to Host C20? A Molecular Modeling Study.* Fullerenes, Nanotubes and Carbon Nanostructures, 2003. **11**(2): p. 155-164.
13. Mar, N., et al., *Symmetric nested complexes of fullerenes.* Journal of molecular modeling, 2015. **21**(4): p. 101.
14. Grimme, S., C. Mück-Lichtenfeld, and J. Antony, *Noncovalent interactions between graphene sheets and in multishell (hyper) fullerenes.* The Journal of Physical Chemistry C, 2007. **111**(30): p. 11199-11207.
15. Zope, R.R., et al., *Site specific atomic polarizabilities in endohedral fullerenes and carbon onions.* The Journal of Chemical Physics, 2015. **143**(8): p. 084306.

16. Kresse, G. and J. Furthmüller, *Efficient iterative schemes for ab initio total-energy calculations using a plane-wave basis set.* Physical Review B, 1996. **54**(16): p. 11169.
17. Perdew, J.P., K. Burke, and M. Ernzerhof, *Generalized gradient approximation made simple.* Physical Review letters, 1996. **77**(18): p. 3865.
18. Henkelman, G., A. Arnaldsson, and H. Jónsson, *A fast and robust algorithm for Bader decomposition of charge density.* Computational Materials Science, 2006. **36**(3): p. 354-360.
19. Schwarz, K. and P. Mohn, *Itinerant metamagnetism in YCO2.* Journal of Physics F: Metal Physics, 1984. **14**(7): p. L129.
20. Al Ma'Mari, F., et al., *Emergent magnetism at transition-metal–nanocarbon interfaces.* Proceedings of the National Academy of Sciences, 2017. **114**(22): p. 5583-5588.
21. Tamai, A., et al., *Electronic structure at the C 60/metal interface: an angle-resolved photoemission and first-principles study.* Physical Review B, 2008. **77**(7): p. 075134.

Chapter 7

Extended conclusions

The work presented in this Thesis is meant to extend the available understanding of the fundamentals of electronic re-hybridisation and emergence of magnetic ordering at the interfaces between Cu and organic substrates. Specifically, this Thesis has investigated the role of the Cu lattice distortion, metal-organics charge-transfer, organic π-conjugation and strain of the π-systems as well as molecular encapsulation for the magnetic hardening at the interfaces between Cu and an organic substrate. This exploration has been conducted by application of Density Functional Theory formalism as implemented in the VASP code.

The first part of this Thesis overviews previous experimental and theoretical investigations, highlighting the versatility of metal-organic interfaces in terms of low cost and their ease of functionalization for spintronics devices. To explore the influence of the composition and structure on the magnetic properties arising at the interfaces, several interfaces between FM metals-organic molecules (polymers) have been described. Furthermore, attention is paid also to recent experiments where interfaces between originally non-FM metals and non-magnetic organic molecules have been found capable to promote magnetism. It is detailed how several effects such as the role of metal-organics charge-transfer, organic π-conjugation and strain of the π-systems for the magnetic hardening at the metal-organic interface, have not been studied in detail. The work presented here aims to continue to expand our understanding of the in hybrid metal-organic interface and quantify the relative importance of the lattice distortion and charge transfer for the Cu magnetic hardening.

Chapter 2 describes the formulation of Density Functional Theory (DFT). The chapter begins with an introduction to the ground state many-body-time-independent Schrödinger equation and describing the practical impossibility of solving it for any meaningful system, which leads to the necessity of introducing approximations such as the Born-Oppenheimer one and the use of the total electron density instead of the coordinates of all the electrons in the system. The fundamentals of DFT its underpinning by the Hohenberg-Kohn theorems are described. Then, it is explained how the Kohn-Sham (KS) equations enables practical approximate solution to the many-body problem. Finally, the most important approximations and numerical strategies employed to practically solve the KS equations are described. In the second part of the Chapter, the basic theory of magnetism, including Stoner model for ferromagnetism and itinerant metamagnetism, is introduced.

In the second part of this Thesis the results of the simulations carried out are presented. Chapter 3 explores the influence of the isotropic deformation of the Cu bulk in the FCC and the effects of tetragonal, orthorhombic and monoclinic distortions on the magnetic properties of Cu. The expansion (compression) of the bulk FCC leads to a 30% increase of the magnetic hardening (softening) of the Cu. However, this increment is substantially smaller (-30%) than the previously reported for Cu-C_{60} interfaces, confirming that the isotropic FCC expansion may not be the most effective path to induce Cu magnetic hardening. On the other hand, distortion of the FCC-symmetry leads to slightly magnetic softening of the Cu bulk. These results suggest that the protection of a local FCC coordination is necessary to magnetically harden Cu.

The next chapter (Chapter 4) is focussed on disentangling the role of the molecular π-conjugation for the magnetic hardening of Cu-organics interfaces. For this purpose, several interface models made up of Cu and different polymers of different steric hindrance, π-conjugation and electron-accepting properties, namely polyethylene (PE), polyacetylene (PAC), polyethylene terephthalate (PET) and polyurethane (PUR) have been simulated. The results indicate that all the considered interface systems are metallic. Surprisingly, in-plane Cu-PE interface models exhibit the largest $I_s \times DOS(E_F)$ product, thence magnetic hardening, out of all the systems

studied. On the other hand, PAC-Cu systems with the most extended π-conjugation and the largest charge-transfer result in the smallest computed magnetic hardening. These results suggest that neither molecular π-conjugation nor substantial charge-transfer may be strictly needed for magnetic hardening of Cu-substrates. The work presented here open up new research directions in the study of non π-conjugated molecules for magnetic hardening and emergent magnetism at transition-metal-organic interfaces.

Chapter 5 explores the role fullerene curvature and adsorption sites for the magnetic hardening of Cu-fullerene interfaces. Analysis of Cu-fullerenes interfaces of different size, curvature and strain of the molecular π-system, namely C_{20}, C_{30} and C_{60} reveals that the interface of all the Cu-fullerenes systems leads to metallization of the fullerene. Furthermore, contrary to the results for the polymer-Cu systems, the interfacial charge-transfer decreases with the loosening of the Cu-lattice which suggests a non-negligible role of the strain of the molecular π-system in tuning the interfacial relaxation and ensuing charge-transfer. Cu-C_{60} interfaces show larger values for the computed Is×DOS(E_F) products compared to Cu-C_{20} and Cu-C_{30} interfaces, suggesting that C_{60} is more effective in inducing Cu magnetic hardening. Among all the simulated Cu-C_{60} interface models, the systems with smallest charge-transfer exhibit larger values of Is×DOS(E_F). This result confirms that the metal-organic re-hybridisation, rather than the net charge-transfer, plays a critical role for enhancing the magnetic hardening at Cu-organic interfaces. Moreover, analysis on the strain of the molecular π-system reveals that mildly strained π-systems, as present in C_{60}, are more effective in promoting interfacial magnetic hardening than strongly strained (C_{30} and C_{20}) or planar such as the polymers presented in Chapter 4. The analysis of considered adsorption geometries suggest that the initial site adsorption becomes more important for the emerging magnetic properties as the size of the fullerene increases $C_{60} > C_{30} > C_{20}$.

Building on these results, in the final Chapter of this Thesis, the magnetic hardening of interfaces between Cu and fullerenes of smaller curvature (larger fullerenes) as well as fullerene-onions has been analysed. Several models of the interfaces between Cu and C_{100} and C_{180} fullerenes as well as C_{20}@C_{100} and C_{20}@C_{180} onions have been

investigated. Relaxation of the interface consistently leads to metallization of the organic systems which also is extended to the inner fullerene. For the considered fullerene-onions, the loosening of the Cu-lattice does not enhance the interfacial charge-transfer. These results are in qualitative agreement with what found for smaller C_{20}, C_{30} and C_{60} fullerenes Chapter 5, suggesting a non-negligible role of the strain of the molecular π-system in tuning the interfacial charge transfer. These results reiterate that the metal-organic re-hybridisation, rather than the net charge-transfer, is critical for enhancing the magnetic hardening at Cu-organic interfaces. Moreover, the analysis of the curvature of the fullerene in the onions, the strain on the molecular π-systems and the magnetic hardening confirms that mildly strained π-systems, as present in C_{60}, are more effective in promoting interfacial magnetic hardening than more strained (as present in C_{30} and C_{20}) or less strained (as present in the individual C_{100} and C_{180} or the $C_{20}@C_{100}$ and $C_{20}@C_{180}$ onions) ones.

The key results of this Thesis are summarised in Fig 7.1, Table 7.1 and Table 7.2. A schematic representation of the different molecules studied in this system is found in Fig. 7.1 with the values the computed vacuum-aligned LUMO energy (Table 7.1). Based on the results of this Thesis, C_{60}-Cu interface emerges as the most effective system in inducing Cu magnetic among all the studied systems: polymers with planar π-systems, non π-conjugated polymers, highly strained fullerenes, low-strain fullerenes and related carbon-onions as shown in Table 7.2.

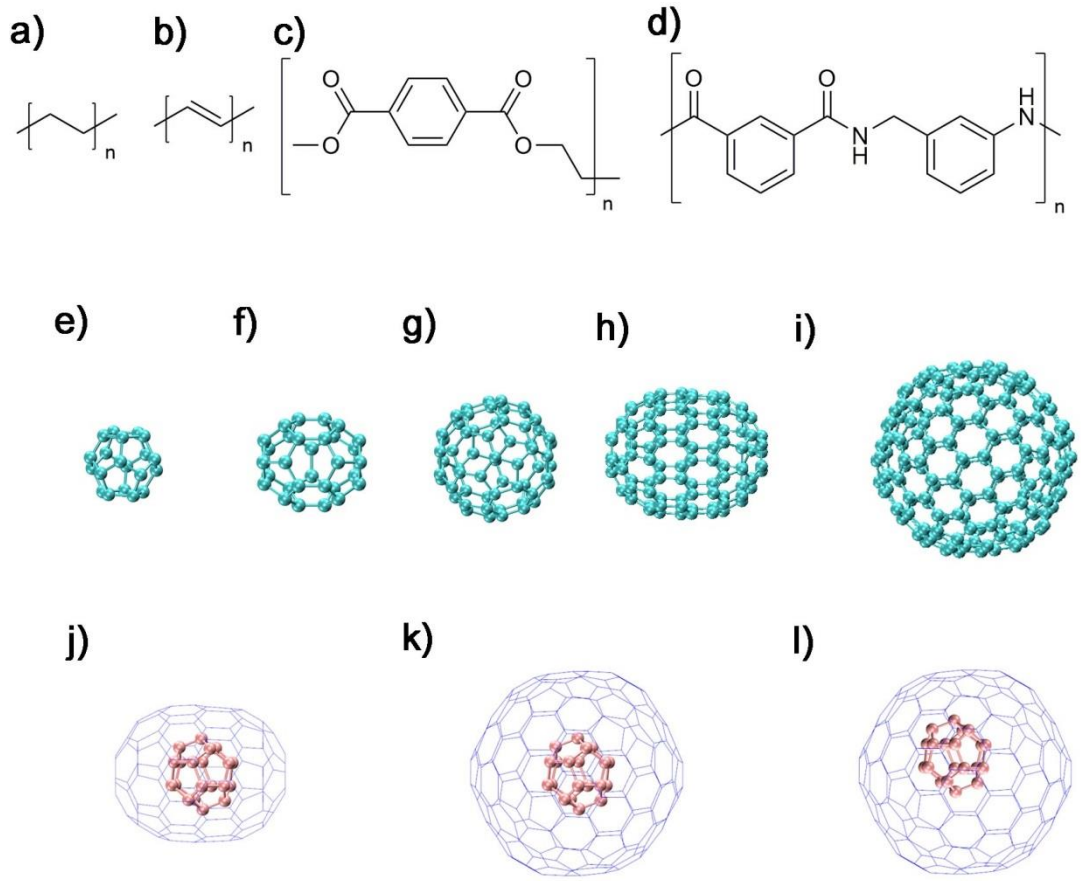

Figure 7.1: Schematic representation of the different molecules considered in this Thesis: **a)** polyethylene (PE), **b)** polyacethylene (PAC), **c)** polyethylene terephthalate (PET), **d)** polyurethane (PUR), **e)** C_{20} (I_h), **f)** C_{30} (C_{2v}), **g)** C_{60} (I_h), **h)** C_{100} (I_h), **i)** C_{180} (I_h), **j)** $C_{20}@C_{100}$, **k)** $C_{20}@C_{180}$ c, **l)** $C_{20}@C_{180}$ u or d.

Table 7.1: Computed vacuum-aligned LUMO energy (E_{LUMO}, eV) for the considered molecules optimised in vacuum.

Molecule	E_{LUMO} (eV)
PE	-0.85
PAC	-3.68
PET	-3.28
PUR	-1.68
C_{20}	-4.07
C_{30}	-4.60
C_{60}	-4.20
C_{100}	-4.83
C_{180}	-4.20
C_{20}@C_{100}	-4.91
C_{20}@C_{180}	-4.47

Table 7.2: Largest computed values of I_SxDOS(E_F) for each considered molecule/Cu interface specifying the inserting geometry and the initial cut-off.

Molecule	Insertion geometry	Cut-off (Å)	I_SxDOS(E_F) (spin^{-1} Cu-atom^{-1})
PE	In-plane	2.0	0.21
PAC	Perpendicular	2.5	0.18
PET	Perpendicular	2.5	0.16
PUR	Perpendicular	1.5	0.14
C_{20}	Top	1.5	0.19
C_{30}	Bridge	2.0	0.20
C_{60}	Fcc	2.5	0.25
C_{100}	Top v	1.5	0.16
C_{180}	Top	2.0	0.19
C_{20}@C_{100}	Top h	2.0	0.17
C_{20}@C_{180}	Top u	2.5	0.20

On a final note, it is observed that the computed strong coupling between inner fullerenes and Cu-substrates found for the $C_{20}@C_{100}$ and $C_{20}@C_{180}$ onions in Chapter 6, suggest that use of endohedral fullerenes (fullerenes with an inorganic host inside) may also be worth of attention towards enhancement of magnetic hardening of Cu via interfacial re-hybridisation. In this respect, experimentally available endohedral fullerenes such as $Li@C_{60}$ or $K@C_{60}$ [1, 2] should be studied following the procedures detailed in this Thesis to quantify the extent of re-hybridisation between the guest ion and the Cu lattice and the effects of interfacial magnetic hardening.

Last but least, based on the computed findings of a larger importance of the fullerene curvature, rather the electron-accepting properties, for the interfacial magnetic hardening, study of fullerenes of similar curvature to but different symmetry and electron-accepting properties from C_{60} (e.g. C_{70} [3]) should be very useful to further substantiate (or perhaps exclude) the proposed leading role of the strain of the fullerene π system for the interfacial magnetic hardening.

1. Pavanello, M., et al., *Fullerene as an electron buffer: charge transfer in Li@ C60.* Chemical Physics letters, 2007. **442**(4-6): p. 339-343.
2. Shinohara, H., *Endohedral metallofullerenes.* Reports on Progress in Physics, 2000. **63**(6): p. 843.
3. Deguchi, S., R.G. Alargova, and K. Tsujii, *Stable dispersions of fullerenes, C60 and C70, in water. Preparation and characterization.* Langmuir, 2001. **17**(19): p. 6013-6017.

Appendix A

This appendix is a further analysis of Chapter 4. The atom-resolved band splitting (ΔE), atomic magnetic moment (m) and Stoner exchange integral (I_S) of the Cu-polymer interfaces have been computed as a function of the shortest Cu-C, Cu-H, Cu-O and Cu-N distances (Fig A.1), cumulative Cu-Cu distances (Fig. A.2) and Cu atomic Bader charge (Fig. A.3).

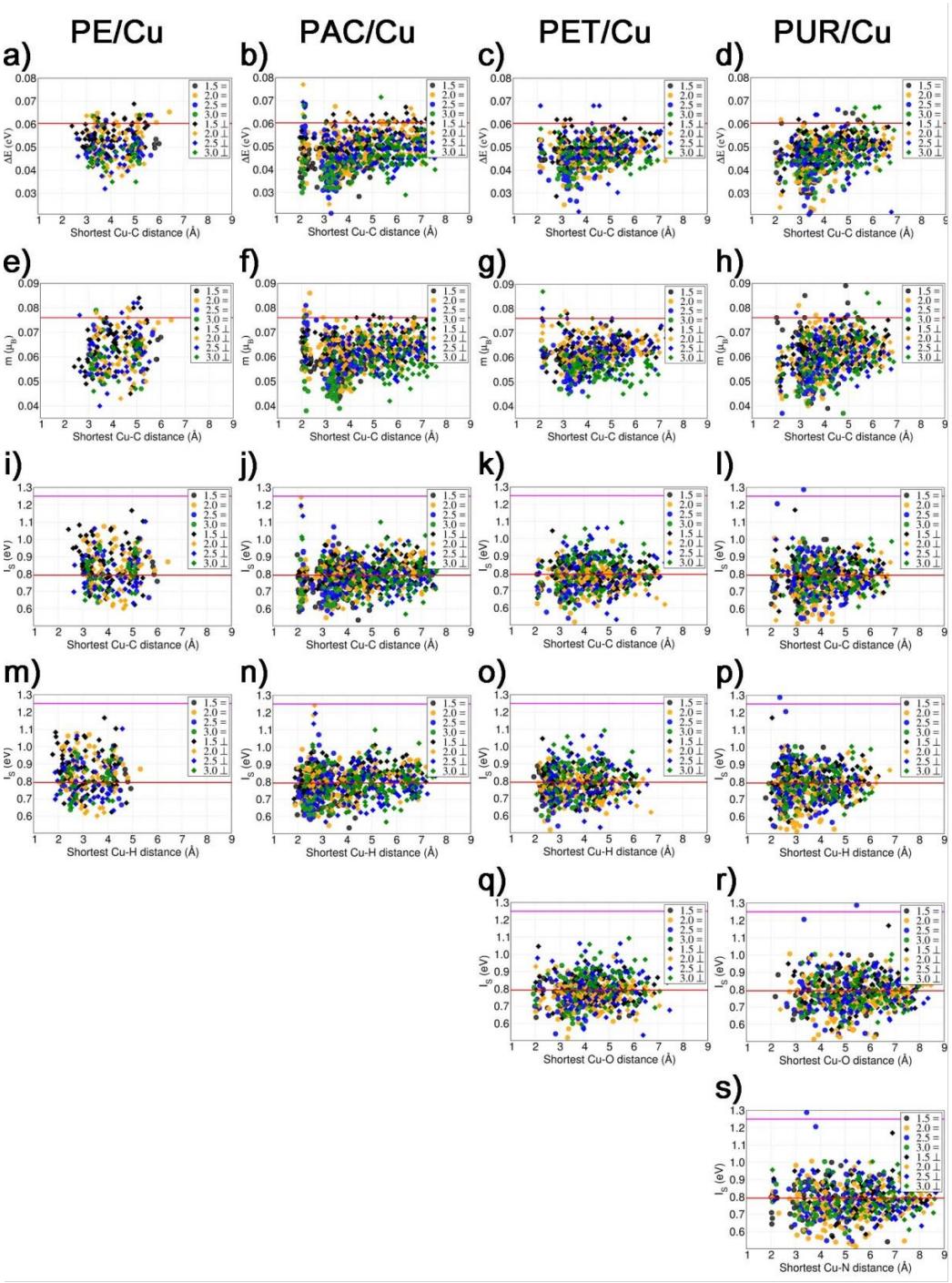

Figure A.1: Cu-atom resolved band-splitting (ΔE), atomic magnetic moment (m) and Stoner exchange integral (I_S) for the Cu-polymer interface models studied as a function of the shortest Cu-C (**a-l**), Cu-H (**m-p**), Cu-O (**q-r**) and Cu-N (**s**) distance. The horizontal red line marks the values for FCC bulk Cu at the optimized lattice parameter (3.649 Å). The horizontal continuous magenta line in panels (i-s) marks the maximum I_S value (1.25 eV) computed for the interface between Cu and as deposited (1.7 gr/cm^3) amorphous carbon, measured to be ferromagnetic in Ref. [7] Chapter 4. It is observed that the band-splitting of the considered polymer-Cu systems is generally smaller than the reference Cu-bulk.

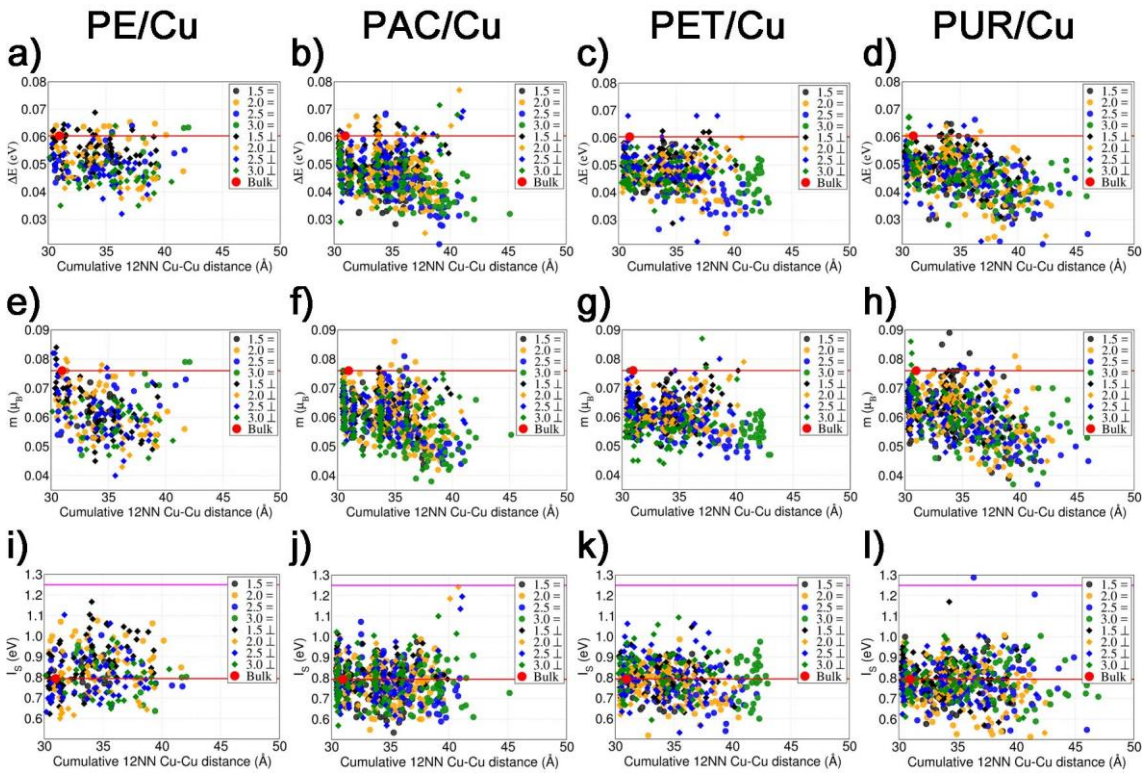

Figure A.2: Cu-atom resolved band-splitting (ΔE), atomic magnetic moment (m) and Stoner exchange integral (I_S) for the Cu-polymer interface models studied as a function of the cumulative 12 NN Cu-Cu distances. The horizontal red line marks the values for FCC bulk Cu at the optimized lattice parameter (3.649 Å). The horizontal continuous magenta line in panels (i-l) marks the maximum I_S value (1.25 eV) computed for the interface between Cu and as deposited (1.7 gr/cm^3) amorphous carbon, measured to be ferromagnetic in Ref. [7] Chapter 4. As observed in Fig. 10 i-l, there is no correlation between the increment of the Stoner exchange integral and the loosening of the Cu lattice.

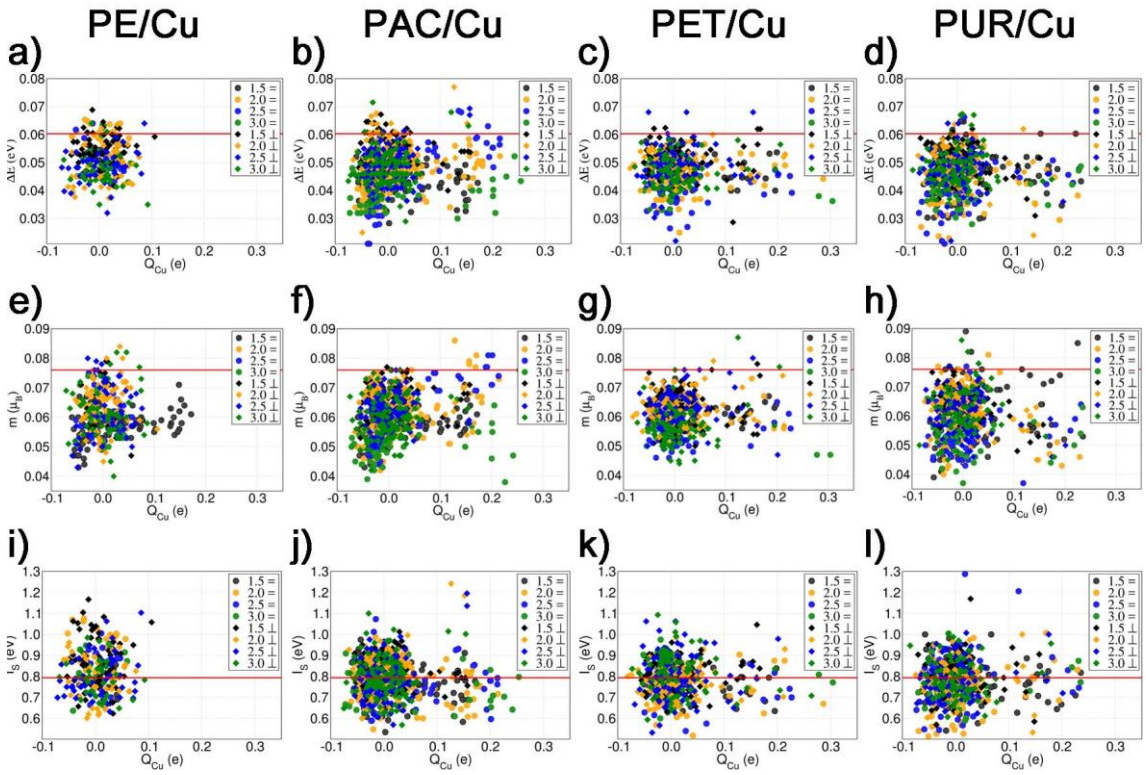

Figure A.3: Cu-atom resolved band-splitting (ΔE), atomic magnetic moment (m) and Stoner exchange integral (I_S) for the Cu-polymer interface models studied as a function of the Cu atomic Bader charge. The horizontal red line marks the values for FCC bulk Cu at the optimised lattice parameter (3.649 Å). The horizontal continuous magenta line in panels (i-l) marks the maximum I_S value (1.25 eV) computed for the interface between Cu and as deposited (1.7 gr/cm^3) amorphous carbon, measured to be ferromagnetic in Ref. [7] Chapter 4. No direct correlation is evident between the atomic charges on Cu atoms and the computed magnetic hardening. This result suggests a main role of the Cu-organic re-hybridisation rather than the charge transfer for the interface magnetic hardening.

Appendix B

This appendix is related to Chapter 5, the magnetic properties of the fullerenes (C_{20}, C_{30} and C_{60}) are analysed as a function of the Cu-C and Cu-Cu distances. Figure B.1, B.2 and B.3 include the computed atom- resolved band splitting (ΔE), magnetic moments (m) and Cu-resolved I_S respectively as a function of the shortest Cu-C distance. On the other hand, Figures B.4, B.5, B.6 represents the computed atom-resolved ΔE, m and I_S, respectively, as a function of the Cu-lattice loosening, quantified by the sum of the 12 nearest-neighbours (NN).

As shown in Fig. B.1, regardless of the size of the fullerene and initial adsorption site, the computed Cu-resolved, PAW-integrated, band splitting (ΔE) turns out to be either minimally increased (by less than 0.01 eV) or substantially decreased (by up to nearly 85%) with respect to the value for bulk FCC Cu. Similar considerations (either minimal increase or substantial decrease) hold also for the computed atom resolved magnetic moments (m) shown in Fig. B.2. No strong correlation is found between the computed ΔE and m for a given Cu-atom and its distance from the fullerene cage.

The direct (inverse) contribution of ΔE and m to the approximated Stoner exchange integral (I_S, Chapter 2, Eq. 2.88) leads to scattering of the computed Cu-resolved I_S values both above and below the result for bulk FCC Cu, with largest values in the 1.1-1.3 eV range for all the different systems considered (Fig. B.3), close and in cases above the largest value computed for as deposited ferromagnetic Cu-aC systems (I_S=1.25 eV) [10].

Analysis of the computed atom-resolved ΔE (Fig. B.4) and m (Fig. B.5) as a function of the Cu-lattice loosening, quantified by the sum of the 12 nearest-neighbours (NN) distances, does not reveal any strong correlation between these parameters. Stronger correlation is instead found for their ratio i.e. the computed I_S as a function of the lattice loosening (Fig. B.6). Interestingly, whereas loosening of the Cu-lattice is

computed to lead to larger Cu-resolved I_S values for the interfaces prepared with initial top and bridge adsorption sites, the opposite trend (smaller I_S values for larger Cu-lattice loosening) is found for the hcp and fcc interfaces. Together with the computed sensitivity of the total (P)DOS(E_F) on the initial geometry (Fig. 5.5 and Fig. 5.6), these results provide further evidence that the details of the interfacial re-hybridization and ensuing tuning of electronic and magnetic properties does depend on the initial geometry of the interface ahead of structural relaxation. In the following I explore the extent to which the interface-averaged magnetic properties depend on the initial geometry.

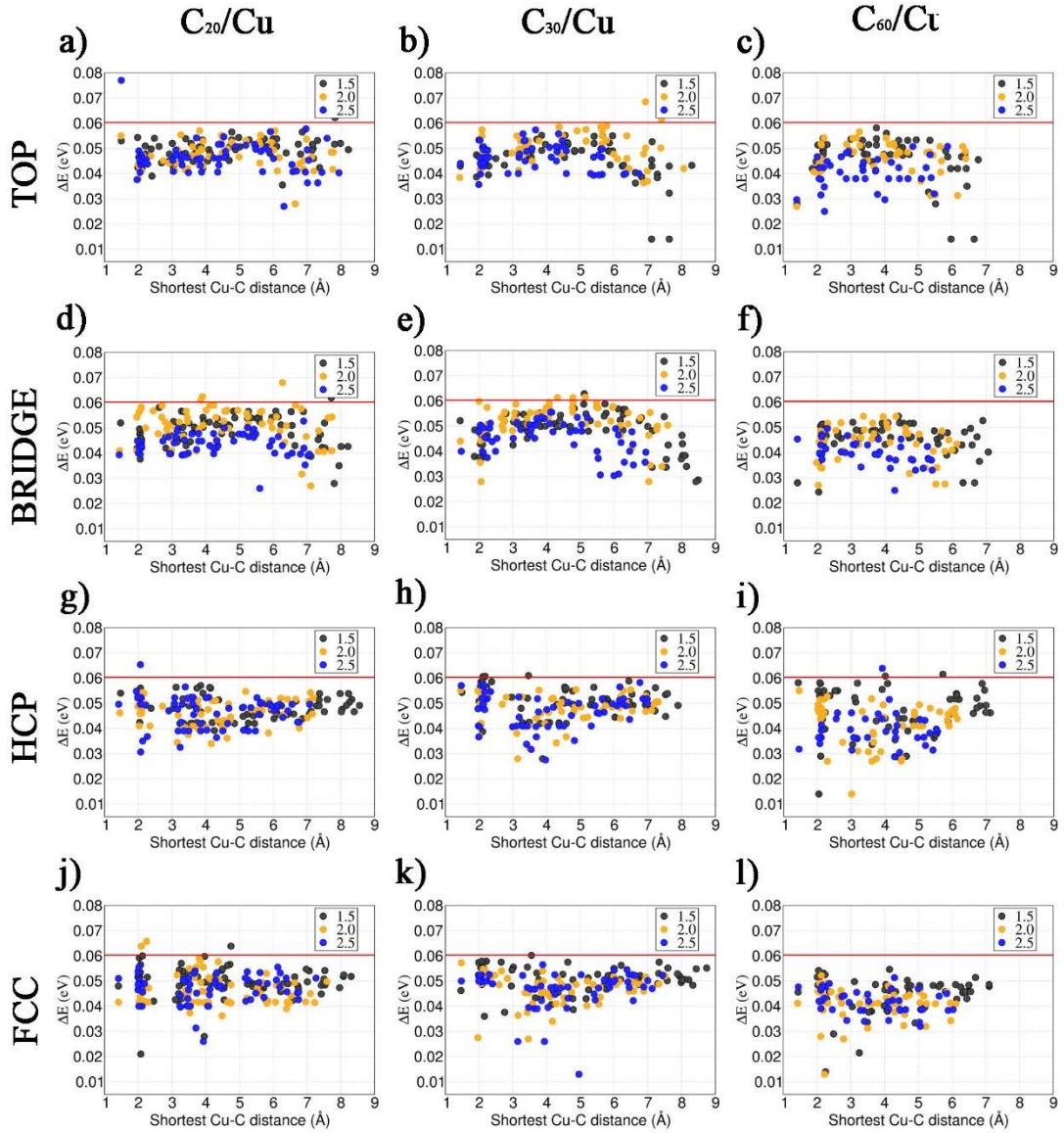

Figure B.1: Cu-atom resolved band-splitting (ΔE) as a function of the shortest Cu-C distance for the simulated Cu-fullerene interfaces. The horizontal red line marks the value of the ΔE for bulk FCC Cu at the optimised lattice parameter (3.649 Å). The computed ΔE is either minimally increased (by less than 0.01 eV) or substantially decreased (by up to nearly 85%) with respect to the value for bulk FCC Cu. Moreover, there is not a strong correlation between the computed ΔE and the Cu-fullerene distance.

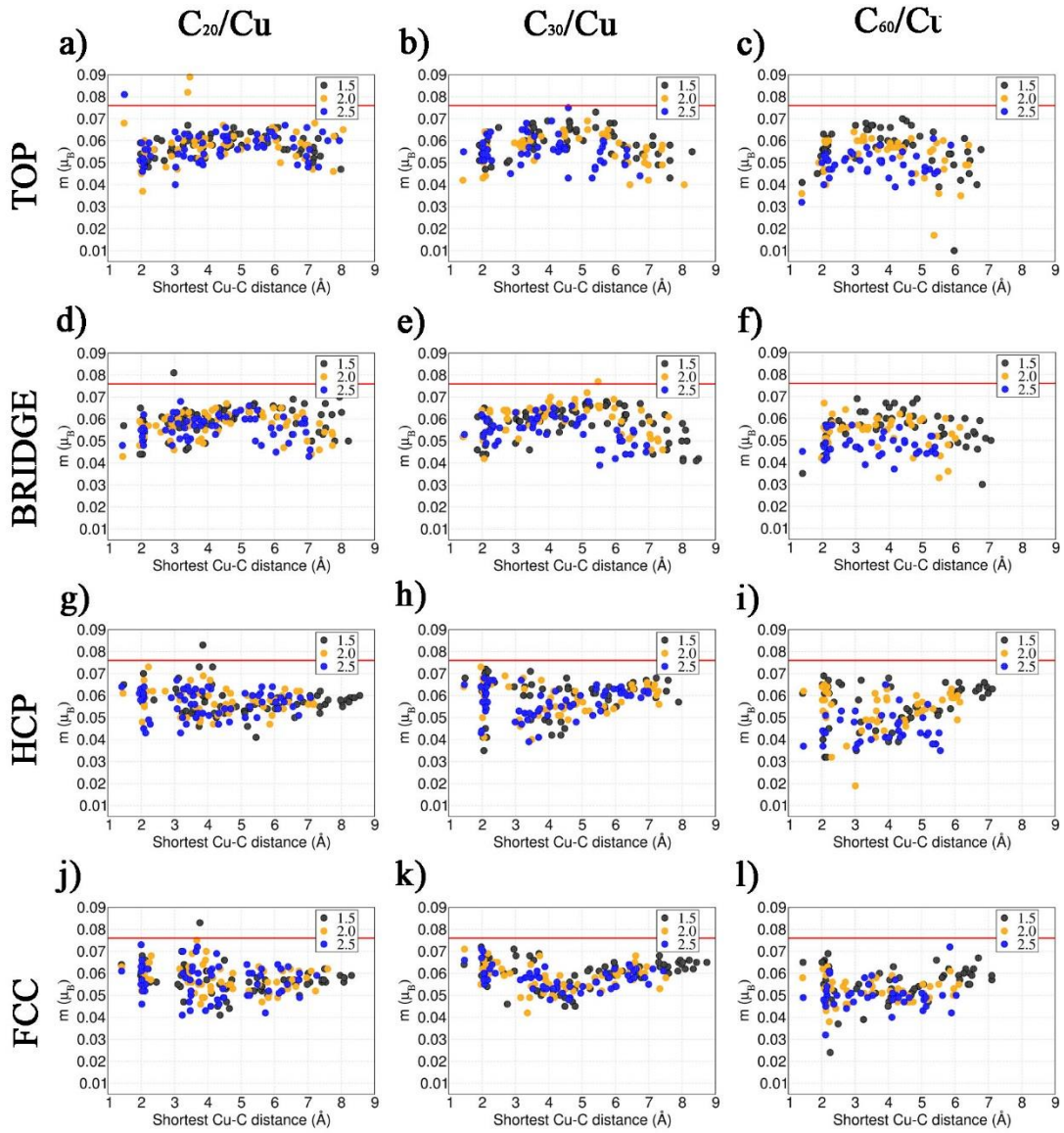

Figure B.2: Cu-atom resolved magnetic moment (m) as a function of the shortest Cu-C distance for the simulated Cu-fullerene interfaces. The horizontal red line marks the value of the ΔE for bulk FCC Cu at the optimised lattice parameter (3.649 Å). Substantial decrease of the atom resolved m is observed. There is no strong correlation between the m for a given Cu-atom and its distance from the fullerene cage.

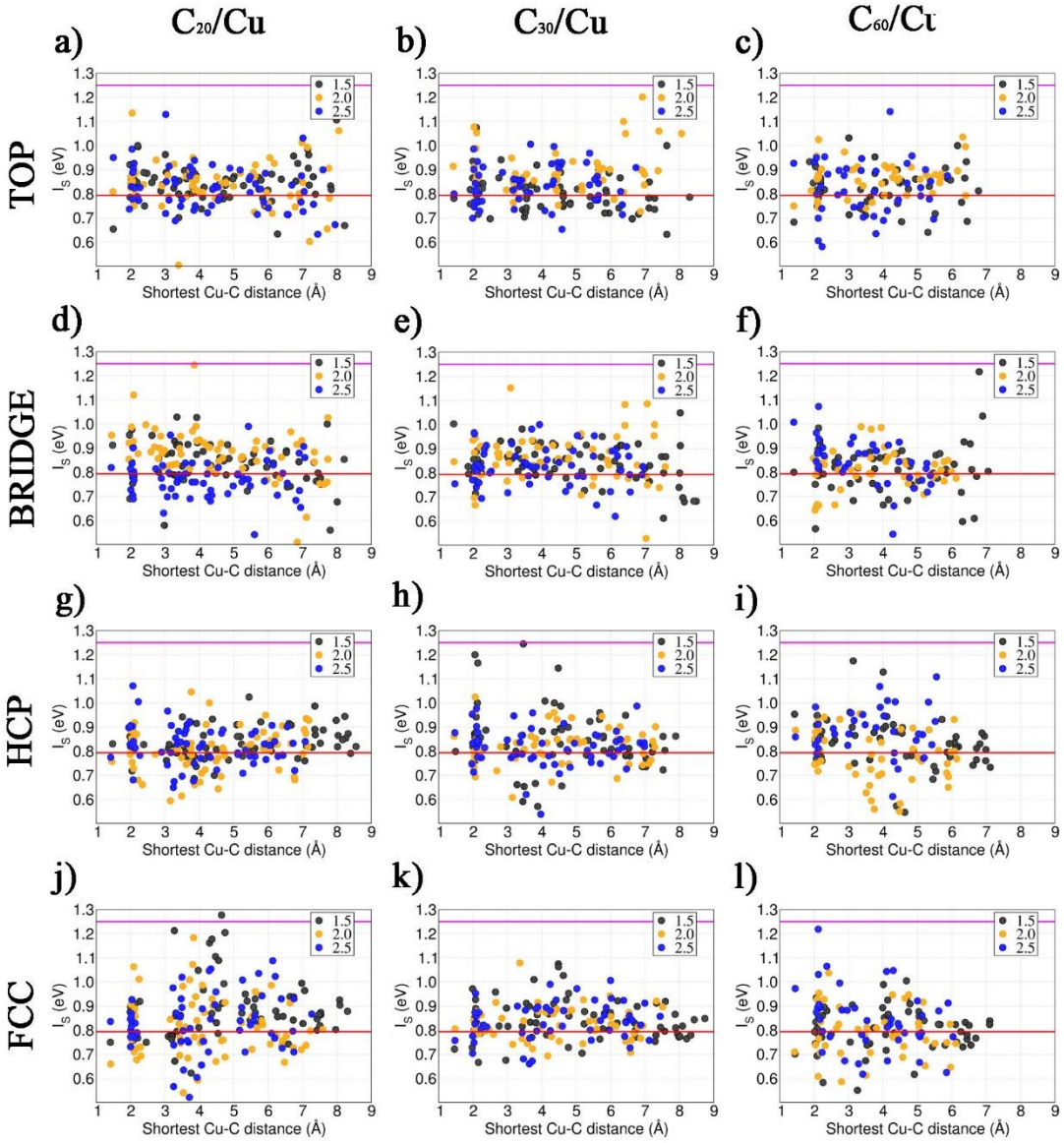

Figure B.3: Cu-atom resolved Stoner exchange integral (I_S) as function of the shortest Cu-C distance for the simulated Cu-fullerene interfaces. The horizontal red line marks the value for bulk FCC Cu at the optimised lattice parameter (3.649 Å). The horizontal magenta line indicates the maximum I_S value (1.25 eV) computed for the interface between Cu and as deposited (1.7 gr/cm^3) amorphous carbon, measured to be ferromagnetic in Ref. [3] in Chapter 5. The computed Cu-resolved I_S values are both above and below the value of the bulk FCC Cu, with largest values in the 1.1-1.3 eV range for all the different systems considered, close and in cases above the largest value computed for as deposited ferromagnetic Cu-aC systems (I_S=1.25 eV).

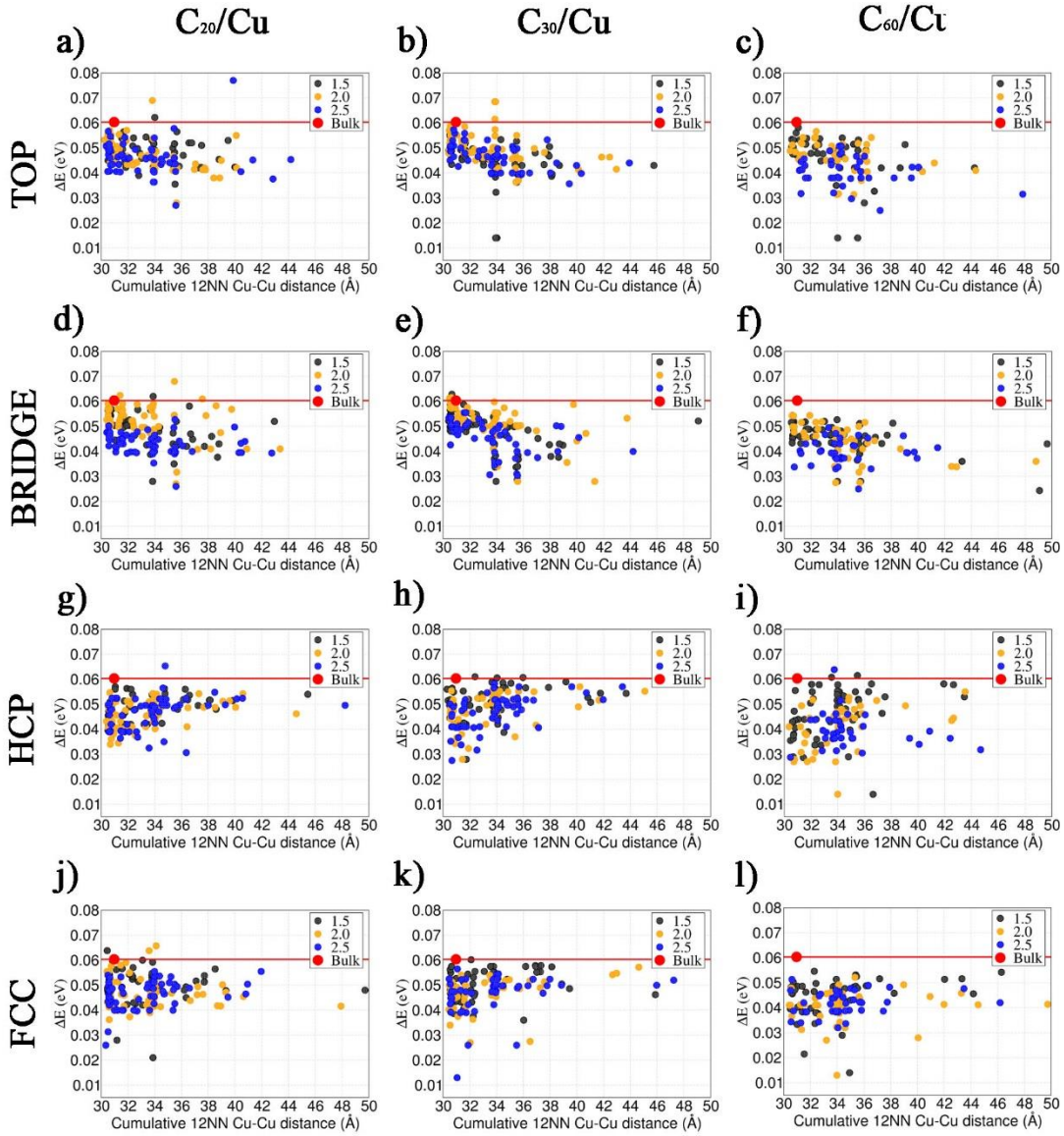

Figure B.4: Cu-atom resolved band-splitting (ΔE) as a function of the sum of the cumulative 12 NN Cu-Cu distance for the considered Cu-fullerenes interfaces. The horizontal red line marks the value for bulk FCC Cu at the optimised lattice parameter (3.649 Å). This analysis does not reveal any strong correlation between the parameters considered.

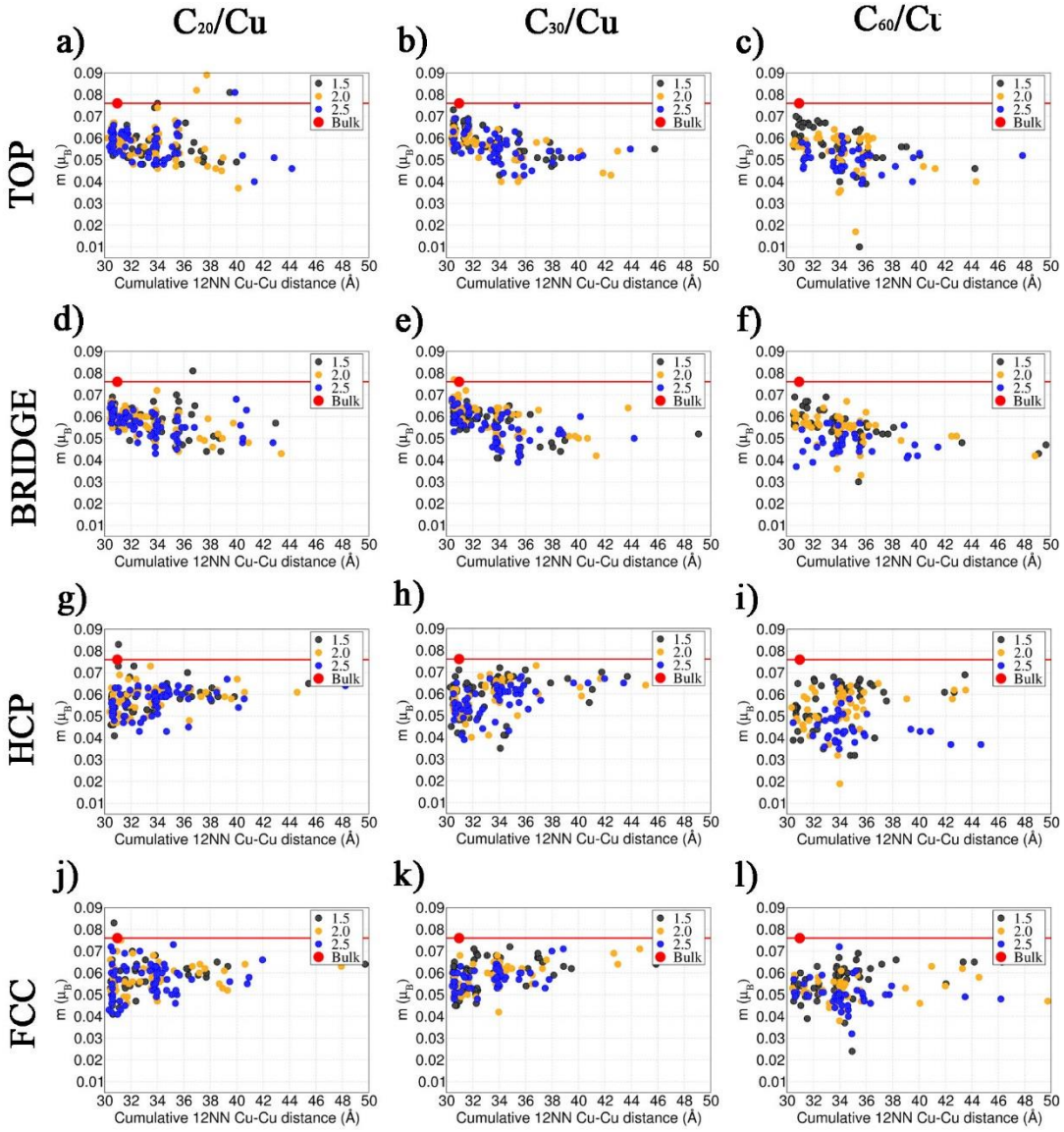

Figure B.5: Cu-atom resolved magnetic moment (m) as a function of the 12 NN Cu-Cu distances for the considered Cu-fullerenes interfaces. The horizontal red line marks the value for bulk FCC Cu at the optimised lattice parameter (3.649 Å). This analysis does not show any strong correlation between the parameters considered.

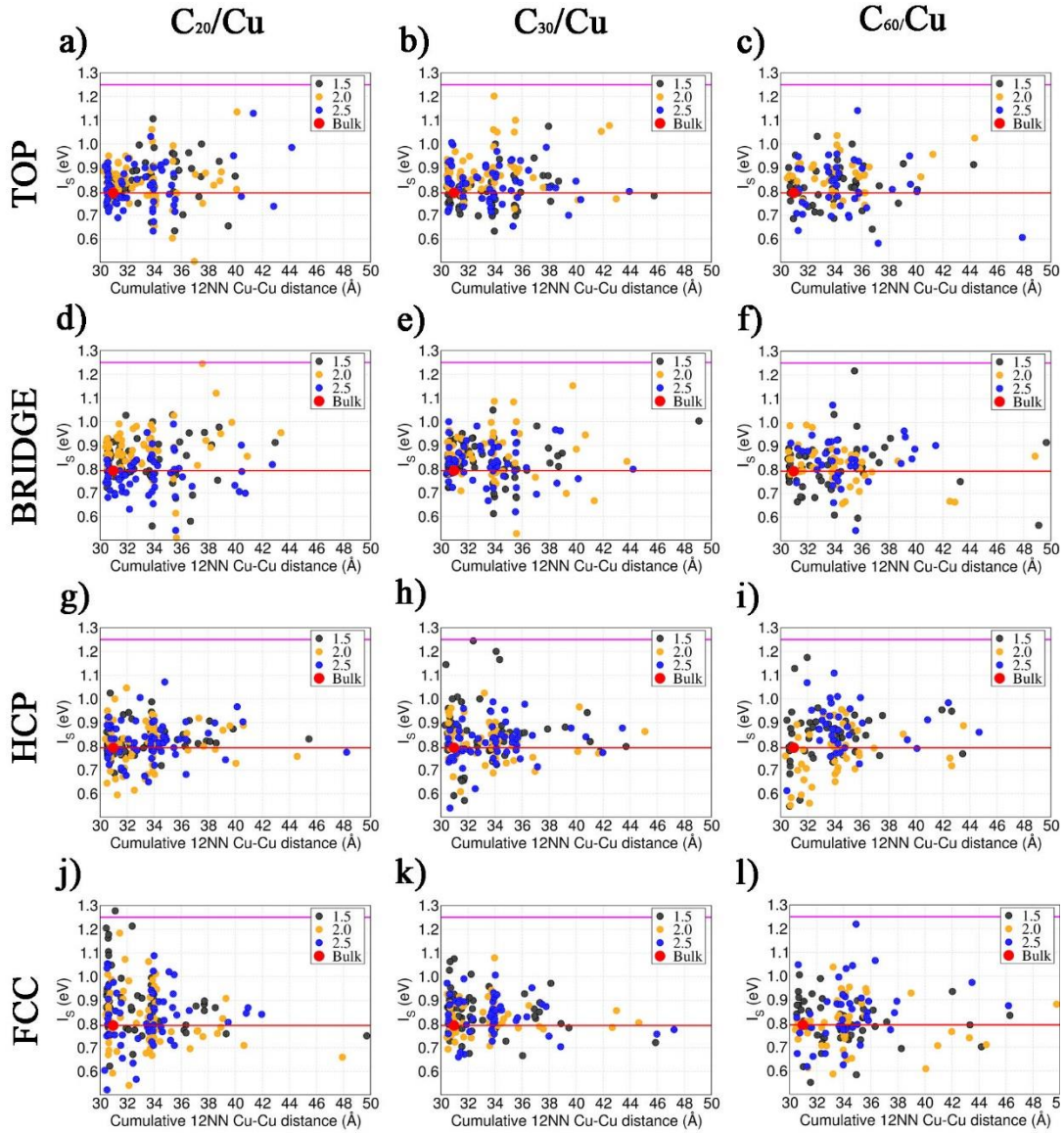

Figure B.6: Cu-atom resolved Stoner exchange integral (I_S) as a function of the 12 NN Cu-Cu distances for the simulated Cu-fullerene interfaces. The horizontal red line marks the value for bulk FCC Cu at the optimised lattice parameter (3.649 Å). The horizontal magenta line indicates the maximum I_S value (1.25 eV) computed for the interface between Cu and as deposited (1.7 gr/cm^3) amorphous carbon, measured to be ferromagnetic in Ref. [3] in Chapter 5. It is observed that loosening of the Cu lattice leads to larger (smaller) Cu-resolved I_S values for the interface models prepared with initial top and bridge (hcp and fcc) adsorption sites. These results highlight the importance of the initial geometry of the systems on the magnetic properties of the interface.

Appendix C

This appendix is a further analysis of Chapter 6. The atom-resolved band splitting (ΔE), atomic magnetic moment (m) and Stoner exchange integral (I_S) of the Cu-fullerenes interfaces have been computed as a function of the shortest Cu-C distances (Fig C.1) and the cumulative 12 NN Cu-Cu distances (Fig. C.2). The total and fullerene-resolved computed Cu → onion Bader charge transferred as a function of the initial Cu-onion cut-off distance and slab-averaged cumulative 12 NN Cu-Cu distance is presented in Fig. C.3.

As shown in Fig. C.1, the computed Cu-resolved, PAW-integrated, band-splitting (ΔE) and atomic magnetic moment (m) turn out to be lower than for bulk Cu FCC for all the Cu-onion interface-models studied. No strong correlation is found between the computed ΔE and m for a given Cu-atom and its distance from the fullerene cage.

The direct (inverse) contribution of ΔE and m to the approximated Stoner exchange integral (I_S, Chapter 2, Eq. 2.88) leads to scattering of the computed Cu-resolved I_S values both above and below the result for bulk FCC Cu, with largest values in the 1.1-1.3 eV range for both the $C_{20}@C_{100}$ and $C_{20}@C_{180}$ interfaces (see Fig C.1). With the exception of one Cu-atom for the v geometry of the Cu-$C_{20}@C_{100}$ interface (Fig. C.1f) and the c geometry of the Cu-$C_{20}@C_{180}$ system (Fig. C.1i), all the Cu-resolved I_s-values turn out to be smaller than the maximum I_S computed for the (top) Cu-C_{60} interface models (in Appendix B, Fig. B.6c). These results provide the first indications that encapsulation of the C_{20} inside C_{100} and C_{180} leads to comparable but not strongly enhanced magnetic hardening of its interfaces with Cu by comparison to C_{60}.

Analysis of the computed atom-resolved ΔE, m, and I_S (Fig. C.2) as a function of the Cu-lattice loosening, quantified by the slab-averaged sum of the 12 nearest-neighbours (NN) distances, does not reveal any strong correlation between these parameters. Given the different adsorption geometries studied (Fig. 6.1 and Fig. 6.3)

this result reiterates that the volume excluded by the carbon-onion appears to be the dominant factor for the magnetic hardening induced by onions of different volume and curvature as considered here.

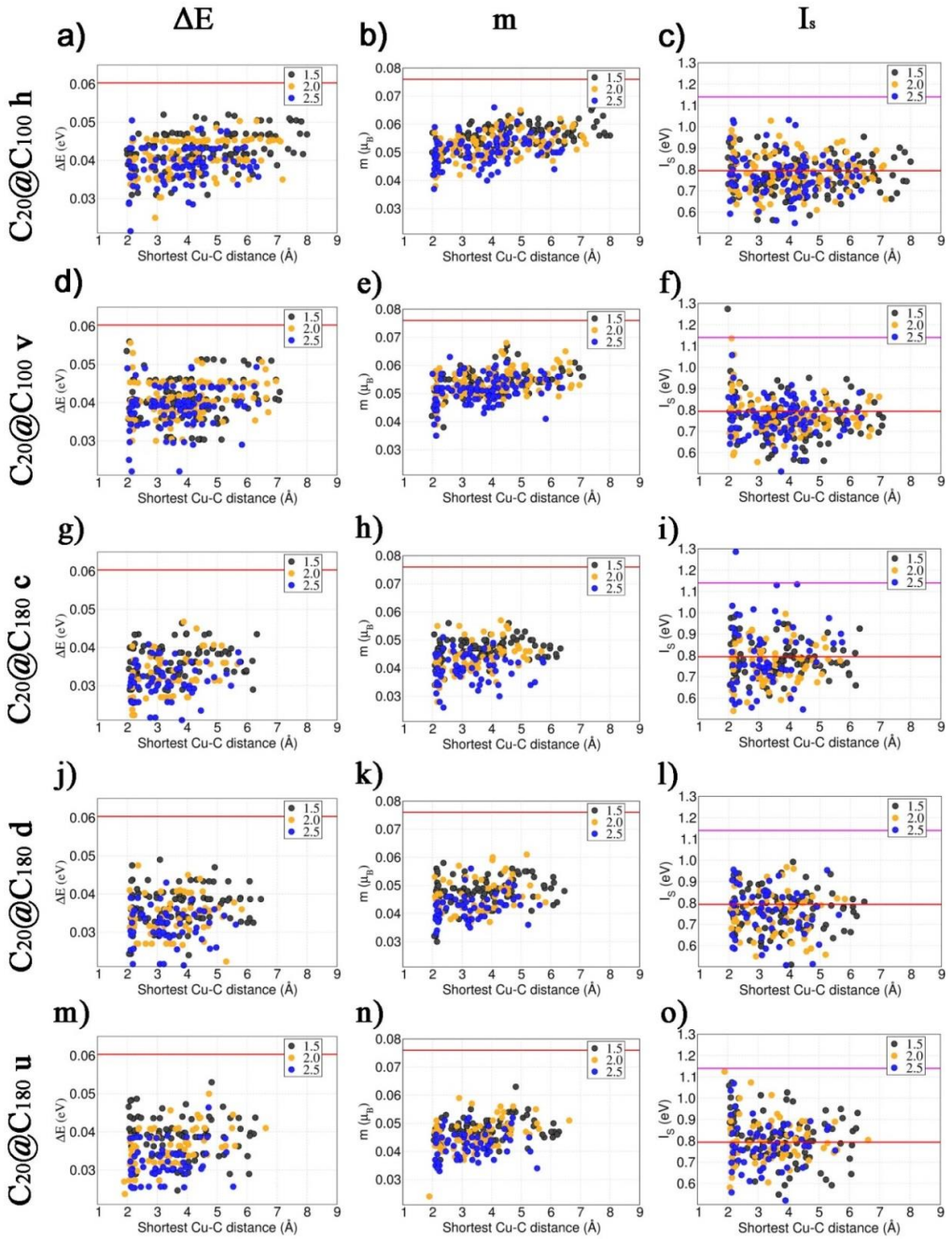

Figure C.1: Cu-atom resolved band-splitting (ΔE), atomic magnetic moment (m) and Stoner exchange integral (I_S) as a function of the shortest Cu-C distance for the interface models studied. The horizontal red line marks the values for bulk FCC Cu at the optimised lattice parameter (3.649 Å). The horizontal magenta line marks the maximum I_S value (1.14 eV) computed for (top) Cu-C_{60} interface in Appendix B (Fig. B.6c). The computed ΔE and m for a given Cu-atom do not show any strong correlation with the distance from the fullerene cage. The computed Cu-resolved I_S show values both above and below the result for bulk FCC Cu, with largest values in the 1.1-1.3 eV range for both the C_{20}@C_{100} and C_{20}@C_{180} interfaces. These results lead to comparable but not strongly enhanced Cu magnetic hardening for the considered onions by comparison to Cu-C_{60} interface models.

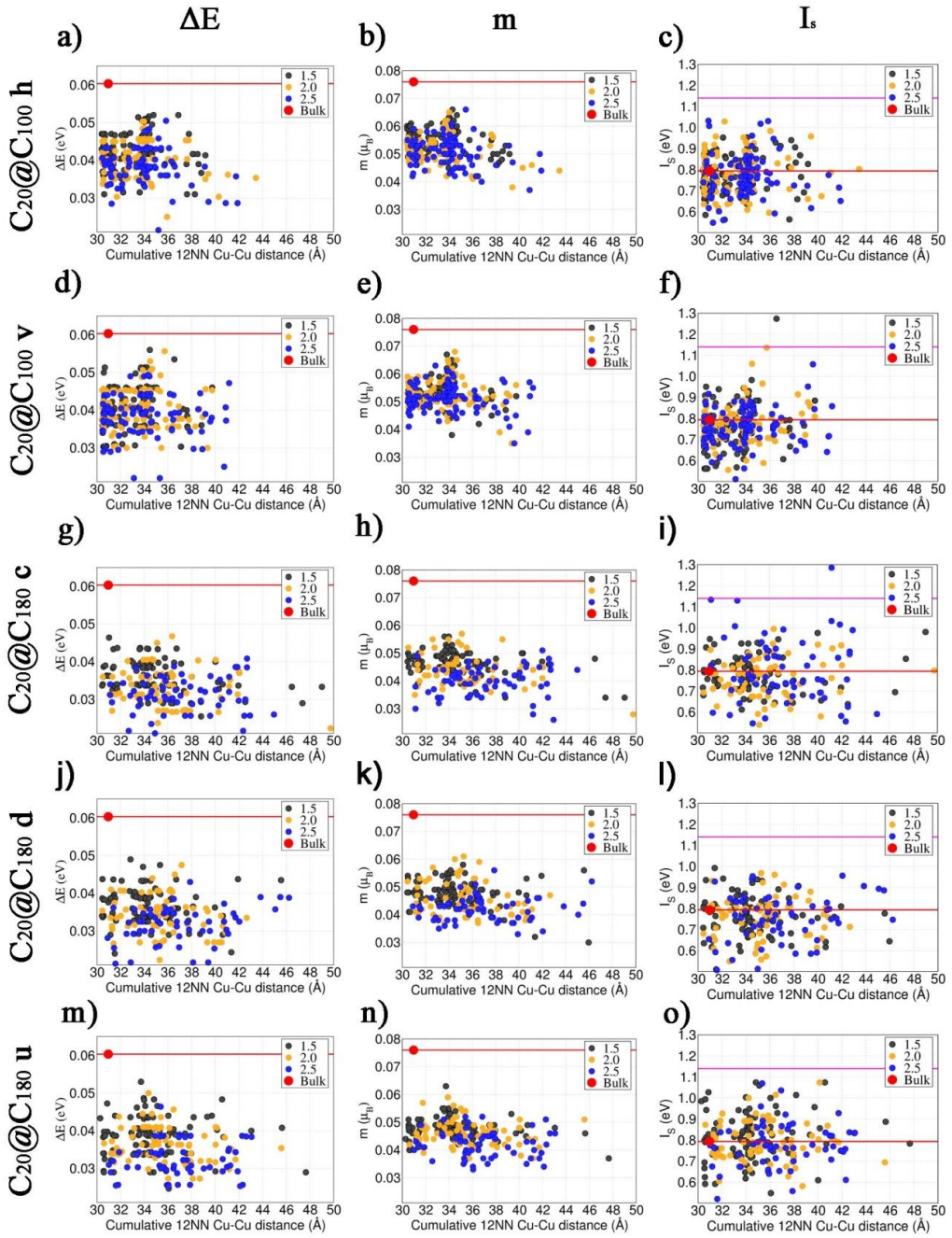

Figure C.2: Cu-atom resolved band-splitting (ΔE), atomic magnetic moment (m) and Stoner exchange integral (I_S) as a function of as a function of the slab-averaged sum of the 12 NN Cu-Cu distances for the interface models studied. The horizontal red line marks the values for bulk FCC Cu at the optimised lattice parameter (3.649 Å). The horizontal magenta line marks the maximum I_S value (1.14 eV) computed for (top) Cu-C_{60} interface in Appendix B (Fig. B.6c). This analysis does not reveal any strong correlation between the parameters considered.

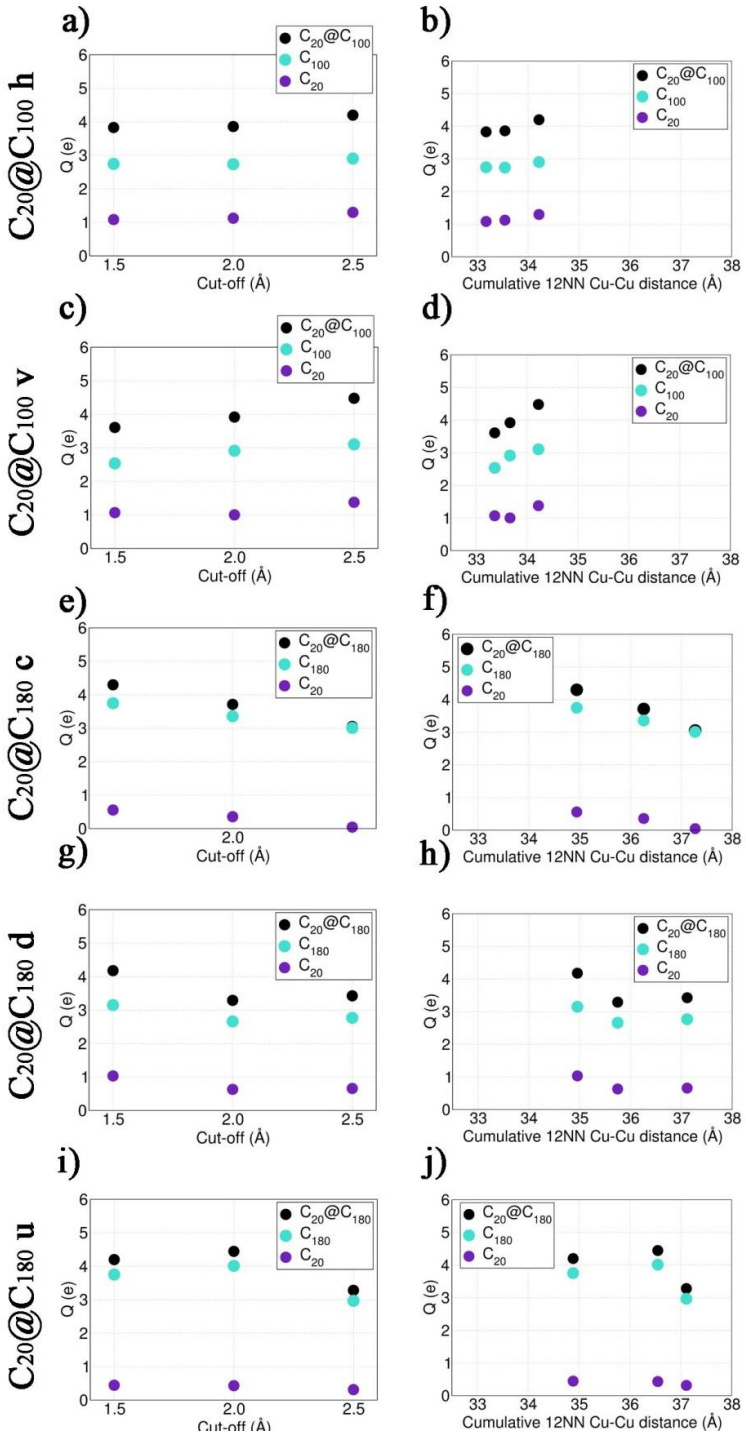

Figure C.3: Total and fullerene-resolved computed Cu → onion Bader charge transferred (Q, e) as a function of the initial Cu-onion cut-off distance (**a, c, e, g, i**) and slab-averaged cumulative 12 NN Cu-Cu distance (**b, d, f, h, j**) for the interface models considered. All the considered systems mostly localise the electronic charge subtracted to the Cu on the outer C_{100} and C_{180} fullerenes (from over 60% to nearly 98%).